

ASYMPTOTIC SOLUTIONS TO THE DIFFUSIVITY EQUATION: VALIDATION
AND FIELD APPLICATIONS

A Dissertation

by

ZHENZHEN WANG

Submitted to the Office of Graduate and Professional Studies of
Texas A&M University
in partial fulfillment of the requirements for the degree of

DOCTOR OF PHILOSOPHY

Chair of Committee, Michael J. King
Committee Members, Akhil Datta-Gupta
Peter Valkó
Richard Gibson
Head of Department, Jeff Spath

December 2018

Major Subject: Petroleum Engineering

Copyright 2018 Zhenzhen Wang

ABSTRACT

Unconventional resources have come to play an increasingly important role in both the US and world energy supply. The success of their development is due to the wide application of hydraulic fracturing techniques, which create complex fracture geometries with large effective areas. A reliable characterization of the fracture/horizontal well system and resulting reservoir depletion becomes a challenging task for both analytic and numerical approaches. In this dissertation, we tried to combine a novel coordinate system together with a series of semi-analytic approximations, to reveal the direct relationship between production data and the transient drainage volume, and predict recovery.

We first studied how a pressure front propagates in an infinite domain under fixed rate production, which is crucial to welltest analysis and drainage volume calculation. To avoid the expenses of numerical simulation, we developed an alternative approach by directly solving the propagation equation for the pressure “front” which can be derived using asymptotic ray theory. It draws upon an analogy between a propagating pressure front and a propagating wave front, making it applicable to pressure transient analysis.

Next, we showed the development and validation of new asymptotic approximations to handle both variable rate drawdown and boundary effects. We extended the utility of the semi-analytic solutions to more realistic cases, including large changes in reservoir properties, pressure transient analysis with wellbore storage, and rate transient analysis in bounded reservoirs. This technique enables us to describe pressure propagation from fractured wells into the surrounding formations and a better drainage volume

characterization, which is useful for both well spacing calculation and multi-stage fracture spacing optimization.

Finally, we proposed a data-driven model-free approach for production data analysis. It provides a simple and intuitive understanding of the transient drainage volume and instantaneous recovery efficiency, irrespective of the complexity of the reservoir depletion geometry. The novel drainage volume diagnostic plot yields better physical resolution and which can identify more detailed characteristics of the underlying flow geometry. The results of the analysis have been used for the characterization of hydraulic fracture and reservoir properties, including the prediction of fracture surface area, matrix permeability, and estimated ultimate recovery.

DEDICATION

To my parents and fiancée for their endless love and support.

ACKNOWLEDGEMENTS

First and foremost, I would like to express my deepest gratitude to my advisor, Dr. Michael J. King for his academic guidance and financial support throughout my five-year Ph.D. education. His immense knowledge, insightful view, and continuous encouragement helped me overcome all the challenges in the completion of this study, which would be extremely helpful for my future career.

I am also very grateful to Dr. Akhil Datta-Gupta, the co-director of the MCERI group, for his innovative ideas and support for industrial internship opportunities. I would like to extend my sincere appreciation to my other respected committee members, Dr. Peter Valkó and Dr. Richard Gibson, as well as Dr. Bobby Reece who served as the substitute during my final exam, for their insightful comments and valuable suggestions to improve the contents of this research.

I also would like to thank Kaveh Dehghani, Xian-Huan Wen, Shusei Tanaka, Adwait Chawathe, Jiang Xie, Jincong He, Han-Young Park, Leonardo Bermudez, Yunhui Tan, Alvaro Rey, Zhiming Wang, Yanbin Zhang, and Song Du for their supervision and mentorship during my summer internships with Chevron ETC. I largely enriched the precious industrial experiences and greatly broadened my horizons.

Thanks also go to Chen Li, Changdong Yang, Xu Xue, Peng Zhou, Rui Kou, and the other unmentioned MCERI members and friends at Texas A&M University, for providing me with a wonderful and memorable life in College Station.

Finally, special thanks to my parents and beloved fiancée, Kejun.

CONTRIBUTORS AND FUNDING SOURCES

Contributors

This work was supervised by a dissertation committee consisting of Professors Michael J. King (advisor), Akhil Datta-Gupta, and Peter Valkó of the Department of Petroleum Engineering and Professor Richard Gibson of the Department of Geology.

The results of Fast Marching Method simulations throughout this dissertation were contributed by Chen Li and was published in 2017. The development of superposition of 20 hydraulic fracture synthetic case was conducted in collaboration with Andrew Malone and was published in 2018.

All the other work for the dissertation was completed independently by the student.

Funding Sources

This work was made possible by the financial support of Energi Simulation (formerly Foundation CMG) through the Texas A&M chair in Robust Reduced Complexity Modeling with Dr. Eduardo Gildin and the support of the members of the Model Calibration and Efficient Reservoir Imaging (MCERI) joint industry project at Texas A&M University.

TABLE OF CONTENTS

	Page
ABSTRACT	ii
DEDICATION	iv
ACKNOWLEDGEMENTS	v
CONTRIBUTORS AND FUNDING SOURCES.....	vi
TABLE OF CONTENTS	vii
LIST OF FIGURES.....	ix
LIST OF TABLES	xviii
CHAPTER I INTRODUCTION	1
1.1 Introduction.....	2
1.2 Asymptotic Pressure Approximation for Fixed Rate Drawdown	5
1.3 Generalized Asymptotic Approximation for Variable Rate Drawdown and Bounded Reservoirs.....	8
1.4 Unconventional Reservoir Analysis.....	12
CHAPTER II ASYMPTOTIC PRESSURE APPROXIMATION FOR FIXED RATE DRAWDOWN.....	15
2.1 Introduction	15
2.1.1 Eikonal Equation and the Diffusive Time of Flight	18
2.1.2 Geometric Pressure Approximation to the Diffusivity Equation	23
2.2 Methodology: 1-D Diffusivity Equation and Properties	25
2.2.1 1-D Formulation of the Diffusivity Equation.....	25
2.2.2 Asymptotic Pressure Approximation	40
2.2.3 Spatial Integral vs. Time Integral	60
2.3 Validation of the Asymptotic Approximation via Simulation	72
2.3.1 Validation of the Asymptotic Approximation: Homogeneous Cases	72
2.3.2 Validation of the Asymptotic Approximation: Simulation with Heterogeneity	85
2.4 Discussion	93
2.5 Chapter Summary.....	97

CHAPTER III GENERALIZATION OF THE ASYMPTOTIC APPROXIMATION TO VARIABLE RATE AND BOUNDED RESERVOIRS	101
3.1 Introduction	101
3.1.1 Pressure Transient Analysis	104
3.1.2 Rate Transient Analysis and Decline Curve Analysis for Conventionals.....	107
3.1.3 Unconventional Reservoir EUR Prediction	112
3.2 Methodology: Extension to Variable Rate Drawdown	116
3.2.1 Superposition in Time	116
3.2.2 Asymptotic Solutions to Variable Rate Drawdown	123
3.2.3 Determining Number of Asymptotic Terms in the Approximation	131
3.2.4 Superposition Time and Material Balance Time.....	150
3.3 Methodology: Extension to Bounded Reservoirs.....	164
3.3.1 Superposition in Space	164
3.3.2 Generalized Asymptotic Solution to Bounded Reservoirs.....	168
3.3.3 EUR Prediction	190
3.4 Discussion	196
3.5 Chapter Summary.....	200
CHAPTER IV UNCONVENTIONAL RESERVOIR ANALYSIS	203
4.1 Introduction	203
4.1.1 Production Analysis for Unconventional Reservoirs	205
4.1.2 Previous Drainage Volume Calculation and Inversion	208
4.2 Methodology: Improved Production Analysis	212
4.2.1 Production Data Processing and Drainage Volume Calculation.....	212
4.2.2 $w(\tau)$ Drainage Volume Geometry Function Inversion.....	224
4.3 Field Application: Montney Field.....	237
4.3.1 Field Introduction and Production Data Illustration	237
4.3.2 Traditional Pressure Transient Analysis	239
4.3.3 Diagnostic Analysis based on the Drainage Volume	243
4.3.4 EUR Prediction	245
4.4 Discussion	248
4.5 Chapter Summary.....	250
CHAPTER V CONCLUSIONS AND FUTURE RESEARCH DIRECTIONS	252
5.1 Summary and Conclusions.....	252
5.2 Future Research Directions	256
NOMENCLATURE.....	257
REFERENCES.....	266

LIST OF FIGURES

	Page
Figure 2.1 Solutions to the Eikonal equation in a heterogeneous medium using the Fast Marching Method (a) $\tau^2/4$ in days (log scale) for a vertical well and (c) for a vertical well with an infinite conductivity fracture (b) log permeability field (Datta-Gupta <i>et al.</i> , 2011)	20
Figure 2.2 Solution to the Eikonal equation for a horizontal well with multistage hydraulic fractures in a homogeneous gas reservoir using the Fast Marching Method (a) Hydraulic fractures ($\tau \approx 0$) (b) $\tau^2/4 \leq 3$ months (c) $\tau^2/4 \leq 6$ months (d) $\tau^2/4 \leq 1$ year (Datta-Gupta <i>et al.</i> , 2011)	21
Figure 2.3 Streamtube geometry used to reduce the 3-D diffusivity equation to 1-D (reprinted with permission from Wang et al, 2018)	26
Figure 2.4 Analog between the $w(\tau)$ formulation in heterogeneous reservoirs and the circular drainage volume in a homogeneous reservoir	29
Figure 2.5 Illustration of heterogeneous reservoir model with $V_{DP} = 0.6$ and $HI = 0.210$ (a) Log10 of permeability distribution; (b) diffusive time of flight distribution; (c) Pressure drop distribution during transient period; (d) Pressure drop distribution during PSS period; (e) Cross plot of pressure drop vs. DTOF during transient period; (f) Cross plot of pressure drop vs. DTOF during PSS period.....	36
Figure 2.6 Illustration of heterogeneous reservoir model with $V_{DP} = 0.6$ and $HI = 0.840$ (a) Log10 of permeability distribution; (b) diffusive time of flight distribution; (c) Pressure drop distribution during transient period; (d) Pressure drop distribution during PSS period; (e) Cross plot of pressure drop vs. DTOF during transient period; (f) Cross plot of pressure drop vs. DTOF during PSS period.....	38
Figure 2.7 Illustration of heterogeneous reservoir model with $V_{DP} = 0.3$ and $HI = 0.032$ (a) Log10 of permeability distribution; (b) diffusive time of flight distribution; (c) Pressure drop distribution during transient period; (d) Pressure drop distribution during PSS period; (e) Cross plot of pressure drop vs. DTOF during transient period; (f) Cross plot of pressure drop vs. DTOF during PSS period.....	39
Figure 2.8 Numerical demonstration of the asymptotic pressure approximation for a well in the center of a heterogeneous reservoir model (reprinted with permission from King et al., 2016).....	49

Figure 2.9 Spatial profile of the fixed rate drawdown solution to the asymptotic pressure approximation in terms of the time derivative of the pressure drop, normalized to its value at the wellbore ($\tau = 0$) (reprinted with permission from Wang et al, 2018)	52
Figure 2.10 Graphical solution to the Eikonal equation and the calculation of $V_p(r)$ for an infinite conductivity fracture (top view)	64
Figure 2.11 Diagnostic plot validation for an infinite conductivity fracture (reprinted with permission from King et al., 2016)	66
Figure 2.12 Graphical solution to the Eikonal equation and PSS flow in the vicinity of an infinite conductivity fracture (top view).....	66
Figure 2.13 Dimensionless pressure distribution w.r.t t_D vs. r_D for (a) and (d) numerical inverse Laplace transform (exact); (b) and (c) asymptotic solution and error of pressure from time integral; (e) and (f) asymptotic solution and error of pressure from spatial integral.....	71
Figure 2.14 Dimensionless pressure time derivative distribution w.r.t t_D vs. r_D for (a) numerical inverse Laplace transform (exact); (b) asymptotic solution; (c) difference between asymptotic and exact solutions	71
Figure 2.15 Dimensionless pressure spatial gradient distribution w.r.t t_D vs. r_D for (a) numerical inverse Laplace transform (exact); (b) asymptotic solution; (c) difference between asymptotic and exact solutions	72
Figure 2.16 Comparison of the distribution of the pressure drop time derivative between the asymptotic and ECLIPSE results at various times	75
Figure 2.17 (a) DOI time map from asymptotic solution; (b) DOI time map from ECLIPSE; (c) Cross plot of DOI time between asymptotic and ECLIPSE results and (d) DOI asymptotic prediction vs. time for infinite acting radial flow (reprinted with permission from Wang et al, 2017)	76
Figure 2.18 Comparison of the distribution of the pressure drop time derivative between the asymptotic derivative and ECLIPSE results at various times for the case of an infinite conductivity hydraulic fracture (reprinted with permission from Wang et al, 2017)	79
Figure 2.19 Cross plots of pressure drop from ECLIPSE vs. DTOF at various times for the case of an infinite conductivity hydraulic fracture.....	80
Figure 2.20 Midland Basin fracture job evolution (Pioneer, 2016)	80

Figure 2.21 Contour of log of normalized dimensionless pressure time derivative of infinite conductivity fracture case	82
Figure 2.22 (a) DOI time map from asymptotic solution; (b) DOI time map from ECLIPSE; (c) Cross plot of DOI time between asymptotic and ECLIPSE results and (d) DOI Boltzmann variable vs. time for case with infinite conductivity hydraulic fracture (reprinted with permission from Wang et al, 2017)	84
Figure 2.23 Illustration of the impact of hydraulic fracture on different locations along the same DTOF contour.....	84
Figure 2.24 Log10 of permeability (first column), the corresponding DTOF (second column), and cross plot between asymptotic solutions vs. ECLIPSE results (third column) with $L_{DCL} = 1.00$ and various V_{DP} values	87
Figure 2.25 Illustration of (a) pressure drop, (b) $w(\tau)$ and (c) $\ln w(\tau)/\ln \tau$ vs. τ for case with $V_{DP} = 0.90$ and $L_{DCL} = 1.00$	88
Figure 2.26 Log10 of permeability (first column), the corresponding DTOF (second column), and cross plot between asymptotic solutions vs. ECLIPSE results (third column) with $V_{DP} = 0.60$ and various L_{DCL} values.....	89
Figure 2.27 Illustration of (a) pressure drop, (b) $w(\tau)$ and (c) $\ln w(\tau)/\ln \tau$ vs. τ for case with $V_{DP} = 0.60$ and $L_{DCL} = 0.02$	90
Figure 2.28 DTOF and pressure drop for cases with (a) and (b) $V_{DP} = 0.6$; (c) and (d) $V_{DP} = 0.6$ at fixed $L_{DCL} = 0.25$	90
Figure 2.29 Summary of pressure drop derivative from asymptotic solution vs. ECLIPSE results for all the nine heterogeneous cases	92
Figure 2.30 Summary of R^2 vs. HI , V_{DP} , and L_{DCL} of all the nine heterogeneous cases.....	93
Figure 3.1 Fayetteville Shale well (a) production data; (b) Diagnostic plot with RNP_{wf} and RNP'_{wf} and (c) illustration of long time drawdown behavior of the MTFW geometry (Song and Ehlig-Economides, 2011).....	106
Figure 3.2 Illustration of both transient and boundary portions ($0 \leq b \leq 1$) of Fetkovich Type Curves.....	111
Figure 3.3 History matching and forecasting of the rate performance using Arps' hyperbolic, SEPD, and Duong's decline methods (Mahmoud <i>et al.</i> , 2018).....	115

Figure 3.4 EUR prediction using different analysis methods (Mahmoud <i>et al.</i> , 2018).....	116
Figure 3.5 Illustration of a production history with variable rate, adapted from Houze <i>et al.</i> (2015)	117
Figure 3.6 Diagnostic plot validation of dimensionless flux generated by superposition in time and the exact solutions from inverse Laplace transform for an infinite acting radial flow with fixed BHP drawdown (reprinted with permission from Wang et al, 2017)	121
Figure 3.7 Diagnostic plots validation of (a) dimensionless flux and (b) dimensionless pressure generated by superposition in time and exact solutions from the inverse Laplace transform for an infinite acting radial flow with wellbore storage and fixed rate drawdown (reprinted with permission from Wang et al, 2017)	122
Figure 3.8 Comparison between ECLIPSE (black curves) and asymptotic solutions (red dots) of pressure drop time derivative vs. product of τ and exponential term for fixed BHP drawdown under (a) linear-linear scale and (b) log-log scale	124
Figure 3.9 Comparison of (a) q_{sfD} , q'_{sfD} (red curves) of fixed BHP drawdown; (b) $1/RNP$ of fixed rate (red curves) and BHP (green curves) drawdown with the corresponding exact solutions from inverse Laplace transform (black dashed curves) for an infinite reservoir	127
Figure 3.10 Comparison of Diagnostic plot of (a) q_{sfD} , q'_{sfD} (red curves) and (b) p_{wfD} , p'_{wfD} (red curves) by RNP transient and the corresponding exact solutions from inverse Laplace transform (black dashed curves) of wellbore storage solutions with zero skin.....	130
Figure 3.11 Comparison of Diagnostic plots of (a) q_{sfD} , q'_{sfD} (red curves) and (b) p_{wfD} , p'_{wfD} (red curves) and the corresponding exact solutions from inverse Laplace transform (black dashed curves) for Scenario 1 of two-term asymptotic approximation	134
Figure 3.12 Comparison of Diagnostic plots of (a) q_{sfD} , q'_{sfD} (red curves) and (b) p_{wfD} , p'_{wfD} (red curves) and the corresponding exact solutions from inverse Laplace transform (black dashed curves) for Scenario 2 of two-term asymptotic approximation	136
Figure 3.13 Comparison of Diagnostic plots of (a) q_{sfD} , q'_{sfD} (red curves) and (b) p_{wfD} , p'_{wfD} (red curves) and the corresponding exact solutions from inverse	

Laplace transform (black dashed curves) for Scenario 3 of two-term asymptotic approximation	137
Figure 3.14 Comparison of Diagnostic plots of (a) q_{sfD} , q'_{sfD} (red curves) and (b) p_{wfd} , p'_{wfd} (red curves) and the corresponding exact solutions from inverse Laplace transform (black dashed curves) for Scenario 4 of two-term asymptotic approximation	138
Figure 3.15 Comparison of Diagnostic plots of (a) q_{sfD} , q'_{sfD} (red curves) and (b) p_{wfd} , p'_{wfd} (red curves) and the corresponding exact solutions from inverse Laplace transform (black dashed curves) for three-term asymptotic approximation	142
Figure 3.16 Comparison of Diagnostic plots of (a) q_{sfD} , q'_{sfD} (red curves) and (b) p_{wfd} , p'_{wfd} (red curves) and the corresponding exact solutions from inverse Laplace transform (black dashed curves) for Scenario 1 of one-term asymptotic approximation	144
Figure 3.17 Comparison of Diagnostic plots of (a) q_{sfD} , q'_{sfD} (red curves) and (b) p_{wfd} , p'_{wfd} (red curves) and the corresponding exact solutions from inverse Laplace transform (black dashed curves) for Scenario 2 of one-term asymptotic approximation	146
Figure 3.18 Comparison of $1/RNP$ vs. time, superposition time, and material balance time for infinite acting radial flow (reprinted with permission from Wang et al, 2017).....	154
Figure 3.19 Comparison of $1/RNP$ vs. time and material balance time for bounded radial flow (reprinted with permission from Wang et al, 2017)	155
Figure 3.20 Diagnostic plot and drainage volume vs. material balance time for the case with an infinite conductivity fracture (reprinted with permission from Wang et al, 2017).....	156
Figure 3.21 Comparison between superposition time calculated by various models and the actual superposition time for infinite acting radial flow (reprinted with permission from Wang et al, 2017)	159
Figure 3.22 Comparison between superposition times calculated by various models and the actual superposition time for bounded radial flow (reprinted with permission from Wang et al, 2017)	160
Figure 3.23 Comparison of difference of RNP time derivative between ECLIPSE and models using asymptotic, superposition time, and material balance	

time solutions for fixed BHP drawdown at various times (reprinted with permission from Wang et al, 2017)	162
Figure 3.24 Cross plots of RNP time derivative between ECLIPSE results vs. models using asymptotic, superposition time, and material balance time solutions for fixed BHP drawdown at various times (reprinted with permission from Wang et al, 2017)	163
Figure 3.25 Illustration of a two-well interference problem (reprinted with permission from Wang et al, 2017)	165
Figure 3.26 Illustration of the pressure distribution during well interference (pressure distribution at $t = 40$ days) of a two-well model	167
Figure 3.27 Comparison of fixed rate drawdown solutions in a bounded reservoir: asymptotic solutions (dash) with reference solutions (solid) in (a) log-log scale and (b) linear-linear scale	168
Figure 3.28 Illustration of the pressure front interaction at the interface between porous media (reprinted with permission from Wang et al, 2017).....	171
Figure 3.29 Comparison of composite reservoir solutions (dash) with reference solutions (solid), dimensionless with respect to the inner region properties (reprinted with permission from King et al., 2016).....	173
Figure 3.30 Comparison of composite reservoir solutions (dash) with reference solutions (solid), dimensionless with respect to the outer region properties (reprinted with permission from King et al., 2016).....	174
Figure 3.31 Comparison of fixed rate drawdown solutions in a bounded reservoir: asymptotic solutions (dash) with reference solutions (solid) (reprinted with permission from King et al., 2016).....	176
Figure 3.32 Drainage volume calculations (reprinted with permission from King et al., 2016)	177
Figure 3.33 Comparison of Fetkovich Type Curve and analytic solutions (reprinted with permission from King et al., 2016).....	186
Figure 3.34 RNP' and drainage volume vs. time calculated using asymptotic 1-exponential, 2-exponential, 3-exponential, and inf-exponential term approximations for bounded radial flow (reprinted with permission from Wang et al, 2017).....	187

Figure 3.35 Comparison of pressure drop time derivative distribution calculated from ECLIPSE and the asymptotic 1-exponential, 3-exponential, and inf-exponential term solutions for bounded radial flow (transition period) (reprinted with permission from Wang et al, 2017)	187
Figure 3.36 Comparison of pressure drop time derivative difference between ECLIPSE and asymptotic 1-exponential, 3-exponential, and inf-exponential term solutions for bounded radial flow (transition period) (reprinted with permission from Wang et al, 2017)	188
Figure 3.37 Comparison of pressure drop time derivative distribution calculated from ECLIPSE and asymptotic 1-exponential, 3-exponential, and inf-exponential term solutions for bounded radial flow (BDF period) (reprinted with permission from Wang et al, 2017)	189
Figure 3.38 Comparison of pressure drop time derivative difference between ECLIPSE and asymptotic 1-exponential, 3-exponential, and inf-exponential term solutions for bounded radial flow (BDF period) (reprinted with permission from Wang et al, 2017)	189
Figure 3.39 Comparison of drainage volume vs. time (in log-log and linear-linear scale, respectively) between ECLIPSE and asymptotic 1-exponential, 3-exponential, and inf-exponential term solutions for bounded radial flow (reprinted with permission from Wang et al, 2017)	190
Figure 3.40 Illustration of EUR prediction	191
Figure 3.41 Model overview of (a) bounded radial flow and (b) bounded linear flow (reprinted with permission from Wang et al, 2018)	191
Figure 3.42 ECLIPSE and asymptotic approximation results of bounded radial flow with (a) fixed rate and (b) fixed BHP drawdown (reprinted with permission from Wang et al, 2018)	193
Figure 3.43 ECLIPSE and asymptotic approximation results of bounded linear flow with (a) fixed rate and (b) fixed BHP drawdown (reprinted with permission from Wang et al, 2018)	196
Figure 4.1 Multiple fractures in a naturally fractured reservoir (a) Model illustration and (b) Pressure distributions at 3 months, 1 year, and 3 years (Yang, 2017)	205
Figure 4.2 Drainage volume diagnostic plot $w(\tau)$ vs. τ for a single-fracture in a bounded reservoir model, adapted from Sharma (2016)	208

Figure 4.3 Overview of previous drainage volume calculation, adapted from Yang <i>et al.</i> (2015).....	209
Figure 4.4 Illustration of reduced oscillation in the previous drainage volume inversion (reprinted with permission from Wang et al, 2018).....	211
Figure 4.5 Illustration of $w(\tau)$ inversion result by previous algorithm with (a) monotonic drainage volume; and (b) non-monotonic drainage volume.....	211
Figure 4.6 Illustration of removing outliers via regression analysis	214
Figure 4.7 Comparison of (a) production history; (b) Diagnostic plot; (c) RNP; and (d) RNP' between variable rate drawdown (RNP: red markers with red curves; RNP': green markers with green curves) and the corresponding fixed rate drawdown (RNP: black solid curves; RNP': black dashed curves) for infinite conductivity hydraulic fracture case	215
Figure 4.8 Illustration of data smoothing procedure with modified Friedman's Super Smoother	219
Figure 4.9 Illustration of outlier removal procedure with Moving Linear Regression Analysis	222
Figure 4.10 Illustration of (a) <i>RNP</i> derivative outlier removal and (b) Diagnostic plot before and after the outlier removal	222
Figure 4.11 Overview of proposed drainage volume calculation (reprinted with permission from Wang et al, 2018)	223
Figure 4.12 (a) $V(t)$ comparison among optimization input from ECLIPSE (black curve), unconstrained (green curve), and constrained (red curve) optimizations; (b) $w(\tau)$ comparison among unconstrained (green curve), constrained (red curve) optimizations, and analytic value (blue line).....	227
Figure 4.13 Comparison of $w(\tau)$ inversion results by SPADES (reference), previous algorithm, and new algorithm with non-monotonic drainage volume	227
Figure 4.14 Comparison of bounded linear flow drainage volume inversion results using various lengths of production history for (a) $w(\tau)$ vs. τ and (b) $V_p(\tau)$ vs. τ (reprinted with permission from Wang et al, 2018)	230
Figure 4.15 Comparison of bounded radial flow drainage volume inversion results using various lengths of production history for (a) $w(\tau)$ vs. τ and (b) $V_p(\tau)$ vs. τ (reprinted with permission from Wang et al, 2018)	230

Figure 4.16 Comparison of bounded linear flow drainage volume inversion results using known τ_{res} and 1-term exponential kernel and various lengths of production history for (a) $w(\tau)$ vs. τ and (b) $V_p(\tau)$ vs. τ	231
Figure 4.17 Comparison of bounded linear flow drainage volume inversion results using known τ_{res} and 3-term exponential kernel and various lengths of production history for (a) $w(\tau)$ vs. τ and (b) $V_p(\tau)$ vs. τ	232
Figure 4.18 ECLIPSE model overview of 10-HF MTFW case (reprinted with permission from Wang et al, 2018)	233
Figure 4.19 Prediction results comparison between 1 & 3 exponential terms asymptotic solutions of 10-HF MTFW case (a) Δp_{wf} vs. Q_w plot for fixed rate drawdown; (b) $1/RNP$ vs. Q_w plot for fixed BHP drawdown (reprinted with permission from Wang et al, 2018)	235
Figure 4.20 Reservoir volume sensitivity for EUR prediction on $1/RNP$ vs. Q_w plot of (a) bounded linear flow; (b) 10-HF MTFW case (reprinted with permission from Wang et al, 2018)	237
Figure 4.21 Overview of production history (reprinted with permission from Wang et al, 2018)	238
Figure 4.22 Illustration of RNP vs. material balance time of Montney Well	238
Figure 4.23 Pressure transient analysis for t_{elf} with (a) Diagnostic plot (b) Specialized plot (reprinted with permission from Wang et al, 2018).....	240
Figure 4.24 Pressure transient analysis for t_{elf} with (a) Diagnostic plot (b) Specialized plot using processed RNP'.....	241
Figure 4.25 Illustration of six buildup periods with (a) buildup data (b) data slopes	242
Figure 4.26 Buildup analysis with (a) Diagnostic plot (b) Specialized plot (reprinted with permission from Wang et al, 2018)	243
Figure 4.27 (a) $V(t)$ comparison among optimization input from field production data (black curve), unconstrained (green curve), and constrained (red curve) optimizations; (b) $w(\tau)$ comparison among unconstrained (green curve) and constrained (red curve) optimizations (reprinted with permission from Wang et al, 2018)	244
Figure 4.28 Montney well EUR predictions with (a) $q_{w,cutoff} = 6.72 \times 10^3$ Mscf/day and (b) $q_{w,cutoff} = 3.36 \times 10^3$ Mscf/day as well as reservoir volume uncertainty on $1/RNP$ vs. Q_w plot.....	247

LIST OF TABLES

	Page
Table 2.1 Initial and boundary conditions for the Eikonal and Diffusivity Equations for an infinite acting reservoir	31
Table 2.2 Reservoir heterogeneity parameters of the heterogeneous models	34
Table 2.3 Solution characteristics of the asymptotic pressure approximation for fixed rate drawdown based upon the time derivative of the drawdown pressure drop (reprinted with permission from Wang et al, 2018).....	53
Table 2.4 τ , V_p , and $w(\tau)$ for infinite acting radial flow and infinite conductivity fracture.....	61
Table 2.5 Reservoir, fluid and wellbore parameters for infinite acting radial flow and a case with an infinite conductivity facture	73
Table 2.6 Summary of determination coefficient R^2 of all the nine heterogeneous cases.....	91
Table 3.1 Summary of equations to be solved in each scenario of wellbore storage cases with 2 asymptotic terms	139
Table 3.2 Summary of equations to be solved in each scenario of wellbore storage cases with 1 asymptotic term.....	147
Table 3.3 Summary of the combinations of equations that provided the best solutions for fixed and variable rate drawdown and the wellbore storage with 1, 2, or 3 asymptotic terms	149
Table 3.4 Standard results for the superposition time functions for multi-rate drawdown and simple models (reprinted with permission from Wang et al, 2017).....	152
Table 3.5 Reservoir, fluid and wellbore parameters for infinite acting radial flow bounded radial flow, and a case with an infinite conductivity facture	153
Table 3.6 Summary of the superposition time models and the corresponding abbreviations.....	159
Table 3.7 Reservoir, fluid and wellbore parameters for homogeneous radial flow with a fixed BHP drawdown in a rectangular reservoir	161

Table 3.8 Reservoir, fluid and wellbore parameters for a two-well model.....	167
Table 3.9 Diffusion kernels for different inner and outer boundary conditions.....	179
Table 3.10 Reservoir, fluid and well properties of the bounded radial flow model (reprinted with permission from Wang et al, 2018)	192
Table 3.11 Fixed rate and BHP drawdown results of bounded radial flow (reprinted with permission from Wang et al, 2018)	194
Table 3.12 Reservoir, fluid and wellbore properties of the bounded linear flow model (all other parameters are the same as the BRF model)	195
Table 3.13 Fixed rate and BHP drawdown results of bounded linear flow (reprinted with permission from Wang et al, 2018)	196
Table 4.1 Reservoir, fluid and wellbore properties of 10-HF MTFW case (reprinted with permission from Wang et al, 2018)	233
Table 4.2 Reservoir, fluid and wellbore properties of Montney field (reprinted with permission from Wang et al, 2018)	239

CHAPTER I

INTRODUCTION

Unconventional resources have come to play an increasingly important role in both the US and world energy supply (Holditch, 2013). The success of their development is due to the wide application of hydraulic fracturing techniques, which create complex fracture geometries with large effective areas. A reliable characterization of the fracture/horizontal well system and resulting reservoir depletion becomes a challenging task for both analytic and numerical approaches.

In this study we introduce an analytic solution technique for the diffusivity equation, which provides a direct relationship between production data and the reservoir drainage volume (King *et al.*, 2016). The analytic formulation provides for the direct calculation and extension of many simple well test, rate transient and well performance concepts such as depth of investigation, welltest derivative, drainage volume, flow regimes and well productivity. As with other analytic approaches, these solutions allow superposition in space and in time, which provides for the solution for multiple wells, multiple flow rates, and bounded and composite reservoirs (Wang *et al.*, 2017). We validate our approach against well-known solutions in pressure and rate transient analysis usually solved in Laplace space, as well as those from numerical reservoir simulation with commercial simulators. Our study demonstrates that the new approach yields results very close to those reference solutions and indicates how to extend these solutions to problems with heterogeneity and complex fractured well geometry. The treatment we present is

faster than numerical finite difference simulation and allows for the development of fundamental relationships between reservoir performance and reservoir and well characteristics. Based on the understanding of capability of the analytic pressure approximation, we further propose a novel data-driven approach for production analysis of unconventional reservoirs without the traditional rate/pressure transient analysis assumptions of specific flow regimes (Wang *et al.*, 2018). The approach relies on a $w(\tau)$ function, which is a drainage volume geometry function, to characterize the flow geometry from the transient drainage volume. The approach has been used to rank refracturing candidates (Yang *et al.*, 2016) and to obtain optimal well spacing (Huang *et al.*, 2017). In this study, we generalize the previous studies (Yang *et al.*, 2015; King *et al.*, 2016; Xue *et al.*, 2016; Wang *et al.*, 2017) to improve the amount of quantitative reservoir information obtained during the production analysis.

1.1 Introduction

Understanding how a pressure front propagates in reservoir formations is very important to welltest analysis and reservoir drainage volume estimation. Due to the large computational time and expenses of numerical simulation, an alternative approach has been developed by directly solving the propagation equation for the pressure “front” defined as the maximum pressure response for an impulse source. Such a propagation equation can be derived using asymptotic ray theory which has been used extensively in electromagnetic and seismic wave propagation (Virieux *et al.*, 1994). The asymptotic

method draws upon an analogy between the propagating pressure front and a propagating wave, making it applicable to pressure transient analysis in the petroleum industry.

The pressure front equation is in the form of the Eikonal equation, which is a high frequency asymptotic solution of the diffusivity equation in heterogeneous reservoirs and whose properties are well developed in the literature. Most importantly, the Eikonal equation can be solved very efficiently by a class of numerical solutions called the Fast Marching Methods (FMM) (Sethian, 1999) for a “diffusive time of flight” (DTOF, denoted as τ) that governs the propagation of the “pressure front” in porous media (Vasco *et al.*, 2000; Kulkarni *et al.*, 2001; Datta-Gupta and King, 2007). The DTOF can be used as a spatial coordinate to reduce the 3-D diffusivity equation into an equivalent 1-D form, leading to a comprehensive simulator for rapid performance prediction in reservoirs. Recently, papers on this specific subject have been published, providing a rapid approximation of drainage volume, pressure depletion and well performance without actually running conventional numerical simulations (Datta-Gupta *et al.*, 2011; Zhang *et al.*, 2013; Zhang *et al.*, 2014; Nunna *et al.*, 2015; Pasumarti *et al.*, 2015; Xie *et al.*, 2015b, a; Yang *et al.*, 2015; Fujita *et al.*, 2016; King *et al.*, 2016; Li and King, 2016; Li, 2016; Yang *et al.*, 2016; Iino *et al.*, 2017; Wang *et al.*, 2017; Wang *et al.*, 2018). A better understanding of the drainage volume is of great help in well spacing and multi-stage fracture spacing optimization. Additional potential applications includes fixed or slowly variable rate drawdown in bounded reservoirs, drainage volume description, production data integration, etc.

The advantage of the approach is its capability to solve fluid flow in both simple and complicated reservoir geometries and with heterogeneity, in contrast to the simple situations that conventional methods are able to handle. Despite many successful applications, however, the accuracy of the approach still remains not fully tested or proven. This study is the first one that tests the accuracy and self-consistency of the approach. This research has pointed out limitations of the previous approach and has provided improved versions of the asymptotic solution, which involves both reflection and transmission processes when pressure fronts cross the interface between different porous media. Results calculated from the new equation were compared to those obtained via the conventional exact solutions in the Laplace domain as well as those from a commercial reservoir simulator, including a discussion of impact of inner boundary conditions, infinite acting radial flow with wellbore storage and skin factor, radial flow in bounded reservoir, radial flow in composite reservoir, etc. This study demonstrates that the new approach yields results very close to the solutions calculated via numerical inversion of Laplace transform or numerical reservoir simulations, indicating a high applicability of the new asymptotic solutions during pressure transient analysis. Therefore, we further propose a novel data-driven approach for production analysis of unconventional reservoirs to better characterize the underlying flow geometry, e.g., complex near fracture flow, linear flow, fracture interference, etc. The results of the analysis have been used for the characterization of hydraulic fracture and reservoir properties, including the prediction of matrix permeability, stimulated reservoir volume (SRV), and finally extended to the calculation of the estimated ultimate recovery (EUR).

1.2 Asymptotic Pressure Approximation for Fixed Rate Drawdown

The propagation of pressure in a reservoir is fundamental to the understanding and prediction of reservoir performance. For reservoirs undergoing primary depletion, the governing equation is the diffusivity equation, which relates pressure drops and flow rates, both for the purpose of performance prediction and for the inversion of production data for reservoir and well characterization. Analytic solutions to the diffusivity equation under-ly the methodologies for both pressure transient analysis (PTA) and rate transient analysis (RTA) (Lee, 1982; Horne, 1995; Bourdet, 2002; Thambynayagam, 2011). Although these solutions are limited to simplified descriptions of reservoir properties and well configurations, they provide significant insight into reservoir and well characteristics. In contrast, numerical simulations are extremely flexible and are in principle able to integrate descriptions of the reservoir, wells, fluids and their interactions. Although extremely powerful, the many degrees of freedom within a simulator, and the corresponding non-uniqueness of a history match, often makes it difficult to gain the simple insights provided by the analytic approaches. These solutions are also potentially costly, especially for detailed simulation in 3-D, while an effective 1-D representation may be far more rapid to compute, whether using numerical or analytic techniques.

Unconventional reservoirs provide us with new challenges in reservoir characterization, but also new opportunities for methods of analysis (Valkó and Lee, 2010; Ilk *et al.*, 2011; Song and Ehlig-Economides, 2011; Cipolla and Wallace, 2014). These are reservoirs that are largely governed by primary depletion, but at sufficiently low

permeabilities that the clear distinctions between PTA and RTA are no longer applicable. The “short time” response of PTA, in which the reservoir is infinite acting, may now cover many years of production, while the “long time” response of RTA controlled by boundary dominated flow, may not have been achieved. In this chapter, a semi-analytic “asymptotic pressure approximation” is developed, which is an extension of the methodology of pressure transient analysis. It is sufficiently flexible to capture reservoir heterogeneity and complex fractured well configurations, while at the same time it provides overall characteristics as in PTA/RTA. As a numerical technique, this methodology has been applied to the investigation of unconventional reservoirs and the development of a comprehensive shale gas reservoir simulator (Datta-Gupta *et al.*, 2011; Zhang *et al.*, 2013; Zhang *et al.*, 2014; Xie *et al.*, 2015b, a; Fujita *et al.*, 2016; Huang *et al.*, 2017; Iino *et al.*, 2017). More recent work has applied the semi-analytic approach to the calculation of drainage volumes and instantaneous recovery ratios in unconventional reservoirs, to upscaling of reservoir flow properties, to pore scale carbonate reservoir characterization, and to the integration of well test data with geologic reservoir models (Nunna *et al.*, 2015; Pasumarti *et al.*, 2015; Yang *et al.*, 2015; King *et al.*, 2016; Li and King, 2016; Li, 2016; Xue *et al.*, 2016; Wang *et al.*, 2017; Wang *et al.*, 2018).

Despite these many successful applications, some questions are still not well resolved. In this chapter, I will try to provide answers to the most important two: What is the level of smoothly-varying heterogeneity required to retain accurate results? What are the integrability requirements of the analytic solutions and how reliable are they? I will focus on the examination of the key assumption that the pressure front propagation is

aligned with the τ contours as well as the validation of the proposed asymptotic pressure approximation. Therefore, the methodology of this chapter is divided into three sections. The first one is an introduction to the diffusive time of flight and its use as a spatial coordinate. By assuming that the pressure solution would always follow τ contours, the 3-D diffusivity equation in space is converted to its 1-D form in the τ coordinate. In the second section, I will mainly discuss an exponential decay of the pressure time derivative along the τ coordinate and further develop the semi-analytic asymptotic pressure approximation, which contains a series of unknown $A_n(t)$ functions to be determined by boundary conditions. The exponential trend is implied by the flux form of the diffusivity equation and describes the effect caused by the propagation of the early pressure front in a smoothly-varying formation heterogeneity. I will explore its validity through cases with permeability distributions at different variances and correlation lengths. The use of the τ coordinate as the basis of a formulation may be applied to either numerical or analytic calculations of pressure and rate. Numerous numerical applications can be found in the above references, but we will now emphasize the analytic calculations. There are two classes of calculations, fixed rate and variable rate drawdown. In this chapter, the asymptotic pressure approximation for a fixed rate drawdown is fully derived (King *et al.*, 2016). The third section is the comparison of the solution (pressure drop) accuracy between the spatial integral and the time integral approaches to the solution of the asymptotic pressure approximation. The asymptotic approximation will then be applied to a number of rate and pressure transient calculations to demonstrate and validate its utility

and characteristics. This will be followed by a discussion of the formulation and conclusions.

1.3 Generalized Asymptotic Approximation for Variable Rate Drawdown and Bounded Reservoirs

We have described a transformation based upon the Fast Marching Method (FMM) to describe the multi-dimensional diffusivity equation with heterogeneity as an equivalent 1-D diffusivity equation. The analytic solutions have been developed for fixed rate drawdown in an infinite acting system, and are not sufficiently general to describe either variable rate drawdown or boundary effects, both of which are required to analyze more realistic production scenarios in actual reservoirs. There is still a need to continue developing and validating new asymptotic analytic approximations to handle these problems, which provide for a number of novel applications including rapid numerical simulation, reservoir and well characterization, sensitivity-based inversion using production data, and dynamic upscaling and downscaling. The novel semi-analytic asymptotic pressure approximation for the solution of an equivalent 1-D diffusivity equation is able to approximate the 3-D solution with heterogeneity. Earlier approaches have relied upon the numerical solution of the 1-D equation, and provide all the flexibility expected of a numerical approach (Zhang *et al.*, 2013; Zhang *et al.*, 2014; Xie *et al.*, 2015b, a; Fujita *et al.*, 2016). However, analytic solutions provide for the derivation of explicit relationships between the geometry of a propagating pressure “front” within a reservoir and pressure and rate measured at wells. In this chapter, I will further develop the proposed

asymptotic pressure approximation to address both the rate and boundary effects. I first extend the analytic treatment beyond simple fixed rate drawdown to variable rate drawdown during the infinite acting transient period and test the predictions against analytic and numerical synthetic cases. When boundary effects (interference) come into the picture, e.g., well interference, fracture interference, and pressure front arrival at boundary, those solutions become less accurate. Even for unconventional reservoirs, fracture interference will occur early in the life of a well. With a wider employment of infill drilling and closer well spacing in shale developments we also expect to see increased well interference effects. In order to resolve these influences during field production analysis, asymptotic approximations are further extended to handle interference with superposition in space and in time (Wang *et al.*, 2017).

In this chapter, I conduct a systemic validation of the semi-analytic solution technique and extend its utility to more realistic cases, including large changes in reservoir properties, pressure transient analysis with wellbore storage, and rate transient analysis in bounded reservoirs with fixed rate or fixed BHP production. This technique provides us with the ability to describe pressure propagation from fractured wells into the surrounding formations and a better drainage volume characterization, which is useful for both well spacing calculation and multi-stage fracture spacing optimization in unconventional reservoirs. Not only is it useful for the direct calculation of various welltest, rate transient and well performance concepts such as depth of investigation, welltest derivative, flow regimes and well productivity, but it is also helpful to predict pressure and flux spatial distributions at any time of interest. The study verifies that the new approach yields results

very close to those generated by commercial simulators, indicating its promising application to rapid field production data analysis. As with other analytic approaches, the derived asymptotic solutions satisfy superposition in space and time, which leaves room for further application to field cases with multiple wells and varying flow rates (Lee *et al.*, 2003).

This chapter consists of two major sections of methodology, following a brief review of the asymptotic approximation for fixed-rate drawdown in an infinite domain as well as an introduction to the rate normalized pressure drop (RNP). In the variable rate drawdown section, superposition in time is utilized to develop a solution. Then, the asymptotic approximation is developed and tested with two special variable rate cases: fixed BHP drawdown and fixed rate drawdown with wellbore storage and a skin factor. Based on the asymptotic approximation and superposition theory, superposition time is defined in a general form for any flow geometry. This study demonstrates that superposition time reduces to material balance time when boundary dominated flow has been fully established within the reservoir or region of interest. The test results are discussed to develop conclusions on the application of superposition time and its approximation, material balance time, together with RNP in production analysis.

In the boundary effects section, I first illustrate how to further derive the analytic solution for multi-well cases based on fixed rate drawdown solution of a single well with the help of superposition in space and in time. The steady state drainage volume of each well can also be estimated accordingly and the proposed solution is tested and compared to simulation results obtained from a commercial simulator. Then, the asymptotic solution

is extended to account for finite reservoir boundary effects. When a pressure front hits the boundary, it will be reflected and start moving towards the well. The reflection will be reflected again when it arrives at the well sandface and this reflection-transmission process goes on forever. Based on the Method of Images (Lee, 1982), we need to have an infinite number of exponential terms in the asymptotic solution to account for imaginary wells (reflections). However, I will show that in the current approach, only a minimal number of exponential terms is required to guarantee an accurate result. The asymptotic solution is generalized as well as the expression for the drainage volume. The new analytic solution is verified using the Fetkovich Type Curves (Fetkovich, 1980), which are widely used in decline curve analysis. Our treatment is faster than numerical finite difference simulation and allows for the development of fundamental relationships between reservoir performance and reservoir & well characteristics. Lastly, the generalized asymptotic approximation will be used for EUR prediction and the results will be validated against mechanistic simulations, e.g., bounded radial/linear flow as well as multiple transverse fracture wells (MTFW) cases. With the mechanistic models, I illustrate how the key features would show on diagnostic plots, e.g., linear flow, onset of fracture interference, partial completion effects, complex non-linear flow, and the development of the SRV.

To sum up, this chapter is made up of two sections of methodology as described above, which address the most important two scenarios during production: rate and boundary effects. Tests on the newly developed asymptotic approximations are also performed to validate the derivations. At the conclusion of this chapter, they are ready for field production analysis.

1.4 Unconventional Reservoir Analysis

Unconventional tight/shale reservoirs have come to play an increasingly important role in energy supply and conducting reliable analysis on them is a challenging task. Due to the ultra low permeability associated with these reservoirs, their exploitation relies on horizontal wells together with multistage hydraulic fractures to achieve an economical production rate. The complex hydraulic plus natural fracture geometry, however, may result in a complex depletion pattern within the reservoir, and thus make the production analysis a challenging task for existing methodologies. Unlike conventional reservoirs, unconventional reservoirs usually have a very long transient period and a relative short or even no production under boundary dominated flow before well abandonment. We will develop a way to conduct both fast and reliable pressure and rate transient analysis on unconventional reservoirs. The proposed techniques should be applicable to the following two scenarios: The first one is for low permeability & long interference time, which will be quite enough for single well analysis; the other one is for boundary dominated flow, which is crucial to handle multi-well interference. Beyond that, a new production analysis workflow is necessary and it should be robust enough to remove or at least minimize the influence of outliers in noisy production datasets. This kind of powerful workflow is unavailable or incomplete in the current literature.

With the asymptotic solutions derived in previous chapters, we further introduce a novel data-driven workflow for production analysis of unconventional reservoirs without the traditional rate transient and pressure transient (RTA/PTA) assumptions of specific

flow regimes. The approach uses a transient generalization of the Matthews-Brons-Hazebroek method (Matthews *et al.*, 1954) for the PSS drainage volume which relies on a $w(\tau)$ function to characterize the flow geometry from the transient drainage volume (Yang *et al.*, 2015). Together with a calculated instantaneous recovery ratio, it has been successfully used to rank refracturing candidates (Yang *et al.*, 2016) and to obtain optimal fracture spacing (Huang *et al.*, 2017). Given well pressure and flow rate data, the transient well drainage volume with time can be calculated. The time evolution of the drainage volume can be inverted to derive the $w(\tau)$ function which then provides a high resolution diagnostic plot that can be used for quantitative analysis to obtain fracture surface area, matrix properties, stimulated reservoir volume (SRV), and additional reservoir and fracture characteristics that are not apparent in the usual rate and pressure transient analysis techniques.

This chapter is organized as follows: I will first review the production analysis approaches for unconventional reservoirs in the general literature as well as the previous drainage volume calculation & inversion technique developed by our research group. Then, I will describe the improved production analysis for field data interpretation, which includes production data processing to obtain drainage volume vs. time calculation as well as a drainage volume geometry function inversion. The proposed methodology has been applied to field examples from the Montney shales successfully and the results are cross-validated by the traditional PTA and buildup analysis. Various flow regimes can be observed from our novel diagnostic plot, e.g., linear flow, partial completion, as well as fracture interference (Wang *et al.*, 2018). It also provides detailed characterization of

complex non-planar hydraulic fracture geometry, partial completion effects, the development and growth of the SRV, leading to the estimation EUR with given economic production rate.

In short, the major advantage of the proposed approach is the data-driven model-free analysis of production data without the presumption of specific flow regimes. It provides a simple and intuitive understanding of the transient drainage volume and EUR, irrespective of the complexity of the geometry of the reservoir depletion.

CHAPTER II
ASYMPTOTIC PRESSURE APPROXIMATION FOR FIXED RATE
DRAWDOWN*

2.1 Introduction

The propagation of pressure in a reservoir is fundamental to the understanding and prediction of reservoir performance. For reservoirs under-going primary depletion, the governing equation is the diffusivity equation, which relates pressure drops and flow rates, both for the purpose of performance prediction and for the inversion of production data for reservoir and well characterization. Analytic solutions to the diffusivity equation under-lye the methodologies for both pressure transient analysis (PTA) and rate transient analysis (RTA) (Lee, 1982; Horne, 1995; Bourdet, 2002; Thambynayagam, 2011; Houze *et al.*, 2015). Although these solutions are limited to simplified descriptions of reservoir properties and well configurations, they provide significant insight into reservoir and well characteristics. In contrast, numerical solutions are extremely flexible and are in principle able to integrate descriptions of the reservoir, wells, fluids and their interactions. Although extremely powerful, the many degrees of freedom within a simulator, and the

*Material adapted with permission from “Asymptotic Solutions of the Diffusivity Equation and Their Applications” by King et al., 2016: Paper SPE-180149-MS presented at SPE Europec featured at the 78th EAGE Conference and Exhibition held in Vienna, Austria, 30 May–2 June 2016. Copyright 2016, Society of Petroleum Engineers. Further reproduction prohibited without permission.

*Material adapted with permission from “Quantitative Production Analysis and EUR Prediction From Unconventional Reservoirs Using a Data-Driven Drainage Volume Formulation” by Wang et al., 2018: Paper EAGE-46177 to be presented at EAGE 16th European Conference on the Mathematics of Oil Recovery held in Barcelona, Spain, 3-6 September 2018. Copyright 2018, Wang et al. Further reproduction prohibited without permission.

corresponding non-uniqueness of a history match, often makes it difficult to gain the simple insights provided by the analytic approaches. These solutions are also potentially costly, especially for detailed simulation in 3-D, while an effective 1-D representation may be far more rapid to compute, whether using numerical or analytic techniques.

Unconventional reservoirs provide us with new challenges in reservoir characterization, but also new opportunities for methods of analysis (Valkó and Lee, 2010; Ilk *et al.*, 2011; Song and Ehlig-Economides, 2011; Cipolla and Wallace, 2014). These are reservoirs that are largely governed by primary depletion, but at sufficiently low permeabilities that the clear distinctions between PTA and RTA are no longer applicable. The “short time” response of PTA, in which the reservoir is infinite acting, may now cover many years of production, while the “long time” response of RTA controlled by boundary dominated flow, may not have been achieved. In this chapter, I will review the development of a semi-analytic “asymptotic pressure approximation” which is an extension of the methodology of pressure transient analysis. It is sufficiently flexible to capture reservoir heterogeneity and complex fractured well configurations, while at the same time it provides overall characteristics as in PTA/RTA. As a numerical technique, this methodology has been applied to the investigation of unconventional reservoirs and the development of a comprehensive shale gas reservoir simulator (Datta-Gupta *et al.*, 2011; Xie *et al.*, 2012a; Xie *et al.*, 2012b; Zhang *et al.*, 2013; Zhang *et al.*, 2014; Fujita *et al.*, 2016). More recent work has applied the semi-analytic approach to the calculation of drainage volumes and instantaneous recovery ratios in unconventional reservoirs, to upscaling of reservoir flow properties, to pore scale carbonate reservoir characterization,

and to the integration of well test data with geologic reservoir models (Nunna *et al.*, 2015; Pasumarti *et al.*, 2015; Yang *et al.*, 2015; Li and King, 2016).

This chapter will not focus on specific field applications. Instead I will apply the asymptotic pressure approximation to numerical or analytic problems for which solutions are available for validation. The focus will be on the development of the formulation and the validation of the approximate asymptotic pressure solutions of the diffusivity equation with fixed rate drawdown.

This chapter is organized as follows. We begin with an introduction to the Eikonal equation, the diffusive time of flight, and its use as a spatial coordinate. This will be followed by a brief summary of the semi-analytic geometric solution to the diffusivity equation derived and applied in the previous literature for performance analysis of unconventional reservoirs with complex geometry as well as anisotropic formation properties (Xie *et al.*, 2012a; Xie *et al.*, 2012b; Zhang *et al.*, 2013; Zhang *et al.*, 2014). Next is the methodology which consists of three subsections. The first one is the new 1-D formulation of the diffusivity equation, which may be applied to either numerical or analytic calculations of pressure and rate. Numerous numerical applications have already been cited, above. The second section of methodology will describe and develop the semi-analytic asymptotic pressure approximation. The asymptotic pressure approximation will then be applied to a number of rate and pressure transient calculations to demonstrate its utility and the nature of the asymptotic approximation. The third one will be a comparison of the accuracy between spatial integral and time integral on the asymptotic pressure

approximation. This will be followed by a validation of the formulation as well as a discussion on what we have learned through these tests.

2.1.1 Eikonal Equation and the Diffusive Time of Flight

The diffusive time of flight is determined from the solution of the Eikonal equation, which arises from the asymptotic (high frequency) limit of the diffusivity equation for the impulse pressure solution in a heterogeneous reservoir. This equation describes the propagation of a “pressure front” defined as the maximum of the pressure response for an impulse source or sink. Such propagation equations can be derived using asymptotic ray theory which has been used extensively in electromagnetic and seismic wave propagation (Virieux *et al.*, 1994), and also for pressure propagation in porous media (Vasco *et al.*, 2000; Kulkarni *et al.*, 2001; Datta-Gupta and King, 2007). The asymptotic method draws upon an analogy between the propagating pressure front and a propagating wave, providing us with the ability to represent pressure propagation from wells, through potentially complex hydraulic fractures, and into heterogeneous reservoir formations.

The diffusivity equation describes pressure transients within a heterogeneous porous medium.

$$\phi(\vec{x})\mu c_i \frac{\partial p(\vec{x}, t)}{\partial t} - \nabla \cdot \left(\vec{k}(\vec{x}) \cdot \nabla p(\vec{x}, t) \right) = 0 \quad (2.1)$$

Source and sink terms are not explicitly stated, but will appear as boundary conditions to the solution of the equation. The porosity and permeability may be heterogeneous, and we utilize the notation of a permeability tensor to represent directional permeability

anisotropy. We may apply a Fourier transform to Eq. (2.1) to obtain the diffusivity equation in the frequency domain:

$$\phi(\vec{x})\mu c_i(-i\omega)\tilde{p}(\vec{x},\omega)-\nabla\cdot\left(\vec{k}(\vec{x})\cdot\nabla\tilde{p}(\vec{x},\omega)\right)=0 \quad (2.2)$$

The intent is to find a pressure solution that mimics the one found in wave propagation, e.g., a solution in terms of an asymptotic series. For transient pressure response, the concepts from diffusive electromagnetic imaging can be utilized to describe frequency domain solutions (Virieux *et al.*, 1994).

$$\tilde{p}(\vec{x},\omega)=e^{-\sqrt{-i\omega}\tau(\vec{x})}\sum_{k=0}^{\infty}\frac{\tilde{A}_k(\vec{x})}{\left(\sqrt{-i\omega}\right)^k} \quad (2.3)$$

The leading terms of the high frequency limit ($\omega \rightarrow \infty$) represent the most rapidly varying portion of the solution and corresponds to the propagation of a sharp front. The quantity $\tau(\vec{x})$ in the leading exponential term of the asymptotic solution is the diffusive time of flight (DFOB), which controls the phase of propagation of the pressure front. It has units of $\sqrt{\text{time}}$. We will see once we develop the asymptotic pressure approximation that the quantity $(\tau^2/4)$ provides a characteristic time of propagation of the pressure front. The quantities $\tilde{A}_k(\vec{x})$ control the amplitude of the pressure front. In practice we will not need to solve for these terms in the asymptotic expansion, but will instead close our equations with one or more constraints expressed in time.

We may substitute the asymptotic series into the diffusivity equation. In the high frequency limit, the leading order term is of order ω . It gives rise to the Eikonal equation for the diffusive time of flight.

$$\nabla \tau(\vec{x}) \bullet \vec{k}(\vec{x}) \bullet \nabla \tau(\vec{x}) = \phi(\vec{x}) \mu c_i \quad (2.4)$$

It is solved subject to the boundary condition of $\tau = 0$ at the wellbore. For instance, for radial flow in an isotropic homogeneous reservoir we have the solution:

$$\tau = (r - r_w) \sqrt{\frac{\phi \mu c_i}{k}} = (r - r_w) / \sqrt{\alpha} \quad (2.5)$$

The quantity $\alpha = (k/\phi\mu c_i)$ is recognized to be the hydraulic diffusivity. For heterogeneous media we solve the Eikonal equation using the Fast Marching Method (FMM) (Sethian, 1999), as described more fully in Zhang *et al.* (2013). Examples of the solution of the Eikonal equation using the FMM are shown in the next two figures.

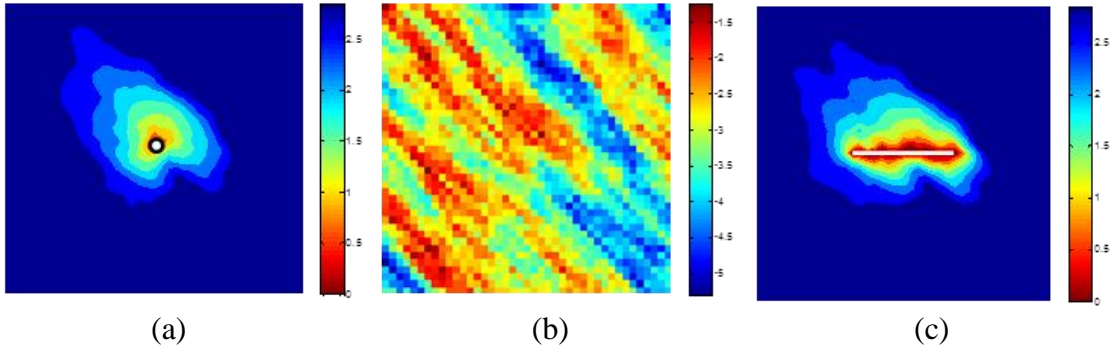


Figure 2.1 Solutions to the Eikonal equation in a heterogeneous medium using the Fast Marching Method (a) $\tau^2/4$ in days (log scale) for a vertical well and (c) for a vertical well with an infinite conductivity fracture (b) log permeability field (Datta-Gupta *et al.*, 2011)

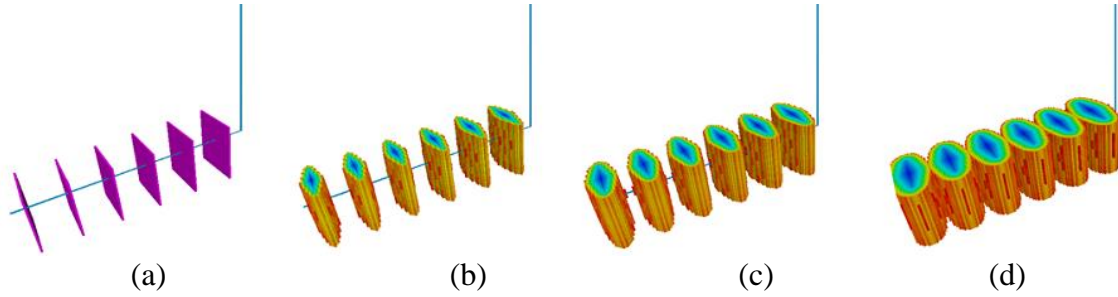


Figure 2.2 Solution to the Eikonal equation for a horizontal well with multistage hydraulic fractures in a homogeneous gas reservoir using the Fast Marching Method (a) Hydraulic fractures ($\tau \approx 0$) (b) $\tau^2/4 \leq 3$ months (c) $\tau^2/4 \leq 6$ months (d) $\tau^2/4 \leq 1$ year (Datta-Gupta *et al.*, 2011)

Figure 2.1 shows the impact of heterogeneity and boundary conditions on the diffusive time of flight. In this figure the color scale of the data display has been thresholded to better display the DTOF contours. In Figure 2.1 (a), instead of obtaining a radial solution, as in a homogenous reservoir, Eq. (2.5), the contours of τ now depend upon the spatial heterogeneity. The boundary condition of the calculation is $\tau = 0$ at the wellbore, $r = r_w$. Figure 2.1 (c) shows the solution for the DTOF for an infinite conductivity fracture. For infinite conductivity, $\frac{d\tau}{dr} = 0$ within the fracture and so the fracture is represented by the $\tau = 0$ contour. Again, the FMM shows the impact of spatial heterogeneity, but now from a fractured vertical well.

Figure 2.2 shows the DTOF for a horizontal well with multiple stages of hydraulic fractures. Simple planar hydraulic fractures and uniform reservoir properties are used in this calculation. The $\tau = 0$ initial condition of the calculation is specified at the perforations of the wellbore. This case includes a large but finite fracture conductance

within the calculation. From Eq. (2.5), τ in the fracture may be calculated analytically, while τ in the reservoir is calculated by the FMM.

A number of interesting features are apparent in this solution. In Figure 2.2 (b) and (c), the τ contours close to the fractures are straight lines forming a diamond shape. Since we have a homogeneous solution, this solution may also be obtained analytically. With infinite conductivity fractures, the straight line segments of the diamond are parallel to the fracture. This shape is controlled by the early time propagation of the pressure front, i.e., locations where pressure drop caused by the early pressure front starts to be detected will form the specific shape. As time increases, the late time PSS pressure contours will approach an elliptical shape, consistent with the well-known contours of pressure around a fracture (Kucuk and Brigham, 1979). This is an example where the pressure front will lose the alignment with the τ contours, and will be discussed in more detail in the section on validation. In Figure 2.2 (d) the τ contours of each fracture begin to overlap at 1 year, indicating the potential onset of interference. Strong interference will occur where the pressure front from one fracture reaches the next, i.e., at twice this distance, with a factor of 4 increase in τ^2 . Since we have close to linear flow between fractures, the depth of investigation $\left(\frac{\tau_{DOI}^2}{4t} = \frac{1}{2} \right)$ indicates that we will have strong interference at twice the characteristic time, i.e., at 8 years. We will return to a more detailed discussion of interference and the impact of no flow boundaries in the next chapter.

A note on units. All equations are derived in fundamental units, although results may be presented either in a dimensionless form or in field units. If we had chosen to express the Eikonal equation in field units we would have:

$$\nabla \tau(\vec{x}) \bullet \vec{k}(\vec{x}) \bullet \nabla \tau(\vec{x}) = 3792 \phi(\vec{x}) \mu c_i \quad (2.6)$$

Here permeability is in md , the units of τ are \sqrt{hr} , and the diffusivity $\alpha = \frac{1}{3792} \frac{k}{\phi \mu c_i}$ is in units of ft^2/hr . The use of fundamental units simplifies the exposition.

2.1.2 Geometric Pressure Approximation to the Diffusivity Equation

Xie *et al.* (2012a) showed a simple way to find the analytic solution to the diffusivity equation. The first step is to expression the diffusivity equation, Eq. (3.1), in a mixed form as

$$A(r) \phi c_i \frac{\partial p}{\partial t} = \frac{\partial q}{\partial r} \quad (2.7)$$

where, the Darcy flux is,

$$q = \frac{kA(r)}{\mu} \frac{\partial p}{\partial r} \quad (2.8)$$

$A(r)$ has different forms for linear, cylindrical, spherical flows, respectively.

Following chain rule, one can derive

$$\frac{\partial q}{\partial r} = \frac{\partial q}{\partial V_p} \frac{\partial V_p}{\partial r} = \frac{\partial q}{\partial V_p} \phi A(r) \quad (2.9)$$

Substituting Eq. (2.9) into Eq. (2.7) gives,

$$c_t \frac{\partial p}{\partial t} = \frac{\partial q}{\partial V_p} \text{ or } c_t \frac{\partial \Delta p}{\partial t} = -\frac{\partial q}{\partial V_p} \quad (2.10)$$

If we now neglect the Darcy flux beyond the drainage volume and assume that we have achieved pseudo steady state flow (PSS) within the entire drainage volume, then we can further obtain that

$$\frac{\partial \Delta p}{\partial t} \cong \frac{\partial \Delta \bar{p}}{\partial t} = \frac{q_w}{c_t V_p(t)} \quad (2.11)$$

$$\frac{d \Delta p_{wf}}{d \ln t} = t \frac{d \Delta p_{wf}}{dt} = \frac{q_w t}{c_t V_p(t)} \quad (2.12)$$

Eq. (2.11) was further used to determine pressure distribution and Eq. (2.12) was used for flow regime diagnostic, as shown in the literature (Xie *et al.*, 2012a; Xie *et al.*, 2012b; Zhang *et al.*, 2013; Zhang *et al.*, 2014).

There are a number of issues and limitations with this approach. The first is that it gives the incorrect answer for the pressure transient except in 2D, even for homogeneous systems (Gupta, 2012). A major limitation is that the derivation is based on a fixed rate drawdown and infinite acting reservoirs. The authors did not describe or provide suggestions on how to extent the applications to variable rate drawdown or bounded reservoir problems. Thus, their analytic approach may not be applicable even for fixed BHP drawdown. In this study, we will resolve these issues and limitations. Chapter 2 mainly focus on dealing with the first issue via a new approach as well as a new definition of drainage volume based on the entire domain.

2.2 Methodology: 1-D Diffusivity Equation and Properties

The methodology section consists of three subsections. The first one is a review of the new 1-D formulation of the diffusivity equation, which may be applied to either numerical or analytic calculations of pressure and rate. The second section of the methodology will describe and develop the semi-analytic asymptotic pressure approximation. The asymptotic pressure approximation will then be applied to a number of rate and pressure transient calculations to demonstrate its utility and the nature of the 1-D and asymptotic approximations. The third section will provide a comparison of the relative accuracy between the use of spatial integrals and time integration when developing solutions to the asymptotic pressure approximation.

2.2.1 1-D Formulation of the Diffusivity Equation

In this subsection, we transform the 3-D diffusivity equation for a heterogeneous porous medium into an equivalent diffusivity equation for flow along a 1-D streamtube of variable cross-sectional area. The formulation is based upon a transformation of the spatial variables into streamtube coordinates, with τ , the diffusive time of flight, as the spatial coordinate along the streamtube. The current development is an expansion of the derivation provided in the literature (Xie *et al.*, 2012a; Xie *et al.*, 2012b; Zhang *et al.*, 2013; Zhang *et al.*, 2014).

2.2.1.1 Diffusivity Equation along a Streamtube

We have noted a strong relationship between pressure contours and τ contours. This is not surprising since the Eikonal equation must be satisfied at all orders of the asymptotic expansion, Eq. (2.3), which itself is obtained from the diffusivity equation. We may reduce the 3-D diffusivity equation, Eq. (3.1), to an equivalent 1-D form if we assume that $p(\bar{x}, t) \approx p(\tau(\bar{x}), t)$, and then integrate the diffusivity equation over a streamtube volume from the well into the reservoir, up to a τ contour, Figure 2.3.

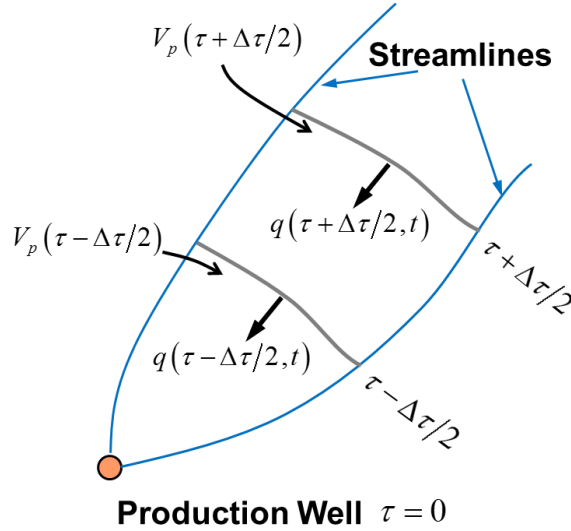


Figure 2.3 Streamtube geometry used to reduce the 3-D diffusivity equation to 1-D (reprinted with permission from Wang et al, 2018)

The spatial integration gives us an equation for the average pressure in the volume.

$$c_i V_p(\tau) \frac{\partial \bar{p}(\tau, t)}{\partial t} = -q_w + q(\tau, t) \quad (2.13)$$

Here $V_p(\tau)$ is the streamtube pore volume up to the τ contour. If we instead integrate the diffusivity equation over a thin volume at the τ contour, we obtain the diffusivity equation for $p(\tau, t)$, expressed in terms of the flux $q(\tau, t)$.

$$c_t \frac{\partial p(\tau, t)}{\partial t} = \frac{\partial q(\tau, t)}{\partial V_p(\tau)} = \frac{1}{w(\tau)} \frac{\partial q(\tau, t)}{\partial \tau} \quad \text{where} \quad w(\tau) = \frac{dV_p(\tau)}{d\tau} \quad (2.14)$$

To complete the derivation of the diffusivity equation, we need an expression for the flux.

To obtain the flux, $q = -\frac{1}{\mu} \vec{n} \cdot \vec{k} \cdot \nabla p$, we first obtain the inwardly directed normal area

from the gradient of the streamtube pore volume up to the τ contour.

$$\vec{n} = -\frac{1}{\phi(\vec{x})} \nabla V_p(\tau) = -\frac{w(\tau)}{\phi(\vec{x})} \nabla \tau \quad (2.15)$$

Let us not yet make the assumption $p(\vec{x}, t) \approx p(\tau(\vec{x}), t)$. We can then express the pressure as a function of τ and the two bi-streamfunctions, ψ and χ (Bear, 1972). The inwardly directed flux can then be obtained.

$$\begin{aligned} q &= -\frac{1}{\mu} \vec{n} \cdot \vec{k} \cdot \nabla p = \frac{w(\tau)}{\phi \mu} \nabla \tau \cdot \vec{k} \cdot \left\{ \nabla \tau \frac{\partial p}{\partial \tau} + \nabla \psi \frac{\partial p}{\partial \psi} + \nabla \chi \frac{\partial p}{\partial \chi} \right\} \\ &= c_t w(\tau) \left\{ \frac{\partial p}{\partial \tau} + \frac{1}{\phi \mu c_t} \left(\nabla \tau \cdot \vec{k} \cdot \nabla \psi \frac{\partial p}{\partial \psi} + \nabla \tau \cdot \vec{k} \cdot \nabla \chi \frac{\partial p}{\partial \chi} \right) \right\} \\ &\approx c_t w(\tau) \frac{\partial p}{\partial \tau} \end{aligned} \quad (2.16)$$

It is important for the internal consistency of our method that none of the spatial heterogeneity of properties in \vec{x} explicitly enter into this equation for the flux. Instead the

impact of our reservoir heterogeneity appears solely through the function $w(\tau)$, which is obtained as a consequence of the solution to the Eikonal equation.

The approximation to the flux as solely a τ gradient is the primary approximation that we make when transforming from the 3-D to the 1-D diffusivity equation. In specific applications, the validity of this approximation should be tested. However, in general, there are two instances in which we may justify this approximation. If the pressure and τ contours are exactly aligned, then the Darcy velocity is parallel to $-\vec{k} \cdot \nabla \tau$, and the two geometric terms, $\nabla \tau \cdot \vec{k} \cdot \nabla \psi$ and $\nabla \tau \cdot \vec{k} \cdot \nabla \chi$, will be exactly zero. Alternatively, if the transverse pressure gradients $\frac{\partial p}{\partial \psi}$ and $\frac{\partial p}{\partial \chi}$ are small, then those terms may also be neglected. We will return to the justification of this approximation in the discussion.

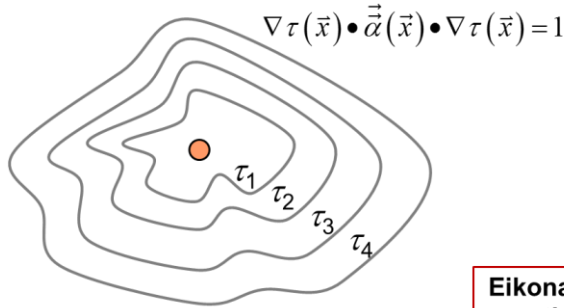
2.2.1.2 Diffusivity Equation: from 3-D to 1-D

We may now substitute the flux into Eq. (2.14), to obtain the equivalent 1-D diffusivity equation.

$$\frac{\partial p(\tau, t)}{\partial t} - \frac{1}{w(\tau)} \frac{\partial}{\partial \tau} \left(w(\tau) \frac{\partial p(\tau, t)}{\partial \tau} \right) = 0 \quad (2.17)$$

All of the spatial heterogeneity of the porosity, permeability and τ have vanished from the formulation in favor of the quantity $w(\tau)$, which first appeared in Eq. (2.14). To within a factor given by the diffusivity, it is proportional to the cross-sectional area of the streamtube. This interpretation is also consistent with the functional form of Eq. (2.17).

1D/2D/3D: Heterogeneous Case

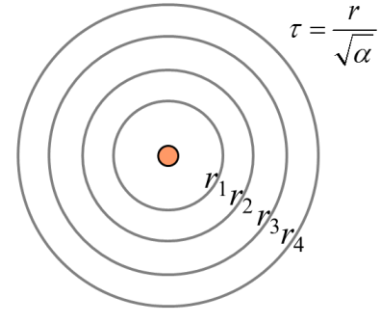


$$\frac{\partial p(\tau, t)}{\partial t} = \frac{1}{w(\tau)} \frac{\partial}{\partial \tau} \left(w(\tau) \frac{\partial p(\tau, t)}{\partial \tau} \right)$$

Eikonal
equation

→

2D Areal: Homogeneous Case



$$\frac{\phi \mu c_t}{k} \frac{\partial p(r, t)}{\partial t} = \frac{1}{2\pi r h} \frac{\partial}{\partial r} \left(2\pi r h \frac{\partial p(r, t)}{\partial r} \right)$$

Figure 2.4 Analog between the $w(\tau)$ formulation in heterogeneous reservoirs and the circular drainage volume in a homogeneous reservoir

We may make one additional simplification. If $p(\vec{x}, t) \approx p(\tau(\vec{x}), t)$, then we may select the volume of integration of Figure 2.3 to be completely periodic, so that the streamtube covers the entire reservoir, as shown in Figure 2.4. This figure again emphasizes the interpretation of $w(\tau)$ as a cross-sectional area, where for the special case of radial flow in a 2-D homogeneous reservoir, $\tau \rightarrow r$ and $w(\tau) \rightarrow 2\pi r h$, to within overall constants.

2.2.1.3 Flux Diffusivity Equation

We may obtain another form of the diffusivity equation, which is often easier to solve than Eq. (2.17). Eqs. (2.14) and (2.16) provide us with expressions for $\frac{\partial p}{\partial t}$ and $\frac{\partial p}{\partial \tau}$.

However, integrability of the pressure requires that the mixed partial derivatives $\frac{\partial^2 p}{\partial \tau \partial t}$ and

$\frac{\partial^2 p}{\partial t \partial \tau}$ must be equal. This integrability requirement leads to a diffusivity equation for the

flux, which is of the same form as Eq. (2.17) but with $w(\tau) \rightarrow 1/w(\tau)$.

$$\frac{\partial q(\tau, t)}{\partial t} - w(\tau) \frac{\partial}{\partial \tau} \left(\frac{1}{w(\tau)} \frac{\partial q(\tau, t)}{\partial \tau} \right) = 0 \quad (2.18)$$

We will return to this equation in the development of the asymptotic pressure approximation.

2.2.1.4 Initial and Boundary Conditions

The diffusivity equation requires one initial condition and two boundary conditions. The Eikonal equation requires one boundary condition. They are summarized in Table 2.1 for an infinite reservoir with skin. Some care needs to be taken if $w(0) = 0$. This is never the case if we have a finite wellbore radius, but this situation will arise in the line source approximation where $r_w \rightarrow 0$. Earlier treatments set $\tau = 0$ at $r = 0$, but the current approach has improved accuracy for fixed rate drawdown solutions and for the definition of the drainage volume. The wellbore sandface flux is defined at $\tau = 0$, $r = r_w$ while the wellbore pressure drop is defined at the effective wellbore radius of $\tau = \tau_{wf}$, $r = r_w e^{-S}$, where $\tau_{wf} = (e^{-S} - 1)r_w / \sqrt{\alpha}$ to represent wellbore skin effects (damage or stimulation).

	$\tau(\vec{x})$	$\Delta p(\tau, t) \equiv p_{init} - p(\tau, t)$	$q(\tau, t)$
Initial: $t = 0$	–	$\Delta p = 0$	$q = 0$
Wellbore Sandface Flux: $r = r_w$	$\tau = 0$	$-c_t w(\tau) \frac{\partial \Delta p}{\partial \tau} = q_{sf}$	$q = q_{sf}(t)$
Wellbore Pressure Drop (with Skin): $r = r_w e^{-s}$	$\tau = \tau_{wf}$	$\Delta p_{wf} = \Delta p(\tau_{wf}, t)$	–
Far Field: $\tau \rightarrow \infty$	–	$\Delta p \rightarrow 0$	$q \rightarrow 0$

Table 2.1 Initial and boundary conditions for the Eikonal and Diffusivity Equations for an infinite acting reservoir

This completes the description of the $w(\tau)$ methodology. In summary, we have assumed that pressure may be approximated using τ as a spatial coordinate, $p(\vec{x}, t) \approx p(\tau(\vec{x}), t)$, and the flux by a τ gradient, $q = c_t w(\tau) \frac{\partial p}{\partial \tau}$. In other words, we have assumed that the pressure and τ contours are identical. This has allowed us to reduce the 3-D diffusivity equation to an equivalent 1-D form. It also allows us to obtain a diffusivity equation for the flux, which may be easier to solve than the diffusivity equation for the pressure, especially when utilizing analytic techniques. At this point in our methodology there is no restriction on the method of solution: either numerical or analytic. As cited above, numerous examples have utilized the numerical solution of these equations. Next, we will develop approximate “asymptotic” analytic solutions to these equations.

2.2.1.5 Pressure Drop as a Function of τ

Here we will test the fundamental assumption $p(\bar{x}, t) \approx p(\tau(\bar{x}), t)$ as a function of reservoir heterogeneity, and return to it later for additional analysis. I will conduct the test twice: once when we look at the distribution of Δp from ECLIPSE and τ from FMM (in this section), and again when we look at the distribution of $\partial\Delta p/\partial t$ from the asymptotic pressure approximation vs. ECLIPSE (end of this chapter).

The heterogeneity examined throughout this dissertation represents the spatial variation of permeability only, since it is much more widely variable than porosity. Three different parameters will be used to describe the heterogeneity variance and distribution: the Dykstra-Parsons coefficient (V_{DP}), the dimensionless correlation length (L_{DCL}), and the Heterogeneity Index (HI).

Dykstra-Parsons Coefficient The Dykstra-Parsons coefficient (V_{DP}) is the most widely used measurement of permeability variation in the petroleum industry (Jensen *et al.*, 1997). It is a dimensionless coefficient and its definition is given by an expression as (Dykstra and Parsons, 1950):

$$V_{DP} = \frac{k_{50} - k_{84.1}}{k_{50}} \quad (2.19)$$

where, a permeability distribution is descending sorted, k_{50} is the median permeability and $k_{84.1}$ is the permeability at one standard derivation away. When $\ln k \sim N(\mu_{\ln k}, \sigma_{\ln k}^2)$, as can be observed in many reservoirs, an alternative and simple equation can be used to estimate V_{DP} (Jensen *et al.*, 1997):

$$V_{DP} = 1 - \exp(-\sigma_{\ln k}) \quad (2.20)$$

where $\sigma_{\ln k}$ represents the standard deviation of the natural log permeability. The Dykstra-Parsons coefficient varies from 0 to 1. According to the definition, a homogeneous reservoir has a V_{DP} value of 0; while for extremely heterogeneous reservoirs, V_{DP} may approach to 1. Most reservoirs have Dykstra-Parsons coefficients between 0.5 and 0.9 (Willhite, 1986).

Dimensionless Correlation Length The dimensionless correlation length (L_{DCL}), is defined as the ratio between the correlation length of the permeability and the distance from injector to producer (Jensen *et al.*, 1997). Since all the reservoir models tested here only have one production well in the reservoir center, the reference distance is set to be the reservoir size. The correlation length is the maximum length between different locations where the permeability is still dependent, i.e., the range of influence of permeability on its neighboring values increases as the correlation length increases, and thus, a zero L_{DCL} means a random spatial distribution of permeability.

Heterogeneity Index Another useful parameter is the Heterogeneity Index (HI) or Gelhar-Axness coefficient (Gelhar and Axness, 1983), defined as:

$$HI = \sigma_{\ln k}^2 L_{DCL} \quad (2.21)$$

HI has the advantage of combining both the heterogeneity variance and spatial correlation into a single parameter.

Heterogeneous Reservoir Model Following Jennings Jr. *et al.* (2000), a stable semivariogram model which links power-law exponents to the strength of spatial

correlation is used to generate permeability semivariogram and control the spatial distribution. Here, permeability distribution is the only parameter to be changed and other properties remain fixed, as listed in Table 2.2. We have chosen L_{DCL} of 0.02, 0.25, and 1.00 in the reservoir models. Furthermore, V_{DP} is varied for 0.30, 0.60, 0.90 and a detailed procedure can be found in the work by Wang (Wang, 2013; Wang *et al.*, 2014; Wang *et al.*, 2016). The DTOF are generated using the FMM numerical scheme following Li and King (2016).

Property	Value
V_{DP}	0.30, 0.60, 0.90
L_{DCL}	0.02, 0.25, 1.00
HI	0.003 - 5.302

Table 2.2 Reservoir heterogeneity parameters of the heterogeneous models

In total, nine combinations of V_{DP} and L_{DCL} are selected to create heterogeneous reservoir models, with a vertical well located in the center of the reservoir. I will use them as examples to illustrate how well the pressure and τ contours align with each other now and will return to these examples later for additional analysis. In this subsection, three out of the nine heterogeneous reservoir models to be shown are as follows: high heterogeneous reservoir with short correlation length ($V_{DP} = 0.60, HI = 0.210$), high heterogeneous reservoir with long correlation length ($V_{DP} = 0.60, HI = 0.840$), and low heterogeneous reservoir with short correlation length ($V_{DP} = 0.30, HI = 0.032$).

For the base case with $V_{DP} = 0.60$ and $HI = 0.210$, the logarithm of the permeability field and the corresponding τ map are shown in Figure 2.5 (a) & (b). Figure 2.5 (c) & (d) represent the pressure drop distribution from ECLIPSE during transient and PSS periods, respectively. Figure 2.5 (e) & (f) are the corresponding cross plots of pressure drop from ECLIPSE vs. τ from FMM. A comparison between subplots (c) & (d) to (b) illustrates that pressure contours align well with τ contours in general, especially during the infinite acting transient period when the pressure drop has not yet reached the boundary. During the PSS period, the pressure contours are smoother than the τ contours and they are less well aligned near the reservoir boundary due to an extra pressure drop caused by the reflection of the pressure front. This alignment can also be observed in subplots (e) & (f), where the trend of pressure depletion along with τ is less scattered during transient period in subplot (e), compared to PSS period in subplot (f), especially for large τ closer to the boundary of the reservoir.

If we keep the variance of heterogeneity as in the base case and increase the correlation length L_{DCL} , we get case with $V_{DP} = 0.60$ and $HI = 0.840$, as shown in Figure 2.6. A comparison between the current and base cases shows that increasing L_{DCL} will make the alignment somewhat less satisfactory at late time, since Figure 2.6 (f) is more scattered than Figure 2.5 (f), but with comparable results during the early transient.

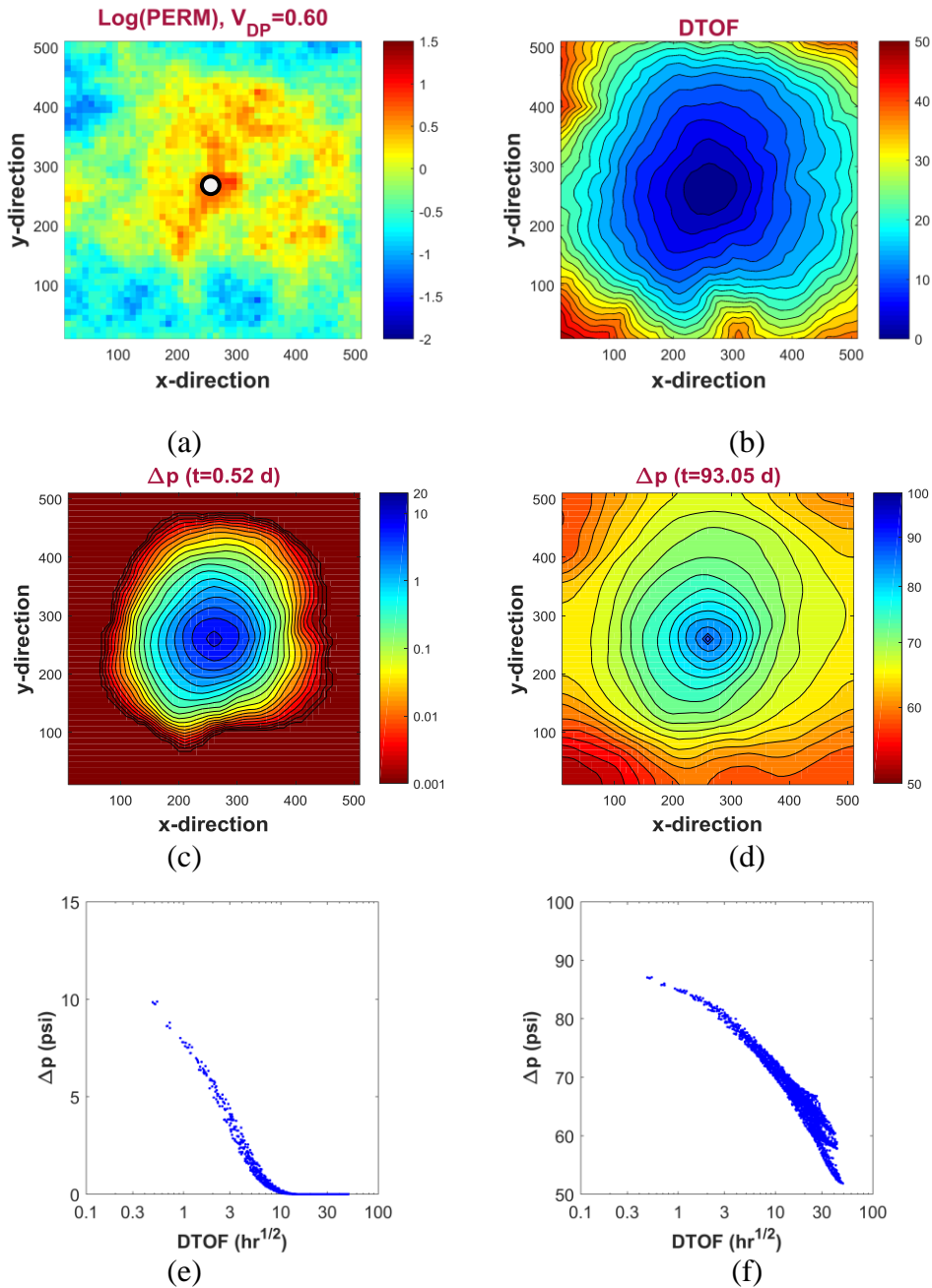


Figure 2.5 Illustration of heterogeneous reservoir model with $V_{DP} = 0.6$ and $HI = 0.210$ (a) Log10 of permeability distribution; (b) diffusive time of flight distribution; (c) Pressure drop distribution during transient period; (d) Pressure drop distribution during PSS period; (e) Cross plot of pressure drop vs. DTOF during transient period; (f) Cross plot of pressure drop vs. DTOF during PSS period

If we keep the correlation length of heterogeneity as in the base case and decrease V_{DP} , we get a case with $V_{DP} = 0.30$ and $HI = 0.032$, as shown in Figure 2.7. A comparison between the current and base cases shows that the decreasing V_{DP} will make the alignment even more satisfactory, both at early time and surprisingly, even at PSS.

Through the above demonstration, $p(\vec{x}, t) \approx p(\tau(\vec{x}), t)$ is a reasonable assumption for heterogeneous reservoirs, even for fairly large variance and long correlation lengths. However, once boundary reflection terms begin to contribute, the finite difference simulation shows an additional pressure drop within the model that is not captured by a single $\tau(\vec{x})$ coordinate. This effect has been studied by other members of our research group (Huang *et al.*, 2017) and an additional boundary reflection $\tau(\vec{x})$ coordinate introduced. We will return to this discussion when studying bounded reservoir systems in the next chapter.

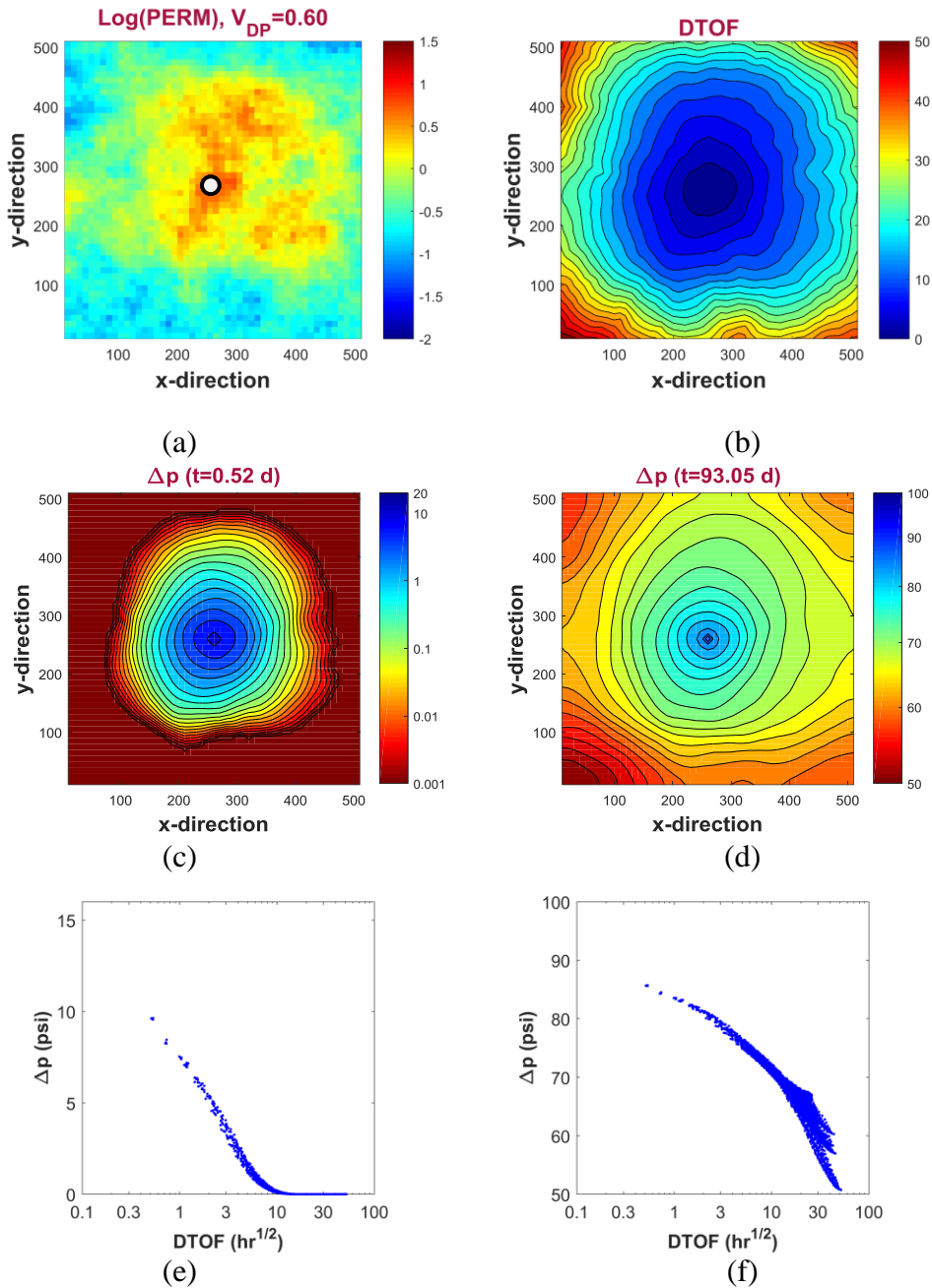


Figure 2.6 Illustration of heterogeneous reservoir model with $V_{DP} = 0.6$ and $HI = 0.840$ (a) Log10 of permeability distribution; (b) diffusive time of flight distribution; (c) Pressure drop distribution during transient period; (d) Pressure drop distribution during PSS period; (e) Cross plot of pressure drop vs. DTOF during transient period; (f) Cross plot of pressure drop vs. DTOF during PSS period

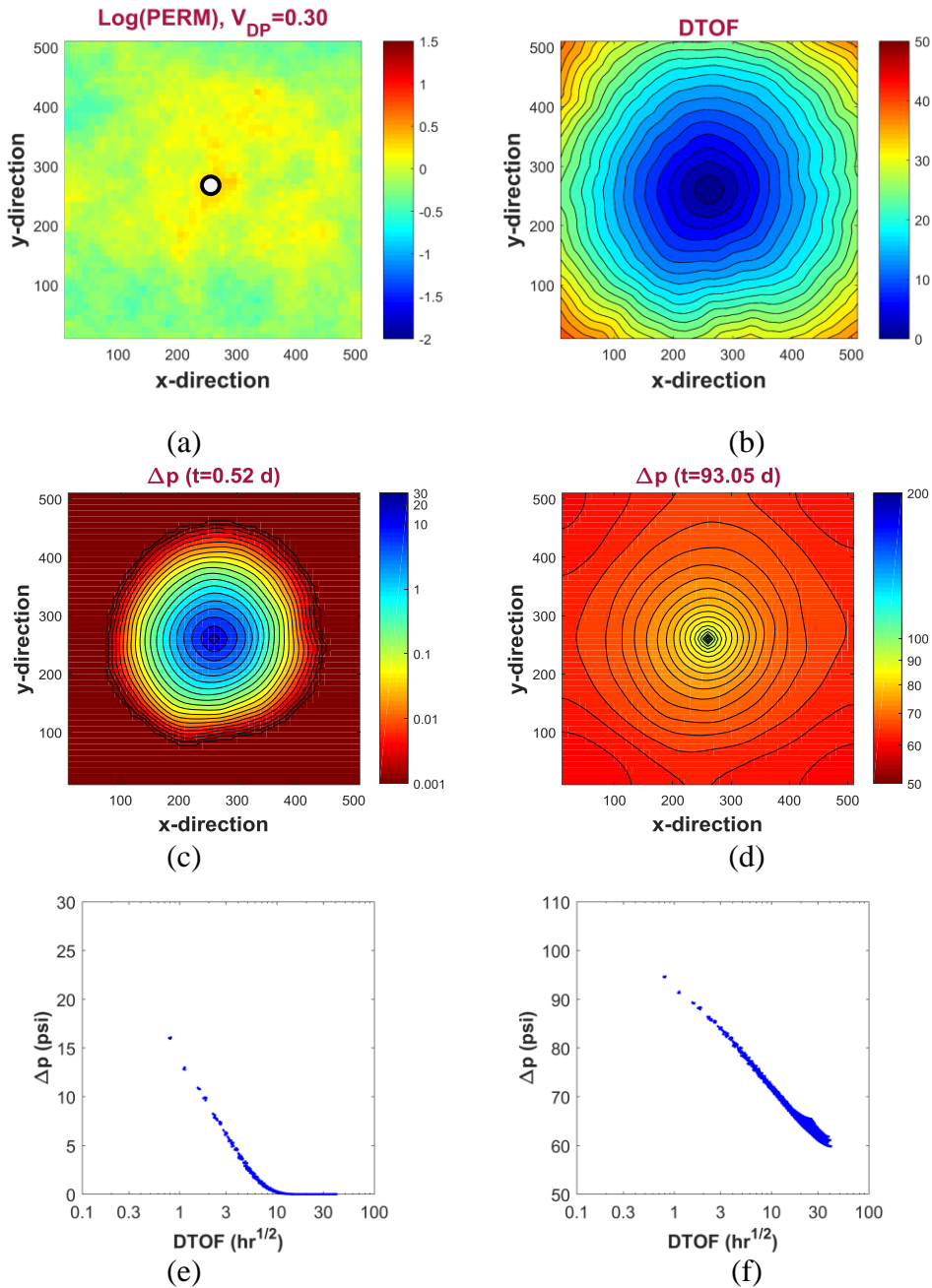


Figure 2.7 Illustration of heterogeneous reservoir model with $V_{DP} = 0.3$ and $HI = 0.032$ (a) Log10 of permeability distribution; (b) diffusive time of flight distribution; (c) Pressure drop distribution during transient period; (d) Pressure drop distribution during PSS period; (e) Cross plot of pressure drop vs. DTOF during transient period; (f) Cross plot of pressure drop vs. DTOF during PSS period

2.2.2 Asymptotic Pressure Approximation

The numerical solution of the 1-D diffusivity, Eq. (2.17), and its extension to include more complexity in fluid and rock properties, is a powerful and efficient approach for performance prediction. Its power and flexibility is in common with other numerical solutions, but it has the added efficiency obtained by reducing the 3-D flow equations to 1-D (Zhang *et al.*, 2014). However, it does not approach the ease of use and simplicity of interpretation provided by analytic techniques. In this subsection, I will show how we will develop such an analytic approach.

To motivate the asymptotic expansion, let us first examine the fixed rate drawdown analytic solution to the flux diffusivity equation, Eq. (2.18), for the case of simple geometries in the line source approximation where $w(\tau) \sim \tau^m$ and $m \geq 0$. The restriction of $m \geq 0$ ensures that we have a finite cross-sectional area at the wellbore. This analytic solution includes all of the simple flow regimes described in textbooks, but also includes the more exotic case of diffusion on a fractal geometry describing a fractured reservoir, where m is not an integer (Barker, 1988; Lee *et al.*, 2003).

$$\frac{\partial q(\tau, t)}{\partial t} - \tau^m \frac{\partial}{\partial \tau} \left(\frac{1}{\tau^m} \frac{\partial q(\tau, t)}{\partial \tau} \right) = 0 \quad (2.22)$$

A dimensional analysis of this equation and the initial and boundary conditions for fixed rate drawdown (Table 2.1) shows that the flux may depend upon τ and t only through the dimensionless Boltzmann ratio.

$$\xi = \frac{\tau^2}{4t} \quad (2.23)$$

This is true of the flux because it satisfies Dirichlet boundary conditions. However, because of the scaling of the Neumann boundary condition for pressure at the wellbore, it is only true of the pressure drop for $m = 1$, and then only in the line source limit. The space and time derivatives of the flux function can be expressed in terms of the derivative with respect to the Boltzmann variable.

$$\frac{\partial q}{\partial t} = \frac{\partial \xi}{\partial t} \frac{dq}{d\xi} = -\frac{\tau^2}{4t^2} \frac{dq}{d\xi} \quad (2.24)$$

$$\frac{\partial q}{\partial \tau} = \frac{\partial \xi}{\partial \tau} \frac{dq}{d\xi} = \frac{\tau}{2t} \frac{dq}{d\xi} \quad (2.25)$$

Based on the Boltzmann ratio, we may relate $\frac{\partial q}{\partial t}$ to $\frac{\partial q}{\partial \tau}$: $\frac{\partial q}{\partial t} = -\frac{\tau}{2t} \frac{\partial q}{\partial \tau}$. Hence,

$$\left(\frac{1}{\tau^m} \frac{\partial q(\tau, t)}{\partial \tau} \right)^{-1} \frac{\partial}{\partial \tau} \left(\frac{1}{\tau^m} \frac{\partial q(\tau, t)}{\partial \tau} \right) = -\frac{\tau}{2t} \quad (2.26)$$

This equation may be integrated to within an arbitrary function of time. The solution is an exponential decay in $\tau^2/4t$.

$$\frac{1}{w(\tau)} \frac{\partial q(\tau, t)}{\partial \tau} \sim \frac{1}{\tau^m} \frac{\partial q(\tau, t)}{\partial \tau} \sim -e^{-\tau^2/4t} \quad (2.27)$$

We can examine the bounds of the solution for Eq. (2.18) for fixed rate drawdown.

If we expand the derivative term then we can express the diffusivity equation as:

$$\frac{\partial q(\tau, t)}{\partial t} + \left(\frac{d \ln w(\tau)}{d \ln \tau} \right) \frac{1}{\tau} \frac{\partial q(\tau, t)}{\partial \tau} - \frac{\partial^2 q(\tau, t)}{\partial \tau^2} = 0 \quad (2.28)$$

If we replace the expression $\left(\frac{d\ln w(\tau)}{d\ln \tau}\right)$ by either its upper or its lower bound, then we recover Eq. (2.22) with a value of m given by the bound. If the lower bound has $m < 0$ then we no longer expect that the solution for the flux will be an exponential decay of the form $e^{-\tau^2/4t}$. We will see that this is the case for bounded systems.

The motivation of the asymptotic expression has relied upon a specific functional form for $w(\tau)$. However, Eq. (2.29) is more general than this may indicate. If we return to the asymptotic series of Eq. (2.3), the leading order term of the expansion is of the form $e^{-\sqrt{-i\omega\tau}} \tilde{A}_0(\vec{x})$. If the amplitude is slowly varying then we may transform from frequency to the time domain and we again obtain Eq. (2.29) but with a power law form for $A_0(t)$ (Virieux *et al.*, 1994). The expression $A_0(t)e^{-\tau^2/4t}$ is also recognized as the Green's function for diffusion for an impulse solution (Ramey, 1966; Gringarten & Ramey, 1973).

For arbitrary (non power-law) $w(\tau)$ this suggests the following asymptotic expansion for the pressure transient.

$$c_t \frac{\partial p(\tau, t)}{\partial t} = \frac{1}{w(\tau)} \frac{\partial q(\tau, t)}{\partial \tau} = - \left\{ \sum_{n=0}^{\infty} \tau^n A_n(t) \right\} e^{-\tau^2/4t} \quad (2.29)$$

The $\{A_n(t)\}$ are unknown functions to be determined by the initial and boundary conditions. Each bound in Eq. (2.28) has a spatial dependence given by the exponential decay of Eq. (2.29), although with different functions for $A_n(t)$. This indicates that all solutions with smoothly variable $w(\tau)$ will follow the same exponential trend. Truncating

the infinite series at one term is equivalent to the Born approximation in scattering theory (Jauch and Rohrlich, 1976). We will show that the first two terms in this expansion have specific interpretations.

Combining Darcy's equation Eq. (2.16) and Eq. (2.29), we get an expression for the flux evolution.

$$\begin{aligned}\frac{\partial q(\tau, t)}{\partial t} &= c_t w(\tau) \frac{\partial^2 p}{\partial \tau \partial t} = w(\tau) \frac{\partial}{\partial \tau} \left(c_t \frac{\partial p(\tau, t)}{\partial t} \right) \\ &= w(\tau) \left\{ \sum_{n=0}^{\infty} \tau^n \left[\frac{1}{2t} A_{n-1}(t) - (n+1) A_{n+1}(t) \right] \right\} e^{-\tau^2/4t}\end{aligned}\quad (2.30)$$

Here, $A_{-1} = 0$. Applying this expression at $\tau = 0$, we obtain:

$$\frac{dq_{sf}(t)}{dt} = -w(0) A_1(t) \quad (2.31)$$

Similarly, when applying Eq. (2.29) at $\tau = 0$ (neglecting skin), we get the expression for the pressure drop at the wellbore as:

$$\frac{d\Delta p_{wf}(t)}{dt} = -\frac{dp_{wf}(t)}{dt} = A_0(t) \quad (2.32)$$

With skin, additional terms will arise. Eqs. (2.31) and (2.32) are very useful since they provide physical interpretations to $A_0(t)$ and $A_1(t)$. For fixed rate drawdown, the inner

boundary condition requires $\frac{dq_{sf}(t)}{dt} = \frac{dq_w}{dt} = 0$ and $\frac{d\Delta p_{wf}(t)}{dt} \neq 0$. Therefore $A_1(t)$

must vanish, and $A_0(t)$ will describe the pressure transient at the wellbore and in the

reservoir. For fixed BHP drawdown, the inner boundary requires $\frac{dq_{sf}(t)}{dt} \neq 0$ and

$\frac{d\Delta p_{wf}(t)}{dt} = \frac{d\Delta p_{wf}}{dt} = 0$. Therefore $A_0(t)$ must vanish, and $A_1(t)$ will describe the rate

transient at the wellbore and in the reservoir.

2.2.2.1 Flux and Pressure of the Drawdown Solution

In this section, I will show how we derive the general solutions for both flux and pressure regardless of inner boundary condition, based on the proposed asymptotic solution Eq. (2.29) above.

A first integral of this equation determines the flux.

$$q(\tau, t) = q_{sf}(t) - \sum_{n=0}^{\infty} A_n(t) V_n(\tau, t) \quad (2.33)$$

The flux solution is obtained by integrating its spatial gradient from the wellbore sandface $q(\tau=0, t) = q_{sf}(t)$, to a location in the reservoir. The solution is stated in terms of the incomplete volume moment integrals and the unknown $A_n(t)$.

$$V_n(\tau, t) \equiv \int_0^{\tau} dV_p(\tau) \tau^n e^{-\tau^2/4t} = \int_0^{\tau} d\tau w(\tau) \tau^n e^{-\tau^2/4t} \quad (2.34)$$

The volume moment integrals are known functions determined from the pore volume, $V_p(\tau)$. When applying this flux expression to the far field boundary τ_{res} , $\tau_{res} \rightarrow \infty$, where $q(\tau_{res}, t) = 0$ we obtain an expression for the flux at the sandface:

$$q_{sf}(t) = \sum_{n=0}^{\infty} A_n(t) V_n(t) \quad (2.35)$$

where,

$$V_n(t) \equiv V_n(\tau_{res}, t) = \int_0^{\tau_{res}} d\tau w(\tau) \tau^n e^{-\tau^2/4t} \quad (2.36)$$

For infinite systems, $\tau_{res} \rightarrow \infty$, but we will also apply this solution for bounded reservoirs.

Substitute the flux expression, Eq. (2.33) into Eq. (2.30), we obtain the integrability condition for the asymptotic solution as:

$$\begin{aligned} \frac{\partial q(\tau, t)}{\partial t} &= \frac{dq_{sf}(t)}{dt} - \sum_{n=0}^{\infty} \left\{ \frac{dA_n(t)}{dt} V_n(\tau, t) + A_n(t) \frac{\partial V_n(\tau, t)}{\partial t} \right\} \\ &= w(\tau) \left\{ \sum_{n=0}^{\infty} \tau^n \left[\frac{1}{2t} A_{n-1}(t) - (n+1) A_{n+1}(t) \right] \right\} e^{-\tau^2/4t} \end{aligned} \quad (2.37)$$

which will provide a series of evolution equations which can be used to determine the unknown functions. Once we satisfy the integrability condition, then the infinite series represents the solution to the diffusion problem. It doesn't mean we have to solve the equations in this way, but what it does show is that there is a set of equations that make the approximation consistent. Integrability condition is there for the formal structure of the equations and evolution equations will be used instead. We will return to this discussion in the next chapter.

From Darcy's equation we have the pressure drop within the reservoir.

$$\begin{aligned} c_t \Delta p(\tau, t) &= c_t \Delta p(\tau_{wf}, t) - q_{sf}(t) \int_{\tau_{wf}} \frac{d\tau}{w(\tau)} + \sum_{n=0}^{\infty} A_n(t) \int_{\tau_{wf}}^{\tau} \frac{d\tau}{w(\tau)} V_n(\tau, t) \\ &= c_t \Delta p(\tau_{wf}, t) - \sum_{n=0}^{\infty} A_n(t) \int_{\tau_{wf}} \frac{d\tau}{w(\tau)} \{V_n(t) - V_n(\tau, t)\} \\ &= c_t \Delta p_{wf}(t) - \sum_{n=0}^{\infty} A_n(t) W_n(\tau, t) \end{aligned} \quad (2.38)$$

The solution is stated in terms of the incomplete pressure drop moment integrals and the unknown $A_n(t)$.

$$\begin{aligned}
W_n(\tau, t) &\equiv \int_{\tau'=\tau_{wf}}^{\tau} \frac{d\tau'}{w(\tau')} \{V_n(t) - V_n(\tau', t)\} \\
&= \int_{\tau'=\tau_{wf}}^{\tau} \frac{d\tau'}{w(\tau')} \int_{\tau''=\tau'}^{\tau_{res}} d\tau'' w(\tau'') \tau''^n e^{-\tau''^2/4t} \\
&= \int_{\tau'=\tau_{wf}}^{\tau} d\tau' w(\tau') \left(\int_{\tau''=\tau}^{\tau''=\tau'} \frac{d\tau''}{w(\tau'')} \right) \tau'^n e^{-\tau'^2/4t}
\end{aligned} \tag{2.39}$$

Application of the pressure drop expression to the far field boundary $\tau_{res} \rightarrow \infty$, where $\Delta p(\tau_{res}, t) = 0$, leads to the following expression for the pressure drop at the wellbore.

$$c_i \Delta p_{wf}(t) = \sum_{n=0}^{\infty} A_n(t) W_n(t) \tag{2.40}$$

where,

$$W_n(t) \equiv W_n(\tau_{res}, t) = \int_{\tau_{wf}}^{\tau_{res}} \frac{d\tau'}{w(\tau')} \{V_n(t) - V_n(\tau', t)\} \tag{2.41}$$

These expressions are only applicable for infinite systems since for bounded reservoirs the pressure drop at the boundary of the reservoir will not vanish.

The general expressions for pressure drop in an unbounded reservoir can be expressed as follows:

$$\begin{aligned}
c_i \Delta p(\tau, t) &= \sum_{n=0}^{\infty} A_n(t) \{W_n(t) - W_n(\tau, t)\} \\
&= \sum_{n=0}^{\infty} A_n(t) \int_{\tau'=\tau}^{\tau_{res}} d\tau' w(\tau') \left(\int_{\tau''=\tau}^{\tau''=\tau'} \frac{d\tau''}{w(\tau'')} \right) \tau'^n e^{-\tau'^2/4t}
\end{aligned} \tag{2.42}$$

In bounded reservoirs, the bottomhole flowing pressure is determined by the overall mass balance, which fixes the pore volume averaged pressure within the reservoir.

$$\overline{\Delta p}(t) = \frac{Q_w(t)}{c_t \cdot V_{res}} \quad Q_w(t) = \int_{t=0}^t q_w(t) dt \quad V_{res} = \int_{\tau=0}^{\tau_{res}} w(\tau) d\tau \quad (2.43)$$

According to the definition of average reservoir pressure, we know that:

$$\begin{aligned} \overline{\Delta p}(t) \cdot V_{res} &= \int_{\tau=0}^{\tau_{res}} \Delta p(\tau, t) w(\tau) d\tau \\ &= \int_{\tau=0}^{Max(0, \tau_{wf})} \Delta p_{wf}(t) w(\tau) d\tau + \int_{Max(0, \tau_{wf})}^{\tau_{res}} \Delta p(\tau, t) w(\tau) d\tau \end{aligned} \quad (2.44)$$

where, $\Delta p(\tau, t) = \Delta p(\tau_{wf}, t)$ for $\tau < \tau_{wf}$. Substitute the pressure expression Eq. (2.42)

into Eq. (2.44), we obtain that,

$$\begin{aligned} \overline{\Delta p}(t) &= \frac{\Delta p_{wf}(t)}{V_{res}} \int_{\tau=0}^{\tau_{res}} d\tau w(\tau) - \frac{1}{c_t \cdot V_{res}} \sum_{n=0}^{\infty} A_n(t) \cdot \int_{Max(0, \tau_{wf})}^{\tau_{res}} d\tau w(\tau) W_n(\tau, t) \\ &= \Delta p_{wf}(t) - \frac{1}{c_t \cdot V_{res}} \sum_{n=0}^{\infty} A_n(t) \cdot X_n(\tau, t) \end{aligned} \quad (2.45)$$

where, we further define the (incomplete) average pressure drop moment integrals below:

$$\begin{aligned} X_n(\tau, t) &\equiv \int_{Max(0, \tau_{wf})}^{\tau} d\tau' w(\tau') W_n(\tau', t) \\ X_n(t) &\equiv X_n(\tau_{res}, t) \end{aligned} \quad (2.46)$$

Lower limit is $Max(0, \tau_{wf})$ since it's always in an integral starting from $\tau = 0$.

Boundary conditions are typically specified in terms of the flux or the pressure drop at the wellbore, or a combination of the two. For fixed rate drawdown we have already obtained the result that $A_1(t)$ must vanish. Combining Eq. (2.29) and Eq. (2.31)

we have showed the requirement for a fixed BHP drawdown, i.e., $A_0(t)$ must vanish. For variable rate drawdown, e.g., in the analysis of wellbore storage, we will examine solutions that include combinations of $A_0(t)$, $A_1(t)$ and $A_2(t)$, which will be fixed by the boundary condition at the wellbore. The discussion will be provided in Chapter 3.

2.2.2.2 Infinite Acting Asymptotic Approximation of Fixed Rate Drawdown

We will approximate this asymptotic expansion using the first term. We will show that this simplification provides an excellent approximation to known reference solutions. More importantly, this provides us with an analytic methodology that can be used for both heterogeneous and homogeneous problems, and for both pressure and rate transient analysis. We will see that the first term in the expansion is directly related to the drainage volume of a well. The second term describes the deviation of the pressure profile from a pseudo steady state (PSS) solution. We may expect that the higher order terms become more important for large τ . However, in this limit, it is instead more important to modify the exponential term in the expansion to represent finite reservoir boundaries.

As a demonstration of the asymptotic formulation, we have performed finite difference calculations of the diffusivity equation for constant rate drawdown using

ECLIPSE. We then cross-plot $\frac{\partial \Delta p(\vec{x}, t)}{\partial t}$ and $e^{-\tau(\vec{x})^2/4t}$ for each cell in the reservoir model

at a time before the solution is strongly impacted by finite size boundary effects. Two models were examined, with increasing variance in their heterogeneity, Figure 2.8. The calculation shows that for sufficiently smooth heterogeneity patterns, that we obtain

excellent agreement with Eq. (2.29). As heterogeneity increases, the scatter around the trend increases, but Eq. (2.29) still describes the overall trend.

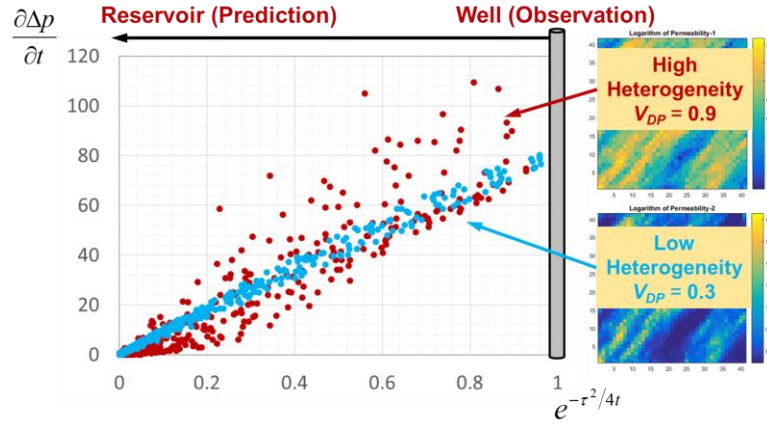


Figure 2.8 Numerical demonstration of the asymptotic pressure approximation for a well in the center of a heterogeneous reservoir model (reprinted with permission from King et al., 2016)

This figure serves to validate several of our approximations: first that

$$c_i \frac{\partial \Delta p}{\partial t} \approx A_0(t) \cdot e^{-\tau^2/4t} \quad , \quad \text{which itself is based on } p(\vec{x}, t) \approx p(\tau(\vec{x}), t) \quad \text{and}$$

$$q(\tau, t) \approx c_i w(\tau) \frac{\partial p(\tau, t)}{\partial \tau} \quad . \quad \text{Detailed examination of the simulation models shows that the}$$

most significant errors occur adjacent to low permeability cells, where the pressure front reflects from local no flow cell boundaries. Since the Eikonal equation was derived in the high frequency (early time) limit, we expect $\tau(\vec{x})$ to be the dominant spatial coordinate at early time, corresponding to the refraction and first passage of pressure depletion through the porous media. Barriers generate transverse flow where the terms that were neglected in the expression for the flux, Eq. (2.16), are locally not negligible. However,

Figure 2.8 still demonstrates that the exponential shows the overall trend. A further exploration of how heterogeneity impacts the accuracy of Eq. (2.29) will be provided in the validation subsection.

2.2.2.3 Drainage Volume

We began the development from Eq. (2.35) for the flux. The fixed rate drawdown boundary condition at the wellbore, $q = q_{sf}(t) = q_w$ at $\tau = 0$, fixed $A_1(t) = 0$ and determines $A_0(t)$.

$$A_0(t) = q_w / V_0(t) \quad \text{where} \quad V_0(t) \equiv V_0(\tau = \tau_{res}, t) = \int_0^{\tau_{res}} dV_p(\tau) e^{-\tau^2/4t} \quad (2.47)$$

Here, $\tau_{res} \rightarrow \infty$ for an unbounded reservoir. Similarly to the flux, from Eq. (2.40), we derive that

$$c_t \Delta p_{wf}(t) = A_0(t) W_0(t) = q_w \frac{W_0(t)}{V_0(t)} \quad (2.48)$$

When developing the expression for the flux with fixed rate drawdown, we obtain the expression of $V_0(t)$, which we recognize to be the transient drainage volume for fixed rate drawdown.

$$V_0(t) = \int_0^{\tau_{res}} dV_p(\tau) e^{-\tau^2/4t} \quad (2.49)$$

We recognize that the near well region is in PSS flow, $e^{-\tau^2/4t} \approx 1$. We may follow the discussion of Matthews *et al.* (1954) to relate the quantity $\frac{1}{V_d} \equiv \frac{c_t}{q_w} \frac{d\Delta p_{wf}}{dt}$ to the drainage

volume of the well. In the case of an infinite acting reservoir we can identify

$$V_d(t) \approx V_0(t) \cdot e^{\tau_{wf}^2/4t} = \int_0^{\tau_{res}} dV_p(\tau) e^{-(\tau^2 - \tau_{wf}^2)/4t}$$

2.9.

The expression for $V_0(t)$ has an intuitive interpretation: $dV_p(\tau)$ is a volume element in the reservoir and the exponential term indicates the timing of the contribution of that element to depletion within the reservoir. For instance, at early times, the exponential is only appreciable for locations close to the well. At late times, the exponential approaches 1, and all portions of a reservoir will be contributing to depletion (PSS limit).

Before solving these equations for particular choices of $w(\tau)$, we can examine the general form of the solution, as shown in Figure 2.9 and Table 2.3. This description is for a fixed rate drawdown in the absence of skin. From Eq. (2.47) the solution is given by $A_0(t) = q_w/V_0(t)$, where $V_0(t)$ has been identified as the drainage volume of the well. The thresholds and descriptions in Table 2.3 are adapted and generalized from discussions within Lee *et al.* (2003) and Kuchuk (2009).

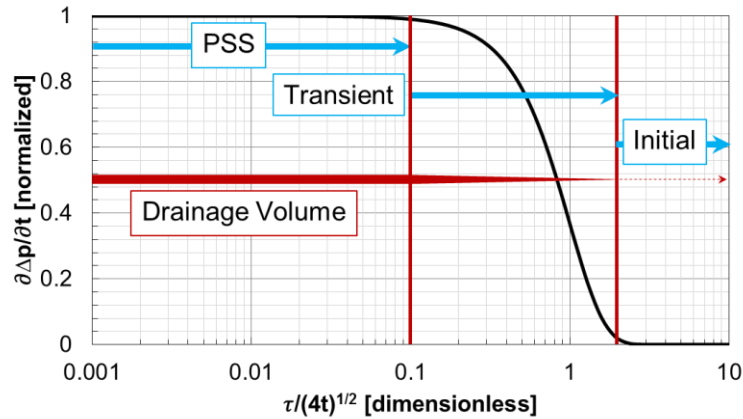


Figure 2.9 Spatial profile of the fixed rate drawdown solution to the asymptotic pressure approximation in terms of the time derivative of the pressure drop, normalized to its value at the wellbore ($\tau = 0$) (reprinted with permission from Wang et al, 2018)

This figure is important as it explains our ability to describe the fixed rate drawdown pressure transient problem, which is diffusive, as if the pressure was a “wave” with a “front”. Following Lee (1982), we may define the depth of investigation for an impulse source as the location of the maximum pressure drop within the reservoir. For a fixed rate drawdown, this is the contour of maximum pressure change, $\frac{\partial^2 p}{\partial t^2} = 0$. This contour has a finite speed of propagation and allows us to describe the pressure as if it were a wave, with a front at the depth of investigation. The specific expression or value for $\tau_{DOI}(t)$ depends upon the flow geometry, and will be discussed in more detail, below.

Solution	Exponential Range	$\frac{\tau}{\sqrt{4t}}$ Range
Pseudo Steady State (PSS)	$e^{-\tau^2/4t} > 0.99$	$\frac{\tau}{\sqrt{4t}} < 0.1$
Transient	$0.99 > e^{-\tau^2/4t} > 0.018$	$0.1 < \frac{\tau}{\sqrt{4t}} < 2$
Limit of Detectability	$e^{-\tau^2/4t} = 0.018$	$\frac{\tau}{\sqrt{4t}} = 2$
Near Initial	$e^{-\tau^2/4t} < 0.018$	$\frac{\tau}{\sqrt{4t}} > 2$

Table 2.3 Solution characteristics of the asymptotic pressure approximation for fixed rate drawdown based upon the time derivative of the drawdown pressure drop (reprinted with permission from Wang et al, 2018)

PSS Limit At the wellbore, $\tau \rightarrow 0$ and $e^{-\tau^2/4t} \rightarrow 1$. The well testing literature will evaluate the pseudo steady state (PSS) limit of transient solutions near the wellbore, for instance to derive the logarithmic limit of the *Ei* function for transient radial flow. This limit is specified by $(\tau^2/4t) < 0.01$ for which we obtain $e^{-\tau^2/4t} > 0.99$. Essentially, all volumes within the PSS limit contribute to the drainage volume of the well.

Limit of Detectability Kuchuk discusses several definitions of the depth of investigation (Kuchuk, 2009). We will follow the formal definition for the depth of investigation provided by Lee *et al.* (2003), as discussed below. However, one of Kuchuk's definitions corresponds to what we will characterize as the "limit of detectability". We define this limit by $(\tau^2/4t) = 4$ where $e^{-\tau^2/4t} \approx 0.018$, which describes

a detectable signature in the well test derivative. This limit is independent of the flow geometry, which makes it extremely useful in welltest interpretation.

This separates the remaining contributions to the drainage volume into two regions. If $(\tau^2/4t) > 4$ and $e^{-\tau^2/4t} < 0.018$, then there is only a negligible contribution to the drainage volume. There has also been a negligible pressure drop and so we can describe this volume as “near initial”. For values of $(\tau^2/4t)$ in the range $0.01 < (\tau^2/4t) < 4$ then we have the fully transient solutions, with contributions to the drainage volume from close to 100% to 0, depending upon the exponential term. This discussion is summarized in Figure 2.9.

Depth of Investigation The characteristics of the solutions as described above are not specific to the geometry of the solution. In contrast, the depth of investigation will be. Following (Lee *et al.*, 2003) and from Eq.(2.29), we can ask at what time does $\partial\Delta p(\tau,t)/\partial t$ reach a maximum value, i.e., $0 = \partial^2\Delta p(\tau,t)/\partial t^2$. Substituting in the expression for the drainage volume gives the following relationship.

$$\tau_{DOI}^2(t) = \frac{1}{V_0(t)} \int_{\tau=0}^{\infty} d\tau w(\tau) \tau^2 e^{-\tau^2/4t} = \frac{V_2(t)}{V_0(t)} \quad (2.50)$$

This reduces to the specific solutions $\tau_{DOI}^2/4t = 1/2, 2/2, 3/2$ for linear, radial and spherical flow, but in general the ratio $(\tau_{DOI}^2/4t)$ need not be constant. For instance, for an infinite conductivity fracture, we will show that $(\tau_{DOI}^2/4t)$ varies between 1/2 at early time and 1 at late time. Comparison with Figure 2.9 shows that the depth of investigation

is well within the transient portion of the pressure profile. As such it will occur later than the limit of detectability and before the onset of PSS flow.

The above description has been developed from the fixed rate drawdown solutions. In contrast, if we examine the fixed BHP solutions, then the leading order terms of the asymptotic expansion depend upon position, and pseudo steady state is never reached. In this case, PSS concepts such as drainage volume cannot be as directly applied to the interpretation. The only exception arises if we utilize superposition time, t_s , and the ratio of $(\Delta p_{wf}/q_w)$. We may then define an apparent drainage volume as

$$\frac{1}{V_d(t)} \equiv c_t \frac{\partial}{\partial t_s} \left(\frac{\Delta p_{wf}}{q_w} \right). \text{ This will be discussed in more detail in the next chapter.}$$

For the remainder of this chapter, we will explore the implications of the asymptotic pressure approximation, Eq. (2.29), to pressure transient analysis. We will defer calculations and validation tests to the next section, where we provide specific examples and applications of the asymptotic formulation.

At this point, it is worth contrasting the new solution approach with the standard methodology. Much of the well testing literature follows the foundational paper of Van Everdingen and Hurst (1949), which is based upon the use of the Laplace transform and solutions in terms of special functions for specific geometries and properties. The pressure drop and the welltest derivative at the wellbore are calculated by numerical inverse Laplace transforms and tabulated into type curves. In contrast, the current formulation does not require the use of the Laplace transform or of special functions. We start with a direct calculation of the drainage volume and the welltest derivative, without the need to

explicitly solve a pressure equation. We also have a prediction of the pressure drop and welltest derivative away from a well, which is useful for modeling well interference and flow barriers. Most importantly, the asymptotic approximation is not restricted to simple flow geometries or to homogeneous reservoirs.

There is much in common with the welltest literature. Many of the most powerful techniques that are utilized in the literature (super-position, de-convolution, pseudo-pressure, rate normalization...), may also be applied in the context of the asymptotic pressure approximation. In this chapter we have focused on the solution to fixed rate drawdown, as it serves as a foundation for these more complex methods of analysis, some of which will be touched upon in our applications.

2.2.2.4 Properties of the Transient Solutions

The asymptotic pressure approximation provides us with a general means of solving the fixed rate drawdown pressure transient equations. We recover the usual and exact results for the linear, radial, and spherical flow regimes, for which we have simple power law expressions for $w(\tau)$. We also obtain new solutions for the transitions between these regimes for non power-law $w(\tau)$, which are usually modelled using inverse Laplace transforms and type curves. The formulation also implies relationships that aid in the interpretation of diagnostic plots, specifically between the welltest derivative and the drainage volume of a well.

Welltest Derivative Bourdet has defined the welltest derivative, $\Delta p'_{wf}$, in terms of the logarithmic time derivative of the pressure drop measured at the wellbore ($\tau = \tau_{wf}$) assuming zero skin factor (Bourdet *et al.*, 1983). This may be simply related to the drainage volume via Eq. (2.29).

$$\Delta p'_{wf}(t) \equiv \frac{d\Delta p_{wf}(t)}{d \ln t} = \frac{q_w t}{c_t V_d(t)} \quad (2.51)$$

This is an exceptionally useful equation as it allows us to determine the welltest derivative without first solving for the pressure drop. It also provides an intuitive means of understanding the welltest derivative, even in situations with complex flow geometry.

As an example, consider the solution for the drainage volume and welltest derivative for infinite acting radial flow in a homogeneous reservoir (no skin). The reservoir pore volume out to a distance r is given by $V_p = \pi(r^2 - r_w^2)h\phi$, where $\tau = (r - r_w)/\sqrt{\alpha}$, which can be easily integrated to obtain

$$V_d(t) = V_0(t) = 2\pi h\phi(2\alpha t + r_w \sqrt{\pi\alpha t}) \quad \text{and} \quad \Delta p'_{wf} = \frac{q_w t}{2\pi h\phi(2\alpha t + r_w \sqrt{\pi\alpha t})}.$$

For the line source limit of infinite acting radial flow, $\Delta p'_{wf} = \frac{q_w}{4\pi\alpha h\phi} = \frac{\mu q_w}{4\pi kh}$, and we have been able to obtain the well-known equation for the welltest derivative for radial flow directly from the asymptotic formulation without the need to first solve for the pressure drop.

Pressure Drop Just as for the welltest derivative, Eq. (2.29) provides an expression for the time derivative of the pressure drop at the wellbore (with skin), which may be integrated to obtain the pressure drop.

$$\Delta p_{wf}(t) = \frac{q_w}{c_i} \int_{t=0}^t \frac{dt}{V_0(t)} e^{-\tau_{wf}^2/4t} \quad (2.52)$$

We have taken advantage of the evolution equation of our formulation to express the pressure drop as a time integral from the initial pressure instead of as a spatial integral, Eq. (2.40). This equation provides an extension of the definition of a specialist plot to arbitrary geometry. For the example of infinite acting radial flow (in the line source limit), the integral gives a logarithmic dependence on time, as expected.

A similar relationship may be obtained for the pressure drop within the reservoir.

$$\Delta p(\tau, t) = \frac{q_w}{c_i} \int_{t=0}^t \frac{dt}{V_0(t)} e^{-\tau^2/4t} \quad (2.53)$$

For instance, for the line source limit of infinite acting radial flow, we obtain

$$\Delta p(\tau, t) = \frac{\mu q_w}{4\pi kh} E_1\left(\frac{\tau^2}{4t}\right),$$

which is again a well-known solution. An advantage of the

asymptotic formulation is that it reduces the calculation of the pressure drop at the wellbore to a single integral, which may be performed either analytically or numerically, without the need to obtain a general solution within the reservoir.

2.2.2.5 Shut-in Analysis

As is usual, we may use super-position to model shut-in based upon pressure drop expression Eq. (2.52). Evaluated at the well we have:

$$\begin{aligned}\Delta p_{ws}(\Delta t) &= p_{ws}(t_p + \Delta t) - p_{wf}(t_p) = \int_{t=t_p}^{t=t_p+\Delta t} dt \left. \frac{\partial p}{\partial t} \right|_{\tau=\tau_{wf}} \\ &= \left(\frac{q_w}{c_t} \right) \left(\int_{t=0}^{\Delta t} \frac{dt}{V_0(t)} e^{-\tau_{wf}^2/4t} - \int_{t=t_p}^{t=t_p+\Delta t} \frac{dt}{V_0(t)} e^{-\tau_{wf}^2/4t} \right)\end{aligned}\quad (2.54)$$

where, Δp_{ws} represents the BHP change from the BHP at the beginning of shut-in, t_p is the total production time before shut-in, and $\Delta t = t - t_p$ is the time interval after shut-in. This is the equivalent of (2.52) for drawdown. It provides an extension to the definition of a shut-in specialist plot to arbitrary geometry.

The shut-in welltest derivative has been defined as:

$$\Delta p'_{ws}(\Delta t) \equiv \frac{d\Delta p_{ws}(\Delta t)}{d \ln \Delta t_s} \quad \text{where} \quad \Delta t_s = \frac{t_p \cdot \Delta t}{t_p + \Delta t} \quad (2.55)$$

$$\begin{aligned}\Delta p'_{ws}(\Delta t) &= \left(\frac{q_w}{c_t} \right) \left(\frac{t_p + \Delta t}{t_p} \cdot \frac{\Delta t}{V_0(\Delta t)} - \frac{\Delta t}{t_p} \cdot \frac{t_p + \Delta t}{V_0(t_p + \Delta t)} \right) \\ &= \frac{t_p + \Delta t}{t_p} \cdot \Delta p'_{wf}(\Delta t) - \frac{\Delta t}{t_p} \cdot \Delta p'_{wf}(t_p + \Delta t)\end{aligned}\quad (2.56)$$

With this definition the welltest derivative is constant and equal to $\frac{\mu q_w}{4\pi kh}$ for infinite acting radial flow. Eq. (2.56) expresses the shut-in welltest derivative in terms of the drainage volume, or equivalently, in terms of the drawdown welltest derivative. Again, as with Eq. (2.53), it may be evaluated without first solving for the drawdown or build-up pressure changes.

2.2.3 Spatial Integral vs. Time Integral

Our methodology provides us with a test of internal consistency as we may calculate $\Delta p(\tau, t)$ either by an integral in time, Eq. (2.53),

$$\begin{aligned}\Delta p_1(\tau, t) &= \frac{q_w}{c_t} \int_{t=0}^t \frac{dt}{V_0(t)} e^{-\tau^2/4t} \\ \Delta p_{wf1}(t) &= \frac{q_w}{c_t} \int_{t=0}^t \frac{dt}{V_0(t)} e^{-\tau_{wf}^2/4t}\end{aligned}\tag{2.57}$$

or as an integral in τ , Eq. (2.42).

$$\begin{aligned}\Delta p_2(\tau, t) &= \frac{q_w}{c_t V_0(t)} \{W_0(t) - W_0(\tau, t)\} \\ &= \frac{q_w}{c_t V_0(t)} \int_{\tau'=\tau}^{\infty} d\tau' w(\tau') \left(\int_{\tau''=\tau}^{\tau'} \frac{d\tau''}{w(\tau'')} \right) e^{-\tau'^2/4t} \\ \Delta p_{wf2}(t) &= \frac{q_w}{c_t V_0(t)} \int_{\tau=\tau_{wf}}^{\infty} d\tau w(\tau) \left(\int_{\tau'=\tau_{wf}}^{\tau} \frac{d\tau'}{w(\tau')} \right) e^{-\tau^2/4t}\end{aligned}\tag{2.58}$$

The subscripts are temporarily used to distinguish between these two calculations: subscript “1” represents calculation via time integral while subscript “2” stands for calculation via spatial integral.

In our specific applications, we will calculate the pressure drop and the welltest derivative by integral in time as well as integral in space, following Eqs. (2.57) and (2.58). Generally they show very good agreement, demonstrating the internal consistency of the methodology, which will be demonstrated in this section below. The geometry parameters τ , V_p , and $w(\tau)$ of the cases are summarized in Table 2.4 below.

	τ	V_p	$w(\tau)$
Infinite Acting Radial Flow	$(r-r_w)/\sqrt{\alpha}$	$\pi(r^2-r_w^2)h\phi$	$\sqrt{\alpha}\phi(A+2\pi h\tau\sqrt{\alpha})$
Infinite Conductivity Fracture (Pillbox)	$r/\sqrt{\alpha}$	$(4x_f r + \pi r^2)h\phi$	$\sqrt{\alpha}\phi(A+2\pi h\tau\sqrt{\alpha})$
Infinite Conductivity Fracture (Ellipse)	$r/\sqrt{\alpha}$	$\pi r(x_f+r)h\phi$	$\sqrt{\alpha}\phi(\pi A/4+2\pi h\tau\sqrt{\alpha})$

Table 2.4 τ , V_p , and $w(\tau)$ for infinite acting radial flow and infinite conductivity fracture

2.2.3.1 Comparison Examples

Before showing the comparison between spatial and time integral results, it's convenient to summarize the description of the methodology for fixed rate drawdown. Let us list the steps of the asymptotic pressure methodology.

Steps:

1. Solve the Eikonal equation to determine τ , $V_p(\tau)$ and $w(\tau)$
2. If we want to predict a flux profile, solve for $q(\tau, t)$
3. Solve for the drainage volume, $V_0(t)$ and $\Delta p'_{wf}(t)$
4. If we want to predict a pressure profile, solve for the pressure drop, $\Delta p(\tau, t)$
5. Solve for the bottomhole flowing pressure drop, $\Delta p_{wf}(t)$

For the purpose of constructing a diagnostic plot, only steps 1, 3 and 5 are required. Step 1 may be performed analytically for the homogeneous problems, but otherwise we use the FMM. Steps 2 and 3 use a spatial integral of the reservoir volumes $dV_p(\tau)$ weighted by the diffusion kernel. Steps 4 and 5 may utilize time integrals from the initial conditions or spatial integrals from the far field infinite acting reservoir boundary.

At this point we have described two ways to calculate the pressure drop, and in the next section we will show that the spatial integral is more accurate in general. Here, we will demonstrate our solution technique on a series of increasingly more interesting fixed rate pressure transient applications, using both approaches.

Infinite Acting Radial Flow with Skin This is the most basic among all the flow regimes, and will be used to provide an example of the steps of the workflow. As described in Table 2.1, skin is represented using an effective wellbore radius at the corresponding value of $\tau = \tau_{wf} = (e^{-S} - 1)r_w / \sqrt{\alpha}$.

Step 1:

$$\begin{aligned}\tau &= (r - r_w) / \sqrt{\alpha} \\ V_p &= \pi(r^2 - r_w^2)h\phi \\ w(\tau) &= 2\pi(\alpha\tau + r_w\sqrt{\alpha})h\phi = \sqrt{\alpha}\phi(A + 2\pi h\tau\sqrt{\alpha})\end{aligned}\tag{2.59}$$

where, $A = 2\pi r_w h$.

Steps 2 and 3:

$$\begin{aligned}V_0(\tau, t) &= \int_0^\tau d\tau w(\tau) e^{-\tau^2/4t} = 4\pi h\phi\alpha t \cdot (1 - e^{-\tau^2/4t}) + A\phi\sqrt{\pi\alpha t} \cdot \operatorname{erf}\left(\frac{\tau}{2\sqrt{t}}\right) \\ V_0(t) &= 4\pi h\phi\alpha t + A\phi\sqrt{\pi\alpha t} = \phi\sqrt{\pi\alpha t} \cdot (4h\sqrt{\pi\alpha t} + A) \\ q(\tau, t) &= q_w \left\{ 1 - \frac{V_0(\tau, t)}{V_0(t)} \right\} = q_w \cdot \frac{4h\sqrt{\pi\alpha t} \cdot (1 - e^{-\tau^2/4t}) + A \cdot \operatorname{erf}\left(\frac{\tau}{2\sqrt{t}}\right)}{4h\sqrt{\pi\alpha t} + A} \\ \Delta p'_{wf}(t) &= \frac{q_w \cdot t}{c_t \cdot V_0(t)} e^{-\tau_{wf}^2/4t} = \frac{q_w \sqrt{t}}{c_t \phi \sqrt{\pi\alpha} \cdot (4h\sqrt{\pi\alpha t} + A)} e^{-\tau_{wf}^2/4t}\end{aligned}\tag{2.60}$$

Steps 4 and 5:

$$\begin{aligned}
\Delta p_1(\tau, t) &= \left(\frac{q_w}{c_t} \right) \int_{t=0} \frac{dt}{V_0(t)} e^{-\tau^2/4t} = \left(\frac{q_w}{c_t \phi \sqrt{\pi \alpha}} \right) \int_{t=0} \frac{dt}{4h\sqrt{\pi \alpha} \cdot t + A\sqrt{t}} e^{-\tau^2/4t} \\
\Delta p_{wf1}(t) &= \left(\frac{q_w}{c_t \phi \sqrt{\pi \alpha}} \right) \int_{t=0} \frac{dt}{4h\sqrt{\pi \alpha} \cdot t + A\sqrt{t}} e^{-\tau_{wf}^2/4t} \\
\Delta p_2(\tau, t) &= \frac{q_w}{c_t V_0(t)} \{W_0(t) - W_0(\tau, t)\} \\
&= \frac{q_w}{c_t V_0(t)} \int_{\tau'=\tau}^{\infty} d\tau' w(\tau') \left(\int_{\tau''=\tau}^{\tau'} \frac{d\tau''}{w(\tau'')} \right) e^{-\tau'^2/4t} \\
&= \left(\frac{q_w}{c_t \phi \sqrt{\pi \alpha t} \cdot (4h\sqrt{\pi \alpha t} + A)} \right) \int_{\tau'=\tau}^{\infty} d\tau' w(\tau') \left(\int_{\tau''=\tau}^{\tau'} \frac{d\tau''}{w(\tau'')} \right) e^{-\tau'^2/4t} \\
\Delta p_{wf2}(t) &= \frac{q_w W_0(t)}{c_t V_0(t)} = \frac{q_w}{c_t V_0(t)} \int_{\tau_{wf}}^{\infty} d\tau w(\tau) \left(\int_{\tau'=\tau_{wf}}^{\tau} \frac{d\tau'}{w(\tau')} \right) e^{-\tau^2/4t}
\end{aligned} \tag{2.61}$$

In the line source limit it can be shown that the τ dependence of the pressure drop integral reduces to the E_1 function at $(\tau + r_w/\sqrt{\alpha}) = (r/\sqrt{\alpha})$. Eq. (2.61) becomes:

$$\begin{aligned}
\Delta p_1(\tau, t) &= \left(\frac{\mu q_w}{4\pi kh} \right) \int_{t=0} \frac{dt}{t} e^{-(\tau+r_w/\sqrt{\alpha})^2/4t} = \left(\frac{\mu q_w}{4\pi kh} \right) \cdot E_1 \left(\frac{r^2}{4\alpha t} \right) \\
\Delta p_{wf1}(t) &= \left(\frac{\mu q_w}{4\pi kh} \right) \cdot E_1 \left(\frac{r_w^2 e^{-2S}}{4\alpha t} \right) \\
\Delta p_2(\tau, t) &= \left(\frac{\mu q_w}{4\pi kht} \right) \int_{\tau'=(\tau+r_w/\sqrt{\alpha})}^{\infty} d\tau' \tau' e^{-\tau'^2/4t} \ln \left(\frac{\tau'}{\tau} \right) = \left(\frac{\mu q_w}{4\pi kh} \right) \cdot E_1 \left(\frac{r^2}{4\alpha t} \right) \\
\Delta p_{wf2}(t) &= \left(\frac{\mu q_w}{4\pi kh} \right) \cdot E_1 \left(\frac{r_w^2 e^{-2S}}{4\alpha t} \right)
\end{aligned} \tag{2.62}$$

Eq. (2.62) shows that we have recovered the well-known line source solution. In the PSS limit at the wellbore, we may use the logarithmic approximation for the E_1 function to obtain a constant value for the welltest derivative. Though Eq. (2.62), we demonstrate the

internal consistency of our methods via either spatial or time integrals, as expected for power law $w(\tau)$.

Infinite Conductivity Fractured Vertical Well (No Damage Skin) We start the analysis with an analytic graphical solution to the Eikonal equation and a calculation of $V_p(\tau)$. Two τ contours are shown in Figure 2.10.

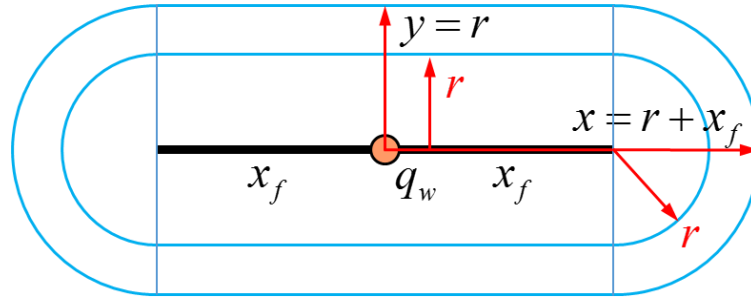


Figure 2.10 Graphical solution to the Eikonal equation and the calculation of $V_p(r)$ for an infinite conductivity fracture (top view)

To determine $\tau(\bar{x})$ at any location, we may integrate $\left(\frac{d\tau}{dr}\right)dr$ obtained from the characteristic directions for the Eikonal equation (This is the solution inherent in the use of the FMM.) For locations in the plane of the fracture, the minimum τ path is directly to the fracture, $\tau = r/\sqrt{\alpha}$. For any other location, the minimum τ path is to the fracture tips, where again, $\tau = r/\sqrt{\alpha}$, with r as shown. The pore volume is the sum of the linear and radial contributions.

Step 1:

$$\begin{aligned}
\tau &= r/\sqrt{\alpha} \\
V_p &= (4x_f r + \pi r^2) h \phi \\
w(\tau) &= (4x_f \sqrt{\alpha} + 2\pi\alpha\tau) h \phi = \sqrt{\alpha} \phi (A + 2\pi h \tau \sqrt{\alpha})
\end{aligned} \tag{2.63}$$

where, $A = 4x_f h$. This equation for $w(\tau)$ is identical to that of radial flow, above, although with a different expression for the area.

For Steps 2 – 5, the expressions of flux and pressure are identical to the solutions of radial flow with finite radius, because they share the same form of $w(\tau)$ formula which is a linear term plus a constant term. We may also calculate the depth of investigation:

$$\frac{\tau_{doi}^2}{4t} = \frac{r_{doi}^2}{4\alpha t} = \frac{1}{2} \frac{x_f + 2\sqrt{\pi\alpha t}}{x_f + \sqrt{\pi\alpha t}} \tag{2.64}$$

It smoothly interpolates between a value of ½ at early time (linear flow) and 1 at late time (radial flow).

Analytic expressions for the two functions required for a diagnostic plot are given in Eqs. (2.60) and (2.61). These solutions are tested against the inverse Laplace transform reference solution in Figure 2.11 (King *et al.*, 2016), and both show excellent agreement with the reference (Gringarten *et al.*, 1975; Bello and Wattenbarger, 2010; Kuchuk *et al.*, 2015).

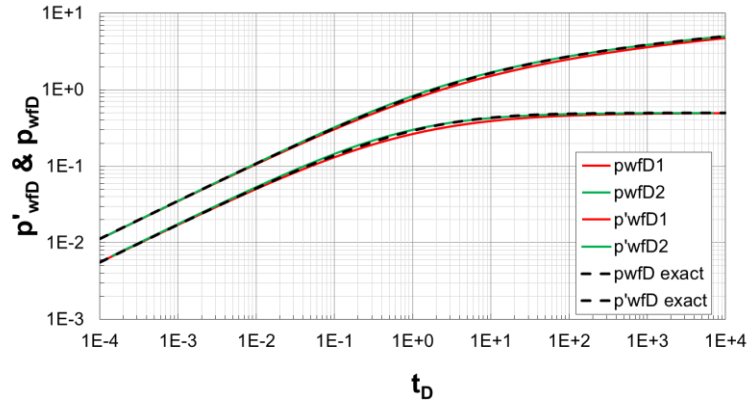


Figure 2.11 Diagnostic plot validation for an infinite conductivity fracture (reprinted with permission from King et al., 2016)

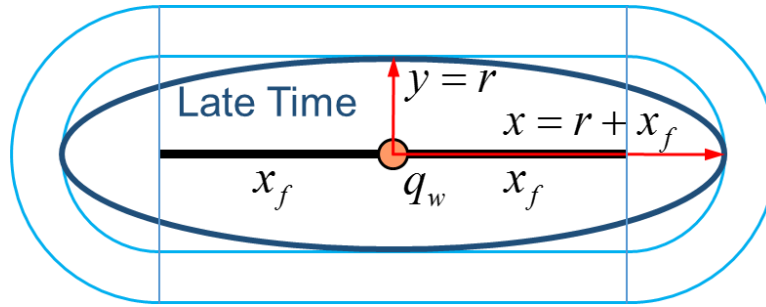


Figure 2.12 Graphical solution to the Eikonal equation and PSS flow in the vicinity of an infinite conductivity fracture (top view)

We may also analyze PSS flow in the vicinity of the infinite conductivity fracture illustrated in Figure 2.12. As time increases, the pressure solutions near the fracture tips become increasingly smooth, eventually approaching an ellipse (Kucuk and Brigham, 1979). Parallel and perpendicular to the axis of the fracture the solutions to the Eikonal solution are exact, providing us with the semi-major and semi-minor axes of the ellipse, from which we obtain an expression for $V_p(\tau)$ to use at late time, e.g., the PSS period.

$$\tau = r/\sqrt{\alpha} \quad V_p = \pi r(x_f + r)h\phi \quad w(\tau) = (\pi x_f \sqrt{\alpha} + 2\pi\alpha\tau)h\phi \quad (2.65)$$

During PSS period of flow, we can get the pressure profile as:

$$\begin{aligned}
q_w = q &= c_t w(\tau) \frac{\partial p}{\partial \tau} \\
p(\tau, t) - p_{wf} &= \frac{q_w}{c_t} \int_{\tau_{wf}} \frac{d\tau}{w(\tau)} = -\frac{q_w}{c_t} \cdot \frac{\mu c_t}{2\pi kh} \int_{\tau_{wf}} \frac{d\tau}{\tau + \tau_w} = \frac{\mu q_w}{2\pi kh} \ln \left(\frac{\tau + \tau_w}{\tau_{wf} + \tau_w} \right) \\
&= \frac{\mu q_w}{2\pi kh} \ln \left(\frac{r}{r_w e^{-S}} \right)
\end{aligned} \tag{2.66}$$

where, $\tau_w = r_w / \sqrt{\alpha}$.

Similarly, for an infinite conductivity fracture which has elliptical pressure contours during PSS, we obtain that:

$$\begin{aligned}
q_w &= \frac{kA(r)}{\mu} \frac{\partial p}{\partial r} = \frac{\pi kh(x_f + 2r)}{\mu} \frac{\partial p}{\partial r} \\
p(\tau, t) - p_{wf} &= \frac{\mu q_w}{\pi kh} \int_0^{x_f + 2r} \frac{dr}{x_f + 2r} = \frac{\mu q_w}{2\pi kh} \ln \left(\frac{x_f + 2r}{x_f} \right)
\end{aligned} \tag{2.67}$$

Compared to radial flow at large distance, we know that $\frac{x_f + 2r}{x_f} \rightarrow \frac{r}{r_w e^{-S}}$, and thus

$\frac{2}{x_f} = \frac{1}{r_w e^{-S}}$, and we obtain that $r_w e^{-S} = x_f/2$ or $S = \ln(2r_w/x_f)$, which is the known

solution (Prats, 1961).

If we repeat for the τ contour (pillbox) and calculate skin, we will get:

$$\begin{aligned}
q_w &= \frac{kA(r)}{\mu} \frac{\partial p}{\partial r} = \frac{\pi kh(4x_f/\pi + 2r)}{\mu} \frac{\partial p}{\partial r} \\
p(\tau, t) - p_{wf} &= \frac{\mu q_w}{2\pi kh} \int_0^{4x_f/\pi + 2r} \frac{dr}{4x_f/\pi + 2r} = \frac{\mu q_w}{2\pi kh} \ln \left(\frac{4x_f/\pi + 2r}{4x_f/\pi} \right)
\end{aligned} \tag{2.68}$$

and the result is $r_w e^{-S} = 2x_f/\pi$ or $S = \ln(\pi r_w/2x_f)$, which is not correct. This means

only the PSS geometry as shown gives the correct expression for the skin of the fracture.

Eq. (2.65) may also be used to infer the effective PSS flowing fracture area. If we return to the interpretation of $w(\tau)/(\phi\sqrt{\alpha})$ as a cross-sectional area, we may calculate the effective flowing area of the fracture from $w(0)/(\phi\sqrt{\alpha}) = \pi x_f h$. In other words, only a fraction of $(\pi/4)$ of the fracture area controls PSS production. This reduction in effective flowing area is consistent with the solution of the PSS Laplace equation using an elliptic-hyperbolic coordinate system to represent the pressure contours and streamlines of flow in the reservoir around the fracture. Outside this fraction of the area, streamlines are closely spaced in the reservoir, with increased local pressure drop and reduced contribution to the well productivity (Kucuk and Brigham, 1979). During early time, pressure drop align with pillbox shaped τ contour so that Eqs. (2.60) and (2.61) are the correct expressions for linear flow. During late time, correct skin can be obtain via elliptical τ contour.

2.2.3.2 Validation of the Asymptotic Solution

Throughout the dissertation, I will show how we apply the asymptotic pressure approximation to a series of examples in pressure and rate transient analysis, and to well productivity. These applications have three purposes:

- To demonstrate or test the accuracy of the approximation against known solutions
- To develop simple solutions which may replace the use of type curves

- To extend the infinite acting fixed rate and fixed BHP drawdown solutions to variable rate drawdown and bounded reservoirs

The reference transient solutions will be solved using numerical inversion of the Laplace transform. Unlike the asymptotic formulation which supports both reservoir heterogeneity and complex well geometries, these solutions are restricted to piecewise homogeneous solutions in regular geometries. Nonetheless, they do provide validation tests and guidance on these extensions to the methodology. Most importantly, through various comparisons between asymptotic solutions and those reference (or, “exact”) solutions, we will have a better understanding of both the accuracy and error of our approximations, so that we will obtain guidance on where we may need to improve our analytic solutions.

Infinite Acting Radial Flow (Finite Radius) Here, I use infinite acting radial flow with a finite wellbore radius as an example to display the dimensionless pressure calculated from either time integral Eq. (2.57) or spatial integral Eq. (2.58) in Figure 2.13. The error maps of both pressure time derivative and pressure spatial gradient w.r.t. results from numerical inverse Laplace transform are shown in Figure 2.14 and Figure 2.15, respectively. The parameters are expressed in the dimensionless form, i.e., $\partial p_D / \partial t_D$ and

$$\partial p_D / \partial r_D, \text{ where } p_D = \frac{2\pi kh\Delta p}{q_w \mu}, r_D = \frac{r}{r_w} = \frac{\sqrt{\alpha\tau}}{r_w} + 1, \text{ and } t_D = \frac{\alpha t}{r_w^2}.$$

The x and y-axis are dimensionless radius r_D and dimensionless time t_D . In subplot (c), the red region represents the time and location that asymptotic solutions are greater than those from inverse Laplace transform and the black dashed curves in Figure 2.14 (c) and Figure 2.15

(c) represent the relation $t = \tau^2/4 \Rightarrow t_D = (r_D - 1)^2/4$, at the depth of investigation for radial flow.

From Figure 2.13 (c) and (f), we observe that both approaches are good approximations to the exact solution, with a maximum error less than 4%. This is the first validation of the asymptotic pressure solution for a non-trivial (non-self-similar) solution. Another observation is that the pressure calculated via spatial integral generally has a smaller error compared to the one from time integral. Furthermore, time integral tends to underestimate pressure drop while spatial integral tends to overestimate pressure drop, which can also be seen in Figure 2.11.

From Figure 2.13 (a), (b), (c) and Figure 2.14 (c), we observe that once an error (in time) arises that it does not get corrected. $\partial p_D / \partial t_D$ has a relatively large error along the black dashed curve. The red region indicates the asymptotic solution underestimates $\partial p_D / \partial t_D$ inner the pressure front while the blue region indicates the asymptotic solution overestimates $\partial p_D / \partial t_D$ outside the pressure front

From Figure 2.13 (d), (e), (f) and Figure 2.15 (c), we observe that errors in the flux at one time do not propagate to later times. For $\partial p_D / \partial r_D$, the error range is much narrower compared to $\partial p_D / \partial t_D$. Again, the maximum error is located along with the black dashed curve, indicating the maximum error of $\partial p_D / \partial r_D$ occurs right at the pressure front as is illustrated in Figure 2.15 (c).

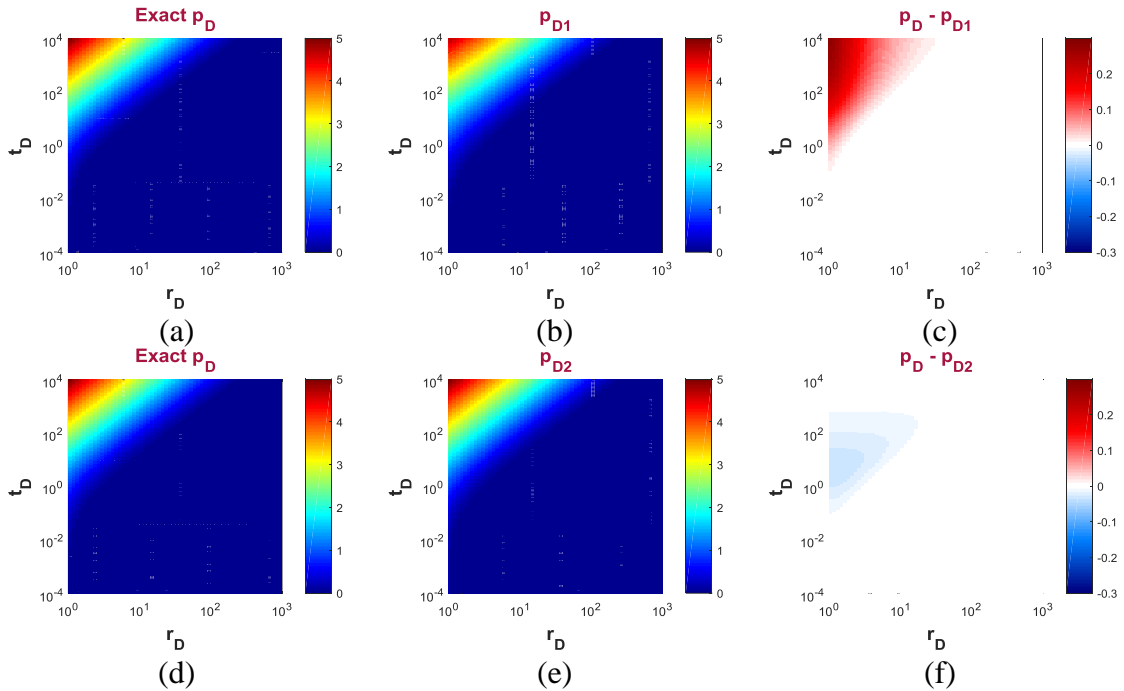


Figure 2.13 Dimensionless pressure distribution w.r.t t_D vs. r_D for (a) and (d) numerical inverse Laplace transform (exact); (b) and (c) asymptotic solution and error of pressure from time integral; (e) and (f) asymptotic solution and error of pressure from spatial integral

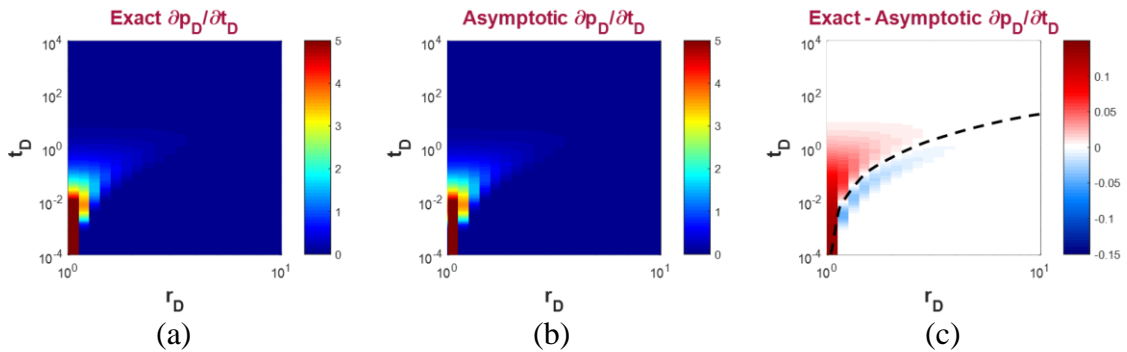


Figure 2.14 Dimensionless pressure time derivative distribution w.r.t t_D vs. r_D for (a) numerical inverse Laplace transform (exact); (b) asymptotic solution; (c) difference between asymptotic and exact solutions

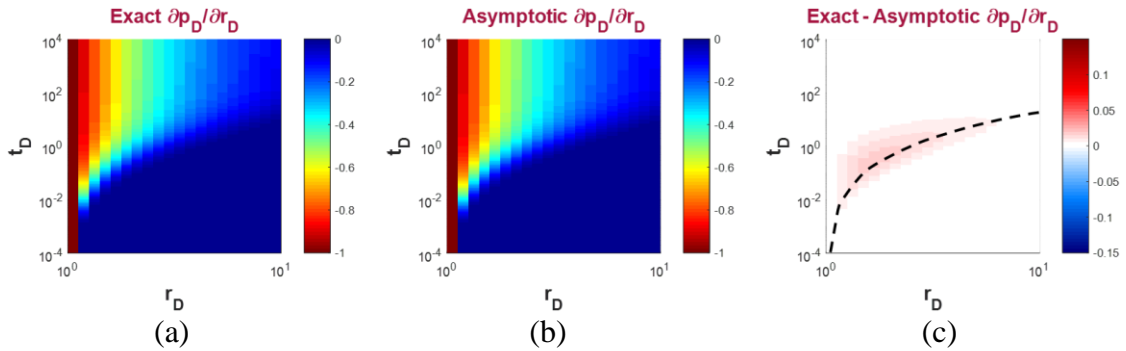


Figure 2.15 Dimensionless pressure spatial gradient distribution w.r.t t_D vs. r_D for (a) numerical inverse Laplace transform (exact); (b) asymptotic solution; (c) difference between asymptotic and exact solutions

2.3 Validation of the Asymptotic Approximation via Simulation

In this section, we will focus on the validation of transient pressure propagation using numerical simulation. The asymptotic approximations are infinite acting, while for the reference ECLIPSE cases, the reservoir size is finite and we may observe boundary effects during later times. The purpose is to validate our transient solutions as well as understand the necessity to develop further transient & PSS solutions. We will first examine the validation of the asymptotic solutions for homogeneous problems where $\tau = (r - r_w) / \sqrt{\alpha}$, and then return to the impact of heterogeneity where τ is obtained from the solution to the Eikonal equation using the Fast Marching Method.

2.3.1 Validation of the Asymptotic Approximation: Homogeneous Cases

In this subsection, let's begin the validation of the asymptotic approximation for the most fundamental case, i.e., infinite acting radial flow with fixed rate drawdown in a homogeneous reservoir, followed by an infinite conductivity hydraulic fracture case. The reservoir, fluid and wellbore parameters of both cases are listed in Table 2.5.

Property	Value	Unit
Grid size	10×10×10	<i>ft</i> ³
Grid number	51×51×1	
<i>h</i>	10	<i>ft</i>
ϕ	0.3	-
<i>k</i>	0.5	<i>md</i>
μ	1.0	<i>cp</i>
<i>c_t</i>	1×10 ⁻⁵	<i>psi</i> ⁻¹
<i>B</i>	1.0	<i>rb/bbl</i>
<i>r_w</i>	0.5	<i>ft</i>
<i>x_f</i>	55	<i>ft</i>
<i>q_w</i>	10	<i>bbl/day</i>

Table 2.5 Reservoir, fluid and wellbore parameters for infinite acting radial flow and a case with an infinite conductivity fracture

2.3.1.1 Infinite Acting Radial Flow

In this case, we have a vertical well located in the center of the square reservoir. The smallest τ value along the reservoir boundary is $\tau_{res} = 38.4 \text{ hr}^{1/2}$ and the corresponding time for the boundary to be detectable at the well is $t_{LOD} = (2\tau_{res})^2 / 16 = 15.4 \text{ d}$. The flow rate is fixed and is sufficiently low that bottomhole flowing pressure constraints are not reached during the flow simulation. Figure 2.16 illustrates the comparison of the distribution of the pressure drop time derivative between the asymptotic approximation and ECLIPSE at various times. We observe that both asymptotic approximation and ECLIPSE predict a circular propagation of pressure depletion during early time, as expected. At $t = 0.52 \text{ d}$, we can see the mismatch between asymptotic solution and ECLIPSE is small with the maximum relative error of 2% near

the wellbore. At $t = 4.26 d$, the mismatch between asymptotic solution and ECLIPSE increases with the maximum relative error of 20% near the boundary. The observation shows the mismatch propagates towards the reservoir boundary during early time. At $t = 7.75 d$, even though the time is earlier than t_{LOD} , we start to see large mismatch at both reservoir boundary as well as near well region, with the 30% maximum relative error near the boundary. Finally, at $t = 20.10 d$ which is a time later than t_{LOD} , we see a clear boundary effect near the well with the maximum relative error of 40%. In Figure 2.16 (f), (i), and (l), we can see that ECLIPSE predicts a higher pressure drop derivative than asymptotic solution near the boundary, as indicated by the red region in the plots, implying the pressure front has actually reached the boundary and the reflected front has started causing additional pressure drop near the boundary. Even though $t < t_{LOD}$, we still see the large mismatch at both reservoir boundary and near well region, since t_{LOD} only represents the time to detect boundary effect at the wellbore which would have already had additional pressure drop at most locations. It also implies that $V_0(t)$ is also overestimated since it is calculated for infinite acting propagation which excludes reflections. This extra pressure drop is more obvious in subplot (l), because $t > t_{LOD}$ and the reflected pressure front has already been detected at the wellbore and the infinite acting radial flow is no longer an accurate an approximation thereafter. The maximum prediction error of asymptotic approximation over ECLIPSE, can be as low as 2% when $t < t_{LOD}$, while it can be as high as 40% when $t > t_{LOD}$. We will illustrate how to resolve this issue in the next chapter.

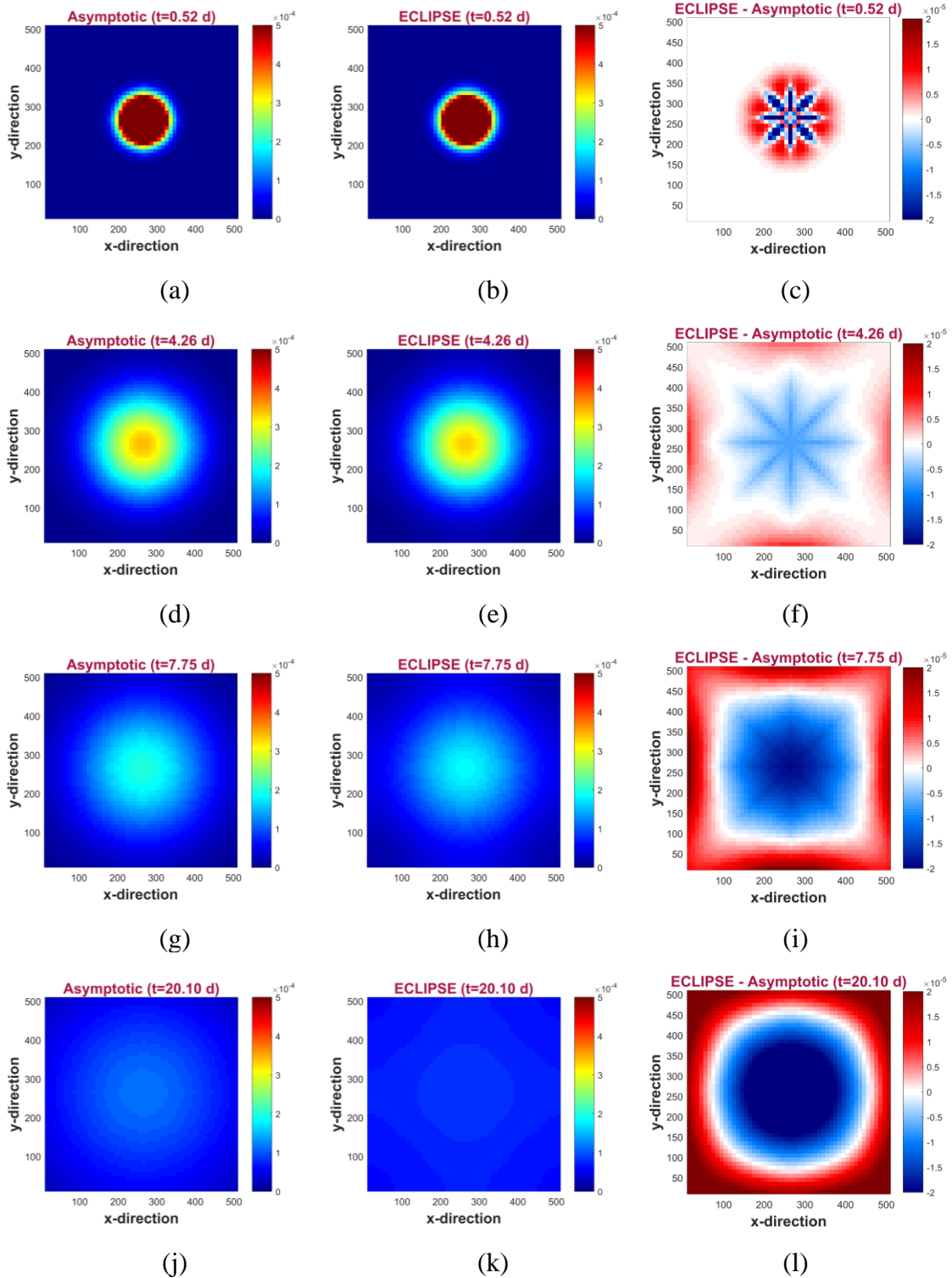


Figure 2.16 Comparison of the distribution of the pressure drop time derivative between the asymptotic and ECLIPSE results at various times

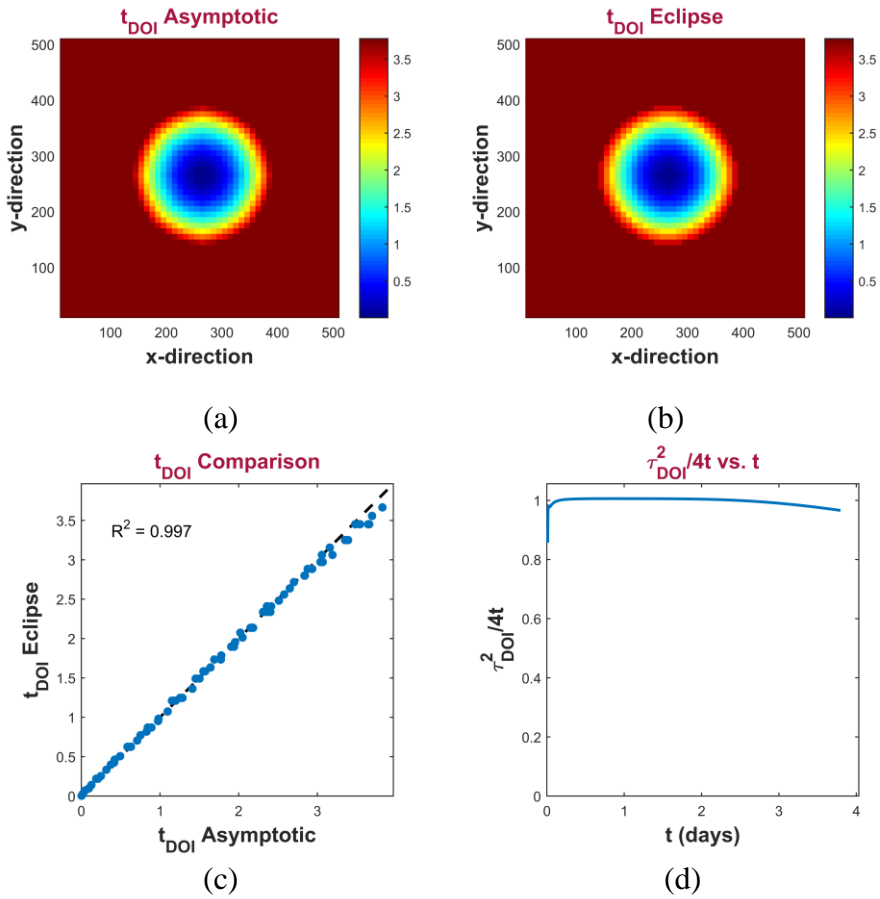


Figure 2.17 (a) DOI time map from asymptotic solution; (b) DOI time map from ECLIPSE; (c) Cross plot of DOI time between asymptotic and ECLIPSE results and (d) DOI asymptotic prediction vs. time for infinite acting radial flow (reprinted with permission from Wang et al, 2017)

Figure 2.17 (a) & (b) illustrate the prediction of time at depth of investigation by asymptotic approximation as well as ECLIPSE. For our analytic approach, it can be calculated directly from relation $\tau^2/4t_{DOI} = 1$ for radial flow; while for ECLIPSE, it can be obtained by checking when $\partial^2\Delta p/\partial t^2 = 0$ at each gridblock. Both subplots show a consistent map of t_{DOI} , as is demonstrated in subplot (c). From Figure 2.17 (d) we once

again observe the characteristics of infinite acting radial flow period of this case, as is indicated by $\xi_{DOI} = \tau_{DOI}^2 / 4t = 1$, where $\tau_{DOI}^2(t) = V_2(t) / V_0(t)$.

2.3.1.2 Infinite Conductivity Fracture

In this case, we have an infinite conductivity hydraulic fracture aligned with the x-direction and located in the center of the reservoir. Figure 2.18 illustrates the comparison of the distribution of the pressure drop time derivative between the asymptotic and ECLIPSE results at various times. We here use dimensionless time $t_D = \frac{4\alpha t}{x_f^2}$ to distinguish early ($t_D < 1$) and late periods ($t_D > 1$). At $t_D = 0.14$, we can see both asymptotic solution and ECLIPSE predict pillbox-shaped contours of pressure drop time derivative, and the mismatch between the two is small with the relative error of 5% near the fracture. Compared to the ECLIPSE simulation, the asymptotic solution tends to predict lower pressure drop time derivative for the pressure front propagating perpendicular to the fracture (red region) and a higher pressure drop time derivative for pressure front propagating from the fracture tips. At $t_D = 0.70$, both of asymptotic solution and ECLIPSE still predict pillbox-shaped contours, however, those given from ECLIPSE seem to shift from pillbox to ellipse and the mismatch grows with the relative error of 10% near the fracture. At $t_D = 2.81$, a late time, we observe different contour shapes between the two: asymptotic solution predicts pillbox-shaped contours while ECLIPSE now predicts elliptical ones, and the mismatch grows with the maximum relative error of 20%

near the fracture. At $t_D = 5.61$, we have similar observation on the mismatch with the maximum relative error of 20% near the fracture. We see an evolving difference between the two approaches from subplots (c), (f), (i), and (l). This issue, however, is not caused by the asymptotic pressure approximation. It is actually a result of the pillbox-shaped τ contour predicted from the solution of the Eikonal equation. If necessary, this discrepancy could be resolved through the use of superposition in space, as described for other examples in the next chapter. Even though, we can observe a good match from cross plots between pressure drop and τ in Figure 2.19. The major difference occurs near the wellbore, as indicated by the flat trend of the blue dots.

Furthermore, in Figure 2.19 (c) and (d) when $t_D > 1$, there are far more vertical (not horizontal) scatter in the plots even than those of cases with heterogeneity. This shows that τ is not as good a coordinate in this case, once $t_D > 1$. This has potential implications for the modeling of wells with multi-fracture. What is more important between multi-fracture interference and single fracture superposition? The answer will depend upon the fracture spacing. According to the Midland Basin fracture job evolution by Pioneer (2016), as shown in Figure 2.20, we can see the cluster spacing reduces from 60 ft in 2013 to 30 ft in 2015, and further down to 15 ft in late 2016 with an increasing amount of fluid and proppant. Compared to fracture half length (several hundred ft), the current fracture cluster spacing is much smaller, and thus multi-fracture interference is more important and we will show relevant field analysis in Chapter 4.

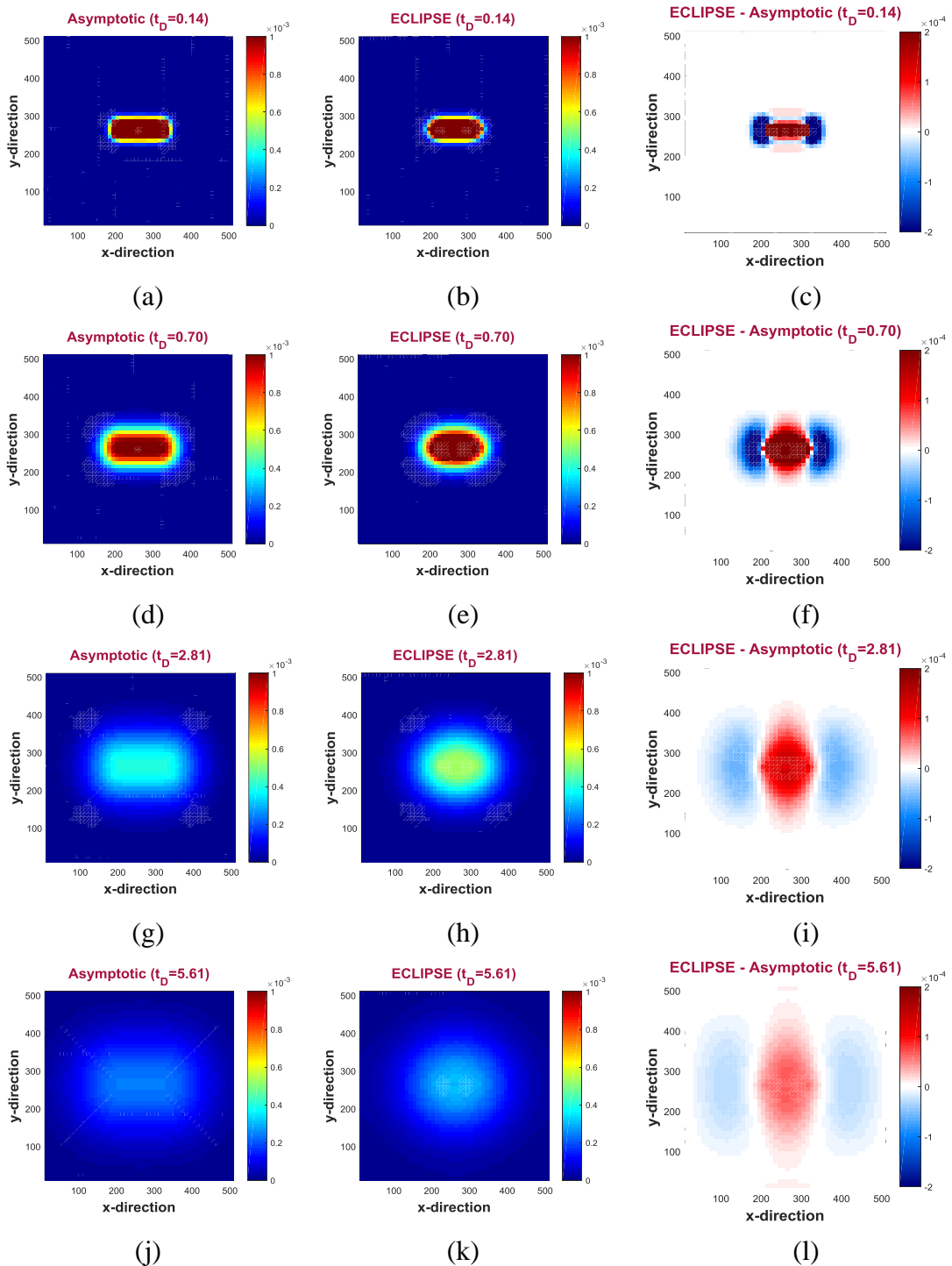


Figure 2.18 Comparison of the distribution of the pressure drop time derivative between the asymptotic derivative and ECLIPSE results at various times for the case of an infinite conductivity hydraulic fracture (reprinted with permission from Wang et al, 2017)

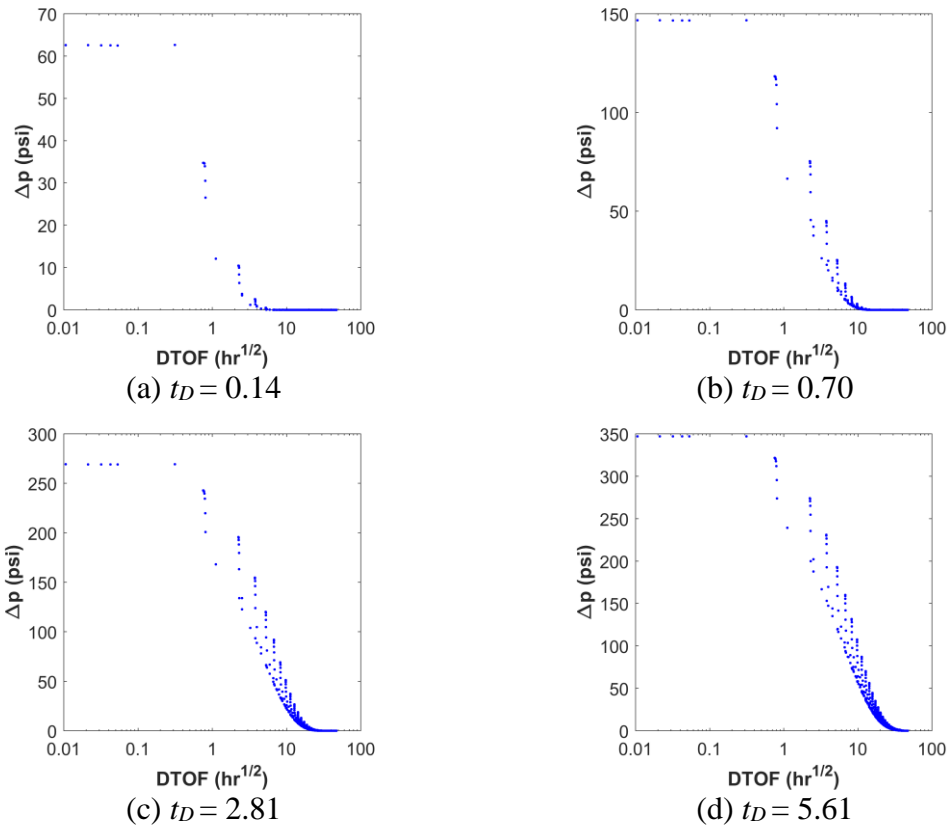


Figure 2.19 Cross plots of pressure drop from ECLIPSE vs. DTOF at various times for the case of an infinite conductivity hydraulic fracture

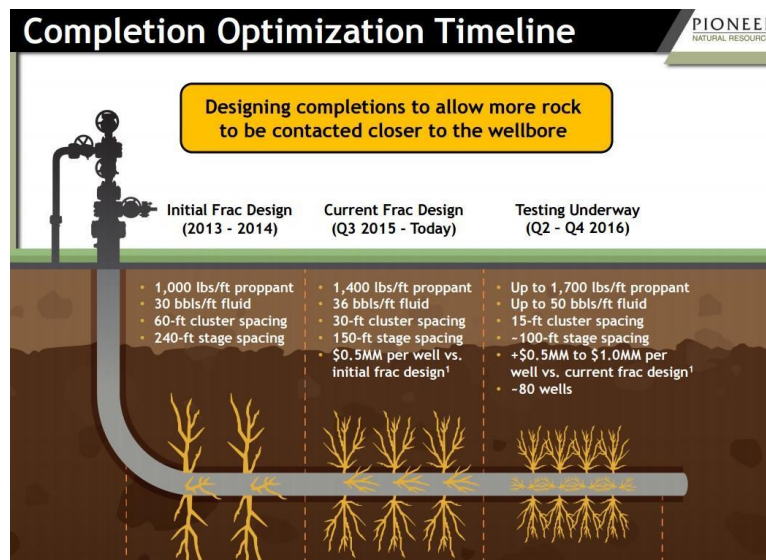


Figure 2.20 Midland Basin fracture job evolution (Pioneer, 2016)

Now, it is time to summarize what we have learned about infinite conductivity fracture case. Previously, I show that both reservoir heterogeneity and limit of Eikonal equation would not exactly follow the assumption of $p(\bar{x}, t) \approx p(\tau(\bar{x}), t)$ to a certain extent. For infinite conductivity fracture case, notice that:

- Eikonal solution is a pillbox at all τ .
- Eikonal equation gives the shape of the drainage volume $V_p(\tau)$ at early time accurately.
- Elliptical pressure solutions will arise at late time (Kucuk and Brigham, 1979).
- Early time PTA response is consistent with the pillbox shape as it reproduces the linear flow response with the full fracture area of $4x_f h$.
- Late time PSS response is consistent with the elliptical shape as it reproduces the fracture skin expression, consistent with the partial fracture area of $\pi x_f h$.

The pressure contour is both a function of time and space, since we observe that it gradually changes from pillbox to ellipse near the fracture, according to ECLIPSE simulation result. It's worth mentioning that the early time solution at any location in the reservoir still follows self-similarity, i.e., the first pressure changes at any location in the reservoir still retain their original pillbox shapes. Figure 2.21 shows a contour map of the logarithm of the dimensionless pressure drop time derivative at a late time of $t_D = 1.99$. Pillbox shaped contours (black solid curves) can still be observed deep in the reservoir,

beyond the depth of investigation (black dashed curve obtained from the simulator). In contrast, the pressure contours have already shifted to ellipses near the fracture, inside the depth of investigation.

Log of Normalized dp_D/dt_D Contour @ $t_D = 1.99$

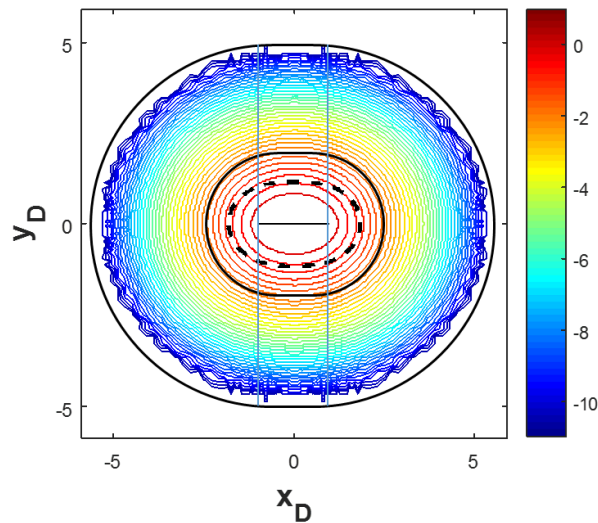


Figure 2.21 Contour of log of normalized dimensionless pressure time derivative of infinite conductivity fracture case

Figure 2.22 (a) & (b) do not show a very consistent map of t_{LOD} . The mismatch can also be seen in cross subplot (c), where we observe that our asymptotic approximation tends to give larger t_{DOI} compared to the ECLIPSE result. Eikonal equation would always yield a pillbox shaped τ contour which implies a strong radial flow regime starting at both fracture tips. This, however, cannot not be observed in the elliptical contours given by ECLIPSE. Once again, ξ_{DOI} is calculated based upon asymptotic approximation as $\xi_{DOI} = V_2(t)/V_0(t)/4t$, as shown in Figure 2.22 (d), where we conclude that the flow

regime during early time is very close to linear flow since ξ_{DOI} is close to 0.5, and the flow regime trends to become more radial as time increases since ξ_{DOI} is approaching to 1. The radial flow is not fully established due to the small reservoir size.

We can understand the discrepancy between τ and the pressure contours using superposition in space, Figure 2.23. Consider the infinite conductivity fracture to be a distribution of multiple point sources instead of being a single source at the $\tau = 0$ contour (the entire fracture), as illustrated in Figure 2.23. Consider two points located along the same τ contour: the blue dot is near the fracture tip while the green dot is perpendicular to the fracture. Consider the volume of influence of each. At the earliest increase of pressure, the volume of influence will just graze the fracture, and each point will experience the influence of just a single point. At this time, the τ coordinate will still give a good representation of the depletion. However, as time increases, the green dot will be influenced by more discrete point sources along the fracture than the blue dot, and thus will have a greater pressure drop compared to the blue dot. The τ coordinate controls the “first passage” early time response, but it will not capture the superposition effects and the evolution towards an elliptical contour.

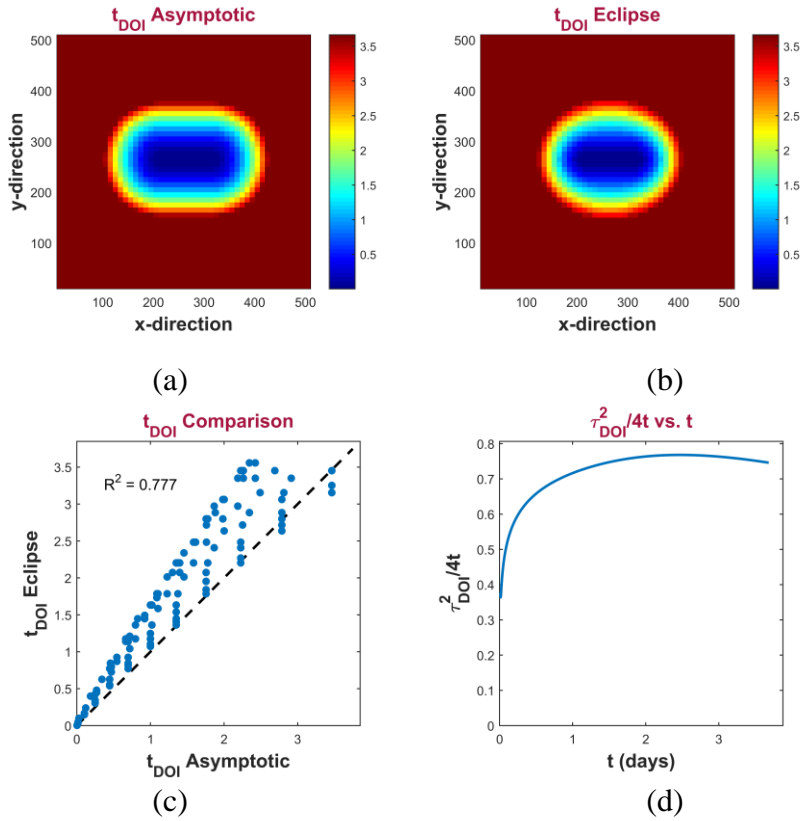


Figure 2.22 (a) DOI time map from asymptotic solution; (b) DOI time map from ECLIPSE; (c) Cross plot of DOI time between asymptotic and ECLIPSE results and (d) DOI Boltzmann variable vs. time for case with infinite conductivity hydraulic fracture (reprinted with permission from Wang et al, 2017)

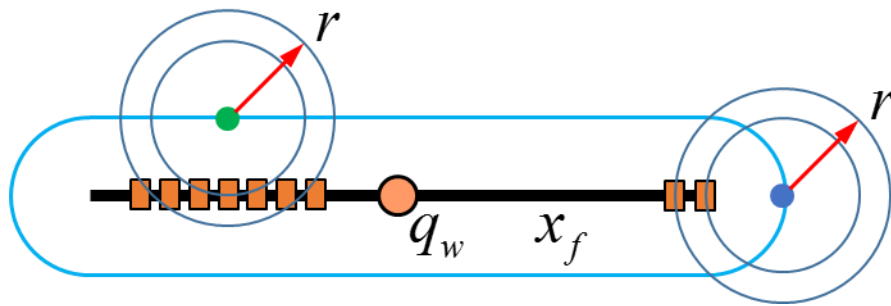


Figure 2.23 Illustration of the impact of hydraulic fracture on different locations along the same DTOF contour

2.3.2 Validation of the Asymptotic Approximation: Simulation with Heterogeneity

As mentioned in the last section, the accuracy of the assumption $p(\bar{x}, t) \approx p(\tau(\bar{x}), t)$ is crucial to the accuracy of the asymptotic approximation. In this subsection, I will explore the limit of validity of this assumption through finite difference simulations with various levels of reservoir heterogeneity. The simulation time is early enough that finite size effects are not expected to be significant. The range of the t_{LOD} is 5.2 – 33.5 days.

Some of the cases are selected and their permeability distributions, the corresponding DTOF and cross plots between $\frac{q_w}{V(t)} e^{-\tau(\bar{x})^2/4t}$ from asymptotic approximation and $c_i \frac{\partial \Delta p(\bar{x}, t)}{\partial t}$ from ECLIPSE for each cell in the reservoir model before the solution is strongly impacted by finite boundary effects ($t = 0.52 d$) are displayed in Figure 2.24 ($L_{DCL} = 1.00$) and Figure 2.26 ($V_{DP} = 0.60$).

Figure 2.24 (a), (d), (g) show that permeability variance increases along with V_{DP} at a fixed pattern, since they are generated with the same L_{DCL} . As heterogeneity variance increases, Figure 2.24 (b), (e), (h) illustrate a growing range of DTOF and Figure 2.24 (c), (f), (i) display an increasingly scattered trend between asymptotic solutions and ECLIPSE results, especially near the wellbore (dark blue dots represent small τ). The color of each dots represent the τ value, with blue corresponding to those near the well and red corresponding to those deep in the reservoir. R^2 is the coefficient of determination and is calculated based on the deviation of the points from the straight trend on the cross plots.

In Figure 2.24 (i), we can even observe two trends, which is caused by the high perm “channel” connected to the wellbore. To better understand the mismatch, I pick the case and plot the pressure drop, $w(\tau)$ and $d \ln w(\tau)/d \ln(\tau)$ vs. τ in Figure 2.25. From Figure 2.25 (a), we know that Δp is not a function of τ because of the large vertical scatter between Δp and τ . In Figure 2.25 (b), we can see two drops of $w(\tau)$ curve at $\tau = 1 hr^{1/2}$ and $\tau = 8 hr^{1/2}$, which correspond to the locations where pressure front first hits the boundary of the high perm channel and the boundary of the reservoir, respectively. Figure 2.25 (c) reveals how the smoothness $d \ln w(\tau)/d \ln(\tau)$ varies along with τ , where the decreasing trend and negative values do great harm to the accuracy of the asymptotic solution. This ties back to the discussion of the analytic bounds with Eq. (2.28). If $d \ln w(\tau)/d \ln(\tau) > 0$, then we still expect to be bounded by the exponential trend. However, if $d \ln w(\tau)/d \ln(\tau) < 0$, then we expect a backwards going reflection term, which is not included in this analytic form. Later in Chapter 3 Subsection 3.3.2, I will show the analytic solution with strong reflectors.

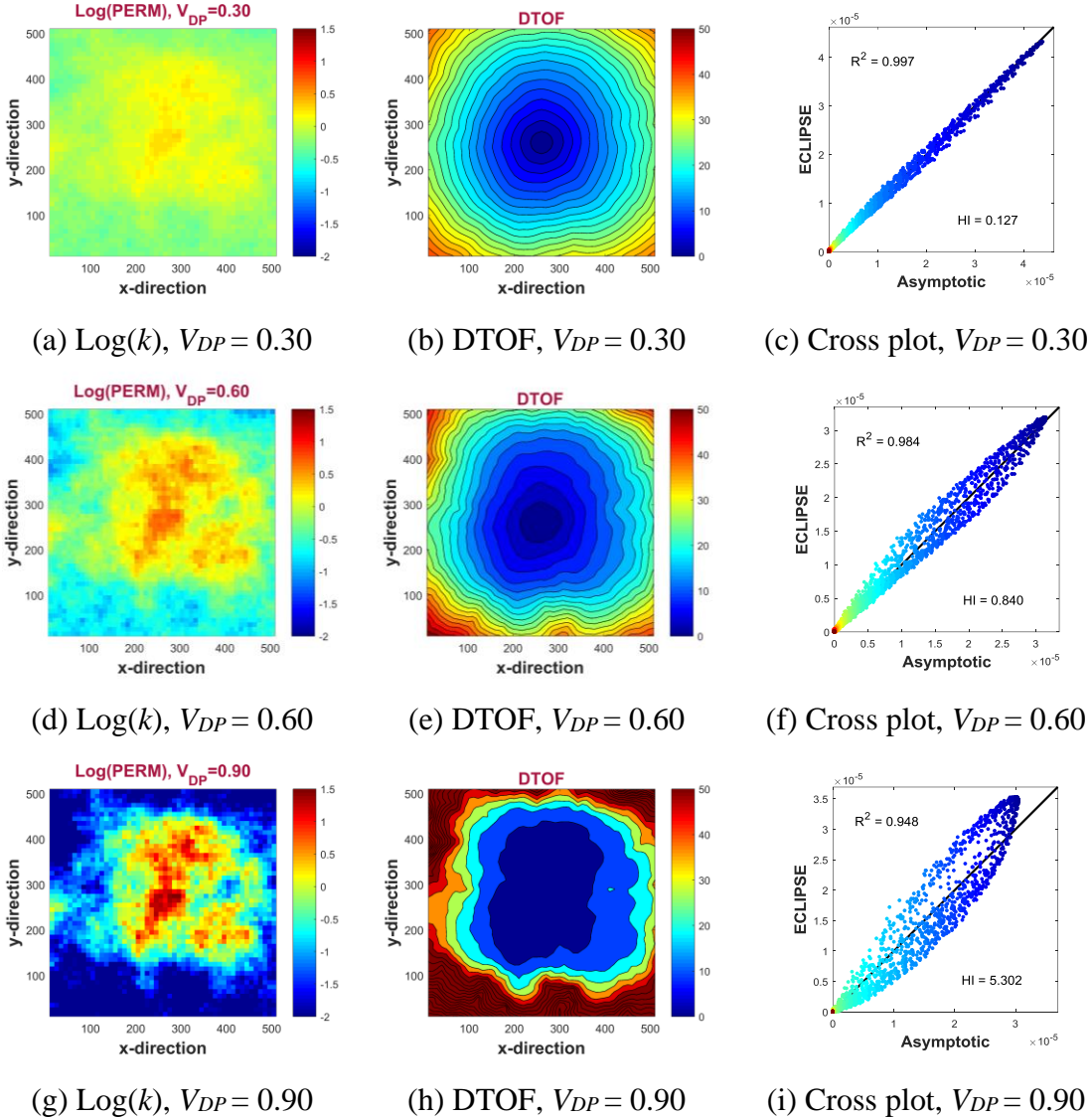


Figure 2.24 Log10 of permeability (first column), the corresponding DTOF (second column), and cross plot between asymptotic solutions vs. ECLIPSE results (third column) with $L_{DCL} = 1.00$ and various V_{DP} values

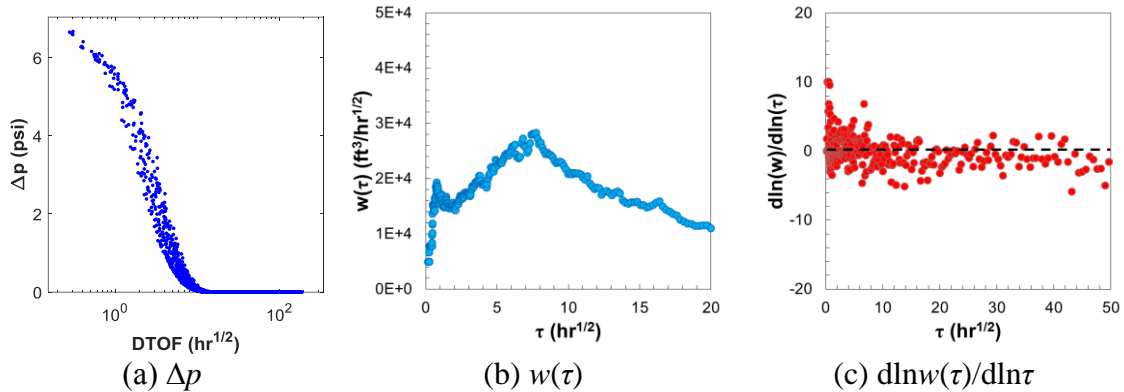


Figure 2.25 Illustration of (a) pressure drop, (b) $w(\tau)$ and (c) $d\ln w(\tau)/d\ln \tau$ vs. τ for case with $V_{DP} = 0.90$ and $L_{DCL} = 1.00$

Figure 2.26 (a), (d), (g) illustrate that as L_{DCL} decreases, the permeability of a grid block keeps losing its correlation with neighboring blocks until $L_{DCL} = 0.02$, which indicates an random permeability distribution at grid resolution. As L_{DCL} decreases, Figure 2.26 (b), (e), (h) illustrate more coarse DTOF contours and Figure 2.26 (c), (f), (i) display a worse alignment between asymptotic solutions and ECLIPSE results, especially near the wellbore (dark blue dots represent small τ). To better understand the mismatch of the first case, I plot the pressure drop, $w(\tau)$ and $d\ln w(\tau)/d\ln(\tau)$ vs. τ in Figure 2.27. From Figure 2.27 (a), we know that Δp is still function of τ because of the reasonable vertical scatter between Δp and τ . In Figure 2.27 (b), we can see the trend of $w(\tau)$ curve is increasing until at $\tau = 26 \text{ hr}^{1/2}$, where pressure front first hits the reservoir boundary. Figure 2.27 (c) reveals how the smoothness $d\ln w(\tau)/d\ln(\tau)$ varies along with τ , where the strong decreasing trend and large negative values represent a series of strong reflections near the wellbore, which would definitely do great harm to the accuracy of the

asymptotic solution. Again, for strong heterogeneity we will need to use the analytic solutions with strong reflectors which will be shown in the next chapter.

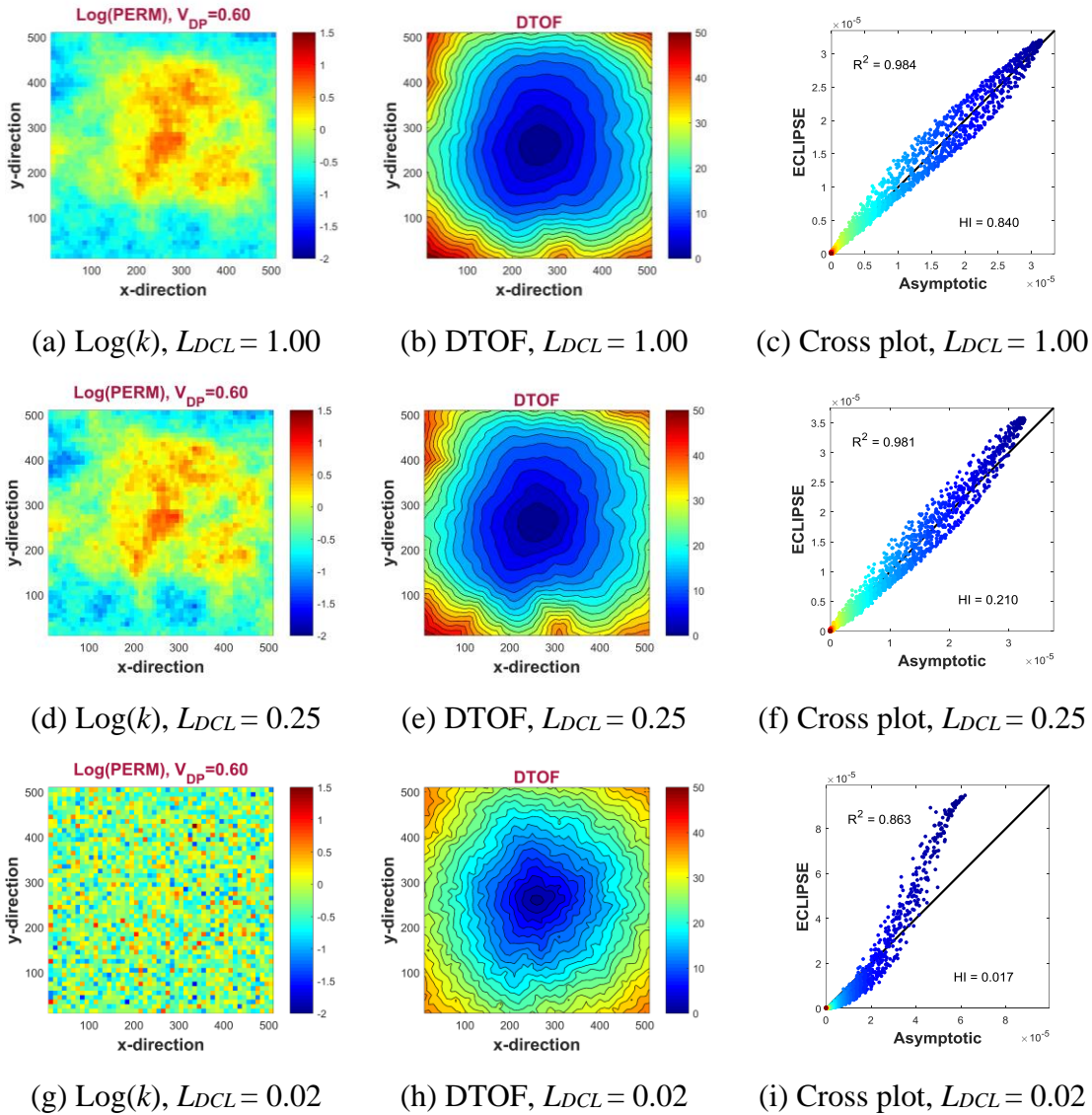


Figure 2.26 Log10 of permeability (first column), the corresponding DTOF (second column), and cross plot between asymptotic solutions vs. ECLIPSE results (third column) with $V_{DP} = 0.60$ and various L_{DCL} values

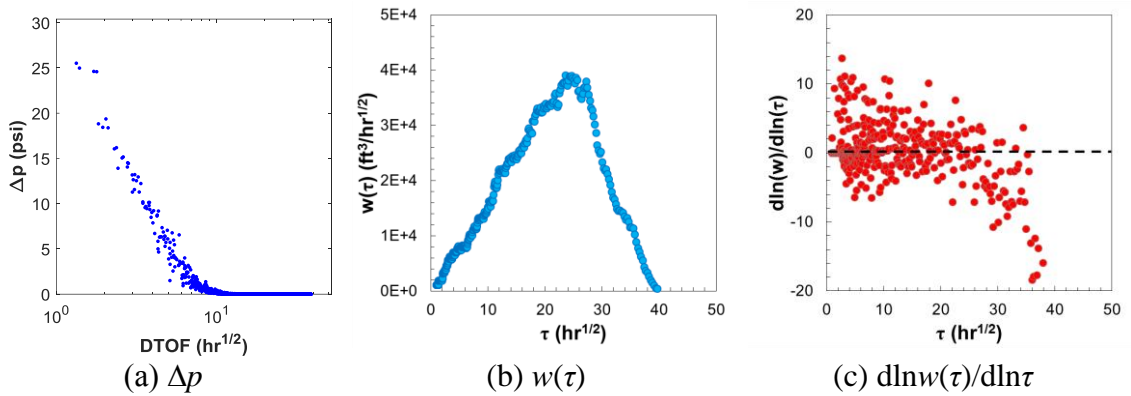


Figure 2.27 Illustration of (a) pressure drop, (b) $w(\tau)$ and (c) $d\ln w(\tau)/d\ln \tau$ vs. τ for case with $V_{DP} = 0.60$ and $L_{DCL} = 0.02$

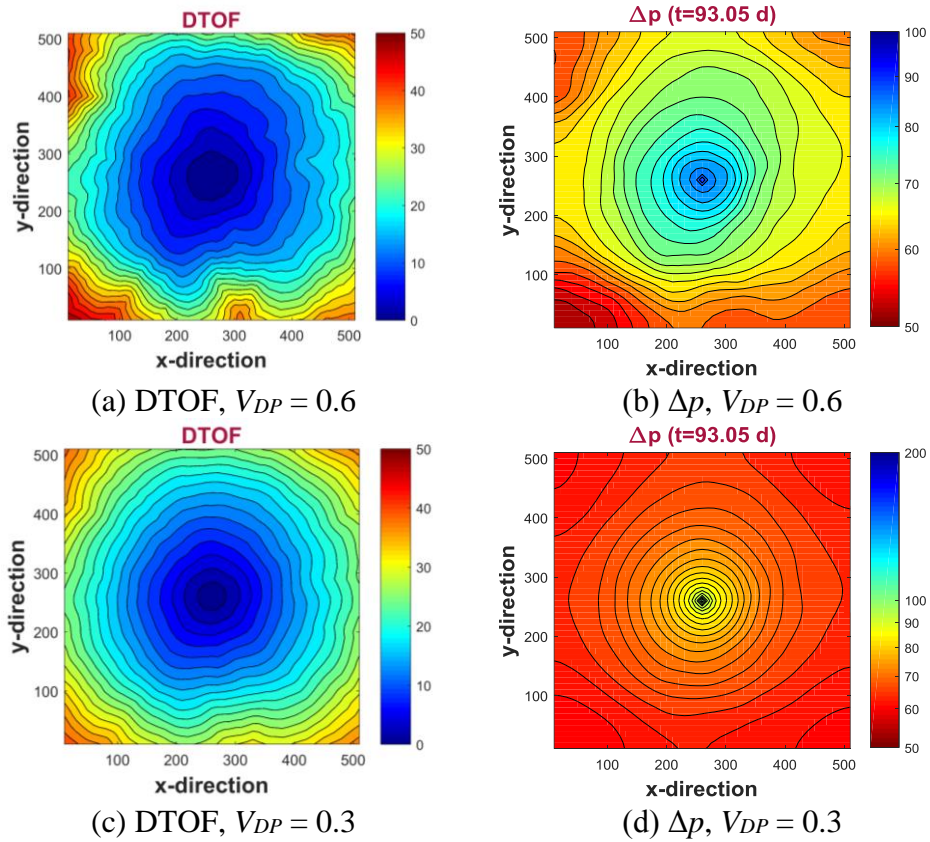


Figure 2.28 DTOF and pressure drop for cases with (a) and (b) $V_{DP} = 0.6$; (c) and (d) $V_{DP} = 0.3$ at fixed $L_{DCL} = 0.25$

Figure 2.28 shows DTOF and Δp distributions with clear boundary effects from ECLIPSE for cases with $V_{DP} = 0.6$ and $V_{DP} = 0.3$ at fixed $L_{DCL} = 0.25$. Comparing Figure 2.28 (a) to (b), and (c) to (d), we can see that the τ and pressure contours align well with each other in the region close to the well and they have similar shapes; while near the reservoir boundary, we observe clear boundary effects in Δp contours, where the extra pressure drop changed the shapes of Δp contours so that their curvatures are different from τ contours. For systems with heterogeneity the second propagation depends upon the reflection magnitude and placement of heterogeneity. Once boundary reflection terms contribute, ECLIPSE simulation shows an additional pressure drop that is not captured by a single τ coordinate. Huang *et al.* (2017) introduced an extra boundary reflection coordinate to resolve this issue.

	$L_{DCL} = 0.02$	$L_{DCL} = 0.25$	$L_{DCL} = 1.00$
$V_{DP} = 0.30$	0.984	0.997	0.997
$V_{DP} = 0.60$	0.863	0.981	0.984
$V_{DP} = 0.90$	0.895	0.911	0.948

Table 2.6 Summary of determination coefficient R^2 of all the nine heterogeneous cases

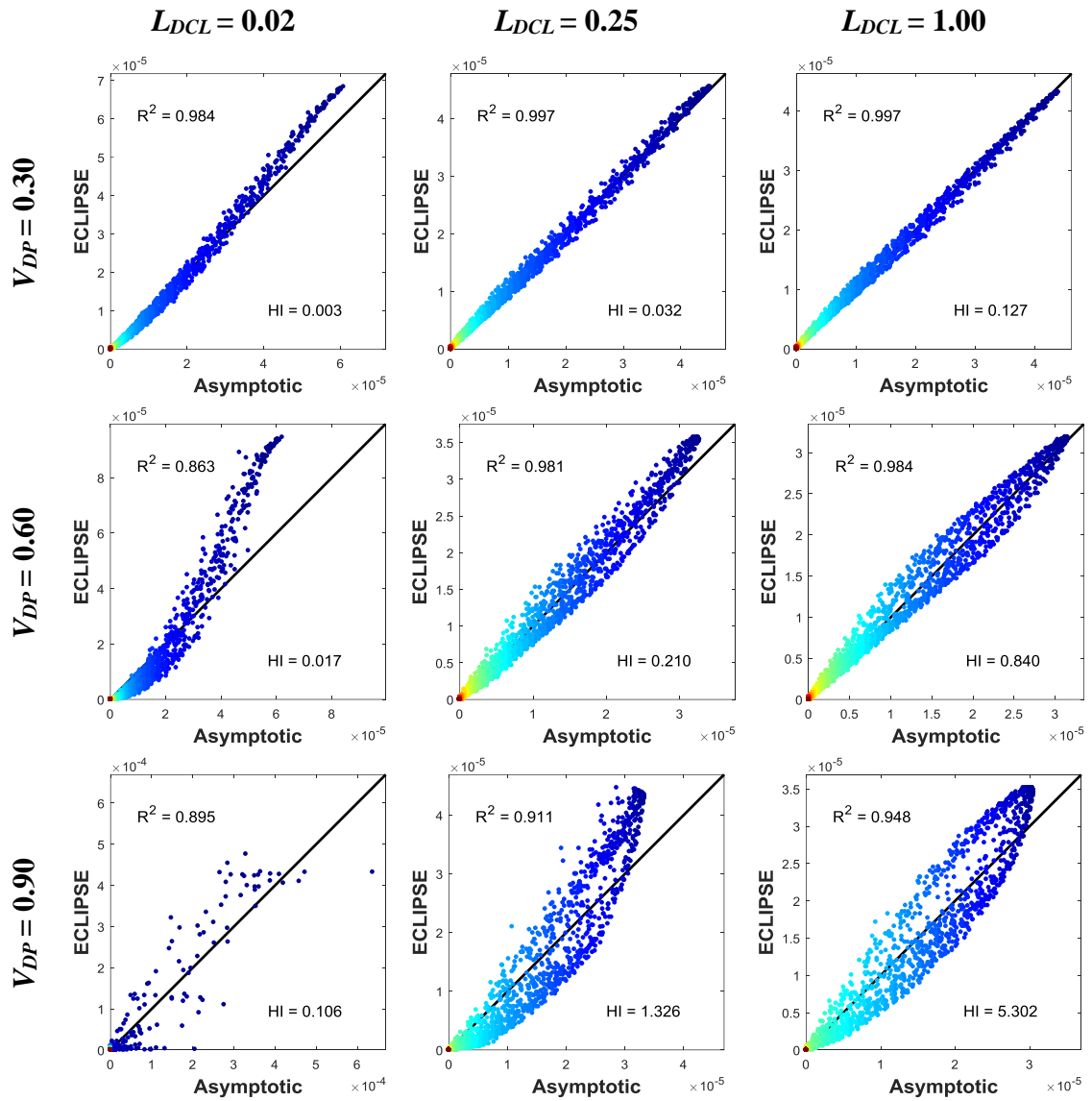


Figure 2.29 Summary of pressure drop derivative from asymptotic solution vs. ECLIPSE results for all the nine heterogeneous cases

A summary of correlation coefficient R^2 and pressure drop derivative comparison of all the nine heterogeneous cases is provided in Table 2.6 and Figure 2.29 and Figure 2.30. Again, the validation shows that for sufficiently smooth heterogeneity patterns, i.e., small variance and high correlation length, we obtain excellent agreement with Eq. (2.29).

From Figure 2.30, we can generally observe a good trend of V_{DP} vs. R^2 and L_{DCL} vs. R^2 , however, there is not a clear trend between HI and R^2 according to this specific study. This means HI is not a particularly useful measure for the validity of the FMM. By examining it in terms of both variance and correlation length, we see that cases with high variance but smooth at the grid block scale perform well until we get some sort of structured heterogeneity, i.e., a channel.

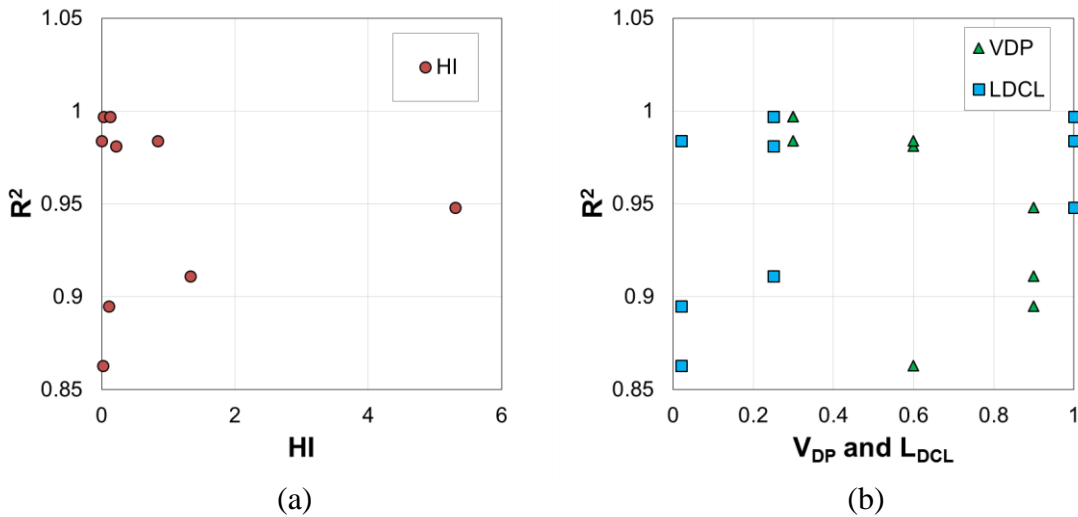


Figure 2.30 Summary of R^2 vs. HI , V_{DP} , and L_{DCL} of all the nine heterogeneous cases

2.4 Discussion

In this chapter, I have done a number of tests on τ as a spatial coordinate as well as testing the accuracy of asymptotic pressure approximation under different circumstances. The key points we have learned so far are listed below.

Let us first discuss the limits of validity of the fundamental assumption in the use of $\tau(\vec{x})$ as a spatial coordinate: $p(\vec{x}, t) \approx p(\tau(\vec{x}), t)$ and its resulting expression for

Darcy's flux $q(\tau, t) \approx c_i w(\tau) \frac{\partial p}{\partial \tau}$, by examining circumstances in which the assumption may fail. This assumption need to be reasonably satisfied in order to reduce the 3-D diffusivity equation to an equivalent 1-D formulation.

As a simple example of a violation of the assumption, consider the pressure drop at a location in a reservoir in the vicinity of a no flow barrier. The pressure drop can be represented as the sum of the pressure drops due to the direct front, which depends upon $\tau(\bar{x})$, and the reflected front, which depends upon a larger diffusive time of flight, $\tau_1(\bar{x})$: $\Delta p(\bar{x}, t) \approx \Delta p(\tau(\bar{x}), t) + \Delta p_1(\tau_1(\bar{x}), t)$. However, if $e^{-\tau_1^2(\bar{x})/4t} \ll e^{-\tau^2(\bar{x})/4t}$, then the assumption of $p(\bar{x}, t) \approx p(\tau(\bar{x}), t)$ is reasonable.

As the second example that violates $p(\bar{x}, t) \approx p(\tau(\bar{x}), t)$, where $\Delta p(\bar{x}, t)$ only depends upon a single $\tau(\bar{x})$, consider a finite conductivity fracture. The bi-linear flow for finite conductivity fractures have an early time $t^{1/4}$ pressure drop response (Bourdet, 2002; Lee *et al.*, 2003). However, all of the drainage volume approaches based on a single $\tau(\bar{x})$ have a $t^{1/2}$ pressure drop response, also at early time. If we return to the discussion of pressure depletion along streamlines, we can only approximate $p(\tau, \psi, \chi) \approx p(\tau)$ if the solutions along adjacent lines are approximately the same. The same value of τ exists in the fracture and in the matrix, but the solutions at these two locations follow different pressure transients and have different pressure drops.

Under what circumstances will the asymptotic pressure approximation fail? We have already discussed that $w(\tau)$ must be “sufficiently smooth” and that $\frac{d\ln w(\tau)}{d\ln \tau}$ must be non-negative. We have already touched upon the question of smoothness. If $w_{Left} \approx w_{Right}$ at a change of properties then $R \approx 0$ and the transmitted front dominates the solution. When reservoir heterogeneity has an extremely large variance of heterogeneity or uncorrelated distribution ($L_{DCL} \rightarrow 0$), the value range of $\frac{d\ln w(\tau)}{d\ln \tau}$ becomes unbounded or even negative: the numerator scales as variance while denominator scales with the correlation length. Large variance usually means the range and contrast of permeability of adjacent locations is high in a statistical manner and uncorrelated distribution implies that it is highly possible that the permeability of each location does not depend on its neighbors. Both of these situations stand for a high contrast reservoir property which breaks the assumption of sufficient smoothness. If the distribution is correlated, i.e., the property change becomes smoother, $V_{DP} = 0.9$ can give a reasonably good match as demonstrated by one of the heterogeneous case in Figure 2.24 (h) and (i); however, if the distribution is uncorrelated, $V_{DP} = 0.6$ can yield a bad match as demonstrated by one of the heterogeneous case shown in Figure 2.26 (h) and (i).

The bound on $\frac{d\ln w(\tau)}{d\ln \tau}$ is also useful to consider. If $\frac{d\ln w(\tau)}{d\ln \tau}$ is negative then as we extrapolate back to $\tau = 0$ the area in the diffusion equation diverges. We are not able to connect a front solution from this location back to the well. Instead we must introduce fronts which propagate in the opposite direction. If we can approximate these multiple

fronts as a single front reflecting backwards from an apparent barrier, then we recover the use of image wells. However, if not, then the simple analytic approximation will lose its utility.

Beyond the discussion on the formation geometry or property heterogeneity, time also matters the accuracy of using τ as a spatial coordinate, especially for cases with multiple source points. Let's once again take infinite conductivity hydraulic fracture as an example. The asymptotic solution yields satisfactory performance during early time ($t_D < 1$), while for late time the alignment between τ and pressure may not be very satisfactory. τ only represents the propagation geometry for the first (or early) pressure front, which is a pillbox shaped contour. During late time when the pressure contour becomes elliptical, τ contours are no longer a good representative of the pressure contours, but τ is still a good approximation for the PTA results at any time since those are controlled by $w(\tau)$ and $V_p(\tau)$ at the foot of the profiles, $\tau^2/4t = 4$. In unconventional reservoirs, the proposed asymptotic approximation along with τ coordinate are still applicable before fracture-fracture interference (typically after several years of production) due to the reduction in fracture cluster spacing nowadays, e.g., from 60 ft in 2013 down to 15 ft in late 2016 in Midland Basin as reported by Pioneer (2016).

For the asymptotic approximation part, we also saw the validation of the integrability and we learned that the spatial and time integrals are internally consistent in general. Both approaches are good approximations to the exact solution, with a maximum error less than 4%. However, a closer look at the comparisons to ECLIPSE references shows that spatial integral yields smaller error than time integral, especially near the

wellbore as shown by Figure 2.13 (c) and (f). Neither approximation is uniformly valid in time, but the time integral will accumulate the error while the τ integral does not. Thus, we may want to choose to calculate asymptotic solutions via spatial integral whenever possible.

2.5 Chapter Summary

We have formulated an asymptotic pressure approximation to the solutions of the diffusivity equation for slightly compressible systems. The formulation is based upon the use of the diffusive time of flight, $\tau(\bar{x})$, as a spatial coordinate, and the function $w(\tau)$ to characterize the geometry of an expanding pressure front within the reservoir. Both of these quantities are determined from a solution to the Eikonal equation. This is an extremely flexible approach as it can integrate the effects of reservoir heterogeneity and complex patterns of natural or hydraulic fractures. According to the study, we learn things that work as summarized below:

I showed how to transform heterogeneous reservoirs into an equivalent 1-D diffusivity equation, which relates rates, pressure drops, and flow geometry. When used for performance prediction, rates and/or pressure drops are predicted from a model of the geometry determined from the Eikonal equation. It is a completely new approach to solve the PTA equations that are not restricted to simple geometries or to homogeneous reservoir descriptions, which is now expressed in the product of diffusion kernel $K_n(\tau, t)$ and unknown functions $\{A_n(t)\}$ controlled by boundary conditions.

We have changed the interpretation of τ coordinate. τ controls the characteristics of limit of detectability instead of depth of investigation. τ best represents the propagation geometry for the first pressure depletion, not necessarily the front as defined by the propagation of the depth of investigation

If the reservoir characteristics of $w(\tau)$ are “sufficiently smooth” then the diffusivity equation may be solved by an analytic asymptotic approximation. The validation of the asymptotic approximation in the presence of heterogeneity has also been conducted. We learn that the asymptotic solution definitely works for reservoirs with small variance and highly correlated permeability. The accuracy of asymptotic approximation depends on how well τ works as spatial coordinate, especially for reservoir permeability with a random distribution and/or channel pattern.

The asymptotic approximation allows us to develop a number of interpretations of our production data. and use leading order term $A_0(t)$ in the asymptotic series yields good results. At a fundamental level, the formulation allows us to relate the pressure drop seen at a producing well to depletion within the reservoir. As a consequence, the production data can be used to infer the instantaneous drainage volume of a well. It also provides a simple interpretation of the welltest derivative in terms of this drainage volume.

Through the study, we also learned the following limitations and issues.

For extremely heterogeneous cases, the sufficiently smooth assumption breaks down and $\frac{d\ln w(\tau)}{d\ln \tau}$ may no longer be non-negative. For those cases, $\frac{d\ln w(\tau)}{d\ln \tau}$ may be

used to determine if there are strong reflectors. If so, they require an extension to the asymptotic pressure approximation and will be provided in the next chapter.

For cases with multiple source points, e.g., hydraulic fracture case, τ only represents the propagation geometry for the first (or early) pressure front, which is a pillbox shaped contour. During late time when the pressure contour becomes elliptical, τ contours are no longer a good representative of the pressure contours. This allows the τ contours to be used for PTA, but for PSS relationships τ is less accurate.

When the sum of the pressure drops due to the direct front, which depends upon $\tau(\vec{x})$, and the reflected front, which depends upon a larger diffusive time of flight, $\tau_1(\vec{x})$, give comparable exponential terms, $e^{-\tau_1^2(\vec{x})/4t} \approx e^{-\tau^2(\vec{x})/4t}$, then the assumption of $p(\vec{x}, t) \approx p(\tau(\vec{x}), t)$ is no longer reasonable and boundary effects come into the picture. When pressure front hits the boundary, the boundary effects will make the asymptotic approximations of infinite domain with single $\tau(\vec{x})$ less accurate, since it does not capture reflection terms including boundary terms. The development of strong reflectors will be provided in the next chapter and the idea was further applied by Huang *et al.* (2017) with an introduction of secondary $\tau_1(\vec{x})$.

To sum up, in this chapter, I started to introduce our analysis with the fixed rate draw-down solution in an infinite acting reservoir. The approximation has been validated against a number of applications for which inverse Laplace transform reference solutions are available. Of course, our intent is not simply to re-derive classical results but to validate a formulation for use with complex fractured wells and heterogeneous reservoirs. In the

next chapter, I will show how to extend the fixed rate solution to variable rate drawdown and to finite reservoirs. The formulation also suggests how to bridge between the methodologies of pressure transient and rate transient analysis, generalized to more complex reservoir and well geometries.

CHAPTER III
GENERALIZATION OF THE ASYMPTOTIC APPROXIMATION TO VARIABLE
RATE AND BOUNDED RESERVOIRS *

3.1 Introduction

The prediction of reservoir performance requires a good understanding of pressure propagation in the reservoir. The governing equation of this process is the diffusivity equation, which relates flow rates to pressure drops. It also satisfies the purpose of performance prediction and the inversion of production data for further reservoir and well characterizations. Analytic solutions to the diffusivity equation under-lye the methodologies for both pressure transient analysis (PTA) and rate transient analysis (RTA) (Lee, 1982; Horne, 1995; Bourdet, 2002; Lee *et al.*, 2003; Thambynayagam, 2011; Houze *et al.*, 2015). Although these solutions are limited to basic reservoir properties and simple well configurations, they are of great help in reservoir and well characteristics. In contrast, numerical solutions are extremely flexible and are able to integrate descriptions

*Material adapted with permission from “Asymptotic Solutions of the Diffusivity Equation and Their Applications” by King et al., 2016: Paper SPE-180149-MS presented at SPE Europec featured at the 78th EAGE Conference and Exhibition held in Vienna, Austria, 30 May–2 June 2016. Copyright 2016, Society of Petroleum Engineers. Further reproduction prohibited without permission.

*Material adapted with permission from “Validation and Extension of Asymptotic Solutions of Diffusivity Equation and Their Applications to Synthetic Cases” by Wang et al., 2017: Paper SPE-182716-MS presented at SPE Reservoir Simulation Conference held in Montgomery, Texas, 20-22 February 2017. Copyright 2017, Society of Petroleum Engineers. Further reproduction prohibited without permission.

*Material adapted with permission from “Quantitative Production Analysis and EUR Prediction From Unconventional Reservoirs Using a Data-Driven Drainage Volume Formulation” by Wang et al., 2018: Paper EAGE-46177 to be presented at EAGE 16th European Conference on the Mathematics of Oil Recovery held in Barcelona, Spain, 3-6 September 2018. Copyright 2018, Wang et al. Further reproduction prohibited without permission.

of the reservoir, wells, fluids and their interactions. Although powerful, large degrees of freedom within a simulator, and the corresponding non-uniqueness of a history match, often make it difficult to provide the simple insights as the analytic approaches. What's worse, numerical simulations are often costly, especially for detailed 3-D reservoir simulation. In order to overcome these limitations, an effective 1-D representation may be needed for more rapid computation, whether using numerical or analytic techniques.

Unconventional reservoirs provide us with not only new challenges in reservoir characterization, but also new opportunities for analysis techniques (Valko & Lee, 2010; Ilk *et al.*, 2011; Song & Ehlig-Economides, 2011; Cipolla & Wallace, 2014). These are reservoirs that are largely governed by primary depletion, but at sufficiently low permeabilities that the clear distinctions between PTA and RTA are no longer applicable. The "short time" response of PTA, in which the reservoir is infinite acting, may now cover years of production, while the "long time" response of RTA controlled by boundary dominated flow, may not have been achieved before the well abandonment. I have shown how the semi-analytic "asymptotic pressure approximation" was developed and serves as an extension of the pressure transient analysis. It is sufficiently flexible to capture reservoir heterogeneity and complex fractured well configurations, while at the same time it provides overall characteristics as in PTA/RTA. As a numerical technique, this methodology has been applied to the investigation of unconventional reservoirs and the development of a comprehensive shale gas reservoir simulator (Datta-Gupta *et al.*, 2011; Zhang *et al.*, 2013; Xie *et al.*, 2014; Zhang *et al.*, 2014; Xie *et al.*, 2015; Fujita *et al.*, 2015). More recent work has applied the semi-analytic approach to the calculation of

drainage volumes and instantaneous recovery ratios in unconventional reservoirs, to upscaling of reservoir flow properties, to pore scale carbonate reservoir characterization, and to the integration of well test data with geologic reservoir models (Yang *et al.*, 2015; Pasumarti *et al.*, 2015; Nunna *et al.*, 2015; Li & King, 2016; King *et al.*, 2016).

In the last chapter, we have already illustrated the methodology to conduct PTA on infinite acting fixed rate drawdown. Here I will focus on the extension of asymptotic approximations to both variable rate and bounded reservoirs.

This chapter is organized as follows. We begin with a discussion of the limitations of performing traditional RTA and the determination of EUR for unconventional reservoirs. Unlike conventional reservoirs, unconventional will exhibit long periods of transient flow and no evidence of boundary dominated flow. A number of researchers have proposed specific empirical Decline Curve Analysis (DCA) models to be better suited to this situation, which we will review. We have developed a completely new method of analysis that is based upon fundamental solutions to the diffusivity equation, and which may replace the more empirical approaches currently in use. The methodology is separated into two major sections: I will first provide a detailed study regarding how our approach addresses variable rate production and determine a minimal number of asymptotic terms that is necessary to accurately approximate the infinite asymptotic series. Superposition in time will be used to provide reference solutions with which we will test the asymptotic approximations to variable rate drawdown. Then, I will extend our approach to bounded reservoirs and generalize the asymptotic approximation, where superposition in space (τ) is applied. It is a new result, as it allows to capture the transition from infinite acting to

bounded solutions, irrespective of geometry. This is the new technology that will allow us to perform PTA and RTA with further EUR analysis for unconventional. I will provide various validation tests for the generalized asymptotic approximation. Finally, I will discuss what has been learned about these extensions to the asymptotic pressure approximation, and provide summary and conclusions.

3.1.1 Pressure Transient Analysis

In the last chapter, we discussed the solution for various cases with a fixed rate drawdown. When the well production is no longer at a constant rate, which is eventually the case for wells under production, following Lee *et al.* (2003), we need to compute the rate normalized pressure drop (RNP), defined as

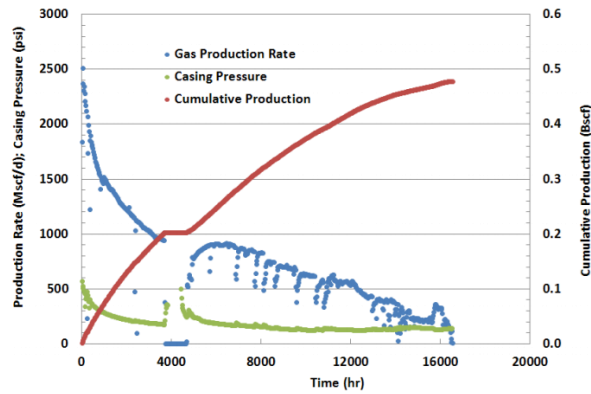
$$RNP_{wf}(t) \equiv \frac{p_i - p_{wf}(t)}{q_w(t)} = \frac{\Delta p_{wf}(t)}{q_w(t)} \quad (3.1)$$

$$RNP'_{wf}(t) = \frac{dRNP_{wf}(t)}{d \ln t_s} \quad (3.2)$$

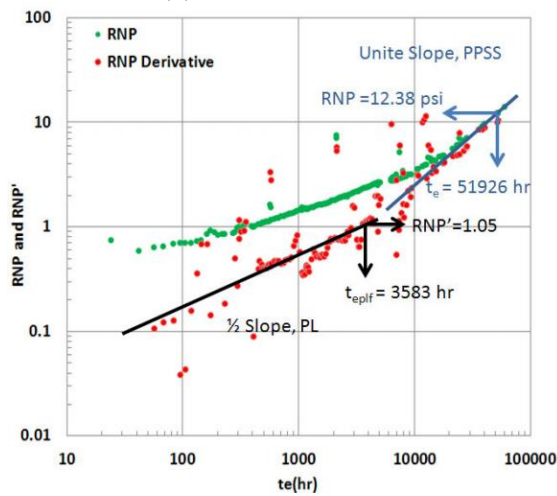
as well as superposition time (t_s). What superposition time says is what the time would have to be to get the right value of RNP as if it was on a fixed rate drawdown. According to the definitions, RNP_{wf} is directly correlated to the production data and can be calculated easily and specific expressions for superposition time depend upon the flow regime. The variable rate drawdown can be interpreted by plotting RNP_{wf} and its welltest derivative RNP'_{wf} against t_s , so that it is converted to an equivalent fixed rate drawdown. If the flow rate variations are sufficiently smooth during infinite acting flow, then $t_s \sim t$ (Winestock

and Colpitts, 1965). We will provide a more general definition for t_s based upon the drainage volume that is not restricted to specific flow regimes. Our general definition of t_s will show that for boundary dominated flow, $t_s = t_e = Q_w(t)/q_w(t)$, where t_e represents the equivalent time (material balance time) which is the ratio between cumulative production and the instantaneous production rate. Palacio and Blasingame (1993) utilized t_e for rate transient analysis during BDF while others researchers have used t_e before the onset of BDF (Song and Ehlig-Economides, 2011). Based on our more general expression for t_s , we will show that t_e is a good approximation to t_s during infinite acting transients.

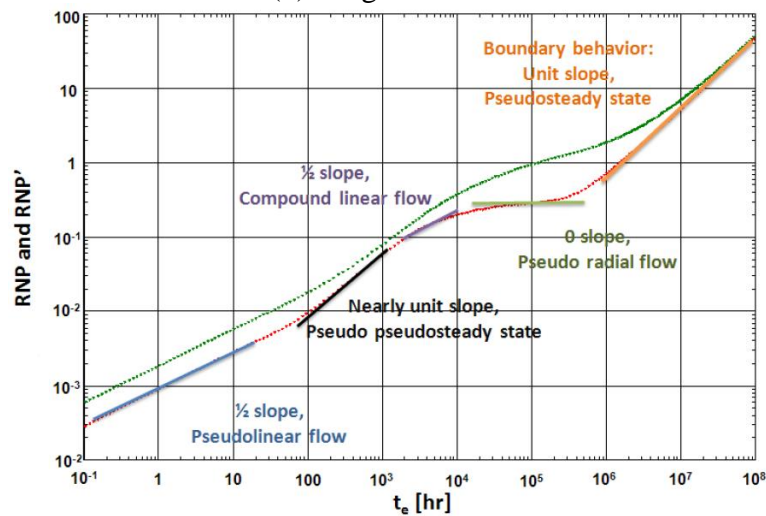
Figure 3.1 shows an example of the analysis of a multiple transverse fracture horizontal well (MTFW) from the Fayetteville Shale performed by Song and Ehlig-Economides (2011). They transformed the raw production data with varying rates and BHP shown in Figure 3.1 (a) to an equivalent fixed rate drawdown displayed as a Diagnostic plot in Figure 3.1 (b), and a general illustration of MTFW drawdown behavior using long time numerical simulation in Figure 3.1 (c). The Diagnostic plot was created by plotting RNP_{wf} and RNP'_{wf} vs. t_e on a log-log scale. The interpretation comes when you draw flow regimes through the data. On this particular plot, two flow regimes are identified: the black line has a $1/2$ slope which indicates linear flow and the blue line has a unit slope, an indication of the stimulated reservoir volume (SRV) and pseudo pseudo steady state (PPSS) flow. Unlike analytic PTA that can only provide analysis on the simple flow regimes, or type curves, that include the transitions between simple flow regimes,



(a) Production Data



(b) Diagnostic Plot



(c) MTFW Drawdown Behavior

Figure 3.1 Fayetteville Shale well (a) production data; (b) Diagnostic plot with RNP_{wf} and RNP'_{wf} and (c) illustration of long time drawdown behavior of the MTFW geometry (Song and Ehlig-Economides, 2011)

numerical simulation can be used to simulate solutions for linear flow, PPSS flow, pseudo radial flow, etc., and most importantly, the transition between these flows. The simulation results in Figure 3.1(c) show that the flow regimes for the MTFW geometry, are not the simple infinite acting radial flow plus boundary dominated flow (Fetkovich, 1980) nor infinite acting linear flow plus boundary dominated flow (Wattenbarger *et al.*, 1998).

3.1.2 Rate Transient Analysis and Decline Curve Analysis for Conventionals

In general, both rate transient analysis (RTA) and pressure transient analysis (PTA) are trying to take advantage of production data and conduct some interpretations, e.g., reservoir characterization, production prediction, EUR estimation, etc. RTA mainly focuses on the interpretation based on the fixed BHP drawdown while the fundamentals of PTA are largely relying on the fixed rate drawdown. They converged in recent years despite their different development paths (Houze *et al.*, 2015).

Decline Curve Analysis (DCA) is an example of RTA. It is an empirical technique that is widely used for analyzing the rate decline from the production history and thus enables us to forecast and predict EUR. There are two major categories of DCA techniques: the curve fit of production rate history with Arps' decline curves and the type curve matching approach.

Palacio and Blasingame (1993) presented a method to analyze gas well production data based on decline type curves analysis. They attempted to take the variable rate drawdown into an equivalent one with constant rate. They introduced time functions which can help to convert production data to the exponential ($b = 0$) of the Fetkovich

Type Curves. Agarwal *et al.* (1999) presented decline type curves for analyzing production data and estimating reserves for oil and gas wells. Those type curves were initially designed for wells with single hydraulic fractures and were then extended to take advantage of cumulative production to improve the type curve matching results.

Palacio and Blasingame (1993) developed type curves for RTA based on pressure drop normalized rate (PNR) as:

$$PNR_{wf}(t) \equiv \frac{q_w(t)}{P_i - P_{wf}(t)} = \frac{q_w(t)}{\Delta P_{wf}(t)} \quad (3.3)$$

However, using PNR_{wf} alone when the bottomhole flow pressure varies significantly did not remedy the problem. They introduced type curves that could be used for variable BHP drawdown by plotting PNR_{wf} against t_e . Following this idea, the Diagnostic plot of RNP_{wf} and its welltest derivative RNP'_{wf} vs. material balance time t_e will also show an equivalent fixed rate drawdown and thus make it straightforward and convenient to conduct PTA on the variable rate production history.

Arps (1945) first collected the methods which had been used for many years for analyzing and forecasting well production. He summarized decline type curves based on an empirical correlation of production rate as well as cumulative production as a function of time, which can be expressed in a general form as:

$$q_w(t) = \frac{q_i}{(1 + bD_i t)^{1/b}} \quad Q_w(t) = \frac{q_i}{D_i(1-b)} \left(1 - (1 + bD_i t)^{-(1-b)/b} \right) \quad (3.4)$$

where, q_i is the initial production rate, D_i is the initial decline rate, b is the decline curve exponent varying between 0 (exponential decline) to 1 (harmonic decline).

Arps' decline curves are simple analytic models and they helped build the foundation of DCA. However, as indicated by the time range in Figure 3.1, there is going to be an extended infinite acting period and it may even take hundreds of years to reach boundary dominated flow for unconventional. Thus, the application of Arps' decline curves to unconventional may result in erroneous interpretation of b , e.g., if we only see infinite acting linear flow, the DCA will give $b = 2$; if we treat SRV as the signal of BDF, we would underestimate the reservoir size as well as EUR. Therefore, the simple Arps' decline curves are not suited for DCA on unconventional. We will come back to the introduction of the state-of-the-art analytic approaches which are more sophisticated and applicable to analysis of unconventional reservoirs in the EUR prediction section.

In 1970's, Fetkovich realized that the Arps decline curve analysis can only be applied when the reservoir is under boundary dominated flow, while the initial infinite acting production period of the well is out of the scope of the analytical decline curve methods. Therefore, Fetkovich used the analytical infinite acting radial flow equation to generate transient flow patterns and combined it with the empirical decline curves of Arps (1945). By doing so, Fetkovich proposed a series of type curves which are applicable to both infinite and bounded systems. As illustrated in , decline curve dimensionless rate q_{Dd} is plotted against decline curve dimensionless time t_{Dd} in terms of reservoir variables, and they are defined as (Fetkovich, 1980),

$$q_{Dd} = q_D \left[\ln \left(\frac{r_e}{r_w} \right) - \frac{1}{2} \right] = \frac{\ln \left(\frac{r_e}{r_w} \right) - \frac{1}{2}}{p_D} \quad (3.5)$$

$$t_{Dd} = \frac{t_D}{\frac{1}{2} \left[\left(\frac{r_e}{r_w} \right)^2 - 1 \right] \left[\ln \left(\frac{r_e}{r_w} \right) - \frac{1}{2} \right]} \quad (3.6)$$

where, q_D , p_D and t_D are dimensionless variables used in PTA:

$$q_D = \frac{q_w \mu B}{2\pi kh(p_i - p_{wf})} \quad (3.7)$$

$$p_D = \frac{2\pi kh \Delta p}{q_w \mu B} \quad (3.8)$$

$$t_D = \frac{kt}{\phi \mu c_t r_w^2} \quad (3.9)$$

Figure 3.2 is made up of bounded radial flows with fixed BHP drawdown at various reservoir sizes (red curves) and Arps decline curves with various exponents (blue curves), respectively. The largest reservoir size is represented by the bottom curve and the smallest reservoir size is the top one. For the blue curves, the leftmost is exponential decline ($b=0$), the rightmost is harmonic decline ($b=1$), and hyperbolic declines lie in between. A match of production data with red curves will provide an estimate of reservoir pore volume, permeability and well skin; and a match of production data with the blue curves will help to evaluate reservoir depletion mechanisms (Arp's exponent b) so that future performance can be forecast.

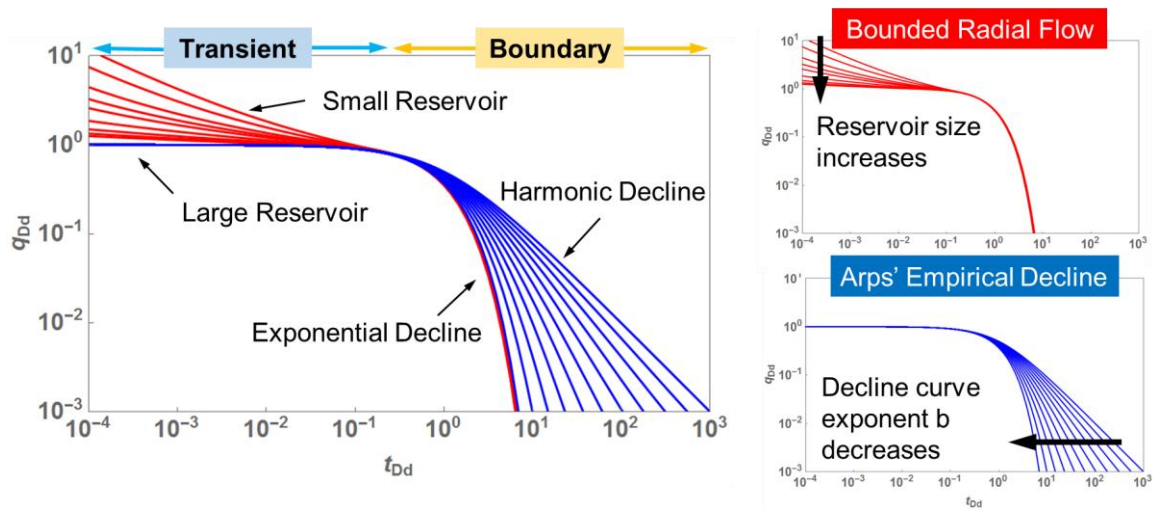


Figure 3.2 Illustration of both transient and boundary portions ($0 \leq b \leq 1$) of Fetkovich Type Curves

Compared to Arps', Fetkovich Type Curves provide more information when matching transient production data on decline curves. However, some limitations are still present when deriving the type curves:

- Solutions are specific to a combination of infinite acting radial flow and circular reservoir outer boundaries, neither of which are present in unconventional reservoir developments (based on MTFW)
- Boundary dominated portions of these solutions are still empirical, impacting the applicability of this solution to EUR determination
- Slightly compressible fluid

When extending the analysis to unconventional reservoirs, the first two are significant limitations. We are going to develop new analytic methods with physical (non-empirical) solutions that transition smoothly from infinite acting to boundary dominated flow, irrespective of the flow geometry. The intent is to remove two of the important restrictions

that limit the analysis for unconventional reservoir developments with complex flow geometries, as will arise with multi-stage fractured horizontal wells.

3.1.3 Unconventional Reservoir EUR Prediction

Predicting the long-term production performance and further estimating EUR in tight rocks and shale plays is an important and challenging task. Throughout the life of a production well, EUR estimate will be updated from time to time. The amount of data available and the technique used for production history matching and performance forecasting are crucial to a reliable EUR prediction.

The traditional and popular methods are volumetric and material balance calculations. Volumetric calculations mainly relies on the areal extent and net-pay thickness of the reservoir, which are often difficult to get in tight reservoirs (Shanley *et al.*, 2004). Material-balance method has been widely used to calculate hydrocarbon in-place and estimate EUR of gas reservoirs due to its simplicity and power (Havlena and Odeh, 1963, 1964). The common use is a simple line plot of p/Z against cumulative gas production, which can be easily extrapolated to evaluate both gas in place and EUR. However, the applications to unconventional gas reservoirs are often unsatisfactory, primarily due to the requirement for boundary dominated flow (Lee and Sidle, 2010). Specifically, application of these methods usually requires an establishment of BDF in the reservoir so the entire reservoir is under the same depletion rate, which is almost impossible for unconventional with extended infinite acting flow period.

The type curves (Palacio and Blasingame, 1993; Agarwal *et al.*, 1999) are modern conventional analysis approaches, again based on BDF. Unconventionals have extended infinite acting flow, which have led to the following new DCA techniques like stretched-exponential decline (SEPD) and Duong's method, and they are briefly introduced below.

Valkó (2009) proposed the stretched-exponential decline (SEPD) approach, which has two main advantages over the Arps' decline curves. On one hand, it is applicable to both transient and boundary dominated flows. On another, the EUR estimate is finite for large production times. SEPD has a limited number of parameters to be determined and its capability was show through analyzing the effect of stimulation and re-stimulation treatments of over 10,000 wells in the Barnett shale by the author. Later, Valkó and Lee (2010) used this method for forecasting with the rate-time relation as:

$$q_w(t) = q_i \cdot \exp \left[- \left(\frac{t_{vk}}{\tau_{vk}} \right)^{n_{vk}} \right] \quad (3.10)$$

where, q_i is the initial (or maximum) production rate, t_{vk} is the time on production in months, τ_{vk} is a characteristic production time in months, and n_{vk} is the dimensionless time exponent. This method uses observed cumulative production along with theoretical cumulative production to estimate EUR. An iterative process is required to determine the values of q_i , τ_{vk} , and n_{vk} .

Duong (2011) proposed an empirical decline curve method for EUR estimate in the case of fracture dominant flow with negligible matrix contribution. This method was developed on the basis that for fracture flows, production rate and time have a power law

relation at a constant flowing bottomhole pressure. This means that rate/time plot on a log-log scale forms a straight line. The rate/time equation in this model is

$$q_w(t) = q_i \cdot t^{-m_{dg}} e^{\frac{a_{dg}}{1-m_{dg}}(t^{1-m_{dg}} - 1)} + q_\infty \quad (3.11)$$

where, a_{dg} is the intercept constant ($1/time$), m_{dg} is the slope (dimensionless), q_∞ is the rate at infinite time. The q_∞ can be zero, positive, or negative (the abandonment rate should be set on the basis of economics). m_{dg} is always a positive value and $m_{dg} > 1$ corresponds to shale reservoirs and $m_{dg} < 1$ may indicate a conventional tight well. Duong developed the method based on a dynamic expanding SRV so that it never reaches BDF. Therefore, the predicted EUR from Duong's model will be high unless using an extra constraint for boundary dominated flow.

Mahmoud *et al.* (2018) examined a vertical well with a single fracture in a tight gas formation with a long production period of 44.14 years and compared the EUR predictions given by the different decline methods mentioned above. The match of the production rate history as well as the rate decline prediction trends (economic limit is set to be 20 Mscf/day) are shown in Figure 3.3 and the EUR estimates are illustrated in Figure 3.4. From Figure 3.3, we observe that linear flow lasts for around 200 months and BDF becomes dominant thereafter since the data slope is close to unity. The SEPD method predicted an EUR of 17,241 MMscf, which is comparable to the Arps' hyperbolic forecast of 17,607 MMscf. Similar estimates can also be observed from material balance and volumetric calculations in Figure 3.4. The Duong's method overestimated the EUR to be 54,903 MMscf, which is at least three times larger than the other methods. The authors

argued that it is based on the expanding SRV assumption while the production history reaches BDF, however, an earlier cutoff of Duong’s method would give a much reduced EUR. Agarwal type curve analysis estimated the EUR to be 13,700 MMscf, which is obviously lower than the remaining methods, because the method is designed for conventional decline analysis and is not well suited for unconventional with extended infinite acting. Beyond that, type curve analysis requires to convert production data to dimensionless parameters, when both reliable and representative reservoir and fluid average properties (permeability, viscosity, payzone thickness, compressibility, etc.) are always required. This, of course, will be very challenging for unconventional reservoir analysis.

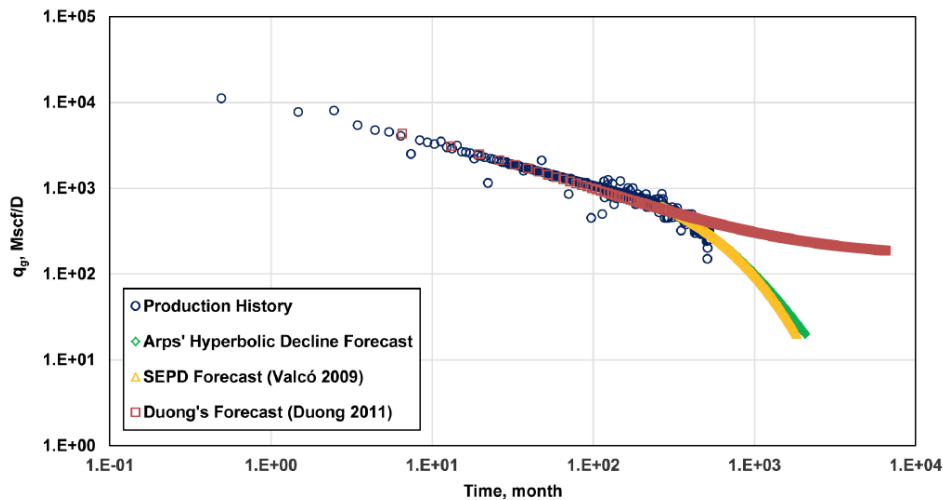


Figure 3.3 History matching and forecasting of the rate performance using Arps’ hyperbolic, SEPD, and Duong’s decline methods (Mahmoud *et al.*, 2018)

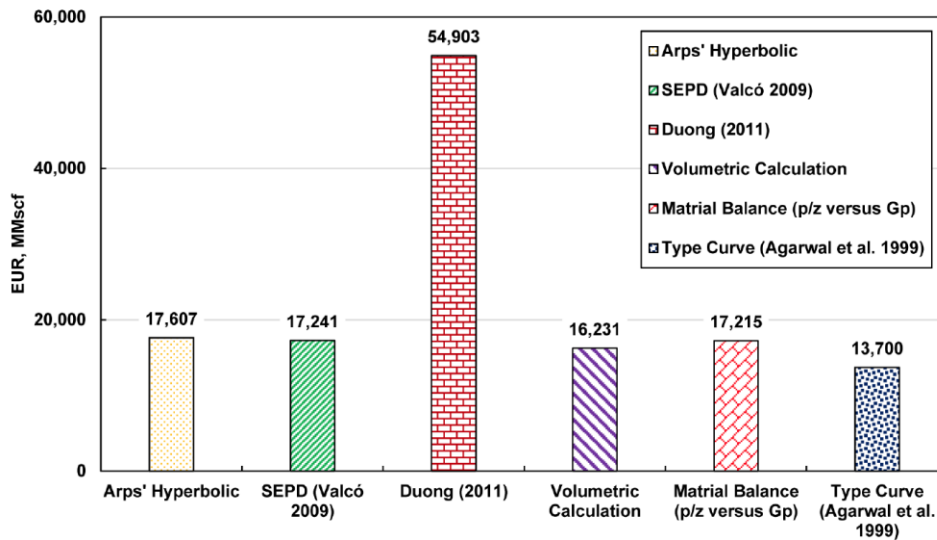


Figure 3.4 EUR prediction using different analysis methods (Mahmoud *et al.*, 2018)

3.2 Methodology: Extension to Variable Rate Drawdown

In the first methodology section, I am going to show how to express superposition time with respect to the drainage volume irrespective of the flow regime. And I will further use these solutions as references for the application of asymptotic approximations for cases with variable rate drawdown.

3.2.1 Superposition in Time

For a multi-rate production history, as illustrated in Figure 3.5, superposition in time is often used to calculate pressure drop at a given time (indicated by the blue dashed line) using rate history as well as pressure drop from a fixed rate model, as illustrated by the equation below.

$$\begin{aligned}\Delta p_{wf}(t) &= \sum_{i=1}^{N(t)} (q_{w_i} - q_{w_{i-1}}) \cdot \Delta p_u(t - t_i) \\ &= \int_0^t \frac{dq_w(t')}{dt'} \cdot \Delta p_u(t - t') dt'\end{aligned}\quad (3.12)$$

where, $\Delta p_u(t)$ is the pressure drop for a constant production with unit rate drawdown, q_{w_i} is the production rate starting at time t_i . The first row of Eq. (3.12) is the discrete form and second row is the integral form.

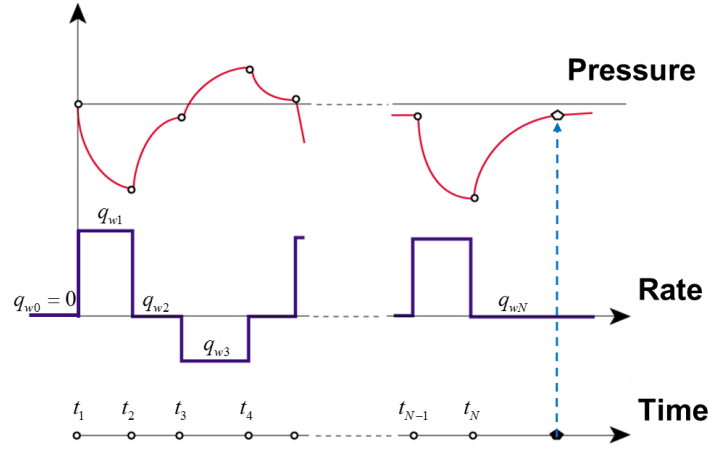


Figure 3.5 Illustration of a production history with variable rate, adapted from Houze *et al.* (2015)

According to the definition of the transient drainage volume, $\Delta p_u(t)$ can be expressed as:

$$\Delta p_u(t) \equiv \frac{\Delta p_{wf}(t)}{q_w} = \frac{1}{c_t} \int_0^t \frac{dt}{V_d(t)} \quad (3.13)$$

Substituting Eq. (3.13) into Eq. (3.12), we obtain that:

$$\Delta p_{wf}(t) = \frac{1}{c_t} \int_0^t \frac{dq_w(t')}{dt'} dt' \int_{t''=0^-}^{t-t'} \frac{dt''}{V_d(t'')} = \frac{1}{c_t} \int_0^t \frac{q_w(t')}{V_d(t-t')} dt' \quad (3.14)$$

where, $q_w(t)$ is known from production history and $V_d(t)$ represents the drainage volume evaluated through the equivalent fixed rate drawdown.

If we want to get the same value of $RNP_{wf}(t)$ as to get Δp_u , what does the time have to be? To answer this question, we need to introduce superposition time (t_s) that says what the time variable would have to be to get the right value of $RNP_{wf}(t)$ as if it was on a fixed rate drawdown. With that in mind, we define superposition time in the equation below.

$$c_t RNP_{wf}(t) \equiv \Delta p_u(t_s) \equiv \int_0^{t_s} \frac{dt}{V_d(t)} \Leftrightarrow c_t \Delta p_{wf}(t) \equiv q_w(t) \int_0^{t_s} \frac{dt}{V_d(t)} \quad (3.15)$$

Substituting Eq. (3.14) into Eq. (3.15), we finally obtain the general definition of superposition time in an implicit form:

$$\int_0^{t_s} \frac{dt}{V_d(t)} = \frac{1}{q_w(t)} \int_0^t \frac{q_w(t')}{V_d(t-t')} dt' \quad (3.16)$$

where the LHS is a function of superposition time t_s and the RHS honors the previous production history $q_w(t)$ and drainage volume $V_d(t)$. We now have a new and general way of expressing superposition time. The $V_d(t) \approx V_0(t)$ asymptotic approximation allows to derive specific expressions for t_s . The more useful thing is not the formula: since we can construct our approximation to the drainage volume, we have a way of approximately calculating superposition time. What is new about this is because we have a model for the drainage volume that is not restricted to simple geometries, we have a way

of constructing superposition time for all times. We can then test it against what material balance time looks like and this will be described in more detail later in the chapter.

In variable rate drawdown, we need to distinguish between smooth changes in flow rate at the sandface, and jumps in rate. For instance, for jumps in rate we have the following rate & BHP drop derivatives.

$$\frac{dq_{sf}}{dt} = \sum_j [q_{sf}]_j \delta(t-t_j) \quad (3.17)$$

$$c_t \frac{d\Delta p_{wf}(t)}{dt} = \sum_j [q_{sf}]_j \frac{\Theta(t-t_j)}{V_d(t-t_j)} \quad (3.18)$$

where, δ is the Dirac delta function and Θ is the Heaviside step function.

For an example, applying Eqs. (3.17) and (3.18) to a fixed rate drawdown problem, we obtain the following results.

$$\frac{dq_{sf}}{dt} = q_w \delta(t) \quad (3.19)$$

$$c_t \frac{d\Delta p_{wf}(t)}{dt} = \frac{q_w}{V_d(t)} \quad (3.20)$$

Trivial fixed rate drawdown solution, as expected.

For smooth changes in flow rate, we can represent the flow rate at the sandface as piecewise linear.

$$\frac{dq_{sf}}{dt} = \sum_j \left(\frac{dq_{sf}}{dt} \right)_j \Theta(t_j - t) \Theta(t - t_{j-1}) \quad (3.21)$$

$$c_t \frac{d\Delta p_{wf}(t)}{dt} = \sum_{j=1} \left(\frac{dq_{sf}}{dt} \right)_j \int_{t'=0^-}^t dt' \frac{\Theta(t_j - t') \Theta(t' - t_{j-1})}{V_d(t-t')} \quad (3.22)$$

Next, I will show the applications of superposition in time to two cases: (1) infinite acting radial flow with fixed BHP drawdown, where rate has a jump plus a smooth transition period; and (2) infinite acting radial flow with wellbore storage and fixed rate drawdown, where the sandface flux changes smoothly from 0 to the fixed production rate q_w . In both cases, we need to apply $V_d(t) \approx V_0(t)$ approximation to estimate drainage volume based on specific models.

3.2.1.1 Infinite Acting Radial Flow with Fixed BHP Drawdown

Let's first apply the derived formula, Eqs. (3.18) and (3.22), to an infinite acting radial flow with fixed BHP drawdown. We represent this problem as a fixed rate drawdown with a fixed well rate q_w starting at $t=0$, with a transition to fixed BHP control at $t=t_p$. The timing of the change in control depends upon the relative values of flow rate and BHP constraint. This gives us one jump at the start of production plus a smooth transition for $t=t_p + \Delta t > t_p$.

$$\begin{aligned}
0 &= c_t \frac{d\Delta p_{wf}(t_p + \Delta t)}{dt} \\
&= c_t q_w \frac{d\Delta p_u(t_p + \Delta t)}{dt} + \sum_j \left(\frac{dq_{sf}}{dt} \right)_j \int_{t'=t_p}^{t_p + \Delta t} dt' \frac{\Theta(t_j - t') \Theta(t' - t_{j-1})}{V_0(t_p + \Delta t - t')}
\end{aligned} \tag{3.23}$$

where, for infinite acting radial flow as shown in Eq. (2.60), we have:

$$V_0(t) = \phi \sqrt{\pi \alpha t} \cdot (4h \sqrt{\pi \alpha t} + A) \quad \text{and} \quad A = 2\pi r_w h \tag{3.24}$$

These linear equations can be solved for dq_{sf}/dt first, then we may integrate dq_{sf}/dt to get q_{sf} . The diagnostic plot of dimensionless flux as well as its welltest derivative $q'_{sfD} \equiv \frac{dq_{sfD}}{d \ln t_D}$ is shown in Figure 3.6, where we can see that the asymptotic solutions (red curves) match well with the inverse Laplace transform reference solutions (black dashed curves).

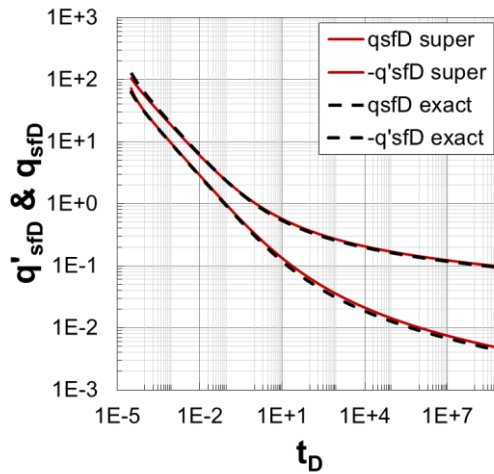


Figure 3.6 Diagnostic plot validation of dimensionless flux generated by superposition in time and the exact solutions from inverse Laplace transform for an infinite acting radial flow with fixed BHP drawdown (reprinted with permission from Wang et al, 2017)

3.2.1.2 Infinite Acting Radial Flow with Wellbore Storage and Fixed Rate

Drawdown

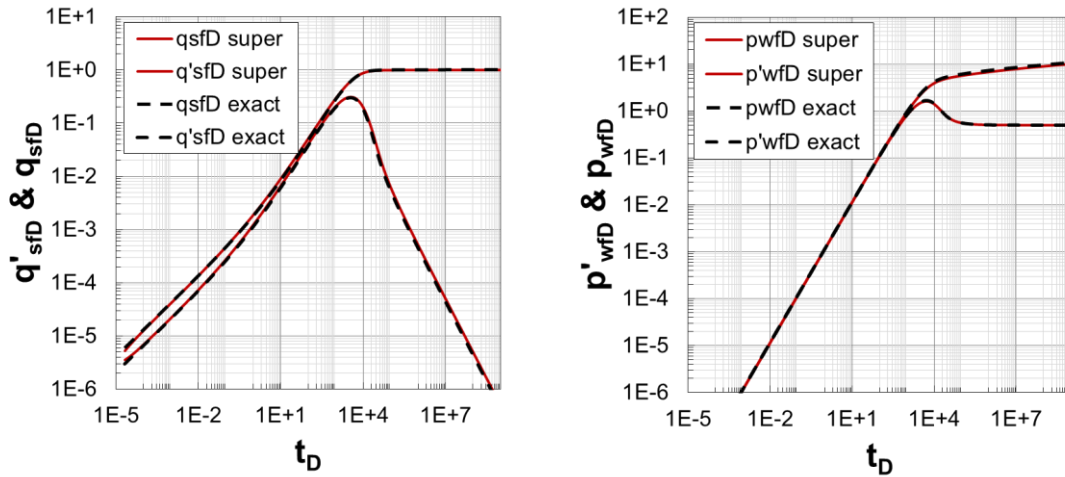
The second example is for infinite acting radial flow with wellbore storage and fixed rate drawdown. Flow rate starts at $q_{sf} = 0$ and increases smoothly. PSS boundary condition inside a liquid filled wellbore gives us the following relations:

$$\frac{q_w - q_{sf}}{V_w} = c_t \frac{d\Delta p_{wf}(t)}{dt} = \sum_j \left(\frac{dq_{sf}}{dt} \right)_j \int_{t'=0^-}^t dt' \frac{\Theta(t_j - t') \Theta(t' - t_{j-1})}{V_0(t-t')} \quad (3.25)$$

or,

$$q_w = \sum_{j=1} \left(\frac{dq_{sf}}{dt} \right)_j \int_{t'=0^-}^t dt' \left(1 + \frac{V_w}{V_0(t-t')} \right) \Theta(t_j - t') \Theta(t' - t_{j-1}) \quad (3.26)$$

Again, these linear equations can be solved for dq_{sf}/dt first, then we integrate dq_{sf}/dt to get q_{sf} . Diagnostic plots of dimensionless flux and pressure are shown in Figure 3.7, where we can see that the asymptotic solutions (red curves) match well with the inverse Laplace transform reference solutions (black dashed curves).



(a) Flux Diagnostic Plot

(b) Pressure Drop Diagnostic Plot

Figure 3.7 Diagnostic plots validation of (a) dimensionless flux and (b) dimensionless pressure generated by superposition in time and exact solutions from the inverse Laplace transform for an infinite acting radial flow with wellbore storage and fixed rate drawdown (reprinted with permission from Wang et al, 2017)

3.2.2 Asymptotic Solutions to Variable Rate Drawdown

We have successfully used superposition in time to address examples with variable rate drawdown. For fixed rate drawdown the inner boundary condition requires

$$\frac{dq_{sf}(t)}{dt} = \frac{dq_w}{dt} = 0 \text{ and } \frac{d\Delta p_{wf}(t)}{dt} \neq 0 .$$

Therefore $A_1(t)$ must vanish, and $A_0(t)$ will

describe the pressure transient at the wellbore and in the reservoir. For fixed BHP drawdown, the inner boundary requires

$$\frac{dq_{sf}(t)}{dt} \neq 0 \text{ and } \frac{d\Delta p_{wf}(t)}{dt} = \frac{d\Delta p_{wf}}{dt} = 0 .$$

Therefore $A_0(t)$ must vanish, and $A_1(t)$ will describe the rate transient at the wellbore

and in the reservoir. For variable rate drawdown, e.g., in the analysis of wellbore storage,

we will examine solutions that include combinations of $A_0(t)$, $A_1(t)$ and $A_2(t)$, which

will be fixed by the boundary condition at the wellbore. So far, the asymptotic solutions

we have examined are only for fixed rate drawdown with a changing bottomhole flowing

pressure in Chapter 2, and I will show how to extend them to variable rate drawdown cases

in this section.

Figure 3.8 shows the comparison between ECLIPSE (black curves) and asymptotic

solutions of pressure drop time derivative vs. product of τ and exponential term for a radial

flow in homogeneous formation with fixed BHP drawdown, where we can see that both

approaches show good alignment in the reservoir. This demonstrates the accuracy of the

asymptotic approximation and shows that $A_1(t)$ is the leading term of fixed BHP

drawdown in the absence of skin, as we will discuss in this chapter.

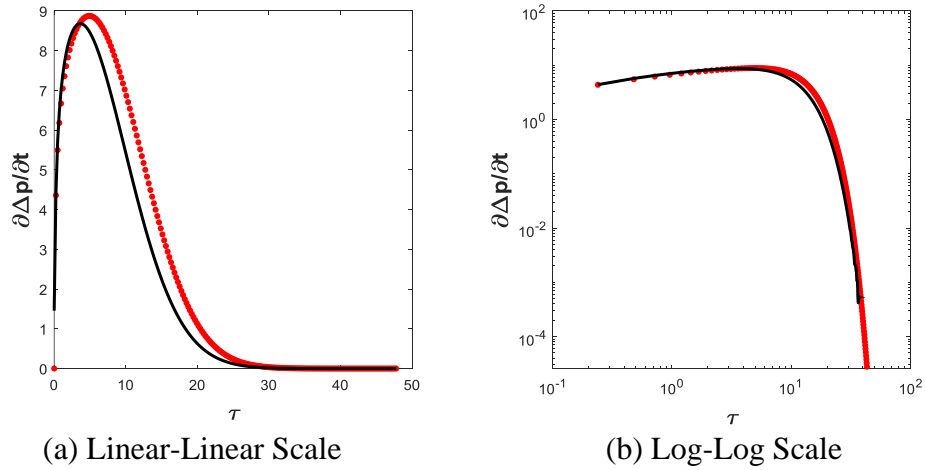


Figure 3.8 Comparison between ECLIPSE (black curves) and asymptotic solutions (red dots) of pressure drop time derivative vs. product of τ and exponential term for fixed BHP drawdown under (a) linear-linear scale and (b) log-log scale

Let's get started by a summary of the important expressions derived from the last chapter, which are for infinite domain and spatial integral instead of time integral is suggested to get solutions. The asymptotic expansion for the pressure transient in an infinite domain is:

$$c_t \frac{\partial \Delta p(\tau, t)}{\partial t} = -\frac{1}{w(\tau)} \frac{\partial q(\tau, t)}{\partial \tau} = \left\{ \sum_{n=0}^{\infty} \tau^n A_n(t) \right\} e^{-\tau^2/4t} \quad (3.27)$$

The diffusion kernel of the n^{th} order is defined as $K_n(\tau, t) = \tau^n \cdot e^{-\tau^2/4t}$. It will be generalized later for bounded reservoirs.

The time derivative of flux is:

$$\frac{\partial q(\tau, t)}{\partial t} = -w(\tau) \left\{ \sum_{n=0}^{\infty} \tau^n \left[(n+1) A_{n+1}(t) - \frac{1}{2t} A_n(t) \right] \right\} e^{-\tau^2/4t} \quad A_{-1} \equiv 0 \quad (3.28)$$

The evolution expressions for the pressure drop (in the absence of skin) and flux time derivative at the sandface requires:

$$\frac{d\Delta p_{wf}(t)}{dt} = A_0(t) \quad (3.29)$$

$$\frac{dq_{sf}(t)}{dt} = -w(0)A_1(t) \quad (3.30)$$

The expressions for pressure drop and flux at the wellbore are:

$$c_i\Delta p_{wf}(t) = \sum_{n=0}^{\infty} A_n(t)W_n(t) \quad (3.31)$$

$$q_{sf}(t) = \sum_{n=0}^{\infty} A_n(t)V_n(t) \quad (3.32)$$

The average pressure drop is defined as:

$$\overline{\Delta p}(t) = p_i - \overline{p}(t) \quad (3.33)$$

The geometry parameters τ , V_p , and $w(\tau)$ of the infinite acting cases are summarized in Table 2.4.

3.2.2.1 Infinite Acting Radial Flow with Fixed BHP Drawdown

To obtain a fixed bottomhole flowing pressure, we have expressed the algebraic term on the right hand side of Eq. (3.27) with a diffusion kernel that vanishes at the wellbore. We are only looking at a one term solution. Since $\frac{d\Delta p_{wf}(t)}{dt} = A_0(t) = 0$, we consider the leading term in the infinite series, which now becomes $A_1(t)$. As not all of the integrals for this case can be performed analytically, they will be left in a symbolic form.

Step 1:

$$\begin{aligned}
\tau &= (r - r_w) / \sqrt{\alpha} \\
V_p &= \pi (r^2 - r_w^2) h \phi \\
w(\tau) &= 2\pi (\alpha \tau + r_w \sqrt{\alpha}) h \phi = \sqrt{\alpha} \phi (A + 2\pi h \tau \sqrt{\alpha})
\end{aligned} \tag{3.34}$$

where, $A = 2\pi r_w h$.

Step 2:

$$\begin{aligned}
V_1(t) &= \int_{\tau=0}^{\infty} d\tau \tau w(\tau) e^{-\tau^2/4t} = \sqrt{\alpha} \phi \int_{\tau=0}^{\infty} d\tau \tau (A + 2\pi h \tau \sqrt{\alpha}) e^{-\tau^2/4t} \\
W_1(t) &= \int_{\tau_{wf}}^{\infty} \frac{d\tau}{w(\tau)} \int_{\tau}^{\infty} d\tau' w(\tau') \tau'^m e^{-\tau'^2/4t} \\
&= 2\phi t \sqrt{\alpha} \int_{\tau_{wf}}^{\infty} \frac{d\tau}{w(\tau)} \left\{ (A + 2\pi h \tau \sqrt{\alpha}) e^{-\tau^2/4t} + 2h\pi^{3/2} \sqrt{\alpha t} \operatorname{Erfc}\left(\frac{\tau}{2\sqrt{t}}\right) \right\} \\
q_{sf}(t) &= c_t \Delta p_{wf} \frac{V_1(t)}{W_1(t)}
\end{aligned} \tag{3.35}$$

It is useful to contrast the rate normalized pressure drop calculated in this fashion, with the solution based upon a fixed well rate, Eq. (2.61), because one is often used as an approximation to the other (Houze *et al.*, 2015).

$$RNP_{BHP} = \frac{\Delta p_{wf}}{q_{sf}(t)} = \frac{1}{c_t} \frac{W_1(t)}{V_1(t)} \tag{3.36}$$

$$RNP_{Rate} = \frac{\Delta p_{wf}(t)}{q_w} = \frac{1}{c_t} \frac{W_0(t)}{V_0(t)} \tag{3.37}$$

The fixed BHP results are shown in Figure 3.9 (a), and are in excellent agreement with the zero skin reference solution of Van Everdingen and Hurst (1949), in the limit of infinite reservoir size.

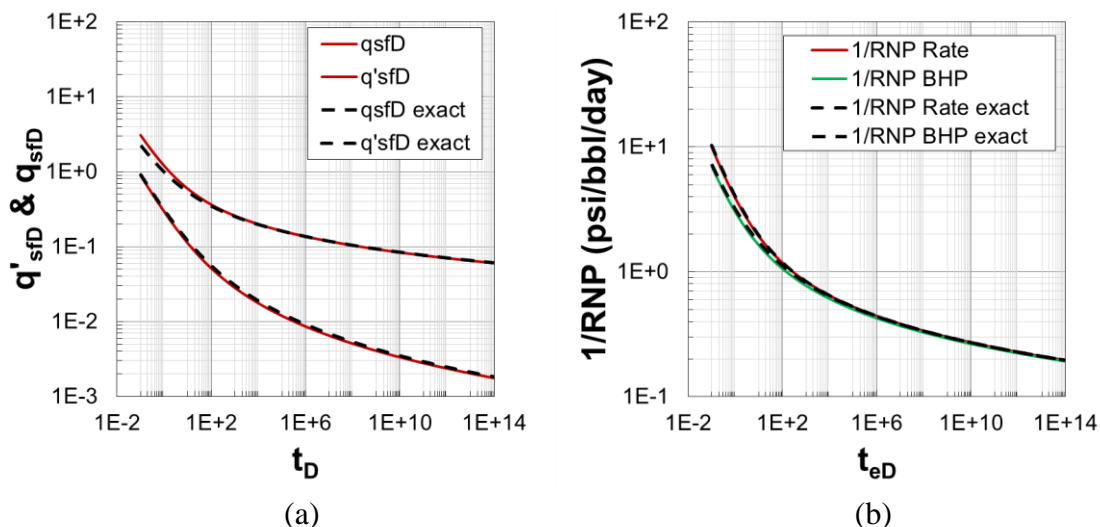


Figure 3.9 Comparison of (a) q_{sfD} , q'_{sfD} (red curves) of fixed BHP drawdown; (b) $1/RNP$ of fixed rate (red curves) and BHP (green curves) drawdown with the corresponding exact solutions from inverse Laplace transform (black dashed curves) for an infinite reservoir

The calculation of RNP at fixed rate is also included within the figure. With the presence of skin (not shown), or for sufficiently large time, the two expressions for the rate normalized pressure drop are fairly close. This is not a new observation, with the fixed rate calculation often being used as an approximation to the fixed BHP case. The approximate equality of these functions is also consistent with the use of the rate normalized pressure drop for smoothly variable rate in welltest interpretations (Winestock and Colpitts, 1965). For our approach, we don't need to use superposition in time to obtain this solution, because the asymptotic form captures this case.

3.2.2.2 Infinite Acting Radial Flow with Wellbore Storage and Fixed Rate

Drawdown

We have just showed that in the simplest fixed BHP drawdown, that the single $A_1(t)$ term gave excellent agreement with the exact solution for IARF. In the previous chapter we did the same thing for fixed rate drawdown with $A_0(t)$. Now we are going to examine the solutions for a less trivial inner boundary condition to see how well they work. Wellbore storage is an example where transient pressure depletion in the reservoir and PSS depletion in the wellbore are coupled. The boundary conditions for the reservoir will reference the flux at the sandface, $q_{sf}(t)$, which initially vanishes and then increases to the flow rate of the well, q_w . The sandface flux is not specified but must be determined as part of the solution of the coupled problem. For the current description we will develop the equations for a fluid filled wellbore, although the form of the solution is the same for a rising liquid level (Hurst, 1953; Van Everdingen, 1953; Wattenbarger and Ramey, 1970; Lee *et al.*, 2003). The reference solution follows Agarwal *et al.* (1970). The calculations that we are about to perform will allow us to examine the accuracy and performance of the different forms of the asymptotic pressure approximation with 1, 2, or 3 asymptotic terms.

This problem is a useful one, as it allows us to study the impact of simultaneously changing the well rate and the bottomhole flowing pressure. We will first examine the use of the rate normalized pressure drop as an equivalent fixed rate drawdown, as suggested

by Winestock and Colpitts (1965) for smoothly varying production rates. Then, we will explore asymptotic pressure approximation with 1, 2, or 3 asymptotic terms.

Applying this approach to the asymptotic formulation we have the starting equation for the RNP transient approach:

$$c_i \frac{\partial}{\partial t} \left(\frac{\Delta p}{q_w} \right) \approx - \frac{1}{w(\tau)} \frac{\partial}{\partial \tau} \left(\frac{q}{q_w} \right) \approx \sum_{n=0}^{\infty} \frac{A_n(t)}{q_w(t)} \cdot \tau^n e^{-\tau^2/4t} \quad (3.38)$$

If we only keep the first term in the asymptotic approximation, we obtain that:

$$c_i \frac{dRNP(r_{weff}, t)}{dt} \approx \frac{1}{V_0(t)} \cdot e^{-(r_{weff}-r_w)^2/4\alpha t} \quad (3.39)$$

Here, $r_{weff} = r_w e^{-S}$ is the effective wellbore radius, and:

$$RNP(r_{weff}, t) \equiv \frac{p_i - p(r_{weff}, t)}{q_{sf}(t)} \quad \text{and} \quad RNP_{wf}(t) = RNP(r_{weff}, t) \quad (3.40)$$

As a result the expression for Δp_{wf} is modified:

$$\Delta p_{wf}(t) = q_{sf}(t) \cdot RNP(r_{weff}, t) \quad (3.41)$$

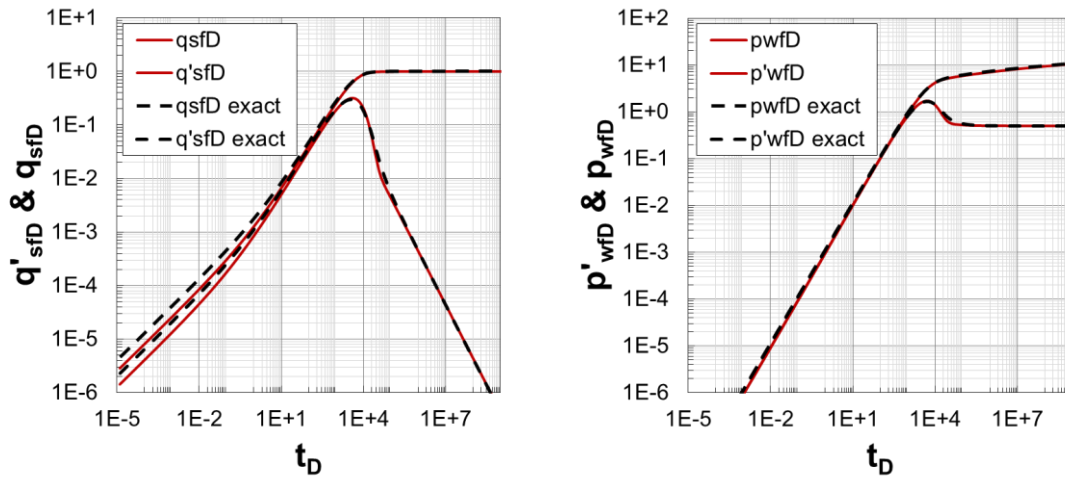
As in the reference calculation, we are using an effective wellbore radius for the skin, although other treatments, e.g., additive skin, are possible. Consequently the equation for the sandface flux is:

$$\frac{q_w - q_{sf}}{V_w} = c_i \frac{d\Delta p_{wf}}{dt} = \frac{q_{sf}}{V_0(t)} \cdot e^{-(r_{weff}-r_w)^2/4\alpha t} + \int_{t=0}^t \frac{dt}{V_0(t)} \cdot \frac{dq_{sf}}{dt} \cdot e^{-(r_{weff}-r_w)^2/4\alpha t} \quad (3.42)$$

This solution for $q_{sf}(t)$ and the exact reference solution are shown in Figure 3.10 (a) with dimensionless parameters. The plot also includes the welltest derivative of q_{sfD} :

$q'_{sfD} \equiv \frac{dq_{sfD}}{d \ln t_D}$, where $q_{sfD} = \frac{q_{sf}}{q_w}$. The calculation in the figure is performed for a skin of

zero, to better understand the solution. The comparison of the exact solution with the calculation based on the *RNP* transient is excellent only except for the early time. This is because setting $A_1(t) = 0$ is not consistent with the inner boundary of $dq_{sf}/dt > 0$ for wellbore storage case, which means the approach is inconsistent especially during early period when the magnitude of dq_{sf}/dt is relatively large.



(a) Flux Diagnostic Plot

(b) Pressure Drop Diagnostic Plot

Figure 3.10 Comparison of Diagnostic plot of (a) q_{sfD} , q'_{sfD} (red curves) and (b) p_{wfd} , p'_{wfd} (red curves) by *RNP* transient and the corresponding exact solutions from inverse Laplace transform (black dashed curves) of wellbore storage solutions with zero skin

Eq. (3.41) shows how to combine the solutions for $q_{sf}(t)$ and $RNP(r_{weff}, t)$, Eq. (3.42). This gives the pressure drop and welltest derivative for the diagnostic plot, Figure

3.10 (b), where $p_{wfd} = \frac{2\pi kh\Delta p_{wf}}{q_w\mu B}$ and $p'_{wfd} \equiv \frac{dp_{wfd}}{d \ln t_D}$. Figure 3.10 (b) shows the results

based upon the RNP transients and has excellent agreement with the reference solution.

From the comparison, we know that RNP transient approach suggested by Winestock and Colpitts (1965) gives an acceptable solution to this specific case. Next, I would like to explore asymptotic pressure approximation with 1, 2, or 3 asymptotic terms and see how our approach works for the wellbore storage case.

3.2.3 *Determining Number of Asymptotic Terms in the Approximation*

In the first section of this chapter, we have applied superposition in time to address variable rate drawdown problems and get the reference solutions for the wellbore storage case. In the previous section, I followed Winestock and Colpitts (1965) and showed the derivation for case with wellbore storage using an extension to the asymptotic solution for a fixed rate drawdown. The flux given by RNP transient approach shows some mismatch w.r.t. to the reference solution during early time. We will now solve the same problem but using the asymptotic form of the pressure evolution equation, Eq. (3.27) to better understand the number of terms that are necessary to accurately approximate the infinite asymptotic series. Fixed rate drawdown with wellbore storage is a good candidate for this discussion, because it has neither fixed rate nor fixed BHP drawdown at the wellbore sandface and we know that only keep the first unknown function in the series of $\{A_n(t)\}$ is not adequate for RNP transient approach. The integrability condition, Eq. (2.37), which gives evolution equations for the higher order terms, will be used during this process.

Boundary conditions are typically specified in terms of the flux or the pressure drop at the wellbore, or a combination of the two. For fixed rate drawdown we have already obtained the result that $A_1(t)$ must vanish. Similarly, we have also showed the requirement for a fixed BHP drawdown without skin, i.e., $A_0(t)$ must vanish. For variable rate/BHP drawdown, e.g., in the analysis of wellbore storage, we will examine solutions that include combinations of $A_0(t)$, $A_1(t)$ and $A_2(t)$, which will be fixed by the boundary condition at the wellbore. The PSS boundary condition of wellbore storage case has been shown previously in Eq. (3.25), where we applied superposition in time to address the problem.

In this section, I will explore all the possible combinations of the solution scenarios to this problem to obtain guidance on determining an adequate number of asymptotic terms for other variable rate/pressure drawdown solutions.

3.2.3.1 Two-Term Asymptotic Approximation

Following the previous exploration of fixed rate/BHP drawdown and the discussion on variable rate/BHP drawdown, we first explore wellbore storage case by taking the first two terms ($n=1$) of flux and pressure drop expressions, we get four unknowns $A_0(t)$, $A_1(t)$, q_{sf} and Δp_{wf} . Since there are five equations, we will have different scenarios to solve this problem. The PSS boundary condition is a must-use one, otherwise the problem will reduce to the fixed rate drawdown problem. Thus, we have the following four scenarios for the two-term asymptotic approximation:

Scenario 1: ①②③⑤

Scenario 2: ①②④⑤

Scenario 3: ①③④⑤

Scenario 4: ②③④⑤

Next, I will illustrate the brief steps and results of each scenario.

Scenario 1 Solve the above equations without using the flux evolution equation,

we can get the expression for q_{sf} without $A_0(t)$ and $A_1(t)$:

$$\Delta p_{wf} = \frac{[(V_w + V_0)W_1 - V_1W_0]q_{sf} + (V_1W_0 - V_0W_1)q_w}{c_t V_w V_1} \quad (3.43)$$

In order to eliminate q_{sf} from the equation, we substitute PSS boundary condition and

rearrange the equation to obtain the 1st order ODE of Δp_{wf} as:

$$fun1(t) \frac{d\Delta p_{wf}}{dt} + fun2(t) \Delta p_{wf} = fun3(t) \quad (3.44)$$

where the prefactor functions are:

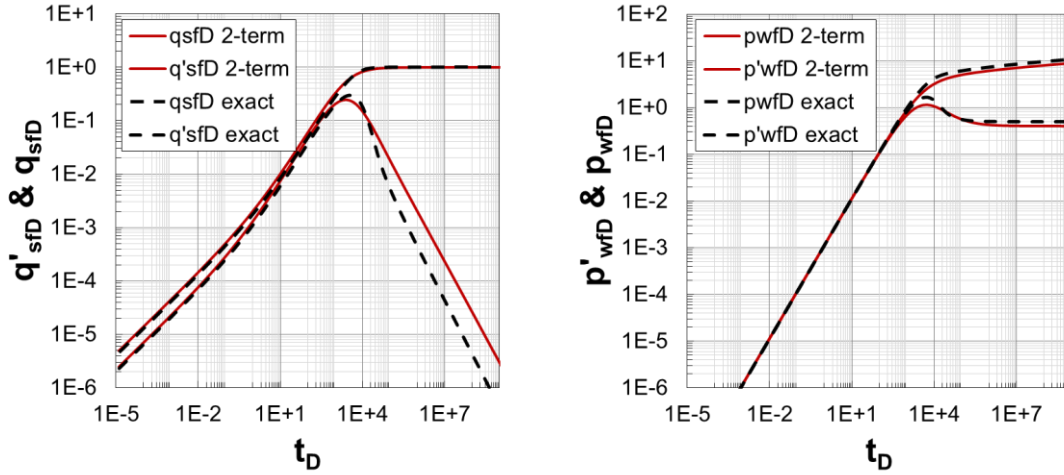
$$\begin{cases} fun1(t) = c_t [(V_w + V_0)W_1 - V_1W_0] \\ fun2(t) = c_t V_1 \\ fun3(t) = q_w W_1 \end{cases} \quad (3.45)$$

Together with the initial condition $\Delta p_{wf}(0) = 0$, the ODE can be solved directly for Δp_{wf} .

Then, $d\Delta p_{wf}/dt$ can be estimated accordingly. $A_0(t)$ is obtained from $d\Delta p_{wf}/dt$

through pressure evolution equation and $A_1(t)$ can be calculated via pressure drop

equation. Next, q_{sf} can be obtained using PSS boundary condition and dq_{sf}/dt is determined after that.



(a) Flux Diagnostic Plot

(b) Pressure Drop Diagnostic Plot

Figure 3.11 Comparison of Diagnostic plots of (a) q_{sfD} , q'_{sfD} (red curves) and (b) p_{wFD} , p'_{wFD} (red curves) and the corresponding exact solutions from inverse Laplace transform (black dashed curves) for Scenario 1 of two-term asymptotic approximation

The Diagnostic plots of q_{sfD} and p_{wFD} as well as the corresponding exact solutions from inverse Laplace transform are shown in Figure 3.11. We observe that this scenario gives accurate q_{sfD} and p_{wFD} values in general, especially before radial flow establishes. Thus, this scenario could be a candidate for variable rate/BHP drawdown analysis.

Scenario 2 Solve the above equations without using the pressure evolution expression, we can get the expression for q_{sf} without $A_0(t)$ and $A_1(t)$:

$$q_{sf} = \frac{c_t V_0 \Delta p_{wf}}{W_0} + \frac{c_t V_w (V_1 W_0 - V_0 W_1)}{w(0) W_0} \frac{d^2 \Delta p_{wf}}{dt^2} \quad (3.46)$$

In order to eliminate q_{sf} from the equation, we substitute PSS boundary condition and rearrange the equation to obtain the 2nd order ODE of Δp_{wf} as:

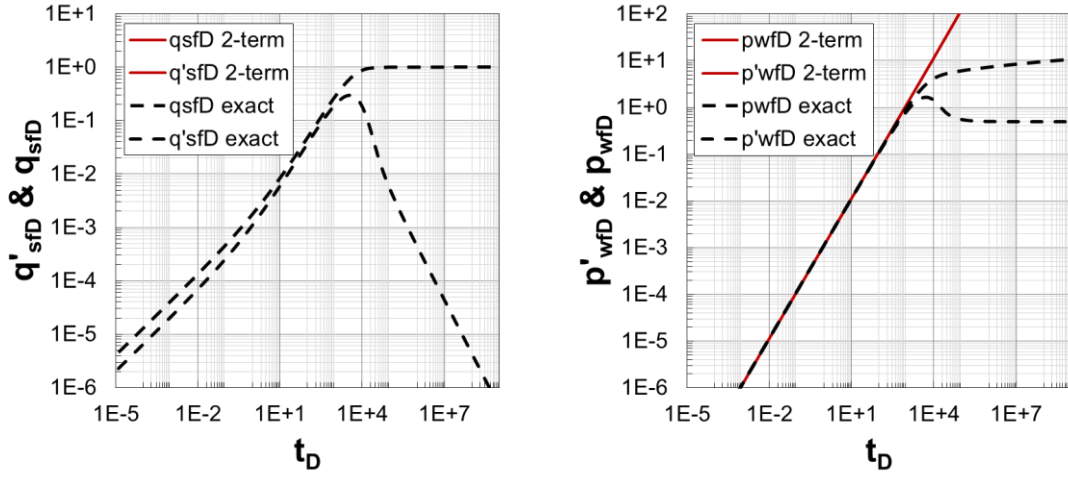
$$fun1(t) \frac{d^2 \Delta p_{wf}}{dt^2} + fun2(t) \frac{d \Delta p_{wf}}{dt} + fun3(t) \Delta p_{wf} = fun4(t) \quad (3.47)$$

where the prefactor functions are:

$$\begin{cases} fun1(t) = c_t V_w (V_1 W_0 - V_0 W_1) \\ fun2(t) = c_t V_w w(0) W_0 \\ fun3(t) = c_t w(0) V_0 \\ fun4(t) = q_w w(0) W_0 \end{cases} \quad (3.48)$$

Together with the initial conditions $\Delta p_{wf}(0) = 0$ & $\left. \frac{d \Delta p_{wf}}{dt} \right|_{t=0} = \frac{q_w}{c_t V_w}$, the ODE is solved directly for Δp_{wf} . Then, $d \Delta p_{wf} / dt$ is estimated accordingly. Next, q_{sf} is obtained using PSS boundary condition and $d q_{sf} / dt$ is determined after that. $A_1(t)$ can be calculated based on $d q_{sf} / dt$ via flux evolution equation and $A_0(t)$ can be finally determined through pressure drop equation.

The Diagnostic plots of q_{sfD} and p_{wfD} as well as the corresponding exact solutions from inverse Laplace transform are shown in Figure 3.12. We observe that this approach yields unstable q_{sfD} and only gives accurate p_{wfD} values before radial flow is established. Thus, this scenario is not appropriate for variable rate/BHP drawdown analysis.



(a) Flux Diagnostic Plot

(b) Pressure Drop Diagnostic Plot

Figure 3.12 Comparison of Diagnostic plots of (a) q_{sfD} , q'_{sfD} (red curves) and (b) p_{wFD} , p'_{wFD} (red curves) and the corresponding exact solutions from inverse Laplace transform (black dashed curves) for Scenario 2 of two-term asymptotic approximation

Scenario 3 Combine all the expressions without using pressure drop equation, we

can get the 1st order ODE of q_{sf} as:

$$fun1(t) \frac{dq_{sf}}{dt} + fun2(t) q_{sf} = fun3(t) \quad (3.49)$$

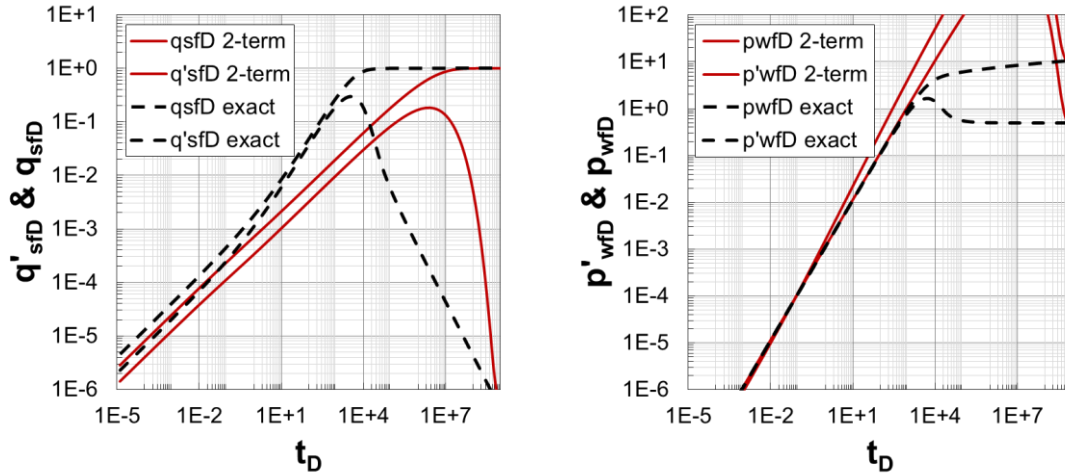
where the prefactor functions are:

$$\begin{cases} fun1(t) = V_w V_1 \\ fun2(t) = w(0)(V_w + V_0) \\ fun3(t) = q_w w(0) V_0 \end{cases} \quad (3.50)$$

Together with the initial condition $q_{sf}(0) = 0$, I solve the ODE for q_{sf} and thus dq_{sf}/dt can be obtained accordingly. Then, $A_1(t)$ is determined via flux evolution equation and $A_0(t)$ is estimated by combining pressure evolution equation and PSS boundary

condition. Finally, $d\Delta p_{wf}/dt$ is evaluated using pressure evolution equation and Δp_{wf} is calculated based on time integral.

The Diagnostic plots of q_{sfD} and p_{wfD} as well as the corresponding exact solutions from inverse Laplace transform are shown in Figure 3.13. We observe that this scenario gives poor results and thus it is not appropriate for variable rate/BHP drawdown analysis.



(a) Flux Diagnostic Plot

(b) Pressure Drop Diagnostic Plot

Figure 3.13 Comparison of Diagnostic plots of (a) q_{sfD} , q'_{sfD} (red curves) and (b) p_{wfD} , p'_{wfD} (red curves) and the corresponding exact solutions from inverse Laplace transform (black dashed curves) for Scenario 3 of two-term asymptotic approximation

Scenario 4 Combine all the expressions except for flux equation, we can get the

2nd order homogeneous ODE of Δp_{wf} as:

$$fun1(t) \frac{d^2 \Delta p_{wf}}{dt^2} + fun2(t) \frac{d \Delta p_{wf}}{dt} + fun3(t) \Delta p_{wf} = 0 \quad (3.51)$$

where the prefactor functions are:

$$\begin{cases} fun1(t) = V_w W_1 \\ fun2(t) = w(0) W_0 \\ fun3(t) = -w(0) \end{cases} \quad (3.52)$$

Together with the initial conditions $\Delta p_{wf}(0) = 0$ & $\left. \frac{d\Delta p_{wf}}{dt} \right|_{t=0} = \frac{q_w}{c_t V_w}$, the ODE is solved directly for Δp_{wf} . Then, $d\Delta p_{wf}/dt$ can be estimated accordingly. Next, q_{sf} is obtained using PSS boundary condition. $A_0(t)$ is determined by pressure evolution equation and $A_1(t)$ is calculated via pressure drop equation. Finally, dq_{sf}/dt is obtained through flux evolution equation.

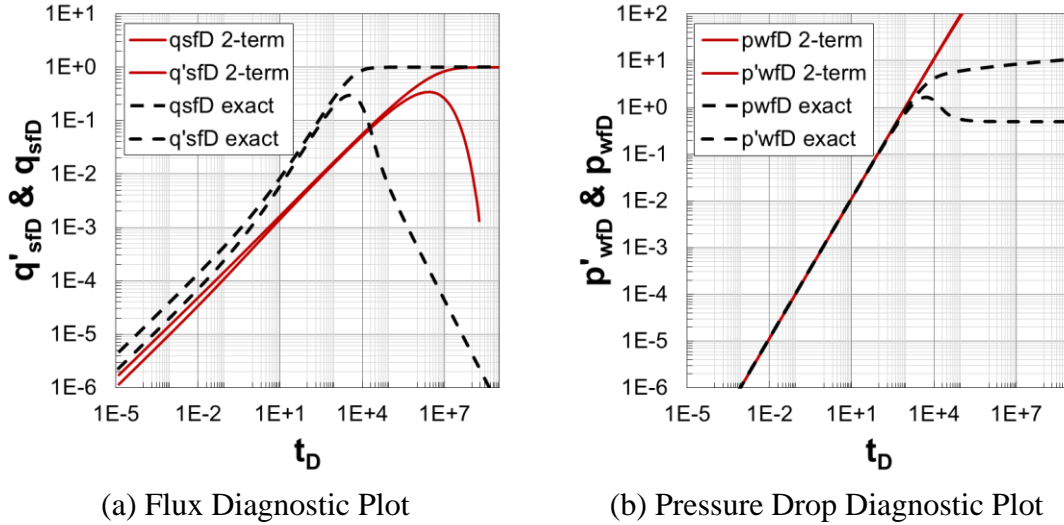


Figure 3.14 Comparison of Diagnostic plots of (a) q_{sfD} , q'_{sfD} (red curves) and (b) p_{wFD} , p'_{wFD} (red curves) and the corresponding exact solutions from inverse Laplace transform (black dashed curves) for Scenario 4 of two-term asymptotic approximation

The Diagnostic plots of q_{sfD} and p_{wfD} as well as the corresponding exact solutions from inverse Laplace transform are shown in Figure 3.14. We observe that this scenario yields poor results and thus it is not appropriate for further analysis.

A summary of all the different scenarios of wellbore storage case with 2-term asymptotic solution is listed in Table 3.1. The gray/white grid blocks mean the corresponding equation is included/excluded from the calculation. For the solution quality, red/orange/green is used for the qualitative assessments as bad/poor/good. Based on the demonstrations for these four scenarios, only the first one out of four scenarios of the two-term asymptotic approximation could be used for variable rate/BHP drawdown analysis.

Wellbore Storage (2-term)	Scenario 1	Scenario 2	Scenario 3	Scenario 4
$q_{sf} = \sum_n A_n \cdot V_n$	Gray	Gray	Gray	White
$c_i \Delta p_{wf} = \sum_n A_n \cdot W_n$	Gray	Gray	White	Gray
$c_i \frac{d\Delta p_{wf}}{dt} = A_0$	Gray	White	Gray	Gray
$\frac{dq_{sf}}{dt} = -w(0) A_1$	White	Gray	Gray	Gray
PSS Boundary Condition (ODE)	Gray	Gray	Gray	Gray
Solution Quality	Green	Red: Unstable	Yellow: Poor	Yellow: Poor

Table 3.1 Summary of equations to be solved in each scenario of wellbore storage cases with 2 asymptotic terms

3.2.3.2 Three-Term Asymptotic Approximation

After exploring the results of two-term asymptotic approximation, we know $A_0(t)$ plus $A_1(t)$ could be a choice for variable rate/BHP drawdown analysis. What if we have one extra term? Will it improve the solution accuracy? Let's begin with the examination of the three-term asymptotic approximation and take the first three terms ($n = 2$) of flux and pressure drop expressions. There are five equations with five unknowns $A_0(t)$, $A_1(t)$, $A_2(t)$, q_{sf} and Δp_{wf} , so all the equations will be used during the calculation. For the three-term asymptotic approximation, we end up with a 2nd order ODE of Δp_{wf} .

From the boundary condition, we know that q_{sf} can be expressed as:

$$q_{sf} = q_w - c_t V_w \frac{d\Delta p_{wf}}{dt} \quad (3.53)$$

Take the time derivative of Eq. (3.53), we obtain that:

$$\frac{dq_{sf}}{dt} = -c_t V_w \frac{d^2\Delta p_{wf}}{dt^2} \quad (3.54)$$

Combine flux evolution equation and Eq. (3.54), $A_1(t)$ can be related to Δp_{wf} as:

$$A_1(t) = \frac{c_t V_w}{w(0)} \frac{d^2\Delta p_{wf}}{dt^2} \quad (3.55)$$

From flux and pressure drop expressions, we can eliminate $A_2(t)$:

$$\Delta p_{wf} = \frac{q_{sf} W_2 + A_0(t)(V_2 W_0 - V_0 W_2) + A_1(t)(V_2 W_1 - V_1 W_2)}{c_t V_2} \quad (3.56)$$

Substitute pressure evolution equation, Eqs. (3.53) and (3.55) into Eq. (3.56), and rearrange to obtain the 2nd order ODE of Δp_{wf} as:

$$fun1(t) \frac{d^2 \Delta p_{wf}}{dt^2} + fun2(t) \frac{d \Delta p_{wf}}{dt} + fun3(t) \Delta p_{wf} = fun4(t) \quad (3.57)$$

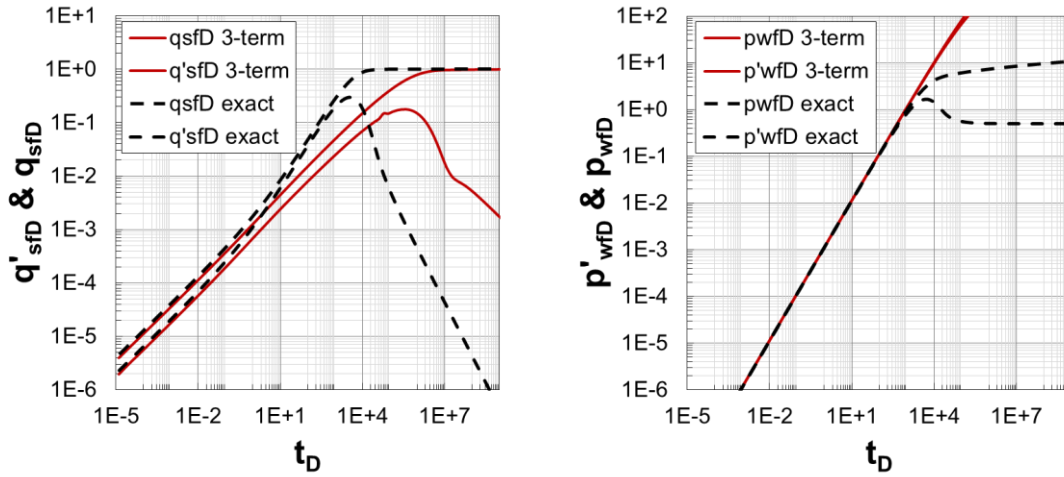
where the prefactor functions are:

$$\begin{cases} fun1(t) = c_t V_w (V_1 W_2 - V_2 W_1) \\ fun2(t) = c_t w(0) [(V_w + V_0) W_2 - V_2 W_0] \\ fun3(t) = c_t w(0) V_2 \\ fun4(t) = q_w w(0) W_2 \end{cases} \quad (3.58)$$

Together with the initial conditions $\Delta p_{wf}(0) = 0$ & $\left. \frac{d \Delta p_{wf}}{dt} \right|_{t=0} = \frac{q_w}{c_t V_w}$, the ODE is

solved directly for Δp_{wf} , and thus $d \Delta p_{wf} / dt$ can be estimated accordingly. Next, $A_0(t)$ is obtained using pressure evolution equation, q_{sf} is calculated with Eq. (3.53) and $d q_{sf} / dt$ is determined after that. Then, $A_1(t)$ can be evaluated based on $d q_{sf} / dt$ via flux evolution equation and $A_2(t)$ can be finally determined through flux equation.

The Diagnostic plots of q_{sFD} and p_{wFD} as well as the corresponding exact solutions from the inverse Laplace transform are shown in Figure 3.15. We observe that this approach only gives accurate q_{sFD} value during early and late periods and accurate p_{wFD} value before radial flow establishes.



(a) Flux Diagnostic Plot

(b) Pressure Drop Diagnostic Plot

Figure 3.15 Comparison of Diagnostic plots of (a) q_{sfD} , q'_{sfD} (red curves) and (b) p_{wfd} , p'_{wfd} (red curves) and the corresponding exact solutions from inverse Laplace transform (black dashed curves) for three-term asymptotic approximation

The boundary condition and the time derivative of boundary condition basically pin down $A_0(t)$ or $A_1(t)$ term or their combination. The $A_2(t)$ term is not anywhere near well-determined and a lack of having a clear control on it is what damaged the solutions. Once we start invoking $A_2(t)$, it really get pretty unstable. For $A_0(t)$ and $A_1(t)$, we got a physical control via evaluating the evolution equation at the wellbore. Based on the demonstration, three-term asymptotic approximation should not be used for variable rate/BHP drawdown analysis.

3.2.3.3 One-Term Asymptotic Approximation

After exploring the results of two/three-term asymptotic approximation, we know $A_0(t)$ plus $A_1(t)$ could be a choice for variable rate/BHP drawdown analysis while adding an extra term would make the solution unstable. What if we only have one term

for pressure transient? In the last section, we have seen the result of RNP transient approach based upon one term asymptotic approximation, but we haven't fully explored all the scenarios for pressure transient yet. Will any of them give an improved accuracy?

Following previous exploration, we now take the first term ($n=0$) of flux and pressure drop expressions. Flux evolution equation is no longer available, so there are four equations with only three unknowns $A_0(t)$, q_{sf} and Δp_{wf} . Again, PSS boundary condition is a must-use one, and we totally have the following three scenarios for the one-term asymptotic approximation:

Scenario 1: ①②⑤

Scenario 2: ①③⑤

Scenario 3: ②③⑤

Next, I will illustrate the brief steps and results of each scenario.

Scenario 1 From flux and pressure drop expressions, we obtain the relationship between q_{sf} and Δp_{wf} as:

$$q_{sf} = c_t \Delta p_{wf} \frac{V_0(t)}{W_0(t)} \quad (3.59)$$

Substitute Eq. (3.59) into PSS boundary condition and eliminate q_{sf} , we obtain a 1st order ODE of Δp_{wf} as:

$$fun1(t) \frac{d\Delta p_{wf}}{dt} + fun2(t) \Delta p_{wf} = fun3(t) \quad (3.60)$$

where the prefactor functions are:

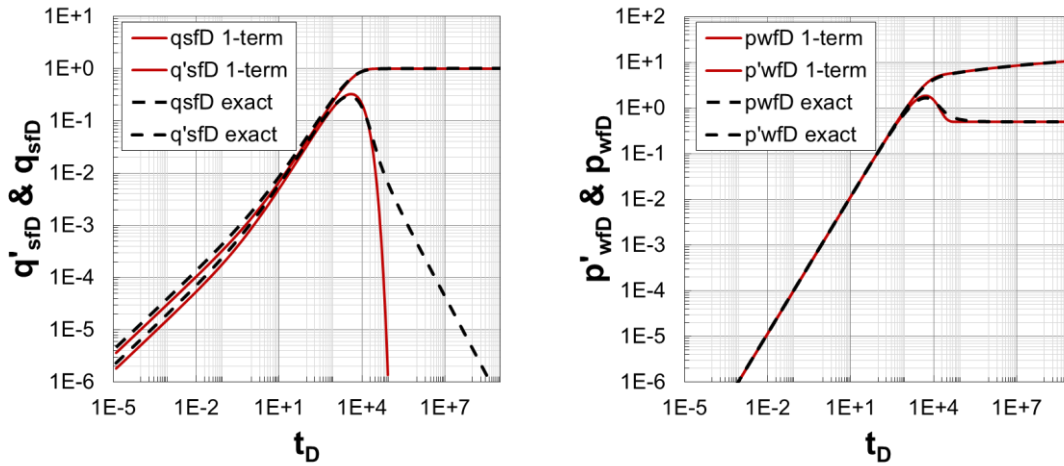
$$\begin{cases} fun1(t) = c_t V_w W_0 \\ fun2(t) = c_t V_0 \\ fun3(t) = q_w W_0 \end{cases} \quad (3.61)$$

Together with the initial condition $\Delta p_{wf}(0) = 0$, the ODE can be solved directly for Δp_{wf} .

Then, $d\Delta p_{wf}/dt$ can be estimated accordingly. Next, q_{sf} can be obtained using Eq. (3.59)

and dq_{sf}/dt is calculated accordingly. Finally, $A_0(t)$ can be determined by pressure drop equation.

The Diagnostic plots of q_{sfD} and p_{wfD} as well as the corresponding exact solutions from inverse Laplace transform are shown in Figure 3.16. We observe that this scenario gives accurate q_{sfD} and p_{wfD} values in general. Thus, this scenario could be a candidate for variable rate/BHP drawdown analysis.



(a) Flux Diagnostic Plot

(b) Pressure Drop Diagnostic Plot

Figure 3.16 Comparison of Diagnostic plots of (a) q_{sfD} , q'_{sfD} (red curves) and (b) p_{wfD} , p'_{wfD} (red curves) and the corresponding exact solutions from inverse Laplace transform (black dashed curves) for Scenario 1 of one-term asymptotic approximation

Scenario 2 Combine flux and pressure evolution equations and eliminate $A_0(t)$,

we connect q_{sf} to $d\Delta p_{wf}/dt$ as:

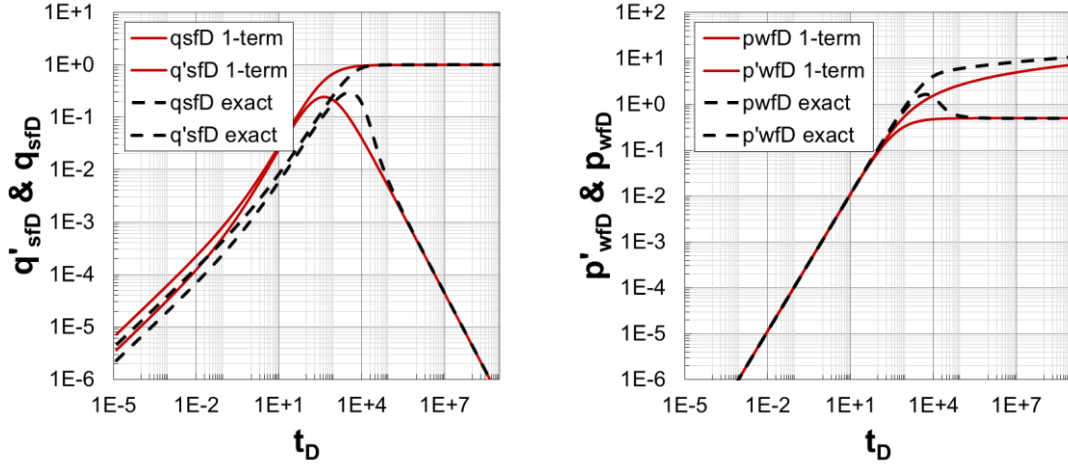
$$\frac{d\Delta p_{wf}}{dt} = \frac{q_{sf}}{c_t V_0(t)} \quad (3.62)$$

Substitute Eq. (3.62) into PSS boundary condition and rearrange the expression, we obtain the formula of q_{sf} :

$$q_{sf}(t) = \frac{V_0(t)}{V_w + V_0(t)} q_w \quad (3.63)$$

q_{sf} can be calculated with Eq. (3.63) and dq_{sf}/dt is determined accordingly. Then, $d\Delta p_{wf}/dt$ can be estimated via Eq. (3.62) and Δp_{wf} can be obtained via numerical integral. Finally, $A_0(t)$ is determined by pressure evolution equation.

The Diagnostic plots of q_{sfD} and p_{wfD} as well as the corresponding exact solutions from inverse Laplace transform are shown in Figure 3.17. We observe that this scenario does not give accurate q_{sfD} value during early time nor p_{wfD} value during late time. Thus, this scenario should not be used for variable rate/BHP drawdown analysis.



(a) Flux Diagnostic Plot

(b) Pressure Drop Diagnostic Plot

Figure 3.17 Comparison of Diagnostic plots of (a) q_{sfD} , q'_{sfD} (red curves) and (b) p_{wFD} , p'_{wFD} (red curves) and the corresponding exact solutions from inverse Laplace transform (black dashed curves) for Scenario 2 of one-term asymptotic approximation

Scenario 3 Combining pressure drop and pressure evolution equations, eliminating $A_0(t)$, we obtain a 1st order ODE of Δp_{wf} as:

$$fun1(t) \frac{d\Delta p_{wf}}{dt} + fun2(t) \Delta p_{wf} = 0 \quad (3.64)$$

where the prefactor functions are:

$$\begin{cases} fun1(t) = W_0 \\ fun2(t) = -1 \end{cases} \quad (3.65)$$

Together with the initial condition $\Delta p_{wf}(0) = 0$, the ODE can be solved directly for Δp_{wf} .

Then, $d\Delta p_{wf}/dt$ can be estimated accordingly. Next, q_{sf} can be obtained using PSS

boundary condition and dq_{sf}/dt is calculated accordingly. Finally, $A_0(t)$ can be

determined by pressure evolution equation. This approach always yields $\Delta p_{wf} = 0$ and $q_{sf} = q_w$, and thus it cannot be used for analysis.

A summary of all the different scenarios of wellbore storage case with 1-term asymptotic solution is listed in Table 3.2. Based on the demonstrations for these scenarios, only the first one out of three scenarios of the one-term asymptotic approximation could be used for variable rate/BHP drawdown analysis.

Wellbore Storage (1-term)	Scenario 1	Scenario 2	Scenario 3
$q_{sf} = \sum_n A_n \cdot V_n$			
$c_i \Delta p_{wf} = \sum_n A_n \cdot W_n$			
$c_i \frac{d\Delta p_{wf}}{dt} = A_0$			
$\frac{dq_{sf}}{dt} = -w(0) A_1$			
PSS Boundary Condition (ODE)			
Solution Quality	Good	Poor	Bad

Table 3.2 Summary of equations to be solved in each scenario of wellbore storage cases with 1 asymptotic term

3.2.3.4 Discussion on Number of Terms

So far, we have tested the asymptotic solutions for fixed rate drawdown, fixed BHP drawdown, as well as wellbore storage cases with 1, 2, or 3 asymptotic terms. Table 3.3

summarizes the combinations of equations that provided the best solutions for these cases. The table lists five equations that we have worked with. The gray/white grid blocks mean the corresponding equation is included/excluded from the calculation. For the solution quality, red/orange/green is used for the qualitative assessments as bad/poor/good. For fixed rate drawdown, $A_1(t)$ must vanish and $A_0(t)$ will describe the pressure transient at the wellbore and in the reservoir. For fixed BHP drawdown in the absence of skin, $A_0(t)$ must vanish and $A_1(t)$ will describe the rate transient at the wellbore and in the reservoir. The boundary condition and the time derivative of boundary condition basically pin down $A_0(t)$ or $A_1(t)$ term or their combination. For wellbore storage case that include combinations of $A_0(t)$, $A_1(t)$ and $A_2(t)$, the $A_2(t)$ term is not anywhere near well-determined and a lack of having a clear control on it is what damaged the solutions. Once we start invoking $A_2(t)$, it really get pretty unstable. For wellbore storage cases that include $A_0(t)$ or a combination of $A_0(t)$ and $A_1(t)$, we got a physical control via evaluating the evolution equation at the wellbore, so the best scenarios give accurate solutions.

	Fixed Rate Drawdown (A ₀ only)	Fixed BHP Drawdown (A ₁ only)	WBS (1-term)	WBS (2-term)	WBS (3-term)
$q_{sf} = \sum_n A_n \cdot V_n$					
$c_t \Delta p_{wf} = \sum_n A_n \cdot W_n$					
$c_t \frac{d\Delta p_{wf}}{dt} = A_0$					
$\frac{dq_{sf}}{dt} = -w(0) A_1$					
Boundary Condition	Algebraic	Algebraic	ODE	ODE	ODE
Solution Quality					

Table 3.3 Summary of the combinations of equations that provided the best solutions for fixed and variable rate drawdown and the wellbore storage with 1, 2, or 3 asymptotic terms

Throughout the full exploration of different combinations of equations for asymptotic approximation with 1, 2, or 3 asymptotic terms, we can summarize the following useful conclusions:

- The exploration of solutions demonstrates that the one-term asymptotic approximation provides a good solution for variable rate drawdown analysis. However, in all the cases examined, the two-term solutions more accurately represent the specific boundary conditions of each case (except for fixed BHP drawdown where only one-term is used).

- We should not go beyond the two-term asymptotic approximation to determine the unknown functions $\{A_n(t)\}$, since the higher order terms are not as well-determined as the lower order terms, damaging the solutions.
- The evaluation expressions have time derivatives. We know that time derivatives may be good at many times, but not at all times. Once we integrate through time over the less accurate times, then the results are not accurate. This impacts dq_{sf}/dt strongly and $d\Delta p_{wf}/dt$ too, but less strongly. Thus, we should exclude them in calculations if possible.

3.2.4 *Superposition Time and Material Balance Time*

We have successfully extended the asymptotic solutions to the prediction of variable rate drawdown, given the function $w(\tau)$ in the last section. However, when interpreting field data, the $w(\tau)$ function is not known, and we must find other ways to solve the pressure and rate flow equations. The usual approach for variable rate field analysis is to obtain an equivalent fixed rate reservoir response through the use of superposition time or material balance time. Earlier in this chapter, we showed a new and general way of expressing the superposition time in terms of the drainage volume regardless of specific flow regimes. Now, we return to the behavior of superposition time in the context of the approximation $V_d(t) \approx V_0(t)$ which allows us to derive specific expressions for the superposition time. I will first show the specific forms of superposition time for some simple models. Then, I will develop the connection between superposition

time and material balance time, and compare their capabilities in removing variable rate effects.

3.2.4.1 Superposition Time Functions for Simple Models

Table 3.4 summarizes the standard results of superposition time functions for simple models, which can be derived from Eq. (3.16) by substituting the corresponding drainage volume expressions. In this table, one result that is useful to point out specifically is that superposition time (t_s) reduces to material balance time (t_e) for boundary dominated flow since then $V_d(t) \approx V_{res}$, and from Eq. (3.16) we have:

$$\frac{t_s}{V_{res}} = \frac{1}{q_w(t)} \int_0^t \frac{q_w(t')}{V_{res}} dt' = \frac{Q_w(t)}{q_w(t)V_{res}} = \frac{t_e}{V_{res}} \Rightarrow t_s = t_e \equiv \frac{Q_w(t)}{q_w(t)} \quad (3.66)$$

In the following applications, both superposition time and material balance time will be calculated using the nominal variable rate production history information. Then the rate normalized pressure drop at all the locations can be further evaluated based on Eq. (2.58):

$$RNP(\tau, t) = \frac{\Delta p(\tau, t)}{q_{sf}(t)} = \frac{\Delta p(\tau, t_s)}{q_w} = \frac{1}{c_t} \frac{W_0(t_s) - W_0(\tau, t_s)}{V_0(t_s)} \quad (3.67)$$

The effectiveness of superposition time and material balance time in handling variable rate drawdown problems will be tested in the next section.

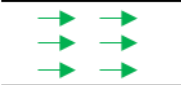
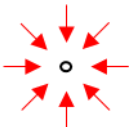
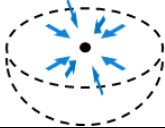
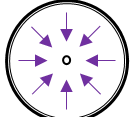
Infinite Acting Linear Flow (IALF)		$\sqrt{t_s} = \sum_{i=1}^{N(t)} \frac{q_{wi} - q_{wi-1}}{q_w(t)} \bullet \sqrt{t - t_{i-1}}$
Infinite Acting Radial Flow (IARF)		$\ln t_s = \sum_{i=1}^{N(t)} \frac{q_{wi} - q_{wi-1}}{q_w(t)} \bullet \ln(t - t_{i-1})$
Infinite Acting Spherical Flow (IASF)		$\frac{1}{\sqrt{t_s}} = \sum_{i=1}^{N(t)} \frac{q_{wi} - q_{wi-1}}{q_w(t)} \bullet \frac{1}{\sqrt{t - t_{i-1}}}$
Boundary Dominated Flow (BDF)		$t_s = t_e \equiv \frac{Q_w(t)}{q_w(t)}$

Table 3.4 Standard results for the superposition time functions for multi-rate drawdown and simple models (reprinted with permission from Wang et al, 2017)

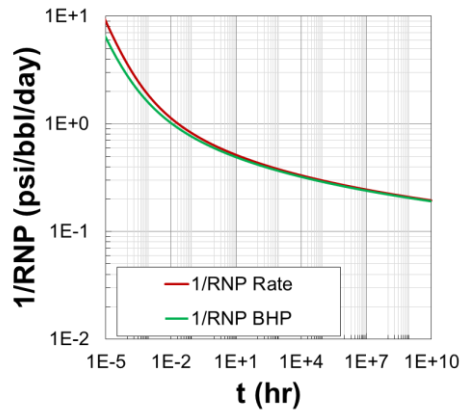
3.2.4.2 Comparison Examples for Superposition Time and Material Balance Time

After validating the effectiveness of solving variable rate drawdown problems by either using asymptotic approximations or with the theory of superposition in time, we now move one step further to test the effectiveness of superposition time which is defined based on asymptotic approximation. In this subsection, we want to test the effectiveness of the analysis that compensates for rate effects by plotting RNP against superposition time t_s or material balance time t_e . Three test cases are infinite acting radial flow, bounded radial flow, and a case with an infinite conductivity fracture, respectively. Both the infinite acting and bounded radial flow results are generated by our fixed rate/BHP asymptotic solutions, and the derivation of the bounded radial flow will be shown later in this Chapter. The results of infinite conductivity fracture case are from ECLIPSE simulation. Unless otherwise noted, the parameters used in these examples are given in Table 3.5, which are largely taken from Bourdet *et al.* (1983).

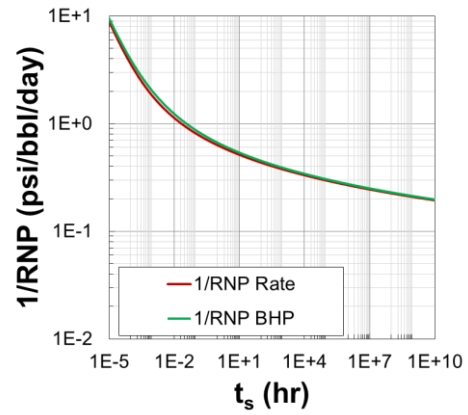
Property	Value	
q_w	184.44	<i>bbl/day</i>
Δp_{wf}	500	<i>psi</i>
ϕ	0.25	
c_t	4.20×10^{-6}	<i>psi⁻¹</i>
h	107	<i>ft</i>
r_w	0.29	<i>ft</i>
μ	2.5	<i>cp</i>
k	10.9	<i>md</i>
V_w	2210	<i>bbl</i>
S	7.7	-
x_f	250	<i>ft</i>

Table 3.5 Reservoir, fluid and wellbore parameters for infinite acting radial flow bounded radial flow, and a case with an infinite conductivity fracture

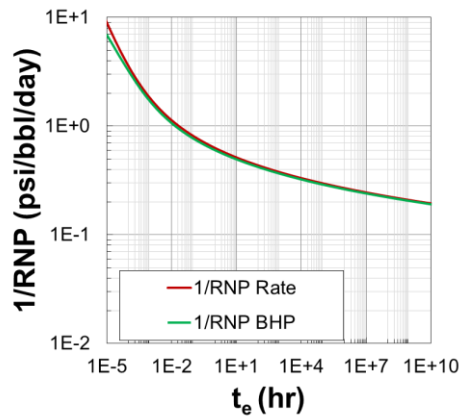
Infinite Acting Radial Flow Figure 3.18 shows the comparison of $1/RNP_{wf}$ w.r.t time, superposition time, and material balance time for infinite acting radial flow with both fixed rate (red curves) and fixed BHP (green curves) drawdown. We observe that superposition time removes variable rate effects as expected and material balance time is also effective in reducing the deviation of fixed BHP drawdown from the reference fixed rate drawdown. Despite this being an infinite acting system, t_e is also effective in reducing rate effects.



(a) Time



(b) Superposition Time



(c) Material Balance Time

Figure 3.18 Comparison of $1/RNP$ vs. time, superposition time, and material balance time for infinite acting radial flow (reprinted with permission from Wang et al, 2017)

Bounded Radial Flow Figure 3.19 shows the comparison $1/RNP_{wf}$ w.r.t time and material balance time for bounded radial flow. We now focus on the comparison during boundary dominated flow where superposition time reduces to material balance time. Material balance time (superposition time) successfully removes the late time variable rate effects, although deviations are still visible at early time.

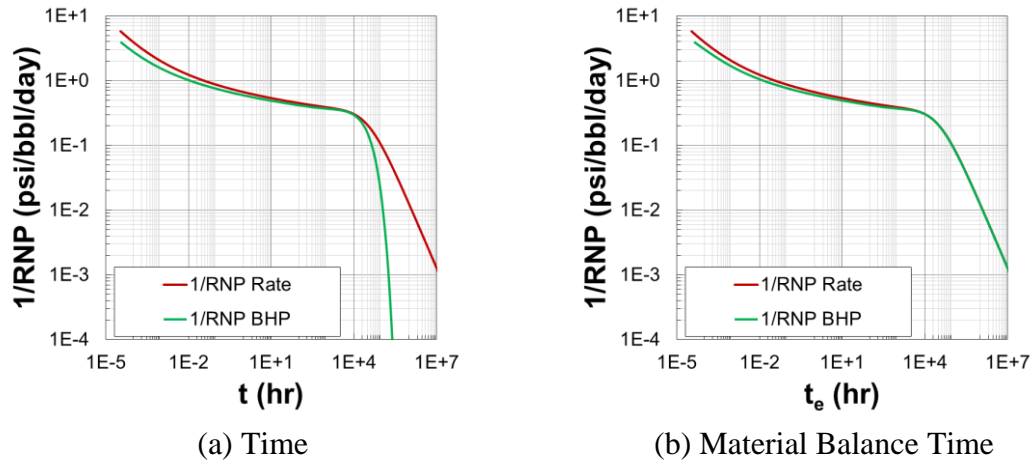


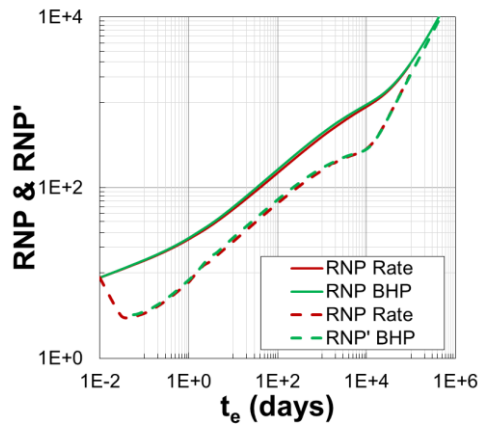
Figure 3.19 Comparison of $1/RNP$ vs. time and material balance time for bounded radial flow (reprinted with permission from Wang et al, 2017)

Infinite Conductivity Fracture In the case with an infinite conductivity hydraulic fracture under fixed rate/BHP drawdown via ECLIPSE simulations, material balance time is still effective during boundary dominated flow as indicated by subplots (a) & (b) in

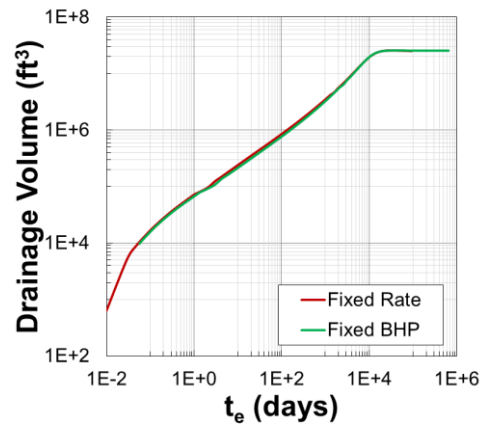
Figure 3.20, where RNP welltest derivative is defined as $RNP' = \frac{dRNP_{wf}}{d \ln(t_e)}$ and drainage

volume is calculated as $\frac{1}{V_d(t)} \approx c_t \frac{dRNP_{wf}}{dt_e}$. We observe that RNP , RNP' and drainage

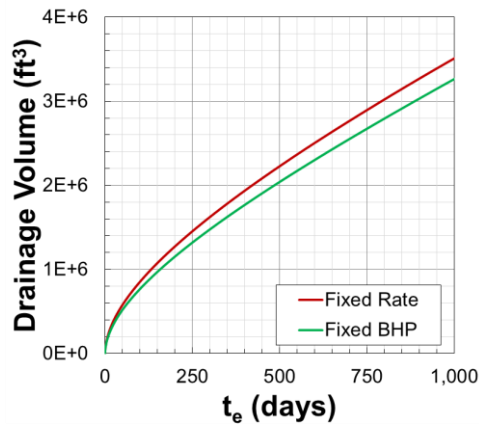
volume from fixed BHP drawdown match well with those from the actual fixed rate drawdown when they are plotting against t_e . During the transient period, the maximum deviation between fixed BHP and rate drawdown is less than 6%, as illustrated more clearly in the linear-linear scale in subplot (c).



(a) Diagnostic Plot



(b) Drainage Volume (Log-Log)



(c) Drainage Volume (Linear-Linear)

Figure 3.20 Diagnostic plot and drainage volume vs. material balance time for the case with an infinite conductivity fracture (reprinted with permission from Wang et al, 2017)

3.2.4.3 Comparison of Superposition and Material Balance Time

Generally speaking, superposition time must always generate a more accurate transformation of production data to an equivalent fixed rate drawdown than material balance time, with the only exception being during boundary dominated flow where superposition time reduces to material balance time as demonstrated by Eq. (3.66) previously. However, since material balance time only relies on the production history, it is more generally applicable than superposition time. Therefore, it is important to know

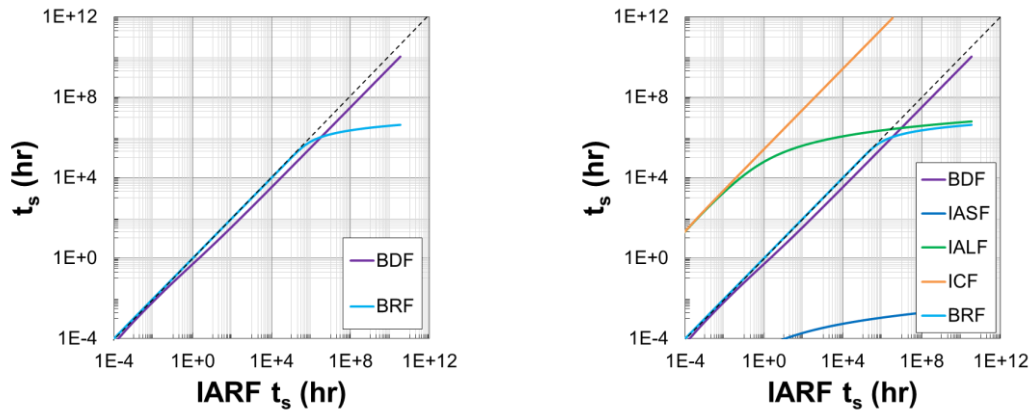
the quality of the approximation we make when we use material balance time instead of superposition time. Here, we will show the comparison between the two using two models: infinite acting radial flow (IARF) and bounded radial flow (BRF) under fixed BHP drawdown. Bounded radial flow model consists of two flow regimes: infinite acting radial flow during early time and boundary dominated flow during late time. Different superposition times are calculated based on six models as listed in Table 3.6. Note that superposition time given by boundary dominated flow (BDF) is material balance time and we are going to test its performance as a general approximation of superposition time.

The comparisons are displayed in Figure 3.21 and Figure 3.22 for infinite acting radial flow and bounded radial flow, respectively. Again, the boundary dominated flow (BDF) model gives material balance time (t_e) while the remaining models yield superposition time (t_s) for the corresponding flow geometries. To better illustrate material balance time as an approximation to superposition time, BDF model together with a reference model are extracted from subplot (b) and plotted again in subplot (a). In both cases, x-axis is the actual superposition time of the given flow regime, while y-axis is the superposition time calculated by various models. In Figure 3.21 (a), we observe that t_e (purple curve) is very close to the unit-slope black-dashed line with an accumulating derivation w.r.t. time, indicating that it generally serves as a good approximation of t_s for IARF, especially during early period. On the contrary, t_s from BRF (light blue curve) has an exact match with black-dashed line during infinite acting period and a large deviation when boundary dominated flow establishes, which is definitely not a good representative

of t_s for IARF. The advantage of using t_e as an approximation instead of wrongly choosing another flow geometry to calculate t_s is more obvious in Figure 3.21 (b), where we can see a large deviation between t_s from the wrong models and the black-dashed line only except for t_e from BDF (purple curve). Similarly, in Figure 3.22 (a), we observe that t_e (purple curve) is very close to the unit-slope black-dashed line especially during boundary dominated flow period, indicating that it generally serves as a good approximation of t_s for BRF. On the contrary, t_s from IARF (red curve) has an exact match with black-dashed line during infinite acting period and a large deviation from the black-dashed line when boundary dominated flow establishes, which is definitely not a good representative of t_s for BRF. Again, the advantage of using t_e as an approximation instead of wrongly choosing another flow geometry to calculate t_s is more obvious in Figure 3.22 (b), where we can see a large deviation between t_s from the wrong models and the black-dashed line only except for t_e from BDF (purple curve). Therefore, using t_e instead of t_s is a safe and sufficiently accurate approach for production analysis, especially when we are uncertain about the flow geometry and observe a clear signal of boundary dominated flow from production data.

Superposition Time Model	Abbreviation
Boundary Dominated Flow	BDF
Bounded Radial Flow	BRF
Infinite Acting Linear Flow	IALF
Infinite Acting Radial Flow	IARF
Infinite Acting Spherical Flow	IASF
Infinite Conductivity Fracture	ICF

Table 3.6 Summary of the superposition time models and the corresponding abbreviations



(a) BDF and BRF

(b) All Models

Figure 3.21 Comparison between superposition time calculated by various models and the actual superposition time for infinite acting radial flow (reprinted with permission from Wang et al, 2017)

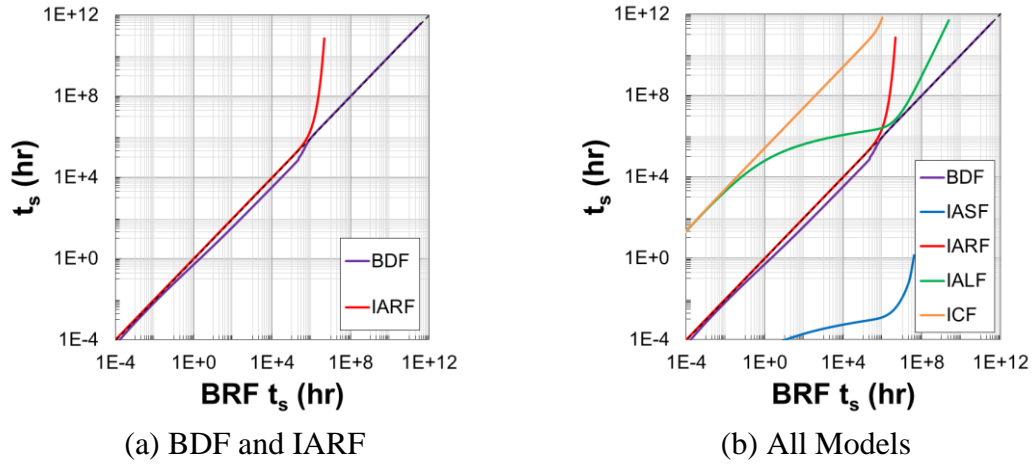


Figure 3.22 Comparison between superposition times calculated by various models and the actual superposition time for bounded radial flow (reprinted with permission from Wang et al, 2017)

3.2.4.4 Comparison of Asymptotic Approximation and Models Using Superposition and Material Balance Time

As mentioned earlier, the multiple-term asymptotic approximation should be able to solve problem with any kind of inner boundary conditions, e.g., variable rate drawdown. By combining Eqs. (3.32) and (2.58), we may obtain the expression for rate normalized pressure drop at any location within the reservoir below.

$$RNP(\tau, t) = \frac{\Delta p(\tau, t)}{q_{sf}(t)} = \frac{\sum_{n=0}^{\infty} A_n(t) \{W_n(t) - W_n(\tau, t)\}}{c_i \sum_{n=0}^{\infty} A_n(t) V_n(t)} \quad (3.68)$$

Taking fixed BHP drawdown as an example, we know that $A_1(t)$ is the only nonzero term and Eq. (3.68) can be further simplified.

$$RNP(\tau, t) = \frac{A_1(t) \{W_1(t) - W_1(\tau, t)\}}{c_i A_1(t) V_1(t)} = \frac{1}{c_i} \frac{W_1(t) - W_1(\tau, t)}{V_1(t)} \quad (3.69)$$

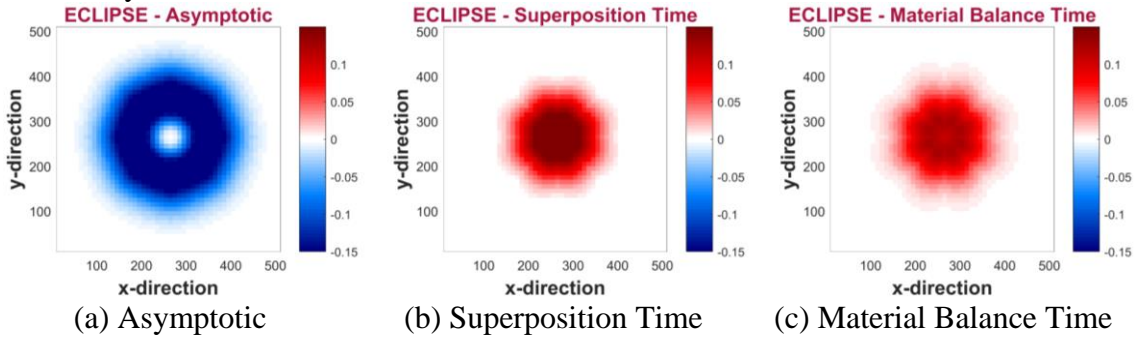
Property	Value	Unit
Grid size	10×10×10	<i>ft</i> ³
Grid number	51×51×1	
<i>h</i>	10	<i>ft</i>
ϕ	0.3	-
<i>k</i>	0.5	<i>md</i>
μ	1.0	<i>cp</i>
<i>c_t</i>	1×10 ⁻⁵	<i>psi</i> ⁻¹
<i>B</i>	1.0	<i>rb/bbl</i>
<i>r_w</i>	0.5	<i>ft</i>
<i>x_f</i>	55	<i>ft</i>
Δp_{wf}	4500	<i>psi</i>

Table 3.7 Reservoir, fluid and wellbore parameters for homogeneous radial flow with a fixed BHP drawdown in a rectangular reservoir

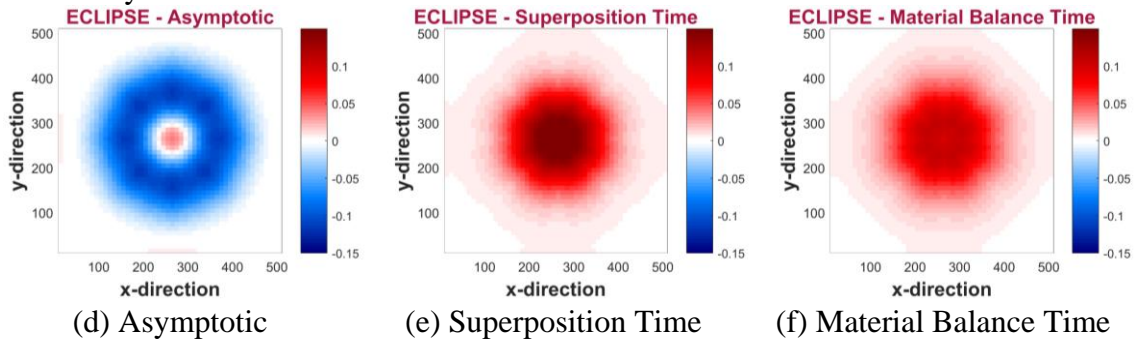
Next, I will compare the results evaluated by three models: model with fixed BHP asymptotic approximation, model using superposition time for infinite acting radial flow, and model using material balance time. The test case is chosen to be a fixed BHP drawdown in a homogeneous rectangular reservoir and the model parameters are listed in Table 3.7. Figure 3.23 illustrates the RNP time derivative difference between ECLIPSE and the three models and Figure 3.24 displays the direct comparisons with cross plots. From these results, we observe that material balance time has a little bit worse but close performance as superposition time. They successfully capture the pressure front propagation generated by a fixed BHP production well. When BDF occurs, the accuracy of their RNP prediction decreases faster than the asymptotic approximation, while the latter will still yield a relatively more accurate RNP time derivative distribution. Generally

speaking, our asymptotic approximation has the best performance among the three models.

$t = 2.0$ days:



$t = 2.8$ days:



$t = 4.5$ days:

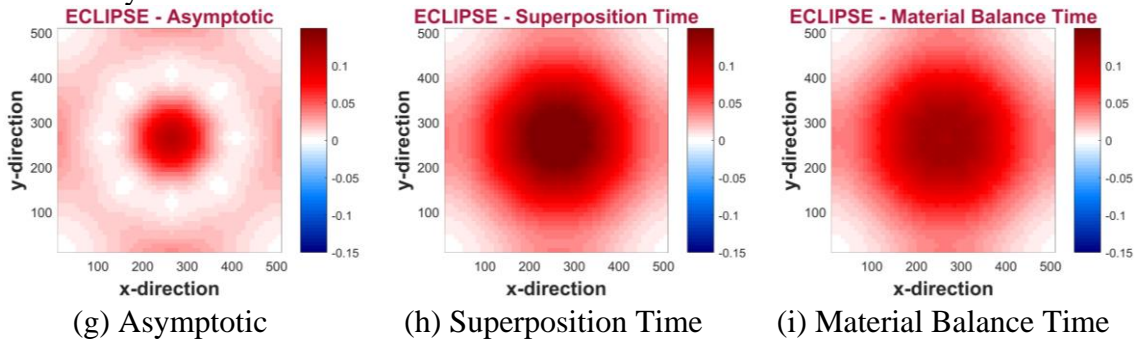
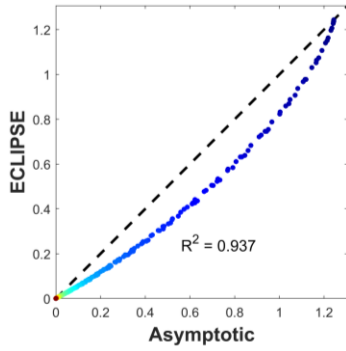
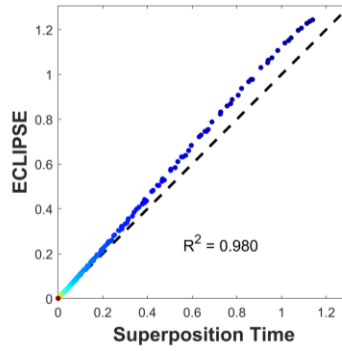


Figure 3.23 Comparison of difference of RNP time derivative between ECLIPSE and models using asymptotic, superposition time, and material balance time solutions for fixed BHP drawdown at various times (reprinted with permission from Wang et al, 2017)

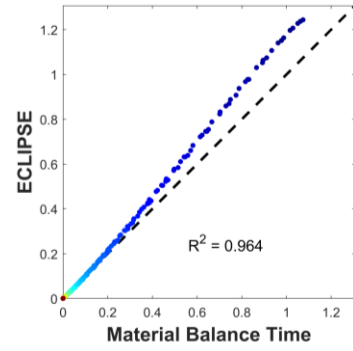
t = 2.0 days:



(a) Asymptotic

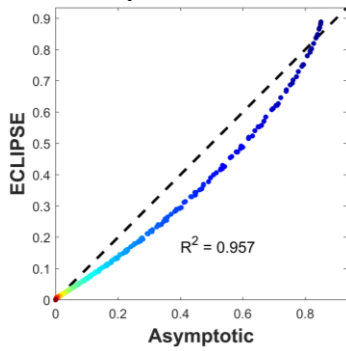


(b) Superposition Time

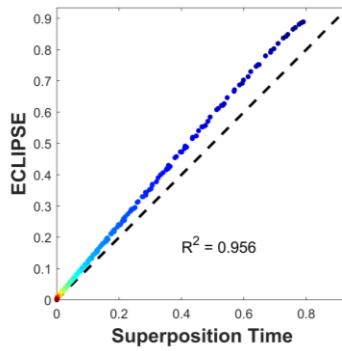


(c) Material Balance Time

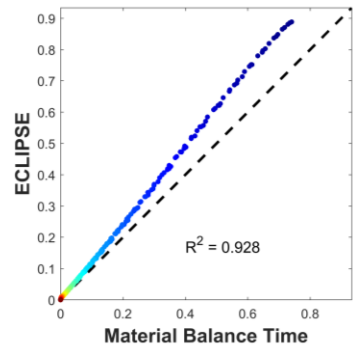
t = 2.8 days:



(d) Asymptotic

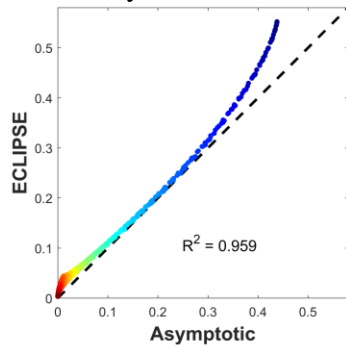


(e) Superposition Time

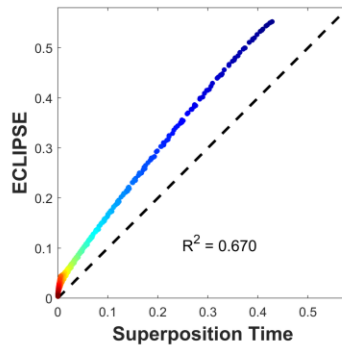


(f) Material Balance Time

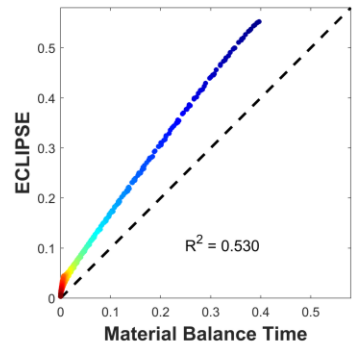
t = 4.5 days:



(g) Asymptotic



(h) Superposition Time



(i) Material Balance Time

Figure 3.24 Cross plots of RNP time derivative between ECLIPSE results vs. models using asymptotic, superposition time, and material balance time solutions for fixed BHP drawdown at various times (reprinted with permission from Wang et al, 2017)

3.3 Methodology: Extension to Bounded Reservoirs

In this section, we will discuss how the no-flow outer boundary affects our solution and how the asymptotic approximation may be generalized to solve this problem. Let's begin the discussion with a very simple but informative model, i.e., a multiple-well case, as an example to illustrate the performance of the asymptotic approximation in handling well interference. I will then use a composite reservoir to illustrate how to deal with the pressure front reflection and transmission at the interface of different media. Finally, bounded reservoir models will be investigated to see how the Fetkovich Type Curves will arise as a special case of our approach.

3.3.1 Superposition in Space

3.3.1.1 Multiple-Well Drainage Volumes

In the presence of multiple wells, e.g., two wells in an infinite homogeneous reservoir as shown in Figure 3.25, the asymptotic approximation can be further extended based on superposition in space.

$$\Delta p(\bar{x}, t) = \Delta p_1(\tau_1, t) + \Delta p_2(\tau_2, t) \quad (3.70)$$

Take the derivative w.r.t time, we obtain that:

$$\frac{\partial \Delta p(\bar{x}, t)}{\partial t} = \frac{\partial \Delta p_1(\tau_1, t)}{\partial t} + \frac{\partial \Delta p_2(\tau_2, t)}{\partial t} \quad (3.71)$$

The leading order asymptotic approximation for fixed rate drawdown for each well gives:

$$c_i \frac{\partial \Delta p(\bar{x}, t)}{\partial t} = \frac{q_{w1} \Theta(t - t_{p1})}{V_{01}(t - t_{p1})} e^{-\tau_1^2/4(t - t_{p1})} + \frac{q_{w2} \Theta(t - t_{p2})}{V_{02}(t - t_{p2})} e^{-\tau_2^2/4(t - t_{p2})} \quad (3.72)$$

where, V_{01} and V_{02} represent the drainage volume V_0 of Well-1 and Well-2, respectively.

Evaluating the expression at Well-1 ($t > t_{p1}$), we obtain:

$$\frac{1}{V_{d1}(t-t_{p1})} \equiv \frac{c_t}{q_{w1}} \frac{d\Delta p(\vec{x}_1, t)}{dt} = \frac{1}{V_{01}(t-t_{p1})} + \frac{q_{w2}}{q_{w1} V_{02}(t-t_{p2})} e^{-\tau_{12}^2/4(t-t_{p2})} \quad (3.73)$$

Similarly, evaluating the expression at Well-2 ($t > t_{p2}$), we get:

$$\frac{1}{V_{d2}(t-t_{p2})} \equiv \frac{c_t}{q_{w2}} \frac{d\Delta p(\vec{x}_2, t)}{dt} = \frac{q_{w1}}{q_{w2} V_{01}(t-t_{p1})} e^{-\tau_{12}^2/4(t-t_{p1})} + \frac{1}{V_{02}(t-t_{p2})} \quad (3.74)$$

where, V_{d1} and V_{d2} are the well drainage volumes obtained for each well individually.

With these analytic solutions, we can calculate total drainage volume and distinguish the contribution of each individual well easily.

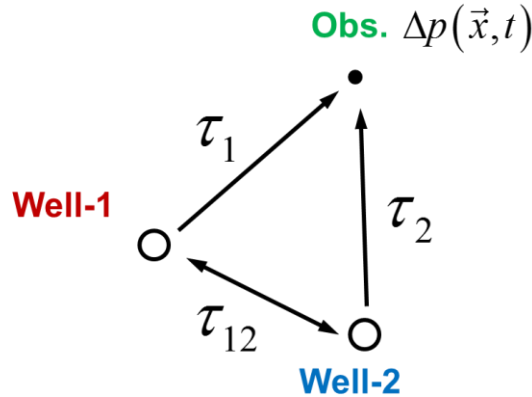


Figure 3.25 Illustration of a two-well interference problem (reprinted with permission from Wang et al, 2017)

Two-Well Interference Case To demonstrate the proposed expressions for multiple-well drainage volumes, I choose a two-well interference case and the homogeneous reservoir, fluid and wellbore parameters are listed in Table 3.8. As shown

in Figure 3.26, two vertical producers are 550 ft away from each other ($\tau_{12} = L_{12}/\sqrt{\alpha} = 117.6 \text{ hr}^{1/2}$) and they have different production schemes: Well-1 starts producing at the beginning with a constant production rate and Well-2 will be opened for production 5 days later with a rate 4 times larger than Well-1. Simulation stops before the pressure front reaches the reservoir boundary, so the entire production is under infinite acting radial flow

Drainage volumes of each individual well obtained from asymptotic solutions as well as ECLIPSE simulation results are shown in Figure 3.27. The ECLIPSE drainage

volume is estimated by $\frac{1}{V_d(t)} \equiv \frac{c_i}{q_w} \frac{d\Delta p_{wf}}{dt}$. From the subplots (a) and (b), we observe that

the drainage volume of the producers match well with ECLIPSE results in both log-log scale and linear-linear scale plots. Another observation is that well interference occurs at around $t = 40 \text{ days}$, when the drainage volume of Well-1 increases slower than before in subplot (b). This time matches with the time of limit of detectability when pressure front from Well-2 arrives at Well-1 which can be estimated as $t = t_1 + t_{LOD} = t_1 + \tau_{12}^2/16 = 41 \text{ days}$.

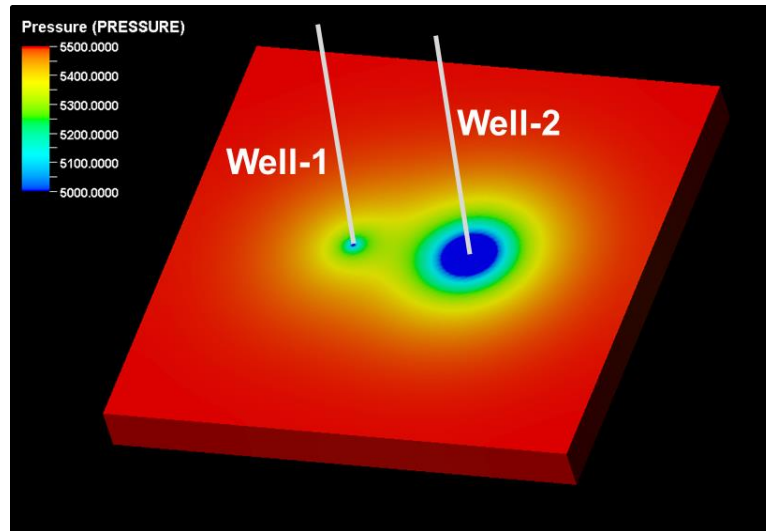
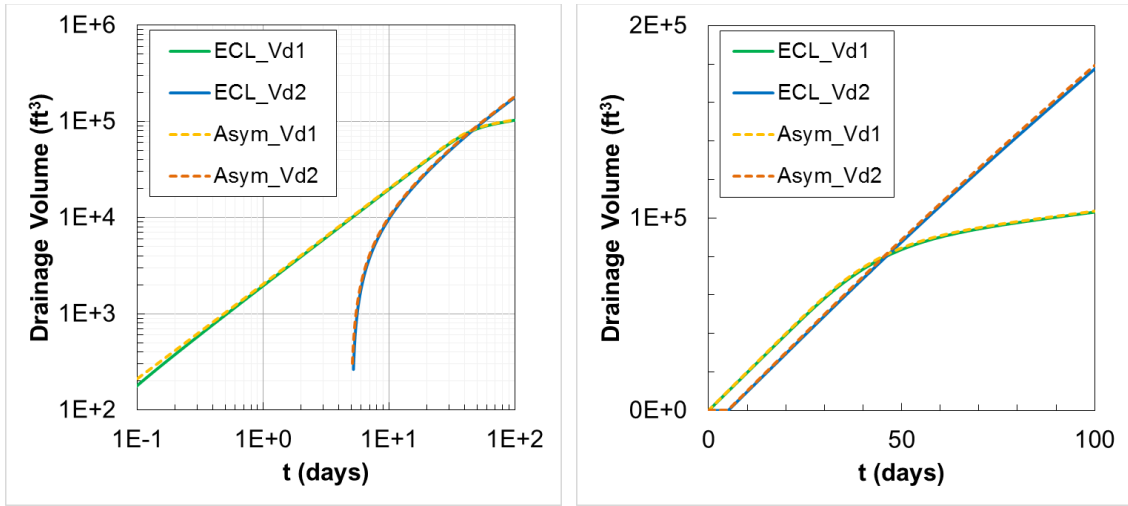


Figure 3.26 Illustration of the pressure distribution during well interference (pressure distribution at $t = 40$ days) of a two-well model

Property	Value	Unit
Grid size	$5.5 \times 5.5 \times 10$	ft^3
Grid number	$399 \times 399 \times 1$	
h	10	ft
ϕ	0.03	-
k	0.005	md
μ	0.2	cp
c_i	1×10^{-5}	psi^{-1}
B	1.0	rb/bbl
r_w	0.5	ft
q_{w1}	0.3	bbl/day
t_{p1}	0	day
q_{w2}	1.2	bbl/day
t_{p2}	5	day

Table 3.8 Reservoir, fluid and wellbore parameters for a two-well model



(a) Log-Log Scale

(b) Linear-Linear Scale

Figure 3.27 Comparison of fixed rate drawdown solutions in a bounded reservoir: asymptotic solutions (dash) with reference solutions (solid) in (a) log-log scale and (b) linear-linear scale

3.3.2 Generalized Asymptotic Solution to Bounded Reservoirs

In the discussion of the validity of the asymptotic pressure approximation we noted

that $w(\tau)$ should be sufficiently smooth and bounded: $\left(\frac{d \ln w(\tau)}{d \ln \tau}\right) \geq 0$. However, for

calculations with finite reservoirs $w(\tau)$ may decrease with τ as the reservoir boundary is reached. For examples where $V_p(\tau)$ and $w(\tau)$ are calculated by the FMM, or for composite reservoirs, they need not be smooth. In these cases we need to extend the form of the asymptotic pressure approximation.

3.3.2.1 Spatial Discontinuities

The exponential in Eq. (3.27) represents a pressure front moving outwards from the producing well, causing depletion in the reservoir. In electromagnetic wave

propagation, this corresponds to a transmitted front which is refracted through the medium (Jackson, 1998). A more complete solution should also consider reflection. In general, reflection from sharp changes in material properties are one of the instances where the transverse flux terms in the Darcy velocity are no longer negligible. However, we will restrict our current analysis to situations where the material changes are assumed to lie along τ contours, in other words, $w(\tau)$ may be discontinuous.

At a material boundary, the pressure and the normal component of the velocity must be continuous. We may express the continuity requirements in terms of pressure and flux, although it is simpler for us to work with the continuity of their time derivatives.

$$\left[\frac{\partial p}{\partial t} \right] = 0 \quad \text{and} \quad \left[\frac{\partial q}{\partial t} \right] = 0 \quad \text{where} \quad [] = \text{discontinuity} \quad (3.75)$$

For a two-domain problem in an infinite reservoir, the fundamental equation has now been modified.

$$c_t \frac{\partial p(\tau, t)}{\partial t} = \frac{1}{w(\tau)} \frac{\partial q(\tau, t)}{\partial \tau} \approx -\frac{q_w}{V(t)} \begin{cases} e^{-\tau^2/4t} + R \cdot e^{-(2\tau_d - \tau)^2/4t} & \tau \leq \tau_d \\ T \cdot e^{-\tau^2/4t} & \tau > \tau_d \end{cases} \quad (3.76)$$

Here, R and T are reflection and transmission coefficients, respectively, and τ_d is the DTOF at the discontinuity in $w(\tau)$. From Darcy's flux, we may also calculate the time derivative of the flux.

$$\begin{aligned} \frac{\partial q(\tau, t)}{\partial t} &= w(\tau) \frac{\partial}{\partial \tau} \left(c_t \frac{\partial p(\tau, t)}{\partial t} \right) \\ &\approx \frac{q_w}{2tV(t)} \begin{cases} w(\tau) \cdot \left\{ \tau \cdot e^{-\tau^2/4t} - (2\tau_d - \tau) \cdot R \cdot e^{-(2\tau_d - \tau)^2/4t} \right\} & \tau \leq \tau_d \\ w(\tau) \cdot \left\{ T \cdot \tau \cdot e^{-\tau^2/4t} \right\} & \tau > \tau_d \end{cases} \end{aligned} \quad (3.77)$$

Note that the functional form of the reflected front has been chosen so that $e^{-(2\tau_d - \tau)^2/4t} = e^{-\tau^2/4t}$ at the discontinuity. The two continuity requirements determine R and T .

$$\begin{aligned} \left[\frac{\partial p}{\partial t} \right] = 0 &\Rightarrow 1 + R = T \\ \left[\frac{\partial q}{\partial t} \right] = 0 &\Rightarrow w_{Left} \cdot (1 - R) = w_{Right} \cdot (T) \end{aligned} \quad (3.78)$$

$$R = \frac{w_{Left} - w_{Right}}{w_{Left} + w_{Right}} \quad T = \frac{2w_{Left}}{w_{Left} + w_{Right}} \quad (3.79)$$

The reflection coefficient varies between -1 and +1. The transmission coefficient is bounded between 0 and 2, and is always positive. For smooth properties, $R = 0$ and $T = 1$.

The formulation has an intuitive interpretation, as shown in Figure 3.28. The outwardly moving transmitted front originates at $\tau = 0$, while the second exponential may be interpreted as a backwards moving front propagating from $\tau = 2\tau_d$. Although the amplitude of the outwards moving front may be modified at a material boundary, its contribution to the pressure drop always remains positive. In contrast, the reflected front may interfere either constructively or destructively with the transmitted front. For instance, to model a constant pressure boundary at $\tau = \tau_d$, we have $\frac{\partial p}{\partial t} = 0$ and $R = -1$. The reflected front acts like an injector and maintains the boundary pressure. In contrast, to model a constant no flow boundary at $\tau = \tau_d$, we have $\frac{\partial q}{\partial t} = 0$ and $R = +1$. The reflected front now enhances the pressure drop. The two-domain formulation has essentially introduced variable strength image wells into the solution.

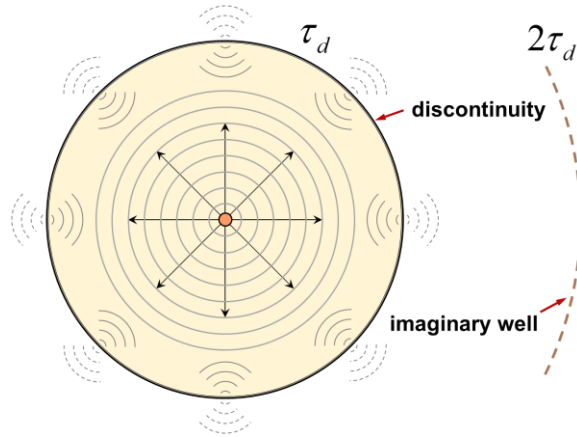


Figure 3.28 Illustration of the pressure front interaction at the interface between porous media (reprinted with permission from Wang et al, 2017)

From Eq. (3.76) we can evaluate the pressure drop at the wellbore. We have a second transient within the inner region which initially vanishes at the wellbore but which will eventually impact the measured pressure drop. This serves to re-define the drainage volume, $V_d(t)$, which in this case is related to but is not equal to $V(t)$.

$$\frac{1}{V_d(t)} \equiv \frac{c_t}{q_w} \frac{d\Delta p_{wf}(t)}{dt} = \frac{c_t}{q_w} \frac{d\Delta p(0,t)}{dt} \approx \frac{1}{V(t)} \left\{ 1 + R \cdot e^{-\tau^2/t} \right\} \quad (3.80)$$

We also must revise the expression for $V(t)$.

$$\begin{aligned} V(t) &= \int_{\tau=0}^{\tau_d} d\tau w(\tau) \left\{ e^{-\tau^2/4t} + R \cdot e^{-(2\tau_d - \tau)^2/4t} \right\} + \int_{\tau=\tau_d}^{\infty} d\tau w(\tau) \left\{ T \cdot e^{-\tau^2/4t} \right\} \\ &= \int_{\tau=0}^{\tau_d} d\tau \left\{ w(\tau) \right\} \cdot e^{-\tau^2/4t} + \int_{\tau=\tau_d}^{2\tau_d} d\tau \left\{ R \cdot w(2\tau_d - \tau) \right\} \cdot e^{-\tau^2/4t} \\ &\quad + \int_{\tau=\tau_d}^{\infty} d\tau \left\{ T \cdot w(\tau) \right\} \cdot e^{-\tau^2/4t} \end{aligned} \quad (3.81)$$

This follows from the flux integral. We will examine the resulting estimate of the drainage volume as part of the discussion of bounded reservoirs, below.

We now have two implementations of the asymptotic pressure approximation. If $w(\tau)$ is sufficiently smooth and not decreasing, then we may utilize the single domain formulation. Otherwise, the two-domain implementation will capture the contributions from the backwards moving front. This methodology can be extended to multiple large changes in $w(\tau)$, however, in that case, the multiple jumps interact and the reflection and transmission coefficients become time dependent. In such a case it is recommended to use a numerical solution for the diffusivity equation instead of the asymptotic approximation.

3.3.2.2 Composite Reservoirs

Radially composite reservoirs arise in a number of field situations where the change of diffusivity is usually due to fluid or formation damage effects. Examples include heavy oil water injection, gas condensates, or a near-well “thick skin” region of formation damage (Muskat, 1949; Hawkins, 1956; Satman *et al.*, 1980; Gringarten *et al.*, 2000). In the following we test our solutions and utilize the solutions (numerical inverse Laplace transform) of Satman *et al.* (1980) for heavy oil water injection as the reference solutions.

The calculations are performed for radial flow with a fixed rate drawdown and a finite wellbore radius, $V_p = \pi(r^2 - r_w^2)h\phi$. We define the mobility ratio, M , as the ratio of the permeability in the inner region to the outer region, which will also be the ratio of inner to outer diffusivity, $\alpha_i = M \cdot \alpha$. In the inner region, $\frac{d\tau}{dr} = \frac{1}{\sqrt{\alpha_i}}$, while in the outer region, $\frac{d\tau}{dr} = \frac{1}{\sqrt{\alpha}}$. Hence, in the notation of the composite solution above,

$w_{Left} = \sqrt{M} \cdot w_{Right}$, to give the following expressions for the reflection and transmission coefficients.

$$R = \frac{\sqrt{M} - 1}{\sqrt{M} + 1} \quad T = \frac{2\sqrt{M}}{\sqrt{M} + 1} \quad (3.82)$$

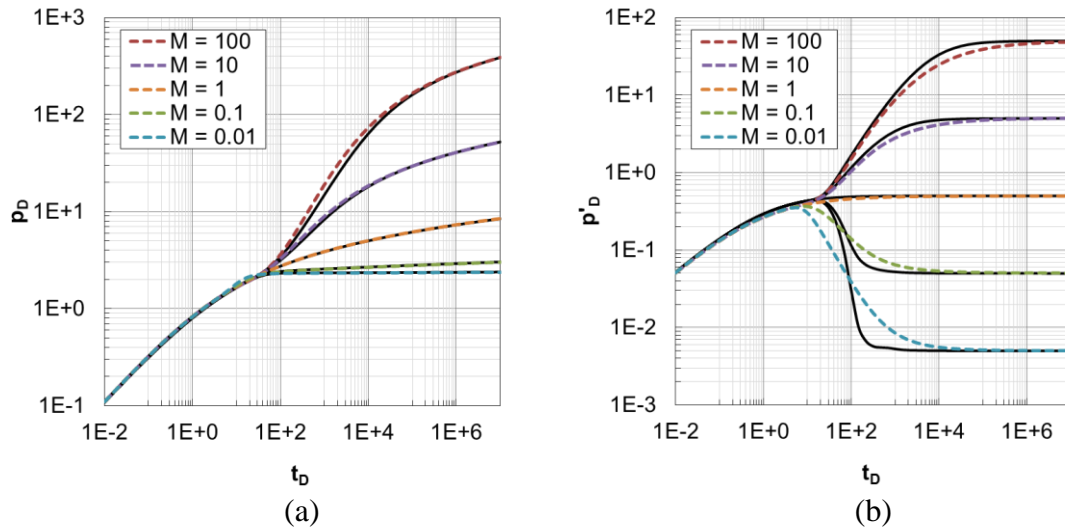


Figure 3.29 Comparison of composite reservoir solutions (dash) with reference solutions (solid), dimensionless with respect to the inner region properties (reprinted with permission from King et al., 2016)

The solutions have been described in the section on composite reservoirs, above. The comparison with the reference solutions are in Figure 3.29 and Figure 3.30. Overall the solutions show good agreement. The timing of the transition from inner to outer is well captured. Generally the solutions for $M > 1$, corresponding to reduced permeability in the outer region, are better than the solutions for $M < 1$. This may indicate that our current methodology is better at representing no flow boundaries than constant pressure boundaries.

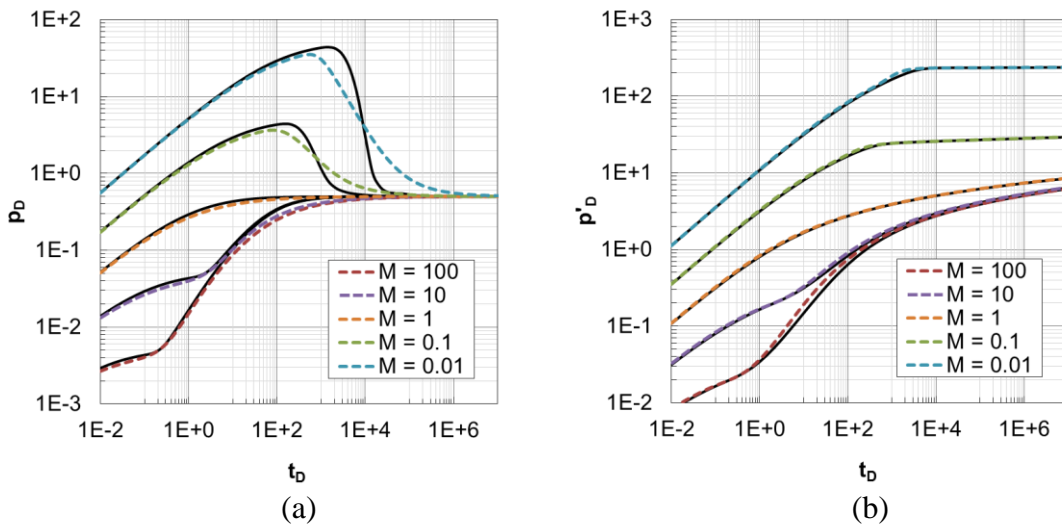


Figure 3.30 Comparison of composite reservoir solutions (dash) with reference solutions (solid), dimensionless with respect to the outer region properties (reprinted with permission from King et al., 2016)

In Figure 3.29, where the solutions are referenced to the inner region properties, the early time solutions are independent of M , and they are identical to infinite acting radial flow. Once the pressure front reaches the region boundary, three cases arise. If $M = 1$, there is no change in properties. The solution continues to follow the infinite acting radial flow. Otherwise, when $M > 1$ we have a reduction of permeability in the outer region, and the pressure drop increases relative to $M = 1$. The welltest derivatives are perhaps more informative; at late time they show the signature of infinite acting radial flow but now for a decreased permeability. The opposite trend is seen for $M < 1$. The timing of the transition from inner to outer region is identical in each calculation, as expected, since the time of propagation of the reflected front depends solely upon inner

region properties $\left(p_D = \frac{2\pi k_i h \Delta p}{q_w \mu B}, t_D = \frac{k_i t}{\phi \mu c_t r_w^2} \right)$. In Figure 3.30, the same data is plotted,

but now made dimensionless with respect to the outer region properties

$\left(p_D = \frac{2\pi kh\Delta p}{q_w \mu B}, t_D = \frac{kt}{\phi \mu c_i r_w^2} \right)$. For instance, this is how a thick region of skin would be

analyzed. Comparison of the pressure drops show that for $M < 1$ we have positive skin, and negative skin for $M > 1$, as expected.

3.3.2.3 Bounded Reservoirs and Generalized Drainage Volume

Fixed rate drawdown in a finite bounded reservoir is a special case of the composite reservoir with a no flow boundary at $\tau = \tau_{res}$, i.e., for $R = 1$. The reference for this calculation follows Van Everdingen and Hurst (1949).

Figure 3.31 demonstrates excellent consistency with the reference solution. In these plots the reference solutions are the solid lines and the asymptotic pressure approximation are the dashed lines. Figure 3.31 (a) and (b) are plots of the pressure drop and the welltest derivative, respectively. The size of the reservoir, $r_{eD} = r_{res}/r_w$, is made dimensionless with respect to the wellbore radius. Time is made dimensionless with respect to the wellbore area, r_w^2 . A value of $r_{eD} = 10$ is an exceptionally small reservoir, and the solution rapidly transitions from a finite wellbore radius ($solution \sim \sqrt{t}$) to boundary dominated flow ($solution \sim t$). The period of the transition beyond infinite acting radial flow is best observed in the welltest derivative, Figure 3.31 (b). At a value of $r_{eD} = 10^5$ there is a clear period of radial flow before the onset of boundary dominated flow.

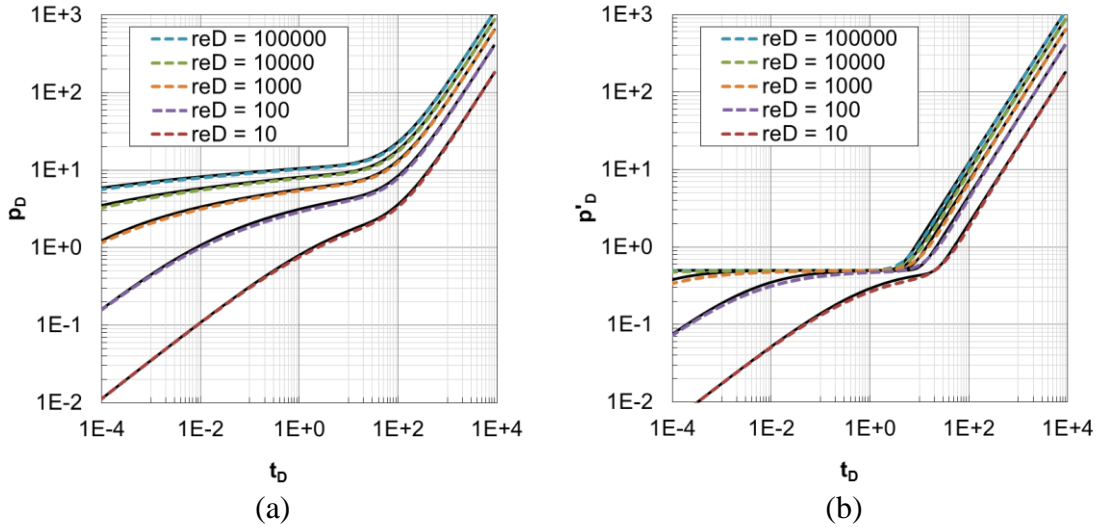


Figure 3.31 Comparison of fixed rate drawdown solutions in a bounded reservoir: asymptotic solutions (dash) with reference solutions (solid) (reprinted with permission from King et al., 2016)

The bounded reservoir case also provides insight as to the calculation of the drainage volume. If we return to Eq. (3.77) for the flux derivative in a composite reservoir, we have two terms corresponding to the outwardly and inwardly directed fronts. The contribution from the outwardly directed front is proportional to τ , and so we may consistently impose a fixed rate drawdown at the well, $\tau = 0$. However, the reflected front is proportional to $(2\tau_{res} - \tau)$. Once the reflected exponential becomes appreciable, the equations no longer support a fixed rate. This may be resolved through the use of an additional image well, this one located at $\tau = -2\tau_{res}$. This additional delayed outward front will cancel the reflection at the wellbore, but it itself will need to be cancelled at the outer no flow boundary. As a consequence we now have an infinite series of image wells.

$$e^{-\tau^2/4t} \rightarrow e^{-\tau^2/4t} + e^{-(2\tau_{res}-\tau)^2/4t} + e^{-(\tau+2\tau_{res})^2/4t} + \dots \quad (3.83)$$

This changes the definitions for $V(t)$ and for the drainage volume, $V_d(t)$.

$$V(t) = \int_{\tau=0}^{\tau_{res}} d\tau w(\tau) \left\{ e^{-\tau^2/4t} + e^{-(2\tau_{res}-\tau)^2/4t} + e^{-(\tau+2\tau_{res})^2/4t} + \dots \right\} \quad (3.84)$$

$$V_d(t) = V(t) / \left\{ 1 + 2e^{-\tau_{res}^2/t} + \dots \right\}$$

If we extend the definition of $w(\tau)$ beyond $\tau = \tau_{res}$, then we may simplify the expression for $V(t)$.

$$w(\tau) = w(2\tau_{res} - \tau) \quad \tau_{res} < \tau \leq 2\tau_{res}$$

$$w(\tau) = w(\tau - 2\tau_{res}) \quad \tau > 2\tau_{res} \quad (3.85)$$

$$V(t) = V_0(t) = \int_{\tau=0}^{\infty} d\tau w(\tau) e^{-\tau^2/4t}$$

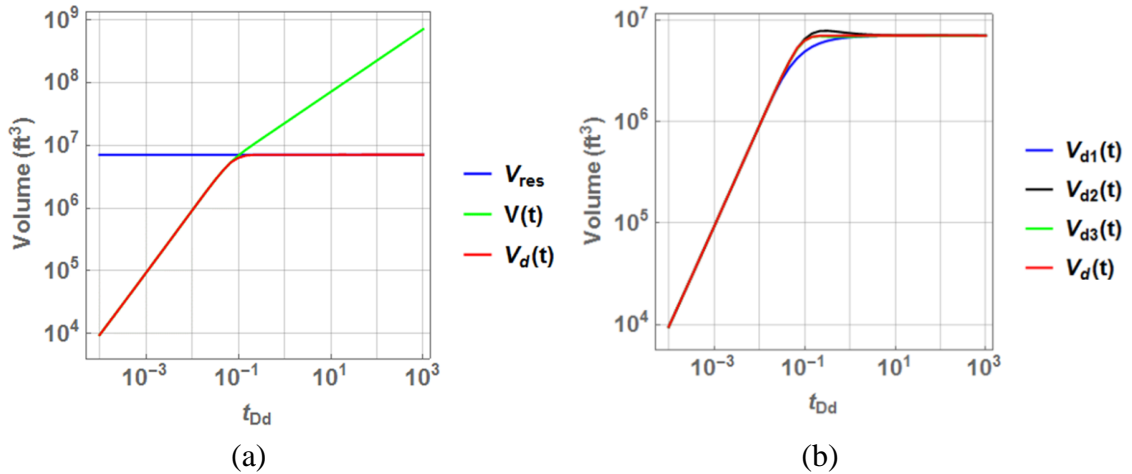


Figure 3.32 Drainage volume calculations (reprinted with permission from King et al., 2016)

Analysis shows that both $V(t)$ and the denominator in the expression for $V_d(t)$ scale as \sqrt{t} for large t , with the ratio approaching the pore volume of the reservoir. This is shown in Figure 3.32.

In Figure 3.32 (a) we plot both $V(t)$ and $V_d(t)$, Eq. (3.84), with the reservoir volume as the reference. Figure 3.32 (b) contrasts the calculation of the drainage volume from Eq. (3.84), and includes the 1, 2 and 3 term approximations. We see that the one term approximation shows the impact of the finite size of the reservoir at earlier times than the full expression. Once we reach two terms, we have a good approximation. Once we have three terms, the approximation is excellent. The second and third terms are of the same magnitude at the wellbore, and so including both terms in the drainage volume calculation provides a consistent approximation. We see that the application of an infinite series to model a bounded reservoir does not appear to be necessary.

3.3.2.4 Generalized Asymptotic Solution

We can develop additional transient asymptotic solutions that satisfy different choices of boundary conditions through the more general form as well as the time derivative of the flux following Eq. (3.77):

$$c_i \frac{\partial \Delta p}{\partial t} = -\frac{1}{w(\tau)} \frac{\partial q}{\partial \tau} \approx A(t) \cdot K(\tau, t) \quad (3.86)$$

$$\frac{\partial q}{\partial t} = w(\tau) \frac{\partial}{\partial \tau} \left(c_i \frac{\partial p}{\partial t} \right) \approx -A(t) w(\tau) \frac{\partial K(\tau, t)}{\partial \tau} \quad (3.87)$$

This allows us to provide closed form solutions for both pressure and rate transient solutions, in both infinite and bounded reservoirs. As before, the function $A(t)$ is to be determined subject to the initial and boundary conditions. Depending upon the specific boundary conditions, the equation for $A(t)$ may be algebraic or it may be an ODE. Here,

$K(\tau, t)$ is the diffusion kernel. Its form depends upon the inner and outer boundary conditions for each problem, but not the flow geometry, as summarized in Table 3.9.

$K(\tau, t)$	Infinite Domain	Bounded Reservoir: No Flow @ $\tau = \tau_{res}$
Fixed Rate @ $\tau = 0$	$e^{-\tau^2/4t}$	$e^{-\tau^2/4t} + e^{-(2\tau_{res}-\tau)^2/4t} + e^{-(2\tau_{res}+\tau)^2/4t} + \dots$
Fixed BHP @ $\tau = \tau_{wf}$	$\frac{(\tau - \tau_{wf})}{\sqrt{4t}} e^{-\frac{\tau^2}{4t}}$	$\frac{(\tau - \tau_{wf})}{\sqrt{4t}} e^{-\frac{\tau^2}{4t}} + \frac{(2\tau_{res} - \tau - \tau_{wf})}{\sqrt{4t}} e^{-\frac{(2\tau_{res} - \tau)^2}{4t}}$ $-\frac{(2\tau_{res} + \tau - 3\tau_{wf})}{\sqrt{4t}} e^{-\frac{(2\tau_{res} + \tau - 3\tau_{wf})^2}{4t}} - \dots$

Table 3.9 Diffusion kernels for different inner and outer boundary conditions

For instance, the kernel for fixed rate solutions ensures that $\partial q / \partial t = 0$ at a specific boundary. The example has already been given in Eq. (3.87) where

$$\frac{\partial q}{\partial t} = \frac{q_w w(\tau)}{V(t)} \cdot \frac{\tau}{2t} \cdot e^{-\tau^2/4t}, \text{ which must vanish at } \tau = 0, \text{ irrespective of the form of } w(\tau).$$

For bounded reservoirs with no flow outer boundaries, again $\partial q / \partial t = 0$, but now at $\tau = \tau_{res}$. The approximations to the kernels for bounded systems should always have an odd number of terms, since every pair of terms are of the same magnitude at the inner boundary, where we will measure and reference the solution. Although bounded systems require an infinite number of terms for an exact solution, the current solution methodology provides excellent approximations with the three terms shown. This is because the solution will be a ratio of infinite sums, as shown in the next examples.

Transient Analysis: Infinite Reservoirs with Fixed Rate or Fixed BHP

Drawdown The solutions for infinite reservoirs are identical to those developed above, with the trivial modifications:

$$V(\tau, t) \equiv \int_0^{\tau} d\tau' w(\tau') K(\tau', t) \quad (3.88)$$

$$V(t) \equiv V(\tau_{res}, t)$$

$$W(\tau, t) \equiv \int_{\tau_{wf}}^{\tau} \frac{d\tau'}{w(\tau')} \{V(t) - V(\tau', t)\} \quad (3.89)$$

$$W(t) \equiv W(\tau_{res}, t)$$

$$X(\tau, t) \equiv \int_{\tau_{wf}}^{\tau} d\tau' w(\tau') W(\tau', t) \quad (3.90)$$

$$X(t) \equiv X(\tau_{res}, t)$$

$$RNP_{wf}(t) \equiv \frac{\Delta p_{wf}(t)}{q_w(t)} = \frac{1}{c_t} \frac{W(t)}{V(t)} \quad (3.91)$$

$$RNP(\tau, t) \equiv \frac{\Delta p(\tau, t)}{q_w(t)} = \frac{1}{c_t} \frac{W(t) - W(\tau, t)}{V(t)}$$

Two cases arise. If we have a fixed rate drawdown, then the expression for $RNP_{wf}(t)$ predicts $\Delta p_{wf}(t)$. Alternatively, if the BHP is fixed, then we have a prediction for the decline rate, $q_w(t)$. The expression for $RNP(\tau, t)$ is useful when evaluating interference effects between multiple wells.

Transient Analysis: Bounded Reservoirs with Fixed Rate or Fixed BHP

Drawdown The bounded reservoir cases we will examine will have a no flow outer boundary at $\tau = \tau_{res}$ and either fixed rate or fixed BHP boundary conditions at the

wellbore, $\tau = 0$. Again, the solution will be expressed for an arbitrary geometry. It is very important as it demonstrates how to extend the classic transient PTA/RTA boundary dominated DCA to the transition between infinite acting and boundary dominated flow and that it does this for arbitrary geometry. However, special cases of our results correspond to Fetkovich's work on bounded radial flow (Fetkovich, 1980) and Wattenbarger's work on bounded linear flow (Wattenbarger *et al.*, 1998).

The solutions are similar to those given above. Again, we will use the outer boundary of the reservoir as the reference for the flux integration. However, since the pressure drop at the outer boundary is not known, we will instead reference the pressure drop to the bottomhole flowing pressure drop.

$$q(\tau, t) = q_w(t) \left\{ 1 - \frac{V(\tau, t)}{V(t)} \right\} \quad (3.92)$$

$$\Delta p(\tau, t) = \Delta p_{wf}(t) - \frac{q_w}{c_t} \frac{W(\tau, t)}{V(t)} \quad (3.93)$$

To solve for $\Delta p_{wf}(t)$ in an unbounded reservoir we can take the limit of this equation to large τ where $\Delta p(\tau, t) \rightarrow 0$. However, for bounded reservoirs we do not have this relationship but we can instead relate the pressure solution to the average reservoir pressure drop, which is itself related to the cumulative production and the pore volume of the reservoir.

$$\begin{aligned}\overline{\Delta p}(t) &= \frac{Q_w(t)}{c_t \cdot V_{res}} \\ Q_w(t) &= \int_{t'=0} dt' q_w(t') \\ V_{res} &= \int_{\tau=0}^{\tau_{res}} w(\tau) d\tau\end{aligned}\tag{3.94}$$

After some manipulation:

$$\Delta p_{wf}(t) = \frac{q_w}{c_t \cdot V_{res}} \left\{ t + \frac{X(t)}{V(t)} \right\}\tag{3.95}$$

There are a number of useful results we can obtain from this relationship. First, we can use this solution to provide an extension of the definition of the well productivity, J , to include the transient period before PSS or boundary dominated flow.. Just as we previously extended the definition of the drainage volume of the well from PSS to transient flow, this is a transient extension for the well productivity. This expression will reduce to a constant well productivity in the long time (BDF or PSS) limit.

$$\frac{1}{J(t)} \equiv \frac{\Delta p_{wf} - \overline{\Delta p}}{q_w} = \frac{1}{c_t \cdot V_{res}} \frac{X(t)}{V(t)}\tag{3.96}$$

These solutions have been written in the form where in the limit of infinite reservoir volume they will reduce to the previous expressions.

These last two expressions may also be combined in the form of the flowing material balance relationship.

$$\frac{q_w(t)}{J(t)} = \Delta p_{wf}(t) - \frac{Q_w(t)}{c_t \cdot V_{res}}\tag{3.97}$$

The ultimate (technical limit) recovery is obtained in the limit $q_w \rightarrow 0$ for a specified Δp_{wf} .

$$UR = \Delta p_{wf} \cdot c_t \cdot V_{res} \quad (3.98)$$

The economic limit (EUR) is obtained from the same expression with a cutoff value for q_w .

$$EUR = UR \cdot \left\{ 1 - \left(\frac{1}{J} \frac{q_w}{\Delta p_{wf}} \right)_{cutoff} \right\} \quad (3.99)$$

The general form of these solutions are applicable for either fixed rate or fixed BHP drawdown at the wellbore.

Pressure Transient Analysis: No-Flow Outer Boundary Reservoir with Fixed

Rate Drawdown This case has a fixed flow rate so that $q_w(t) = q_w$ and $Q_w(t) = q_w \cdot t$.

From Eq. (3.97) we have an algebraic solution.

$$RNP_{wf}(t) = \frac{\Delta p_{wf}(t)}{q_w} = \frac{t}{c_t \cdot V_{res}} + \frac{1}{J(t)} \quad (3.100)$$

In the long time limit $J(t) \rightarrow J_{PSS}$ and $1/RNP_{wf} \sim 1/t$, recovering the Arps $b=1$ solution (Arps, 1945). Fetkovich studied these solutions for radial flow (Fetkovich, 1980), and this is one of the cases studied by Wattenbarger for linear flow (Wattenbarger *et al.*, 1998).

It is important to return to our definition of the drainage volume. From the form of the solution to Eq. (3.86) with fixed rate drawdown, we now have a modified expression for the drainage volume.

$$\frac{1}{V_d(t)} \equiv \frac{c_t}{q_w} \frac{d\Delta p_{wf}}{dt} = \frac{K(0,t)}{V(t)} \quad \text{or} \quad V_d(t) = V(t)/K(0,t) \quad (3.101)$$

In other words, it is only after being properly normalized that $V(t)$ can be interpreted as the drainage volume. All physical quantities are expressed as rational functions involving the diffusion kernel, which is why the three term approximation to the infinite sum of the kernel is as accurate as it is. These expressions may also be evaluated in the limit of an infinite reservoir, where only a one term diffusion kernel will arise.

Rate Transient Analysis: No-Flow Outer Boundary Reservoir with Fixed BHP

Drawdown These cases have a variable flow rate so that $q_w(t) = dQ_w/dt$. From Eq. (3.97) with a fixed BHP pressure drop, we now have an ODE for the cumulative production.

$$\frac{1}{J(t)} \frac{dQ_w}{dt} + \frac{1}{c_t \cdot V_{res}} Q_w = \Delta p_{wf} \quad (3.102)$$

The solution may be expressed in terms of material balance time, t_e .

$$RNP_{wf}(t) = \frac{\Delta p_{wf}}{q_w(t)} = \frac{t_e}{c_t \cdot V_{res}} + \frac{1}{J(t)} \quad \text{where} \quad t_e = \frac{Q_w}{q_w} \quad (3.103)$$

The solution may be obtained in the long time limit where $J(t) \rightarrow J_{BDF}$ and we recover an exponential decay with decline rate of $D = \frac{J_{BDF}}{c_t \cdot V_{res}}$. This is the Arps $b=0$ solution (Arps, 1945).

This expression is closely related to the expression for the rate normalized pressure drop for a fixed rate drawdown, although the diffusion kernels are different in these two

cases. If we approximate superposition time by material balance time, then this solution provides the following approximate expression for the transient drainage volume.

$$\frac{1}{V_d(t_e)} \approx c_t \cdot \frac{dRNP_{wf}}{dt_e} = \frac{1}{V_{res}} + c_t \frac{d}{dt_e} \left(\frac{1}{J(t)} \right) \quad (3.104)$$

This correctly reduces to the pore volume of the system once the transient terms become negligible. This approach is closely related to the calculation of the welltest derivative in production analysis by Song and Ehlig-Economides (2011).

Bounded Radial Flow and Comparison to Fetkovich Type Curves Before explaining the results, let's briefly review the key features of the Fetkovich Type Curves as illustrated in Figure 3.33. The transient period (red curves on the left portion) is generated by Fetkovich using the exact solution of bounded radial flow with various reservoir sizes and the BDF period (blue curves on the right portion) is obtained through Arps' decline curves with the exponential decline curve at the leftmost and harmonic decline curve at the rightmost and the rest are all hyperbolic decline curves. The two series of dots are calculated by asymptotic approximation with fixed rate (orange dots) and fixed BHP (green dots) drawdown. We observe that the exponential decline corresponds to constant pressure drawdown while harmonic decline corresponds to constant rate drawdown, as expected. By adding additional exponential terms (reflections), we have the analytic solution which covers the entire period: transient, transition, and BDF. This means that our approach can be further used for EUR predictions.

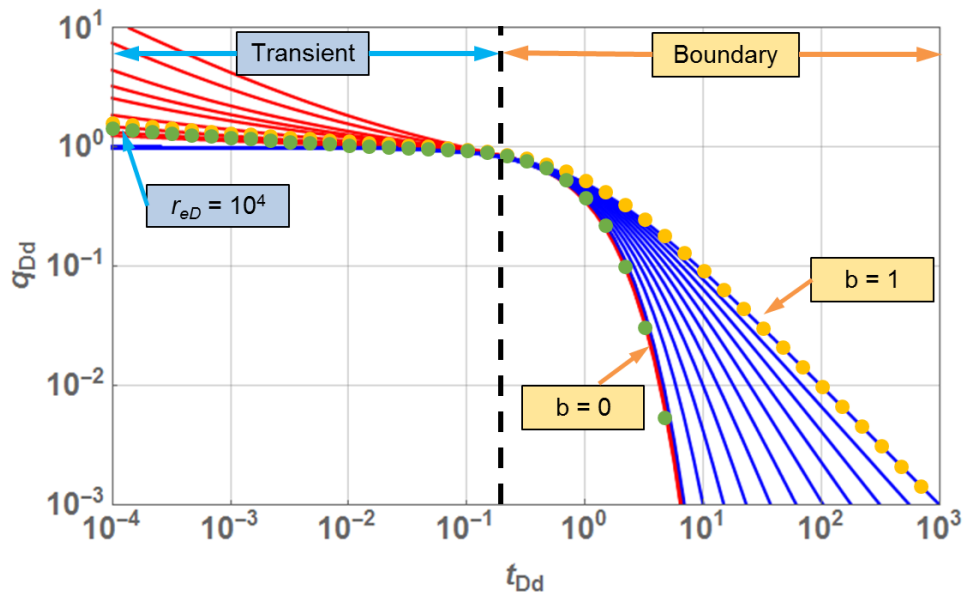


Figure 3.33 Comparison of Fetkovich Type Curve and analytic solutions (reprinted with permission from King et al., 2016)

Next, it is important to know the number of exponential terms that is necessary to obtain a sufficiently accurate result. For example, Figure 3.34 shows the comparison of using 1-exponential, 2-exponential, 3-exponential, and inf-exponential term asymptotic approximations when determining the distance to boundary for fixed rate drawdown with bounded radial flow. It is obvious that by using only one exponential term (without considering any front reflection at the outer boundary), we tend to have an earlier boundary effect as well as an underestimation of the drainage volume. If we use two exponential terms (considering one reflection at the outer boundary), the timing of the boundary effect seems fine although there will be an overshoot of the computed drainage volume during the transition period. Through comparison, three-exponential term is an excellent approximation of inf-exponential terms. Furthermore, three-exponential term also satisfies the fixed rate condition as what has discussed before.

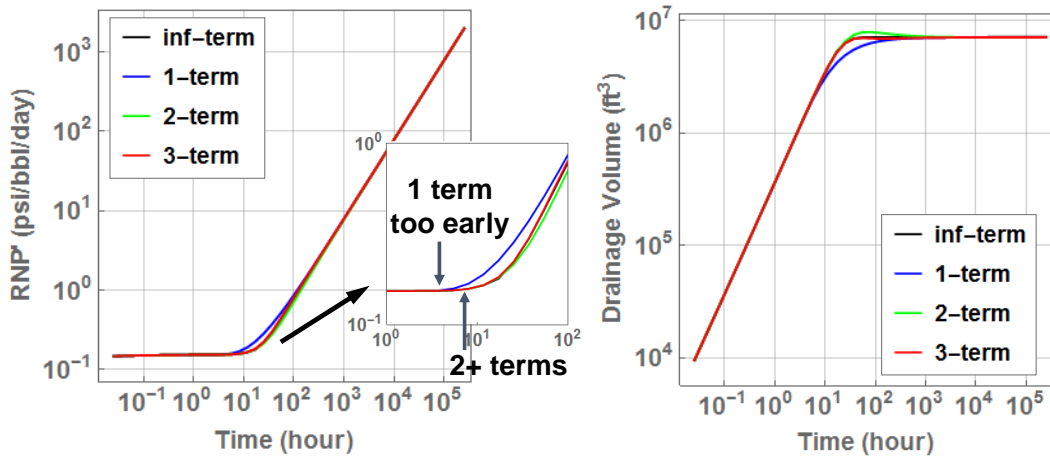


Figure 3.34 RNP' and drainage volume vs. time calculated using asymptotic 1-exponential, 2-exponential, 3-exponential, and inf-exponential term approximations for bounded radial flow (reprinted with permission from Wang et al, 2017)

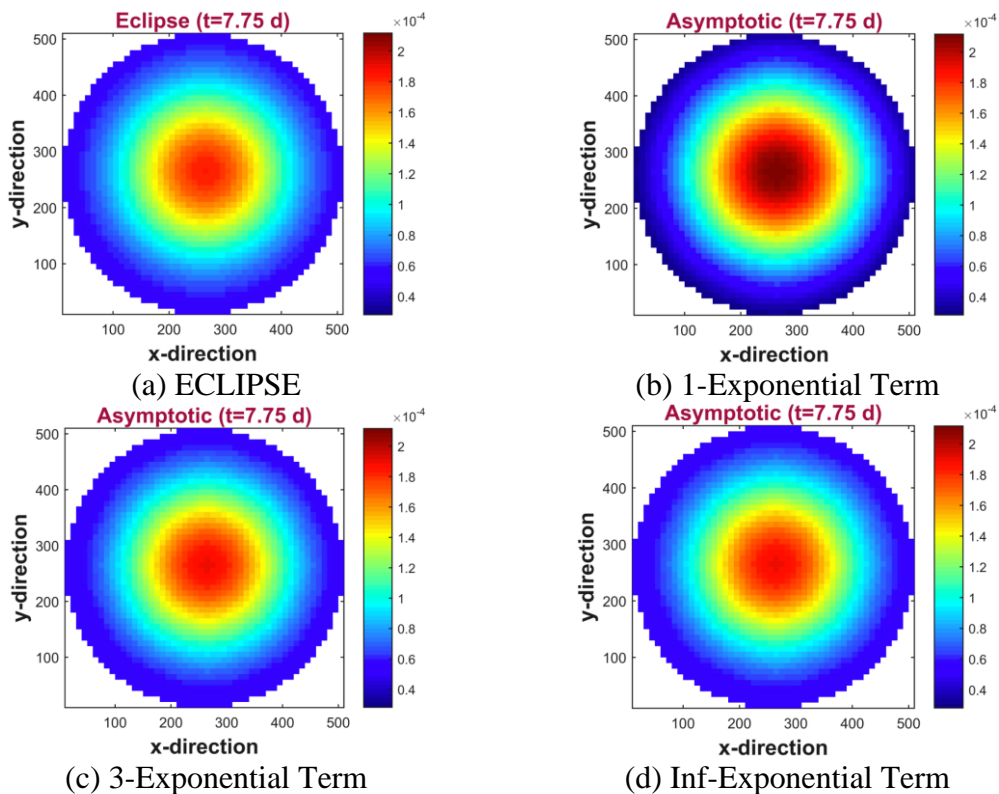


Figure 3.35 Comparison of pressure drop time derivative distribution calculated from ECLIPSE and the asymptotic 1-exponential, 3-exponential, and inf-exponential term solutions for bounded radial flow (transition period) (reprinted with permission from Wang et al, 2017)

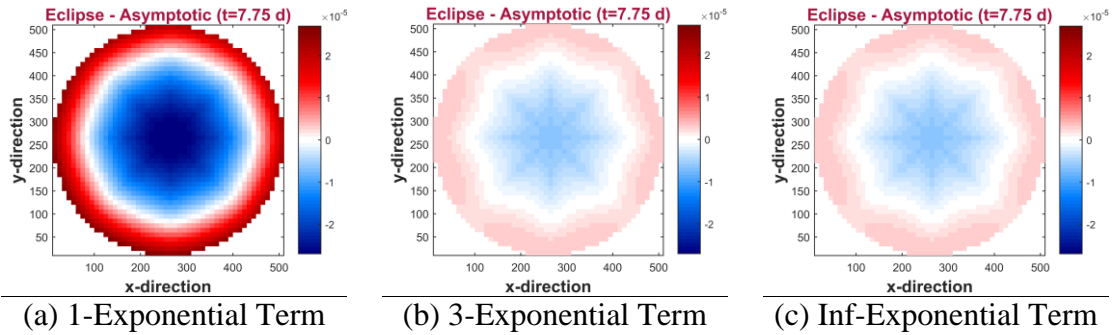


Figure 3.36 Comparison of pressure drop time derivative difference between ECLIPSE and asymptotic 1-exponential, 3-exponential, and inf-exponential term solutions for bounded radial flow (transition period) (reprinted with permission from Wang et al, 2017)

A comparison between asymptotic approximation with various terms and ECLIPSE results will provide a proof of the claims above. Figure 3.35 and Figure 3.36 show the comparison of pressure drop time derivative distribution during transition period and Figure 3.37 and Figure 3.38 display the comparison during BDF period. The observation is what has been expected, i.e., the 1-exponential term asymptotic solution has the largest deviation while inf-exponential term asymptotic solution has the smallest derivation from the ECLIPSE results during the whole simulation period. 3-exponential term solution is an excellent approximation to inf-exponential term, with small mismatch during transition period, as shown in the linear-linear scale drainage volume plot in Figure 3.39.

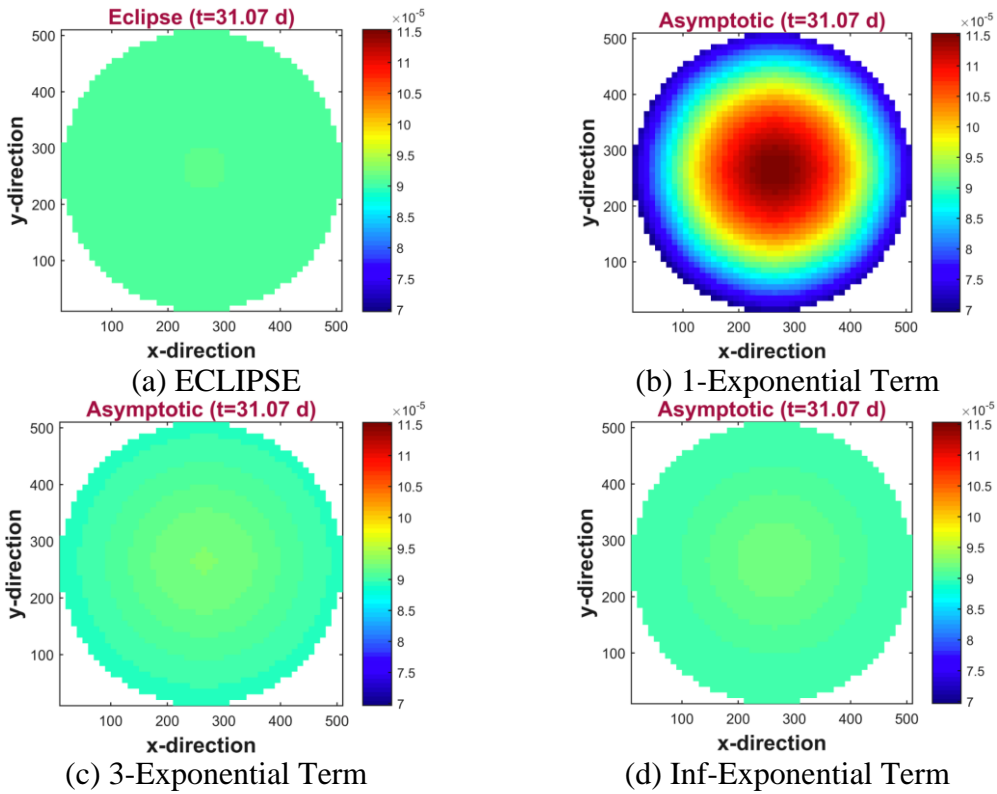


Figure 3.37 Comparison of pressure drop time derivative distribution calculated from ECLIPSE and asymptotic 1-exponential, 3-exponential, and inf-exponential term solutions for bounded radial flow (BDF period) (reprinted with permission from Wang et al, 2017)

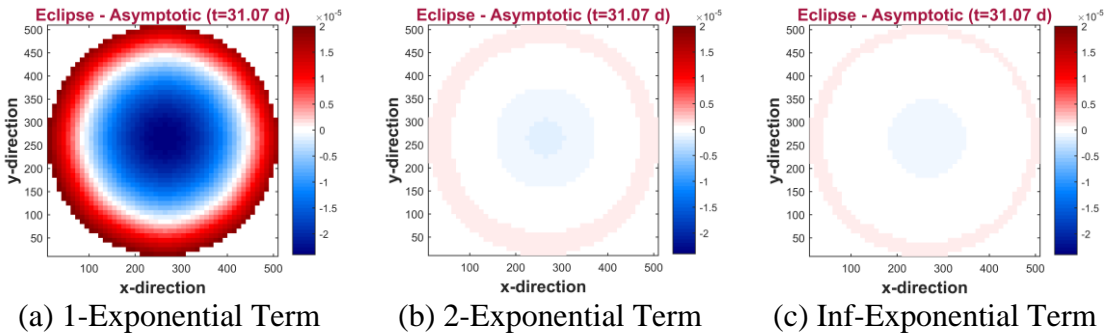


Figure 3.38 Comparison of pressure drop time derivative difference between ECLIPSE and asymptotic 1-exponential, 3-exponential, and inf-exponential term solutions for bounded radial flow (BDF period) (reprinted with permission from Wang et al, 2017)

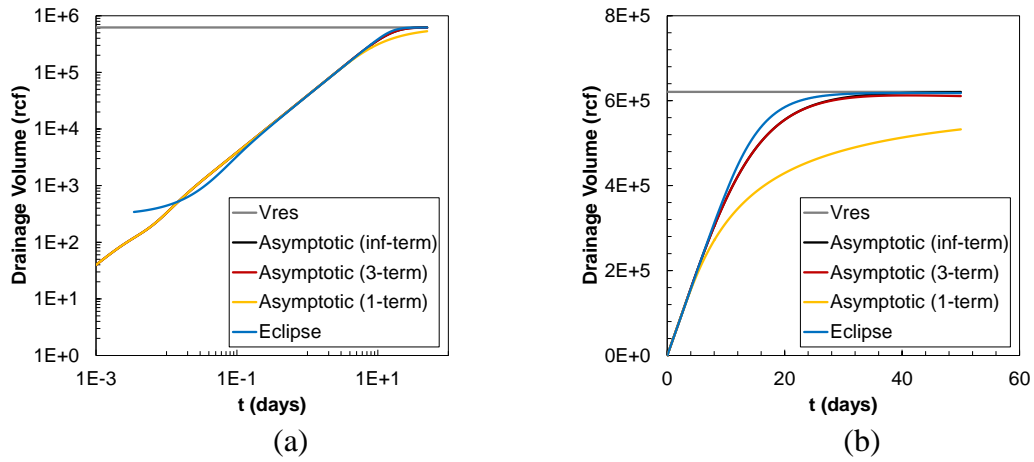


Figure 3.39 Comparison of drainage volume vs. time (in log-log and linear-linear scale, respectively) between ECLIPSE and asymptotic 1-exponential, 3-exponential, and inf-exponential term solutions for bounded radial flow (reprinted with permission from Wang et al, 2017)

3.3.3 EUR Prediction

After exploring effect of the number of exponential terms on the accuracy of asymptotic solutions, we can further use it together with a specific forward model, $w(\tau)$, to predict production performance and further estimate EUR. As illustrated in Figure 3.40, $1/RNP_{wf}$ is plotted against Q_w and the PSS/BDF portion of data is fitted using a straight line. The EUR prediction is the x-axis value of the intersection between the straight line and $1/RNP_{wf}$ cutoff. The field application will be shown in the next chapter. Here, I would like to simply validate the asymptotic solutions with several synthetic forward models.

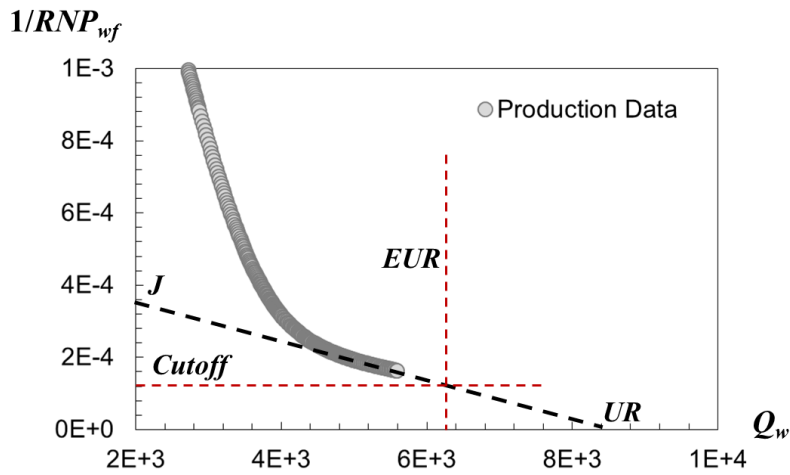


Figure 3.40 Illustration of EUR prediction

3.3.3.1 Forward Model Validation

In order to validate the proposed asymptotic pressure approximation, I will show the comparison between our solutions to the following ECLIPSE models: bounded radial flow (BRF) and bounded linear flow (BLF).

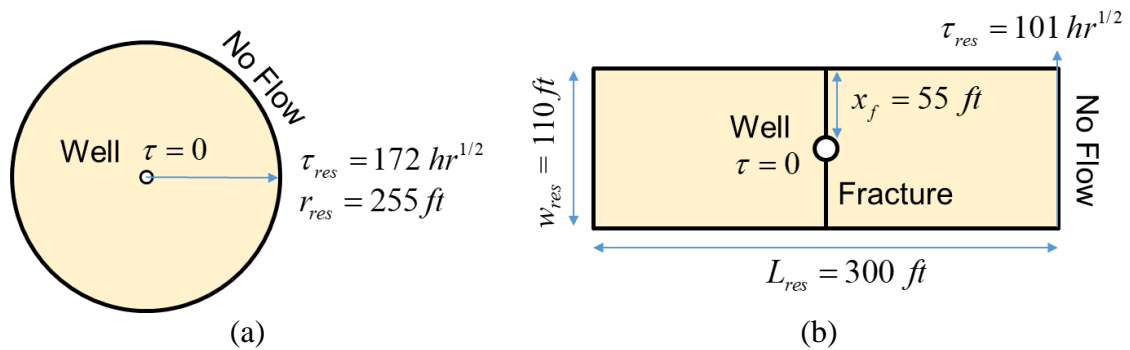


Figure 3.41 Model overview of (a) bounded radial flow and (b) bounded linear flow (reprinted with permission from Wang et al, 2018)

Property	Value	Unit
h	100	ft
r_{res}	255	ft
V_{res}	6.21×10^5	ft^3
k	500	nd
ϕ	0.03	-
μ	0.2	cp
c_i	1×10^{-5}	psi^{-1}
B	1.0	rb/bbl
r_w	0.5	ft
q_w	0.03	bbl/day
Δp_{wf}	4500	psi
t_{prod}	1500	day

Table 3.10 Reservoir, fluid and well properties of the bounded radial flow model (reprinted with permission from Wang et al, 2018)

Bounded Radial Flow Both fixed rate and fixed BHP drawdown cases are modeled using the ECLIPSE reservoir simulator (Cartesian grid with inactive cells outside r_{res}) as well as the 1-exponential term and the 3-exponential term diffusion kernels (Eq. (3.100) for fixed rate and Eq. (3.102) for fixed BHP). The model is shown in Figure 3.41 (a) and properties are listed in Table 3.10. The analytic solution in terms of τ is obtained from the equation for the pore volume, $V_p = \pi(r^2 - r_w^2)h\phi$, and from the solution to the Eikonal equation for a homogeneous medium, $\tau = (r - r_w)/\sqrt{\alpha}$, where $\alpha = k/\phi\mu c_i$ is the diffusivity. τ_{res} is calculated from the distance to the boundary of the reservoir as $\tau_{res} = (r_{res} - r_w)/\sqrt{\alpha}$. It will be used in the diffusion kernel as well as the upper limit of integration for the bounded reservoir solutions. The results are displayed in Figure 3.42, where the black dashed line is the linear regression line using ECLIPSE data during the

boundary dominated flow (BDF) period. The regression formula is also provided in the plot: for fixed rate, the slope is $1/c_t \cdot V_{res}$ and can be used to estimate a reservoir pore volume of $PV_{BDF} = 6.20 \times 10^5 \text{ ft}^3$. For fixed BHP, the x-intercept is the estimate of ultimate recovery, $UR_{BDF} = 2.76 \times 10^4 \text{ ft}^3$. These estimates, as listed in Table 3.11, and are very close to the model $V_{res} = 6.21 \times 10^5 \text{ ft}^3$ and theoretical $UR = \Delta p_{wf} \cdot c_t \cdot V_{res} = 2.79 \times 10^4 \text{ ft}^3$.

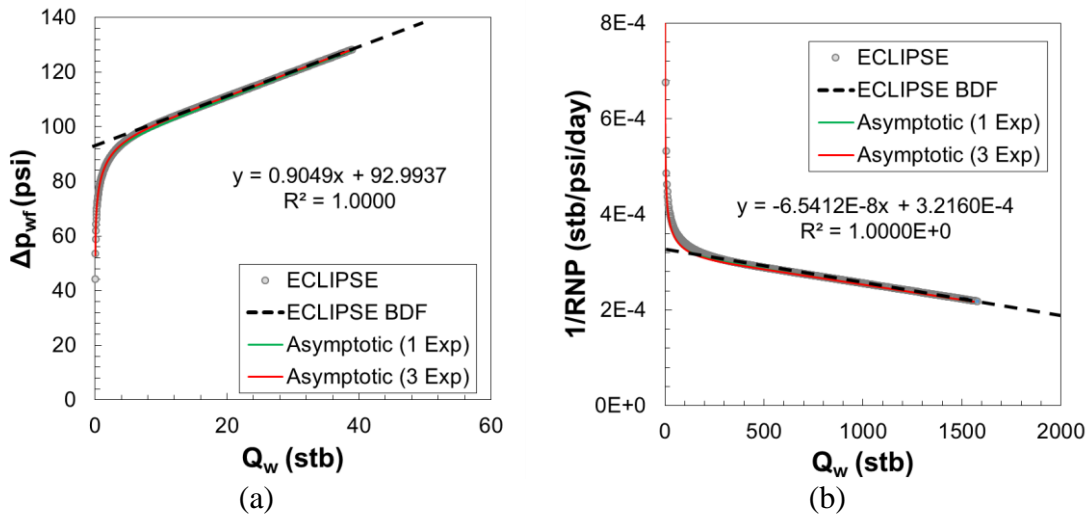


Figure 3.42 ECLIPSE and asymptotic approximation results of bounded radial flow with (a) fixed rate and (b) fixed BHP drawdown (reprinted with permission from Wang et al, 2018)

From Figure 3.43, we observe that the asymptotic approximation results match well with those from the ECLIPSE simulator, at both early and late time: our method of analysis is not restricted to BDF flow, but also captures the early time transient. Another observation is that both the 1-exponential term and the 3-exponential term diffusion kernels generate very similar Δp_{wf} and RNP_{wf} results. However, a more detailed

examination of the drainage volume and the welltest derivative, both of which depend upon the time derivatives of the solution, show a better correspondence with the ECLIPSE reference solution with the 3-exponential term solution (Wang *et al.*, 2017).

Fixed Rate Drawdown			Fixed BHP Drawdown		
Property	Value	Unit	Property	Value	Unit
<i>Slope</i>	0.9049	<i>psi/stb</i>	<i>Slope</i>	-6.54×10^{-8}	<i>1/psi/day</i>
<i>y-intercept</i>	92.994	<i>psi/stb</i>	<i>x-intercept</i>	4920	<i>stb</i>
<i>PV_{BDF}</i>	6.20×10^5	<i>ft³</i>	<i>y-intercept</i>	3.22×10^{-4}	<i>stb/psi/day</i>
			<i>J</i>	3.22×10^{-4}	<i>stb/psi/day</i>
			<i>UR_{BDF}</i>	2.76×10^4	<i>ft³</i>

Table 3.11 Fixed rate and BHP drawdown results of bounded radial flow (reprinted with permission from Wang et al, 2018)

Bounded Linear Flow Both fixed rate and fixed BHP drawdown cases are modeled using the ECLIPSE reservoir simulator as well as the 1-exponential term and the 3-exponential term diffusion kernels. (Eq. (3.100) for fixed rate and Eq. (3.102) for fixed BHP). The model is shown in Figure 3.41 (b) and properties are listed in Table 3.12. The analytic solution in terms of τ is obtained from the equation for the pore volume, $V_p = rA\phi$, and from the solution to the Eikonal equation for a homogeneous medium, $\tau = r/\sqrt{\alpha}$, τ_{res} was calculated from the distance to the reservoir boundary using $\tau_{res} = L_{res}/2\sqrt{\alpha}$. It will be used in the diffusion kernel as well as the upper limit of integration in the solution integrals. The properties in the well cell of ECLIPSE were modified (permeability was increased and porosity was reduced) to minimize the impact of the Peaceman radial flow well connection factor on linear flow during the early transient

period. The results are displayed in Figure 3.43. Analysis gives that for the fixed rate, the estimated reservoir pore volume is $PV_{BDF} = 9.72 \times 10^4 \text{ ft}^3$, and for fixed BHP, the estimate of ultimate recovery is $UR_{BDF} = 4340 \text{ ft}^3$. These estimates, as listed in Table 3.13, are close to the actual model values of $V_{res} = 9.9 \times 10^4 \text{ ft}^3$ and theoretical $UR = \Delta p_{wf} \cdot c_t \cdot V_{res} = 4460 \text{ ft}^3$. Similar to bounded radial flow, we once again observe that the asymptotic approximation yield results matching well with those from ECLIPSE simulator and that both the 1-exponential term and the 3-exponential term diffusion kernel approximations generate very similar Δp_{wf} and RNP_{wf} results.

Property	Value	Unit
L_{res}	300	<i>ft</i>
w_{res}	110	<i>ft</i>
x_f	55	<i>ft</i>
V_{res}	9.9×10^4	ft^3
q_w	0.3	<i>bbl/day</i>
t_{prod}	1200	<i>day</i>

Table 3.12 Reservoir, fluid and wellbore properties of the bounded linear flow model (all other parameters are the same as the BRF model)

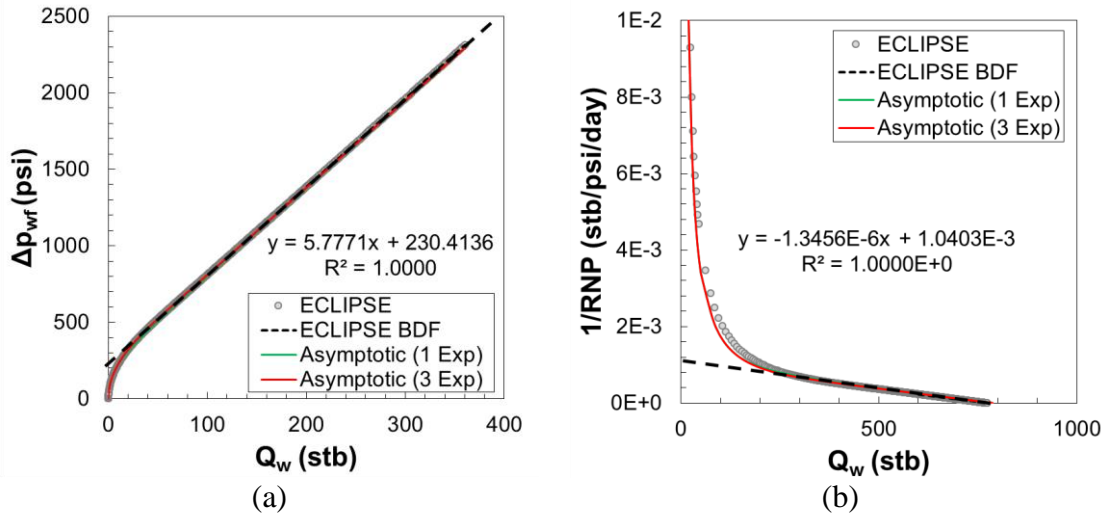


Figure 3.43 ECLIPSE and asymptotic approximation results of bounded linear flow with (a) fixed rate and (b) fixed BHP drawdown (reprinted with permission from Wang et al, 2018)

Fixed Rate Drawdown			Fixed BHP Drawdown		
Property	Value	Unit	Property	Value	Unit
<i>Slope</i>	5.7771	<i>psi/stb</i>	<i>Slope</i>	-1.35×10^{-6}	<i>1/psi/day</i>
<i>y-intercept</i>	230.4	<i>psi/stb</i>	<i>x-intercept</i>	773	<i>stb</i>
PV_{BDF}	9.72×10^4	ft^3	<i>y-intercept</i>	1.04×10^{-3}	<i>stb/psi/day</i>
			<i>J</i>	1.04×10^{-3}	<i>stb/psi/day</i>
			UR_{BDF}	4340	ft^3

Table 3.13 Fixed rate and BHP drawdown results of bounded linear flow (reprinted with permission from Wang et al, 2018)

3.4 Discussion

From fixed or variable rate drawdown cases, we can see that one term asymptotic solution is almost always adequate to provide accurate approximations to the infinite asymptotic series. $A_0(t)$ only vanishes in a single specific case (fixed BHP drawdown), and in that case $A_1(t)$ will be the leading term in the asymptotic expansion. However, in

all the other cases $A_0(t)$ is the leading term and the approximations $A_0 \cdot V_0 \gg \sum_{n=1} A_n \cdot V_n$

and $A_0 \cdot W_0 \gg \sum_{n=1} A_n \cdot W_n$ are shown to be a good approximation, so that we can simply

express $c_t \Delta p_{wf} = \sum_n A_n \cdot W_n \approx A_0 \cdot W_0$ and $q_{sf} = \sum_n A_n \cdot V_n \approx A_0 \cdot V_0$ for the most inner

boundary conditions:

- The integrability condition will give evolution equations for each order of the expansion in terms of the lower order terms. If they are negligible then we can stop with the leading order term of the expansion; otherwise we need to include more asymptotic terms.
- For fixed rate drawdown we can approximate the infinite sum with the $A_0(t)$ term, especially since $A_1(t) = 0$ from the boundary condition.
- For fixed BHP drawdown we cannot approximate the infinite sum with the $A_0(t)$ term, since $A_0(t) = 0$ from the boundary condition. However, we can approximate the infinite sum with the $A_1(t)$ term.
- For cases with variable rate and BHP drawdown, $A_0(t)$ is not zero, and we can approximate the infinite sum with the $A_0(t)$ term. However, this approximation may not be quite as accurate as for fixed rate drawdown since $A_1(t)$ is not zero.

Under what circumstances will the treatment of variable rate finite reservoir transients be correct? At present we have tested the extension from the fixed rate infinite

acting solution with an emphasis on well performance. With an emphasis on field data interpretation, this may be adequate. However, the reference solutions also provide predictions of the profiles of pressure drop and flux, which warrant additional testing in future studies.

When extending asymptotic solutions to address bounded reservoirs, consider the pressure drop at a location in a reservoir in the vicinity of a no flow barrier. The pressure drop can be represented as the sum of the pressure drops due to the direct front, which depends upon $\tau(\vec{x})$, and the reflected front, which depends upon a larger diffusive time of flight, $\tau_1(\vec{x})$: $\Delta p(\vec{x}, t) \approx \Delta p(\tau(\vec{x}), t) + \Delta p_1(\tau_1(\vec{x}), t)$. In the discussion of a composite reservoir we have assumed normal incidence to the change of properties so that the reflected front follows the same path as the original, $\tau_1(\vec{x}) = 2\tau_{res} - \tau(\vec{x})$. In all other cases $\tau_1(\vec{x})$ has no relationship to $\tau(\vec{x})$ and the fundamental assumption appears to fail. However, if the strength of the reflected front is small ($R \approx 0$ and $T \approx 1$) or if $e^{-\tau_1^2(\vec{x})/4t} \ll e^{-\tau^2(\vec{x})/4t}$, then the assumption of $p(\vec{x}, t) \approx p(\tau(\vec{x}), t)$ is reasonable. Stated otherwise, the maximum deviations will occur in the immediate vicinity of flow barriers where $R \approx 1$ and $\tau_1(\vec{x}) \approx \tau(\vec{x})$, except in the direction of normal incidence where $\tau_1(\vec{x})$ and $\tau(\vec{x})$ are directly related.

The reflection coefficient varies between -1 and +1. The transmission coefficient is bounded between 0 and 2, and is always positive. For smooth properties, $R = 0$ and $T = 1$. In contrast, the reflected front may interfere either constructively or destructively

with the transmitted front. For instance, to model a constant pressure boundary at $\tau = \tau_d$, we have $\frac{\partial p}{\partial t} = 0$ and $R = -1$. The reflected front acts like an injector and maintains the boundary pressure. In contrast, to model a constant no flow boundary at $\tau = \tau_d$, we have $\frac{\partial q}{\partial t} = 0$ and $R = +1$. The reflected front now enhances the pressure drop. The two-domain formulation has essentially introduced variable strength image wells into the formulation. When determining the number of image wells represented by 1, 2 and 3-exponential term approximations, we see that the one term approximation shows the impact of the finite size of the reservoir at earlier times than the full expression. Once we reach two terms, we have a good approximation and the approximation becomes excellent once we have three terms. The second and third terms are of the same magnitude at the wellbore, and so including both terms in the drainage volume calculation provides a consistent approximation. We see that the application of an infinite series to model a bounded reservoir does not appear to be necessary. This is very important as it demonstrates how to extend the classic transient PTA/RTA boundary dominated DCA to the transition between infinite acting and boundary dominated flow and that our asymptotic approximation does this for arbitrary geometry. With our analytic approach, one may easily conduct decline analysis for arbitrary geometry with calibrated $w(\tau)$ and assumed uncertain reservoir volume, in order to predict EUR.

3.5 Chapter Summary

In this chapter, I illustrated how to extend our asymptotic solution to resolve the two major limitations of our methodology, i.e., constant rate drawdown and infinite domain drainage volume, and provide a systemic validation to the generalized asymptotic solutions. I started our analysis with the fixed BHP drawdown solution in an infinite acting reservoir. The approximation has been validated against a number of applications for which inverse Laplace transform reference solutions are available. Of course, our intent is not simply to re-derive classical results but to validate a formulation for use in complex fractured wells and heterogeneous reservoirs. The reference solutions include variable rate drawdown, as arises in production analysis and in problems with wellbore storage. Asymptotic solution extended to variable rate drawdown shows us two important conclusions:

- $A_0(t)$ is the leading term for all the variable rate cases besides fixed BHP.
- Increasing the number of asymptotic terms beyond the leading order term $A_0(t)$ generally does not improve the solution. This is consistent with the earlier observation that the time integral accumulates error while the τ integral does not.

Next, I showed how we developed a general analytic solution for bounded transient flow based upon an asymptotic pressure approximation which reduces to Fetkovich's work on bounded radial flow and Wattenbarger's work on bounded linear flow in those specific geometries. The methodology offers similar abilities for analysis without the restriction to specific flow regimes. The formulation also suggests how to bridge between

the methodologies of pressure transient and rate transient analysis, generalized to more complex reservoir and well geometries. Asymptotic solution extended to bounded reservoirs shows:

- Three exponential terms required to account for reflected pressure fronts.
- An infinite series is unnecessary.

Then, I showed how to use the proposed asymptotic solution for EUR estimation. Our approach works for infinite acting transient flow and through the transition to boundary dominated flow, which extends the classic transient PTA/RTA boundary dominated DCA to physics based models for the transition between infinite acting and boundary dominated flow for arbitrary geometry. It was also validated by synthetic models and conventional simulations, where we see the physics-embedded analytic approach allows to predict declines and EUR at specific cutoffs together with reservoir volume uncertainty.

To sum up, the major achievements and conclusions of this chapter are as follows:

The asymptotic solution in resolving variable rate drawdown problems was extended and validated.

- Material balance time is superposition time for boundary dominated flow and it is a reasonable approximation for other flow geometries.
- The fixed BHP asymptotic approximation has a better performance in rate normalized pressure drop calculation than models using superposition time and material balance time.

The asymptotic solution in handling boundary effects was validated.

- The definition of the drainage volume has been updated for bounded systems and the generalized asymptotic approximation works for bounded systems perfectly
- It is very important as it demonstrates how to extend the classic transient PTA/RTA boundary dominated DCA to the transition between infinite acting and boundary dominated flow and that it does this for arbitrary geometry. Fetkovich's work on bounded radial flow and Wattenbarger's work on bounded linear flow can be replaced with our pure analytic solution which gives a better characterization of the transition to PSS

CHAPTER IV

UNCONVENTIONAL RESERVOIR ANALYSIS*

4.1 Introduction

A novel data-driven approach was previously introduced for production analysis of unconventional reservoirs without the traditional RTA/PTA assumptions of specific flow regimes. The approach relied on a $w(\tau)$ function, which is drainage volume geometry function, to characterize the flow geometry from the transient drainage volume. The approach has been used to rank refracturing candidates and to obtain optimal fracture spacing. In this chapter, I will show how we generalize the previous studies (Yang *et al.*, 2015; King *et al.*, 2016; Sharma, 2016; Xue *et al.*, 2016; Wang *et al.*, 2017) to improve the amount of quantitative reservoir information obtained during the production analysis.

Our approach uses a transient generalization of the Matthews-Brons-Hazebroek definition of the PSS drainage volume (Matthews *et al.*, 1954). It is obtained from an asymptotic solution of the diffusivity equation in heterogeneous and/or fractured media. Given field pressure and flow rate data, we calculate the transient well drainage volume with time. The time evolution of the drainage volume can be inverted to estimate $w(\tau)$

*Material adapted with permission from “Quantitative Production Analysis and EUR Prediction From Unconventional Reservoirs Using a Data-Driven Drainage Volume Formulation” by Wang *et al.*, 2018: Paper EAGE-46177 to be presented at EAGE 16th European Conference on the Mathematics of Oil Recovery held in Barcelona, Spain, 3-6 September 2018. Copyright 2018, Wang *et al.* Further reproduction prohibited without permission.

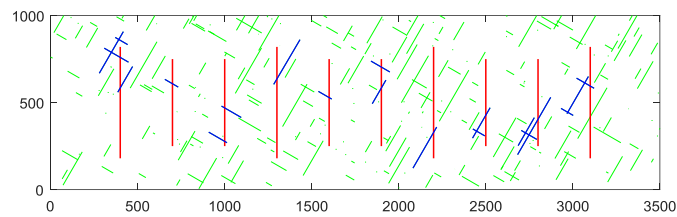
function, which provides a description of the underlying and potentially complex flow geometry and is then used for quantitative analysis.

The proposed approach is a data-driven model-free analysis of production data without the presumption of specific flow regimes. It provides a simple and intuitive understanding of the transient drainage volume and instantaneous recovery efficiency, irrespective of the complexity of the reservoir depletion geometry. In the current study we develop an improved approach for the $w(\tau)$ inversion which yields better physical resolution and which can identify more detailed characteristics of the underlying flow geometry than previous studies, e.g., complex near fracture flow, linear flow, fracture interference, etc. The results of the analysis have been used for the characterization of hydraulic fracture and reservoir properties, including the prediction of fracture surface area, matrix permeability, SRV and extended to the calculation of EUR. The power and utility of the proposed methodology is first validated with synthetic examples and then demonstrated using a field example of a well from the Montney shale.

Compared to the previous approach, the current work is based upon the identical theoretical models for interpretation, but with less restrictive assumptions made during the analysis. Beyond that, I will show how the proposed $w(\tau)$ inversion algorithm does a better job than the previous one in generating more stable $w(\tau)$ curves under varying field production conditions, which further enables us to identify more features. In addition, I will show how the interpretation leads to new approaches to production forecasts and EUR prediction based upon the bounded reservoir model solutions of the previous chapter.

4.1.1 Production Analysis for Unconventional Reservoirs

Unconventional reservoirs are characterized by low permeability and long interference times and conducting reliable production analysis for them is a challenging task. The complex fracture geometry, as illustrated in Figure 4.1 (a), will yield complex depletion patterns within the reservoir shown in subplot (b).



(a) Model Illustration



(b) Pressure Distributions

Figure 4.1 Multiple fractures in a naturally fractured reservoir (a) Model illustration and (b) Pressure distributions at 3 months, 1 year, and 3 years (Yang, 2017)

Recently, a lot of papers have been published to reveal the physics and mechanisms that occur underground during hydraulic fracture stimulation and production process.

Kou *et al.* (2017) proposed a modified Hagen-Poiseuille equation considering the convective-diffusive nature of the overall transport in nanocapillary. Li *et al.* (2018) studied wettability alteration with complex fracture networks and Deng and King (2018) investigated the transition from spontaneous to forced imbibition naturally fractured reservoirs. Kou *et al.* (2018) studied proppant transport behavior in inclined planar fractures via large-scale simulations. These researches provided a better understanding of fluid transport in the matrix and would be helpful for designing a better proppant pumping scheme as well as production strategy for shales.

Some other researches focused on developing more reliable and capable approaches, either numerical or analytic, to capture and predict unconventional reservoir performances.

An *et al.* (2017) built a coupled flow-geomechanics model for organic-rich shale reservoirs, considering the impacts matrix shrinkage and stress changes on stress-dependent permeability as well as gas production. Guo *et al.* (2017) presented the development of an efficient parallel simulator that considers non-isothermal fluid flow coupled with elastoplastic deformation. Liu and Valkó (2017) proposed a new algorithm to accurately and rapidly estimate the well production index with infinite-conductivity fracture based on the well-fracture configuration and thus enabled a quick optimization method for the well and fracture spacing. Guo *et al.* (2018) presented a fully coupled flow and geomechanics model to investigate the most relevant parameters affecting well performance and interference of tightly spaced horizontal wells. He *et al.* (2018a) developed an analytical model of multi-segment horizontal wells to estimate rate

distribution along horizontal wellbore and identify underperforming horizontal sections. Furthermore, He *et al.* (2018b) shed light on the importance of incorporating the effects of non-uniformity for better evaluation of well performance based on long-term production data.

Our research group uses $w(\tau)$ to describe the complex geometry and depletion in unconventional reservoirs, and historically, we mainly got experience on how to do qualitative interpretation with $w(\tau)$, since the $w(\tau)$ interpreted from production data had oscillations and even negative values which made quantitative analysis a difficult task, especially for field cases (Yang *et al.*, 2015; Sharma, 2016; Xue *et al.*, 2016). In the previous chapters, I have shown the demonstrations that the asymptotic pressure approximation can be used to calculate pressure and rate transients given an underlying geometric function $w(\tau) = dV_p/d\tau$. This has led us to explore the use of $w(\tau)$ as a diagnostic tool by solving an inverse problem given field data. The drainage volume $V_d(t)$ can be inverted for $w(\tau)$ where the drainage volume is determined from production data. Specifically, for variable rate drawdown:

$$V_d(t) = \int_0^{\tau_{\max}} e^{-\tau^2/4t} w(\tau) d\tau \quad \text{where} \quad \frac{1}{V_d(t_e)} \equiv c_t \frac{dRNP_{wf}(t)}{dt_e} \quad (4.1)$$

As an example, Figure 4.2 shows the drainage volume diagnostic plot calculated based upon the ECLIPSE simulation for a single-fracture model, as well as the corresponding pressure contours representing early time linear flow, intermediate time radial flow and late time boundary dominated flow. Different slopes of the $w(\tau)$ curve represent different flow regimes: slope = 0 stands for the region of linear flow; slope = 1 implies radial flow;

a sudden drop of $w(\tau)$ slope indicates the value of τ where the pressure front reaches the outer boundary of the reservoir and V_p reaches a constant.

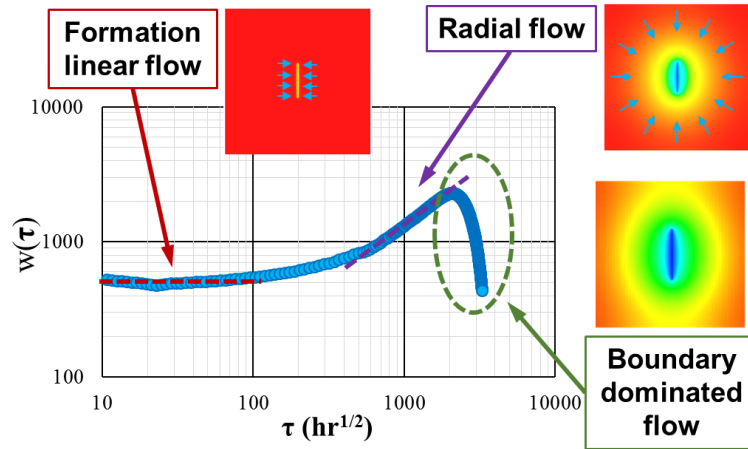


Figure 4.2 Drainage volume diagnostic plot $w(\tau)$ vs. τ for a single-fracture in a bounded reservoir model, adapted from Sharma (2016)

The $w(\tau)$ inversion based on production history has been successfully applied to a number of synthetic and field examples, although some simplifications needed to be implemented, especially when dealing with the field examples (Wang *et al.*, 2018). Next, I will review the previous inversion methodology and provide a more robust approach.

4.1.2 Previous Drainage Volume Calculation and Inversion

In this section, we will review the steps of the previous drainage volume calculation and inversion.

As illustrated in Figure 4.3 from Yang *et al.* (2015), both BHP & rate historical data are curve-fitted globally to capture the general features of the RNP curve and to

ensure a smooth drainage volume calculation. During this process, production details may be lost due to the global fitting procedure.

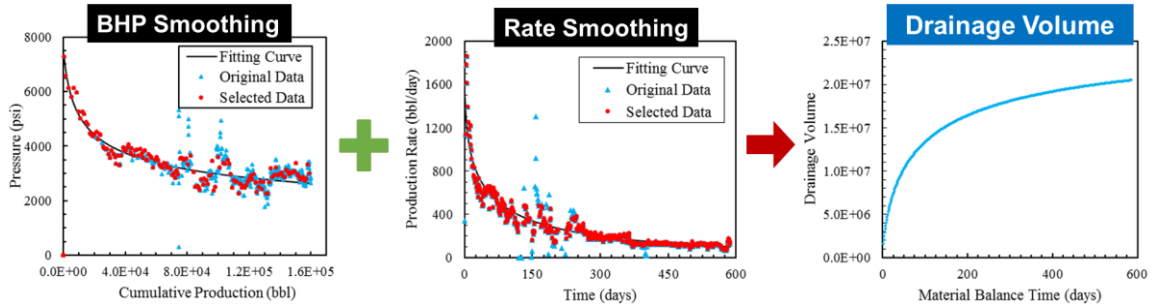


Figure 4.3 Overview of previous drainage volume calculation, adapted from Yang *et al.* (2015)

After obtaining drainage volume from field production data, now the drainage volume integral in Eq. (4.2) becomes a Fredholm integral equation. The only unknown is the drainage volume function $w(\tau)$.

$$\begin{aligned}
 V_d(t) &= \int_0^{\tau_{\max}} e^{-\tau^2/4t} w(\tau) d\tau \\
 \Rightarrow V_d(t_i) &= \sum_{j=1}^N \int_{\tau_{j-1}}^{\tau_j} e^{-\tau^2/4t_i} w(\tau) d\tau \\
 &= \sqrt{\pi t_i} \sum_{j=1}^N w_j \left\{ \operatorname{erf} \left(\frac{\tau_j}{2\sqrt{t_i}} \right) - \operatorname{erf} \left(\frac{\tau_{j-1}}{2\sqrt{t_i}} \right) \right\}
 \end{aligned} \tag{4.2}$$

Here, t_i are the times at which the drainage volume has been calculated, and $\{\tau_j = 2\sqrt{t_j}\}$ are the intervals over which $w(\tau)$ is discretized and is assumed piecewise constant. This relationship is based upon the depth of investigation for radial flow. This is the approach followed in Sharma and Yang's work (Yang *et al.*, 2015; Sharma, 2016).

Unfortunately, in this form, the inversion result is always unstable (oscillatory) because this problem is anti-diffusive and the matrix is near singular. Yang *et al.* (2015) provided a special treatment to the matrix elements along the main diagonal, to make the matrix semi-definite, as shown in Eq. (4.3). As illustrated in Figure 4.4, the oscillation is reduced and the $w(\tau)$ curve obtained from the inversion is also improved. However, unphysical non-positive $w(\tau)$ values may still be obtained. As shown by a field example in Figure 4.5 (a), for smooth and monotonic drainage volume, this algorithm yields smooth and positive $w(\tau)$ values which can be used for further analysis. However, when the volume drainage is non-monotonic, as we may obtain for unconstrained field cases, the algorithm will predict negative $w(\tau)$ values with an unstable trend, which will make the field formation interpretation almost impossible.

$$\begin{pmatrix} k_{1,1}^* & 0 & 0 & \dots & 0 \\ k_{2,1} & k_{2,2}^* & 0 & \dots & 0 \\ k_{3,1} & k_{3,2} & k_{3,3}^* & \dots & 0 \\ \vdots & \vdots & \vdots & \ddots & \vdots \\ k_{N,1} & k_{N,2} & k_{N,3} & \dots & k_{N,N}^* \end{pmatrix} \begin{pmatrix} w_1 \\ w_2 \\ w_3 \\ \vdots \\ w_N \end{pmatrix} = \begin{pmatrix} V_1 \\ V_2 \\ V_3 \\ \vdots \\ V_N \end{pmatrix} \quad (4.3)$$

$$\text{where, } k_{i,j} = \begin{cases} \sqrt{\pi t_i} \left\{ \operatorname{erf} \left(\frac{\tau_j^*}{2\sqrt{t_i}} \right) - \operatorname{erf} \left(\frac{\tau_{j-1}}{2\sqrt{t_i}} \right) \right\} & i \neq j \\ \sqrt{\pi t_i} \left\{ \operatorname{erf} \left(\frac{\tau_j}{2\sqrt{t_i}} \right) - \operatorname{erf} \left(\frac{\tau_{j-1}}{2\sqrt{t_i}} \right) \right\} & i = j \end{cases}, \quad \tau_j = 2\sqrt{t_j}, \quad \tau_j^* = 5\sqrt{t_j}$$

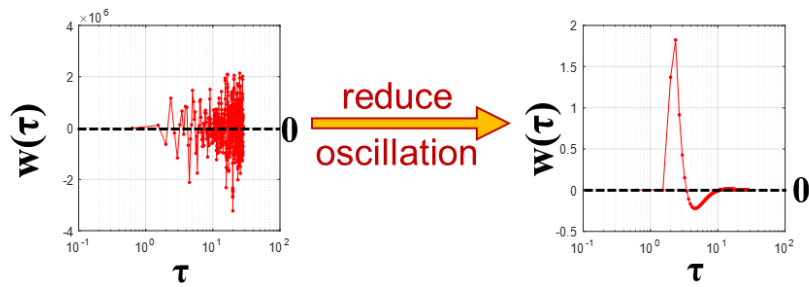
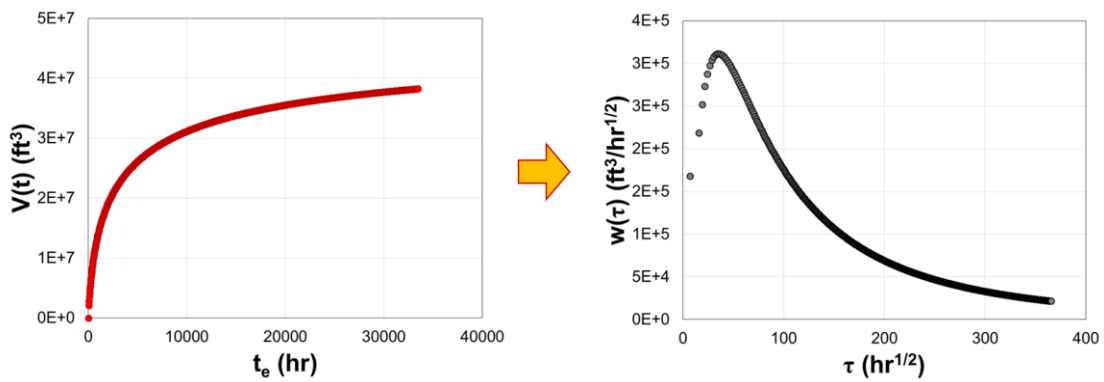
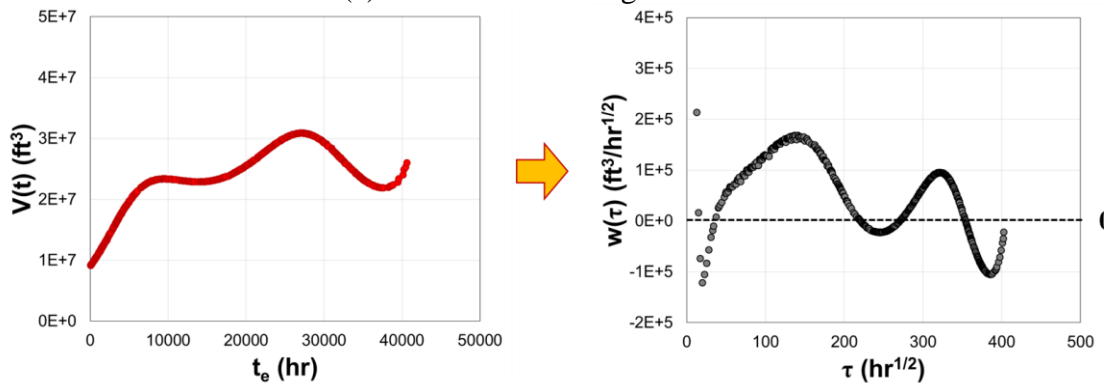


Figure 4.4 Illustration of reduced oscillation in the previous drainage volume inversion (reprinted with permission from Wang et al, 2018)



(a) Monotonic Drainage Volume



(b) Non-Monotonic Drainage Volume

Figure 4.5 Illustration of $w(\tau)$ inversion result by previous algorithm with (a) monotonic drainage volume; and (b) non-monotonic drainage volume

Thus, in order to resolve the weaknesses of the previous approach, the major two targets for continuing this research are summarized below:

- Find an alternative approach to keep more pressure front propagation details and reduce the side effect caused by noisy data points when calculating drainage volume based on production data;
- Treat the inversion problem as an optimization process rather than a well-posed one to ensure a reliable and physical constrained $w(\tau)$ inversion result.

4.2 Methodology: Improved Production Analysis

In the methodology section, I will explain the important steps of the improved production analysis in details. According to the targets of the study, this section is divided into two parts: the first one is the production data processing, which is used to remove the outliers in the field production data and calculate drainage volume based on RNP time derivative; the second one is $w(\tau)$ drainage volume geometry function inversion, where regularized least squares optimization is employed to guarantee a positive and smooth $w(\tau)$ curve from inversion.

4.2.1 *Production Data Processing and Drainage Volume Calculation*

The proposed production data processing and drainage volume calculation workflow include two important steps. First, RNP is calculated based on BHP and rate data and RNP derivative outliers are removed via regression analysis. Then, the drainage volume is determined based upon the local RNP time derivative.

4.2.1.1 Removing Outliers via Regression Analysis

Removing outliers via regression analysis applies a combination of modified Friedman's Super Smoother (MFSS) and Moving Linear Regression Analysis (MLRA), as shown in Figure 4.6. The first step is to calculate RNP and t_e based upon production data. The RNP obtained is labelled as raw data because they are usually scattered with a lot of noisy points. We have clear evidence that t_e does not work well during the infinite acting period, since it is off the trend compared to t_s , as what we have demonstrated in the last chapter. If we plot the raw RNP and its welltest derivative data against t_e , we obtain a Diagnostic plot. For example, I conduct ECLIPSE simulation for the infinite conductivity hydraulic fracture case with variable rate drawdown, and production history is shown in Figure 4.7 (a). I further calculate RNP based on the production data and then estimate RNP' with re-ordered date points in ascending t_e and a weighted central difference vs. $\ln(t_e)$ following Bourdet *et al.* (1983), as shown in Figure 4.7 (b), (c), (d), where RNP (red dots) and RNP' (green dots) are further connected in time. We can see the signature of the history w.r.t. t_e is very erratic and t_e is jumping back and forth in time. According to the definition, t_e is very sensitive to instantaneous production rate and thus any changes in flow rate may result in non-monotonic RNP and RNP' curves w.r.t. t_e . The direct calculation of RNP time derivative ($dRNP/dt_e$) based on RNP and t_e will definitely generate a lot outliers.

To resolve the issue, MFSS is mainly used to estimate RNP time derivative from scattered and noisy production data. MLRA is then employed to filter out the outliers beyond a certain confidence interval based on the RNP time derivative estimates from MFSS.

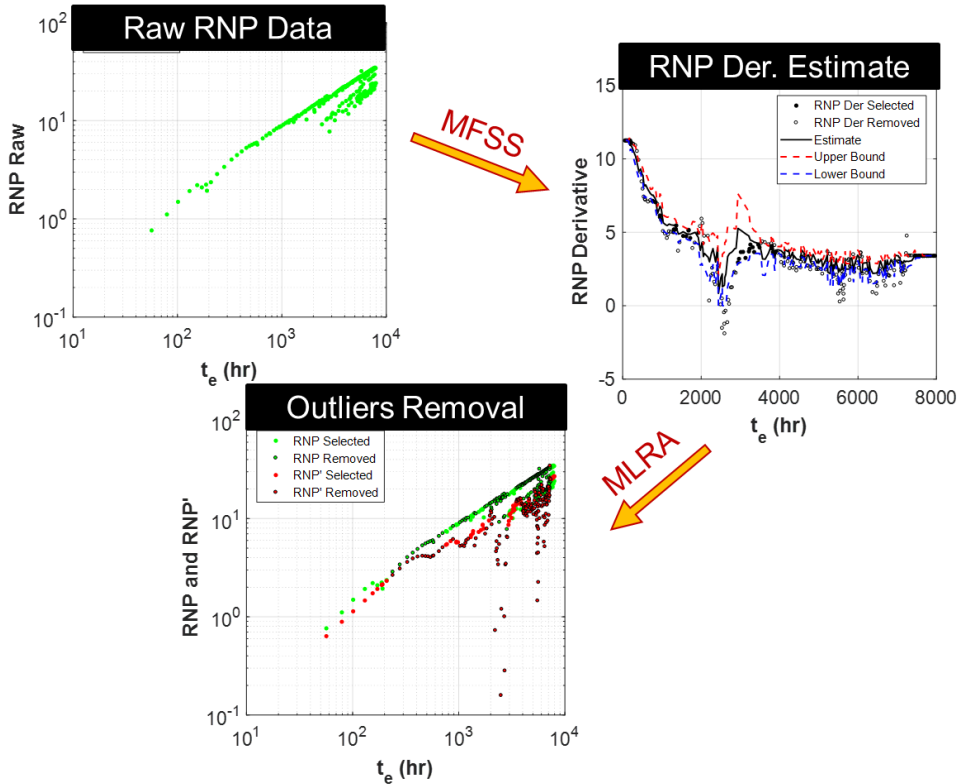


Figure 4.6 Illustration of removing outliers via regression analysis

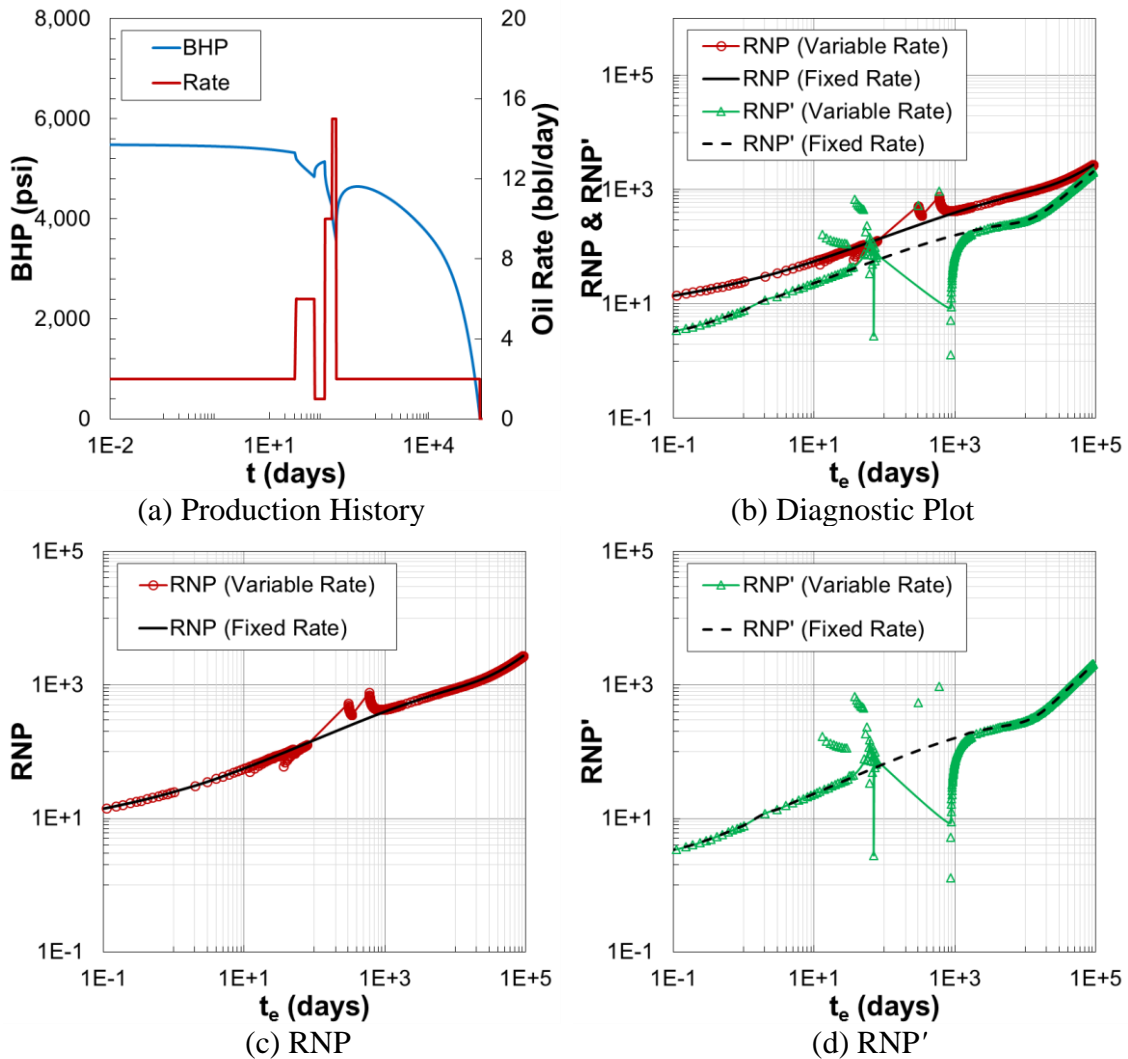


Figure 4.7 Comparison of (a) production history; (b) Diagnostic plot; (c) RNP; and (d) RNP' between variable rate drawdown (RNP: red markers with red curves; RNP': green markers with green curves) and the corresponding fixed rate drawdown (RNP: black solid curves; RNP': black dashed curves) for infinite conductivity hydraulic fracture case

Data Smoothing When preparing field data for further pressure transient analysis (PTA), the first challenge is to estimate the pressure or RNP time derivative. We mainly used MFSS to pre-process the scattered RNP data by local linear regression with adaptive bandwidths (Friedman, 1984). The initial fixed-bandwidth smoothing is slightly adjusted

for better performance and to avoid data over-smoothing, compared to the bandwidth used in the original Friedman's work. The slopes of the RNP from the final linear regression will be treated as the time derivative at each RNP point. The intermediate steps of local linear regression and modified Friedman's Super Smoother are provided below.

Given n_t data points $x_1 \dots x_{n_t}$ (t_e) and $y_1 \dots y_{n_t}$ (RNP) from the production history with joint distribution $P(X, Y)$. We want to estimate the conditional expectation $E(Y | X = x)$ such that the squared error $E(Y - f(X))^2$ is minimized, where $f(X)$ is the optimal function. $P(X, Y)$ can be generated from the relation

$$Y = f(X) + \varepsilon \quad (4.4)$$

where ε represents error.

Then, in order to estimate $E(Y | X = x)$, we need to find the estimate $\hat{f}(x) = \hat{y}$ in

$$y_i = \hat{y}_i + \varepsilon_i \quad (4.5)$$

One way to estimate \hat{y}_i is to locally fit linear least squares regressions of the form

$$\hat{E}(Y | x_i) = \hat{\alpha} + \hat{\beta}x_j, \quad x_j \in N_i \quad (4.6)$$

where $\hat{\alpha}$ and $\hat{\beta}$ are the coefficients from local fit, N_i is the local bandwidth which represents the number of local data points around x_i .

Friedman (1984) originally chose to use $N = 0.05n_t$, $N = 0.2n_t$, and $N = 0.5n_t$, but here I chose smaller bandwidths of $N = 0.05n_t$, $N = 0.1n_t$, and $N = 0.2n_t$ to better fit for field cases with several hundred of data points, which are much larger than the

synthetic cases tested by Friedman. When N is fixed, we can write the local linear estimator as:

$$\hat{y}_j = \hat{\alpha}_i + \hat{\beta}_i x_j, \quad j = i - N/2, \dots, i + N/2, \quad i = N/2, \dots, n_t - N/2 \quad (4.7)$$

where $\hat{\alpha}_i$ and $\hat{\beta}_i$ can be obtained from local fits to data points $i - N/2, \dots, i + N/2$ for each x_i , $i = N/2, \dots, n_t - N/2$. \hat{y}_i and $\hat{\beta}_i$ are the initial estimates at the given bandwidth for RNP and RNP time derivative, respectively.

An optimal bandwidth which minimizes the expected squared error

$$e^2(N) = E(Y - f(X|N))^2 \quad (4.8)$$

can be obtained by estimating $e^2(N)$ through leave-one-out cross-validation:

$$\hat{e}_{cv}^2(N) = \frac{1}{n_t} \sum_{i=1}^{n_t} [y_i - \hat{f}_{(i)}(x_i|N)]^2 \quad (4.9)$$

which can be computed analytically as:

$$\hat{e}_{cv}^2(N) = \frac{1}{n_t} \sum_{i=1}^{n_t} [y_i - \hat{f}(x_i|N)]^2 \left/ \left(1 - \frac{1}{N} - \frac{(x_i - \bar{x}_N)^2}{\sum_{j=i-N/2}^{i+N/2} (x_j - \bar{x}_N)^2} \right) \right. \quad (4.10)$$

where $\bar{x}_N = \frac{1}{N} \sum_{j=i-N/2}^{i+N/2} x_j$.

Minimizing $\hat{e}_{cv}^2(N)$ gives the cross-validated optimal bandwidth:

$$\hat{e}_{cv}^2(N_{cv}) = \min_{0 < N < n_t} \hat{e}_{cv}^2(N) \quad (4.11)$$

Taking the locally adaptive bandwidths into consideration, Friedman (1984) proposed to minimize the estimate for:

$$e^2(f, N) = E(Y - f(X | N(X)))^2 \quad (4.12)$$

with respect to both $f(x)$ and $N(x)$. In order to minimize Eq. (4.12), we first estimate Eq. (4.7) using local linear regression over specified values for N .

The leave-one-out cross-validated residuals for each of these initial constant bandwidth estimates can be calculated by:

$$r_{(i)} = (y_i - \hat{y}_i) / \left(1 - \frac{1}{N} - \frac{(x_i - \bar{x}_N)^2}{\sum_{j=i-N/2}^{i+N/2} (x_j - \bar{x}_N)^2} \right) \quad (4.13)$$

Then, we need to smooth $|r_{(i)}|$ against x_i with bandwidth $N = 0.1n_i$ to estimate $\hat{e}(f, N | x_i)$ which we use to find the optimal bandwidth at each point:

$$\hat{e}(f, N_{cv}(x_i) | x_i) = \min_N \hat{e}(f, N | x_i) \quad (4.14)$$

The optimal bandwidths $N_{cv}(x_i)$ are then smoothed again with bandwidth $N = 0.1n_i$ against x_i and the two initial estimates (RNP time derivative) that have the closest bandwidths are selected.

The second last smooth is then conducted though linear interpolation between these two initial estimates w.r.t. $N_{cv}(x_i)$. Finally, the result of the interpolation (RNP time derivative) is then smoothed again with bandwidth $N = 0.05n_i$.

The key steps of MFSS of smoothing data and calculating RNP time derivative are briefly summarized in Figure 4.8.

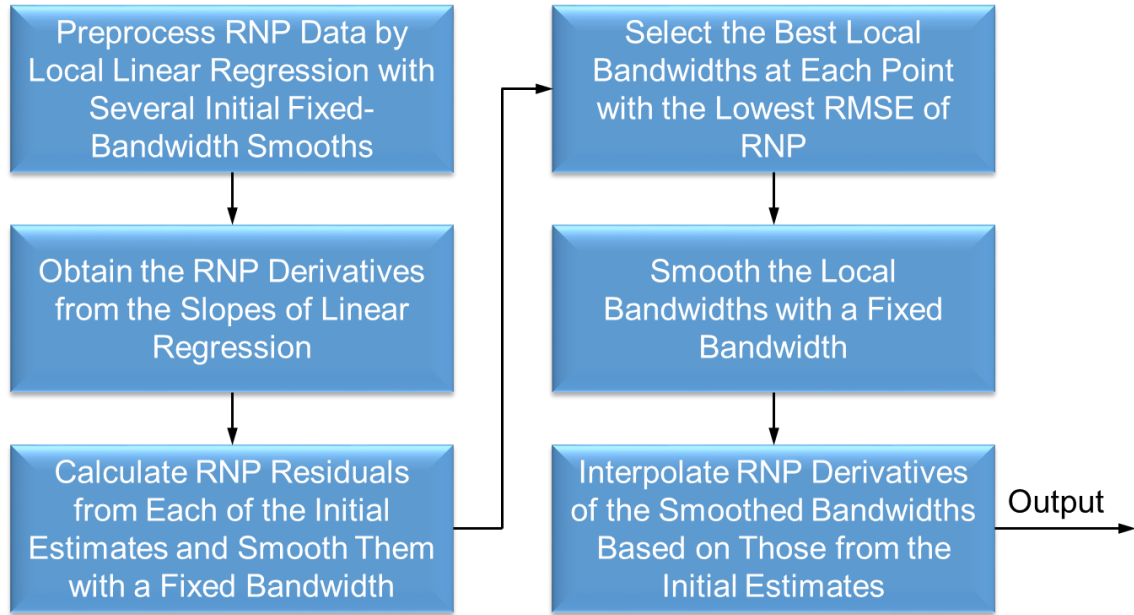


Figure 4.8 Illustration of data smoothing procedure with modified Friedman's Super Smoother

Outlier Removal After obtaining the RNP time derivatives, MLRA is then employed to filter out the RNP derivative outliers beyond confidence intervals. Here, I will show the important steps following Jensen *et al.* (1997).

Based on Eq. (4.7), an unbiased point estimator for estimating $E(Y | X = x_i)$ can be expressed as:

$$\hat{y}_i = \hat{\alpha}_i + \hat{\beta}_i x_i, \quad i = 1, \dots, N \quad (4.15)$$

where, $\hat{\alpha} = \bar{y}_N - \hat{\beta}_i \bar{x}_N$ and thus $Var(\hat{y}_i)$ can be expressed as:

$$\begin{aligned} Var(\hat{y}_i) &= Var(\hat{\alpha}_i + \hat{\beta}_i x_i) \\ &= Var(\bar{y}_N + \hat{\beta}_i (x_i - \bar{x}_N)) = \sigma_\varepsilon^2 \left(\frac{1}{N_i} + \frac{(x_i - \bar{x}_N)^2}{\sum_{j=i-N/2}^{i+N/2} (x_j - \bar{x}_N)^2} \right) \end{aligned} \quad (4.16)$$

We can replace σ_ε^2 by its estimate as:

$$\sigma_\varepsilon^2 = \frac{\sum_{j=i-N/2}^{i+N/2} (y_j - \hat{y}_j)^2}{N_i - 2} \quad (4.17)$$

and we obtain the following sample variance:

$$\text{Var}(\hat{y}_i) = \frac{\sum_{j=i-N/2}^{i+N/2} (y_j - \hat{y}_j)^2}{N_i - 2} \left(\frac{1}{N_i} + \frac{(x_i - \bar{x}_N)^2}{\sum_{j=i-N/2}^{i+N/2} (x_j - \bar{x}_N)^2} \right) \quad (4.18)$$

The estimate for $\text{Var}(\hat{y}_i)$, combined with Student's t-distribution $t(a/2, dof)$ which has the confidence level a and degree of freedom ($dof = N_i - 2$), can be used in the interval for the estimate of $E(Y | X = x_i)$:

$$\hat{y}_i \pm t(a/2, dof) \times \sqrt{\text{Var}(\hat{y}_i)} \quad (4.19)$$

To take a confidence interval into account regarding a new response (x_i, y^*) , we incorporate the variability of error $\text{Var}(\varepsilon)$. Due to the independence of the error, we obtain that:

$$\text{Var}(y^*) = \text{Var}(\hat{y}_i) + \text{Var}(\varepsilon) = \sigma_\varepsilon^2 \left(1 + \frac{1}{N_i} + \frac{(x_i - \bar{x}_N)^2}{\sum_{j=i-N/2}^{i+N/2} (x_j - \bar{x}_N)^2} \right) \quad (4.20)$$

With sample values, this leads to the confidence interval:

$$\hat{y}_i \pm t(a/2, dof) \times \sqrt{\frac{\sum_{j=i-N/2}^{i+N/2} (y_j - \hat{y}_j)^2}{dof} \left(1 + \frac{1}{N_i} + \frac{(x_i - \bar{x}_N)^2}{\sum_{j=i-N/2}^{i+N/2} (x_j - \bar{x}_N)^2} \right)} \quad (4.21)$$

Here \hat{y}_i is the RNP time derivative under investigation, which is located at the interval center, and the other y_j 's refer to the remaining RNP derivatives estimated from linear regression analysis. The x 's represent the corresponding times, and N_i is the number of data points in the interval. It will be used as a tolerance level in order to identify the RNP outliers.

The key steps of MLRA are summarized in Figure 4.9 and Figure 4.10 displays an example of outlier removal using MLRA. As illustrated in Figure 4.10 (a), the red and blue dashed curves represent the upper and lower bounds of the RNP derivative estimate (black solid curve), and points fall outside of the bounds will be removed. The effect on the Diagnostic plot can be seen in Figure 4.10 (b), where the RNP welltest derivative become less scattered than before.

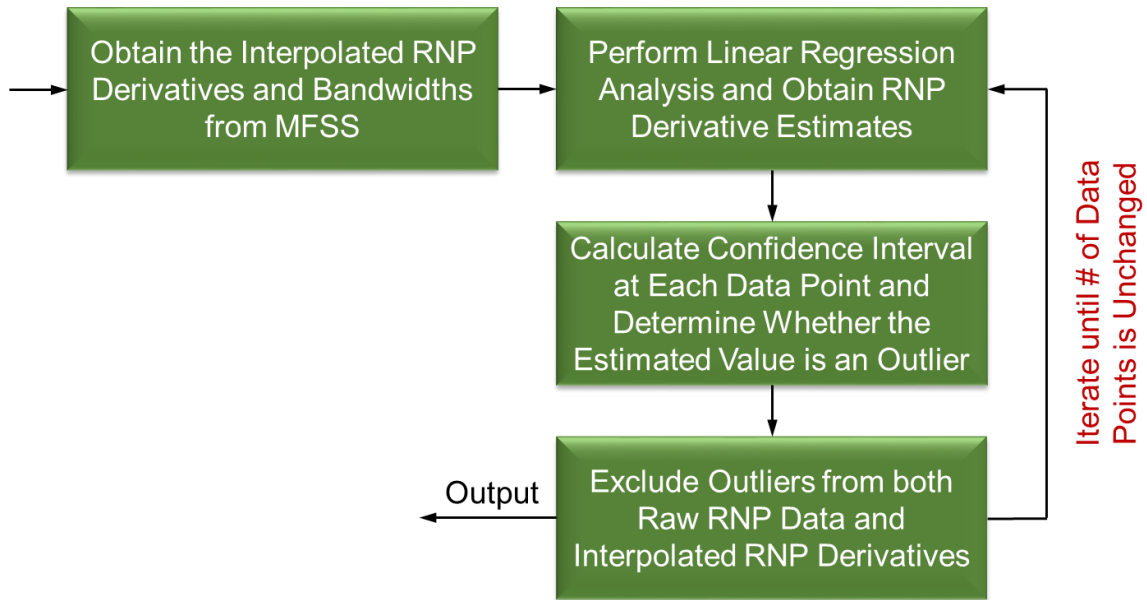


Figure 4.9 Illustration of outlier removal procedure with Moving Linear Regression Analysis

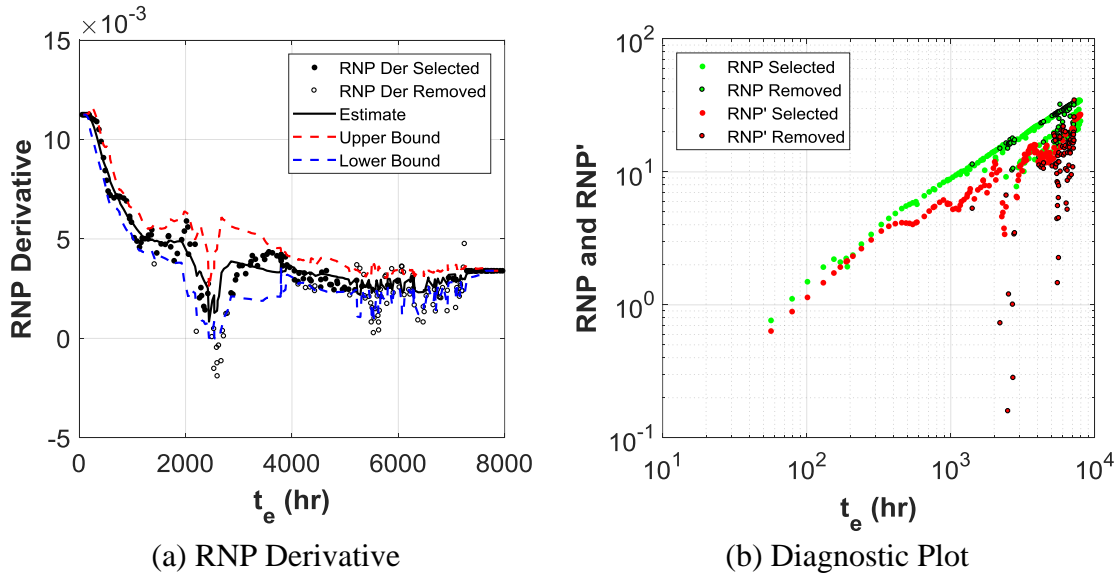


Figure 4.10 Illustration of (a) *RNP* derivative outlier removal and (b) Diagnostic plot before and after the outlier removal

4.2.1.2 Drainage Volume vs. Time Calculation

As described in the last subsection, RNP is calculated based on field BHP and rate data and RNP time derivative is from the output of regression analysis. After that, the drainage volume can be determined based upon the local RNP time derivative w.r.t material balance time t_e :

$$\frac{1}{V_d(t_e)} \equiv c_t \frac{dRNP_{wf}(t)}{dt_e} \quad \text{where} \quad RNP_{wf}(t) = \frac{\Delta p_{wf}(t)}{q_w(t)} \quad (4.22)$$

as exhibited in Figure 4.11. The RNP and RNP time derivative can be further used as Diagnostic plot for PTA and drainage volume vs. time relation obtained during the process will be used as input for $w(\tau)$ inversion. The drainage volume curve obtained is not monotonic, which indicates that it captures more details of rate and BHP change during the production history than a global fitting approach. Thus, we expect to see more flow geometry details in the $w(\tau)$ inversion results.

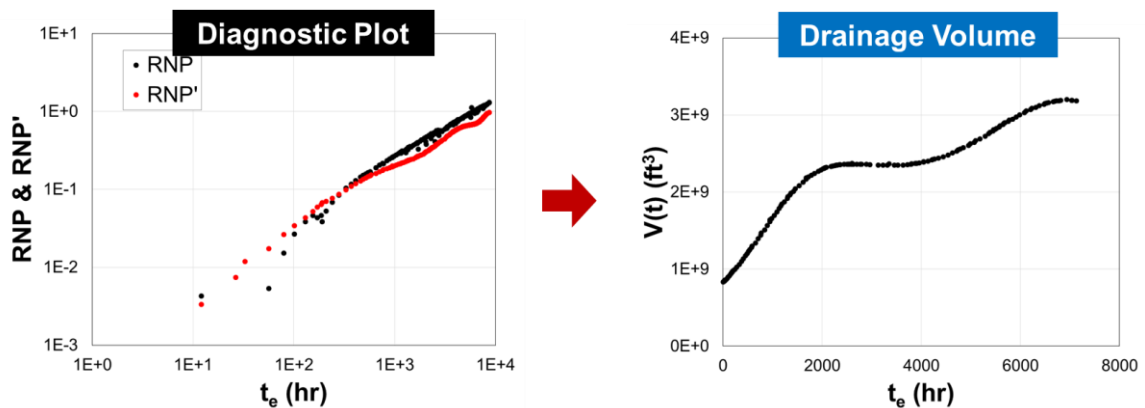


Figure 4.11 Overview of proposed drainage volume calculation (reprinted with permission from Wang et al, 2018)

4.2.2 $w(\tau)$ Drainage Volume Geometry Function Inversion

In the previous section, I have shown how to calculate drainage volume from noisy production data and the drainage volume obtained will be used as the input for $w(\tau)$ inversion. As shown in the chapter introduction, the previous $w(\tau)$ inversion algorithm is unsatisfactory for non-monotonic drainage volume, and thus a better approach is needed to resolve this issue. In this section, I will first explain the steps to convert the inverse problem to an optimization process so that we will obtain a smooth and positive $w(\tau)$ result, followed by a validation with bounded linear flow model. Then, I will show how the most important factor, i.e., the length of production history, affects the $w(\tau)$ inversion results by conducting a sensitivity study on various lengths of production history used as the $w(\tau)$ inversion input. Next, after successfully interpreting $w(\tau)$ from production data, we can further use it as a forward model to predict EUR under reservoir volume uncertainty. Finally, I will show the influences of reservoir volume uncertainty on EUR estimate with synthetic cases.

4.2.2.1 Regularized Least Squares Optimization

In order to resolve the previous inversion issues of generating unstable, nonpositive $w(\tau)$ values as well as unclear signals for non-monotonic drainage volumes, we now treat the problem as an optimization under constraints, and solve the integral equation as a regularized least squares optimization.

We approximate $w(\tau)$ using the 4th order B-spline basis functions (Ramsay *et al.*, 2009), and the drainage volume expression now becomes:

$$V_d(t) \approx \int_0^{\infty} e^{-\tau^2/4t} w(\tau) d\tau \quad \text{where} \quad w(\tau) = \sum_{k=1}^{n_{\text{basis}}} \alpha_k \phi_k(\tau) \quad (4.23)$$

Here ϕ_k 's are the basis functions and the α_k 's are their coefficients, which now become the unknowns.

The objective function is shown in Eq. (4.24): the first term represents residual sum of square errors, the second term is a roughness penalty used to guarantee curve smoothness (Green and Silverman, 1994), subject to a non-negative $w(\tau)$ constraint.

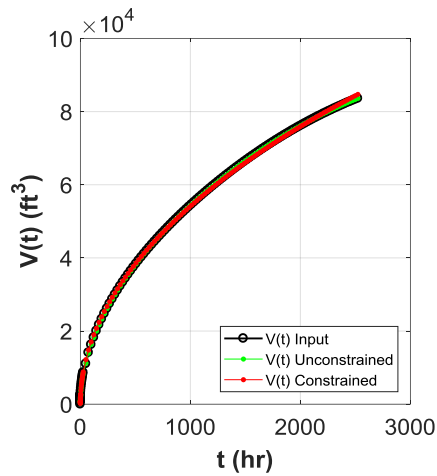
$$\begin{aligned} \min_{\alpha} \quad & \frac{1}{2} \|\mathbf{V} - \mathbf{A}\alpha\|_2^2 + \frac{\lambda}{2} \|\mathbf{w}''\|_2^2 \quad \text{subject to } w(\tau) \geq 0 \\ \Rightarrow \min_{\alpha} \quad & \frac{1}{2} \alpha^T (\mathbf{A}^T \mathbf{A} + \lambda \mathbf{M}) \alpha - \mathbf{V}^T \mathbf{A} \alpha + \frac{1}{2} \mathbf{V}^T \mathbf{V} \quad \text{subject to } w(\tau) \geq 0 \end{aligned} \quad (4.24)$$

where, $A_{ij} = \int_0^{\infty} \phi_j(\tau) e^{-\tau^2/4t_i} d\tau$, $M_{ij} = \int_0^{\infty} \phi_i''(\tau) \phi_j''(\tau) d\tau$, $\mathbf{V} = [V_1, V_2, \dots, V_{n_t}]^T$, and λ is the weight of the roughness penalty term. Selecting λ is not completely arbitrary. λ is calibrated by residual which will make the two terms at a comparable magnitude.

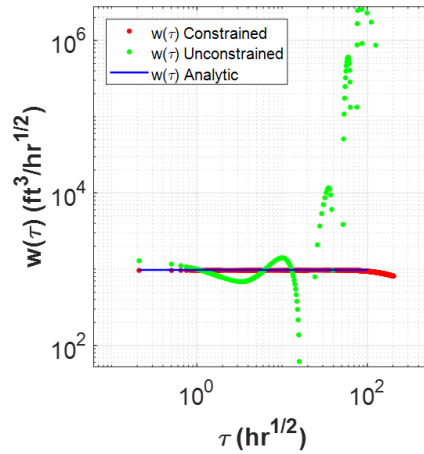
The τ is discretized from 0 to infinity with the following discretization scheme: the first interval is from $\tau = 0$ to τ_1 and the last interval is from τ_{n_t} to infinity, where all the τ_j 's are generated with the detectability condition as: $(2\tau_j)^2 / 4t_j = 4 \Rightarrow \tau_j = 2\sqrt{t_j}$. The roundtrip time is t_j for a detectable pressure response to propagate from the well to location τ_j , and back again.

4.2.2.2 Validation of the Drainage Volume Inversion

The bounded linear flow model was chosen to validate the new inversion algorithm. The drainage volume calculated from ECLIPSE simulation was used as the input for the unconstrained/constrained inversion process to calculate $w(\tau)$. The $w(\tau)$ obtained from inversion can be used to back calculate the drainage volume as a validation of the internal consistency between inverse/forward computation. Figure 4.12 (a) shows that both the unconstrained and the constrained $w(\tau)$ inversions give results consistent with the input drainage volume computed from the ECLIPSE production data. However, in Figure 4.12 (b), we see very different inversion results depending upon the constraints. The new inversion algorithm yields both physical (positive) and smooth $w(\tau)$ values, consistent with the constant value expected for bounded linear flow. At $\tau > \tau_{res}$, the $w(\tau)$ from new algorithm leaves the linear trend due to the boundary effects. In contrast, the unconstrained estimate of $w(\tau)$ is oscillatory, non-positive over portions of the solution, and does not match the analytic constant value, even at small τ .



(a) Drainage Volume



(b) Diagnostic Plot

Figure 4.12 (a) $V(t)$ comparison among optimization input from ECLIPSE (black curve), unconstrained (green curve), and constrained (red curve) optimizations; (b) $w(\tau)$ comparison among unconstrained (green curve), constrained (red curve) optimizations, and analytic value (blue line)

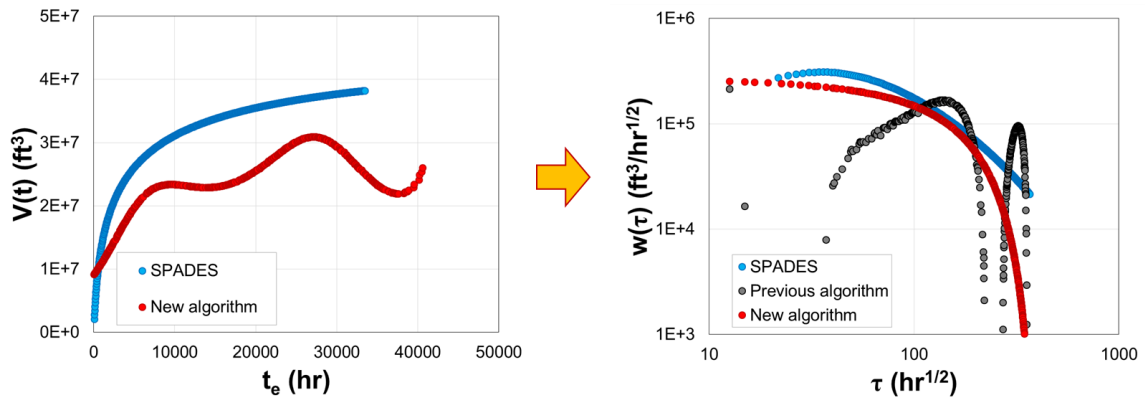


Figure 4.13 Comparison of $w(\tau)$ inversion results by SPADES (reference), previous algorithm, and new algorithm with non-monotonic drainage volume

As a comparison with previous $w(\tau)$ inversion algorithm, we choose the non-monotonic drainage volume as input and plot the inversion results in Figure 4.13. I further show the results from SPADES, an in-house software for unconventional reservoir production data analysis, as a reference. SPADES utilizes global curve fitting for drainage volume calculation plus previous $w(\tau)$ inversion algorithm, so the drainage volume input

for $w(\tau)$ inversion is different for SPADES. as illustrated in Figure 4.13. From the comparison, we know that SPADES yields smooth $w(\tau)$ and it captures the overall trend of $w(\tau)$ successfully. In the left part of $w(\tau)$ plot, we can see the previous algorithm is not stable; while new algorithm yields better resolution so it picks up more features (e.g., zero slope line which indicates linear flow). In the right part of $w(\tau)$ plot, we can see previous algorithm gives oscillatory trend and SPADES goes right in the middle; while the new algorithm still generates a stable curve which tends to compensate the oscillatory curve predicted by the previous algorithm. This demonstrates that the new algorithm gives positive and smooth $w(\tau)$ values which has a better resolution at small τ and picks up more features (clear signal) to identify flow geometry change.

4.2.2.3 Production History Sensitivities

The validation example indicates that our inversion algorithm appears to be both accurate and robust for both bounded reservoirs and cases with non-monotonic drainage volumes. However, when performing production analysis in a bounded system, we expect that the production response will be characterized by one or more flow regimes, long time boundary dominated flow, and the transitions between them. We now examine the impact of the length of the production history, t_h , with specific attention to the transition to boundary dominated flow, for the bounded linear and bounded radial models described previously. We return to the concept of the limit of detectability, in this case, applied to a pressure front that propagates from the well to the reservoir boundary, and back again,

$$\tau = 2\tau_{res} .$$

$$\frac{(2\tau_{res})^2}{4t_{LOD}} = 4 \Rightarrow t_{LOD} = \frac{\tau_{res}^2}{4} \quad (4.25)$$

For our two model examples used for EUR prediction demonstration in the last chapter, we obtain $t_{LOD} = 106.7 \text{ days}$ for bounded linear flow and $t_{LOD} = 308.3 \text{ days}$ for bounded radial flow. During inversion, the diffusion kernel is set to be 1-exponential term since the reservoir size is not known a priori. The τ intervals are generated with the round trip limit of detectability at each time: $(2\tau_j)^2/4t_j = 4$. Various lengths of production history t_h compared to t_{LOD} were used for $w(\tau)$ inversion and the results are shown in Figure 4.14 and Figure 4.15. From both plots, one may conclude that we start to observe the impact of the finite size of the reservoir once the production history reaches a time of $t_h = 2t_{LOD}$. At earlier times $V_p(\tau)$ continues to grow unbounded, while it approaches a finite value after this time. For these longer time cases, $w(\tau)$ also decreases at early τ . Additional analysis has shown that this is a consequence of the approximation of the 3-term exponential kernel $K(\tau, t)$ with the 1-term exponential $e^{-\tau^2/4t}$ during the inversion process. Although this is beyond the scope of the current study, this signature may provide information on reservoir size during the inversion process.

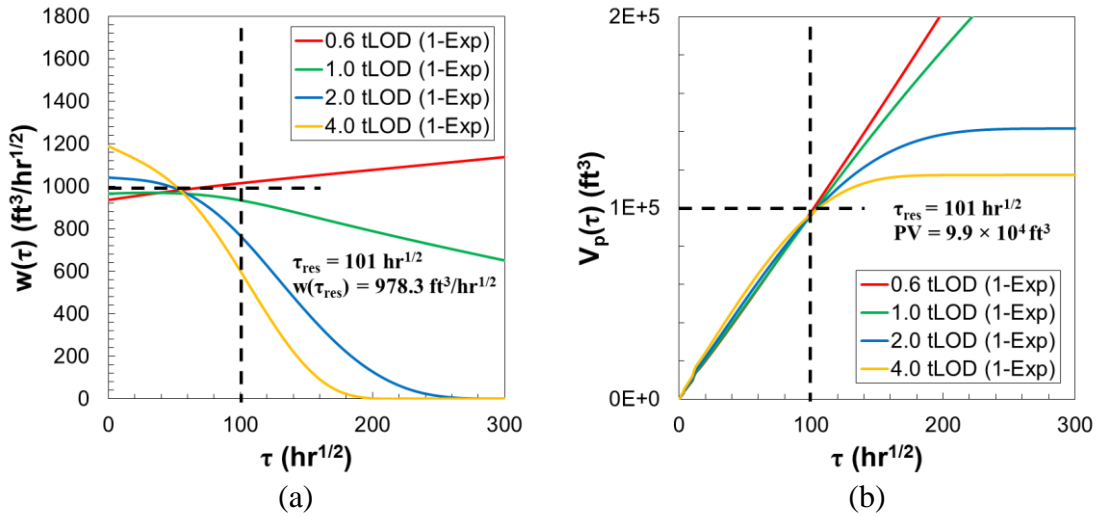


Figure 4.14 Comparison of bounded linear flow drainage volume inversion results using various lengths of production history for (a) $w(\tau)$ vs. τ and (b) $V_p(\tau)$ vs. τ (reprinted with permission from Wang et al, 2018)

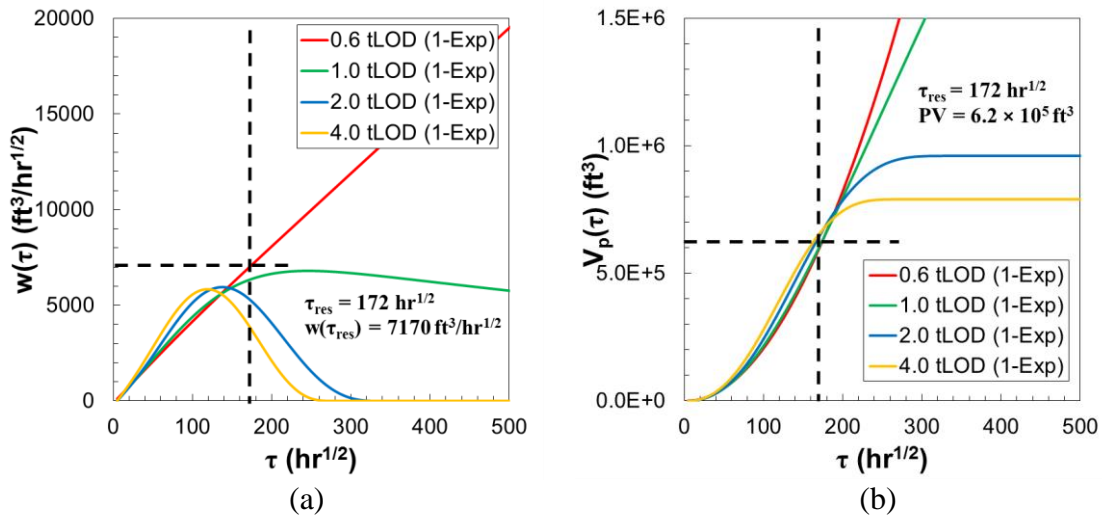


Figure 4.15 Comparison of bounded radial flow drainage volume inversion results using various lengths of production history for (a) $w(\tau)$ vs. τ and (b) $V_p(\tau)$ vs. τ (reprinted with permission from Wang et al, 2018)

The drainage volume inversion above assumes we have no idea about the finite reservoir size and the entire production history is an infinite acting process. What if we know τ_{res} before conducting the inversion? Here, the bounded linear flow model is chosen

and the upper limit of τ is set to be τ_{res} . Drainage volume inversion results with 1-term and 3-term exponential kernels are illustrated in Figure 4.16 and Figure 4.17, respectively. Comparing these two figures with Figure 4.14, we observe that we now have sensitivity to finite reservoir size and having more accurate drainage volume give us nice, stable, and physically meaningful inversion results. Even at $t = 0.6t_{LOD}$ in Figure 4.17 (a), we have already seen the finite size effects, because $w(\tau)$ from inversion is both flat and close to the actual $w(\tau)$ (horizontal black dashed line). This means that the inversion process is actually more sensitive than the limit of detectability, which also goes back to the general claim that working in τ is more precise than working in time. t_{LOD} is very specifically looking at when is the welltest derivative of the reflection becoming about 1% compared to the value of unity.

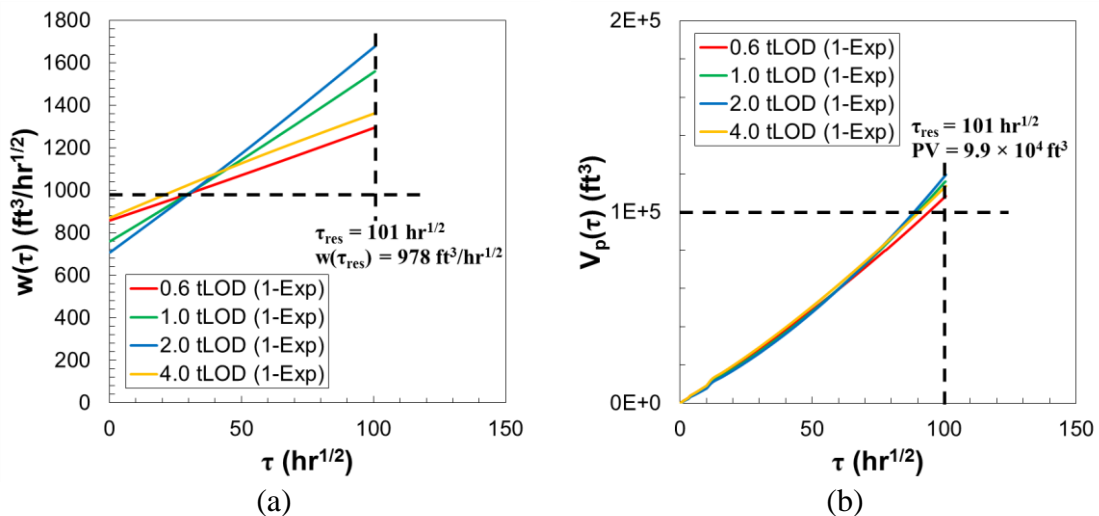


Figure 4.16 Comparison of bounded linear flow drainage volume inversion results using known τ_{res} and 1-term exponential kernel and various lengths of production history for (a) $w(\tau)$ vs. τ and (b) $V_p(\tau)$ vs. τ

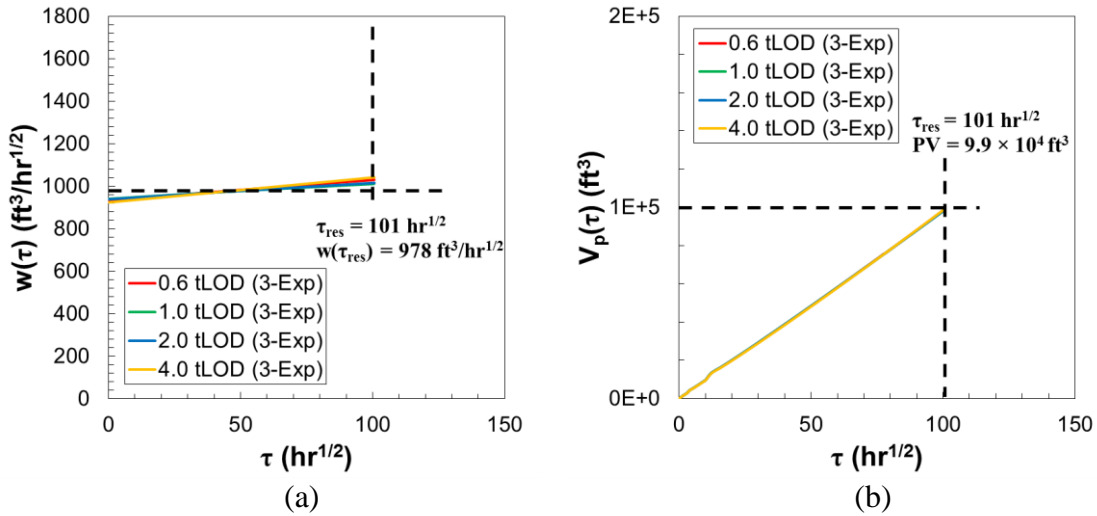


Figure 4.17 Comparison of bounded linear flow drainage volume inversion results using known τ_{res} and 3-term exponential kernel and various lengths of production history for (a) $w(\tau)$ vs. τ and (b) $V_p(\tau)$ vs. τ

4.2.2.4 EUR Prediction

After obtaining physical $w(\tau)$ from inversion, we may take a step further and use $w(\tau)$ as a forward reservoir model to conduct production predictions for field and well development, e.g., EUR prediction. Here, we take the 10-HF MTFW case as an example and the model is shown in Figure 4.18 and properties are listed in Table 4.1.

Property	Value	Unit
h	50	<i>ft</i>
L_{res}	2093	<i>ft</i>
w_{res}	1550	<i>ft</i>
x_f	102.5	<i>ft</i>
w_f	0.24	<i>in</i>
x_s	64.3	<i>ft</i>
V_{res}	6.21×10^5	<i>ft</i> ³
k_m	200	<i>nd</i>
k_f	1000	<i>md</i>
ϕ	0.06	-
μ	1.0	<i>cp</i>
c_t	1×10^{-5}	<i>psi</i> ⁻¹
B	1.0	<i>rb/bbl</i>
r_w	0.5	<i>ft</i>
q_w	0.1	<i>bbl/day</i>
Δp_{wf}	4500	<i>psi</i>
t_{prod}	7.2×10^5	<i>day</i>

Table 4.1 Reservoir, fluid and wellbore properties of 10-HF MTFW case (reprinted with permission from Wang et al, 2018)

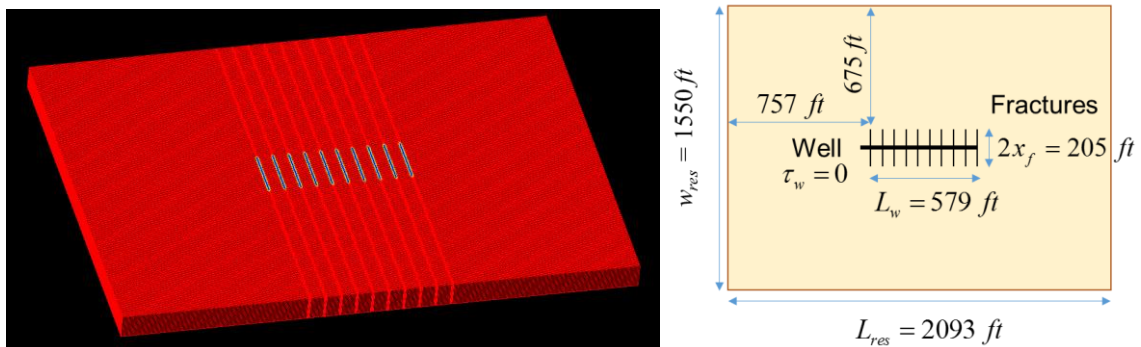


Figure 4.18 ECLIPSE model overview of 10-HF MTFW case (reprinted with permission from Wang et al, 2018)

We make the following two specific predictions: BHP performance prediction at a given fixed rate drawdown, and EUR prediction at a certain fixed BHP drawdown with a specific flow rate cutoff. We mainly focus on $w(\tau)$ inversion with production history from beginning until fracture interference, and then make predictions with our asymptotic approximations. We may choose either 1 or 3 exponential term(s) in the diffusion kernel during prediction process: staying with 1-exponential implies that we believe the reservoir is currently under infinite acting and the production is infinite; while with 3-exponential, we will handle the fracture interference by treating it as an equivalent BDF period within SRV. Note that τ_{res} is a necessary input for 3-exponential diffusion kernel and is chosen to be at the stagnation line between fractures as $\tau_{res} = \tau_{fs}/2$. The results are compared with those from ECLIPSE simulator are shown in Figure 4.19, where the black dashed lines represent so-called pseudo pseudo steady state (PPSS) which is the fracture interference period. We observe that 3-exponential asymptotic approximation predicts the trend of both BHP under fixed rate and 1/RNP under fixed BHP drawdowns successfully; 1-exponential asymptotic approximation also works until PPSS has fully established. This means that when performing reliable production predictions, we may choose either 1-exponential asymptotic approximation for pure transient period or 3-exponential asymptotic approximation for PPSS/BDF with an assumption of τ_{res} . The latter one leads to a further discussion on reservoir volume sensitivities for EUR prediction.

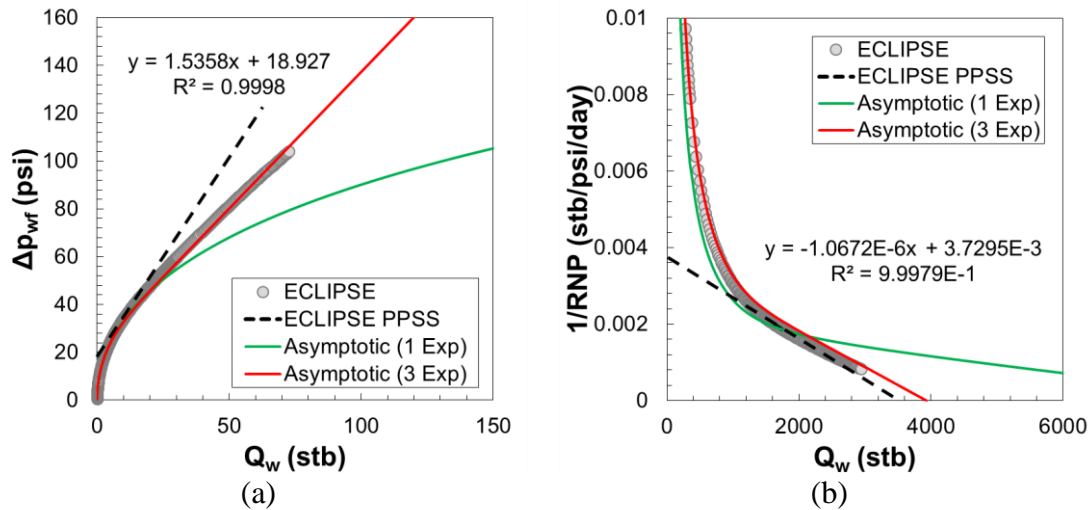


Figure 4.19 Prediction results comparison between 1 & 3 exponential terms asymptotic solutions of 10-HF MTFW case (a) Δp_{wf} vs. Q_w plot for fixed rate drawdown; (b) $1/RNP$ vs. Q_w plot for fixed BHP drawdown (reprinted with permission from Wang et al, 2018)

4.2.2.5 Reservoir Volume Sensitivities

For a given production history, the most important sensitivity for EUR prediction is the reservoir size. If the reservoir response reaches PSS/BDF, then this volume can be estimated. However, in unconventional reservoir analysis this volume is not generally observed, and must be treated as a sensitivity. If production time is too short, and the field response is still infinite acting, then the estimates of reservoir volume should be expected to diverge. If production time captures the transition to SRV, and approximate PSS flow, then the estimates of reservoir volume will be too low, as they do not include the contribution of volumes beyond the SRV.

In this sensitivity study, V_{det} represent the reservoir volume detected from production history t_h . t_{LOD} is chosen to be the reference time. Theoretically, for bounded linear flow, it simply describes the time when boundary effect will be detected at the

wellbore; for 10-HF MTFW case, it refers to the time when two edge fractures start interfering each other. Since we are not quite certain on the actual reservoir size V_{res} when using $t_h = t_{LOD}$, we further select V_{res} to be 1 (extreme lower estimate), 5, & 10 times of V_{det} . The corresponding reservoir boundary, τ_{res} , can then be estimated assuming that $w(\tau) = w(\tau_{det})$ for region $\tau > \tau_{det}$. Here, we choose bounded linear flow and 10-HF MTFW case as examples to show how reservoir volume influences the EUR prediction through $1/RNP$ vs. Q_w plot in Figure 4.20. We observe that, at a given production history of $t_h = t_{LOD}$, the EUR prediction uncertainty is not very sensitive to reservoir volume as long as the cutoff production rate is not too low compared to the one at the end of production history. On the other side, UR is very sensitive to reservoir volume, as what has been expected. It increases along with the reservoir size. Another important observation is that our asymptotic approximation has a good match with historical data for bounded linear flow model, since the actual τ_{res} is constant along reservoir boundary. For 10-HF MTFW case, however, this is not the case since each individual fracture would have its own τ contours and the overlap of τ contours would result in complex τ_{res} along SRV boundary. Thus, the match with historical data is not perfect as shown in Figure 4.20 (b).

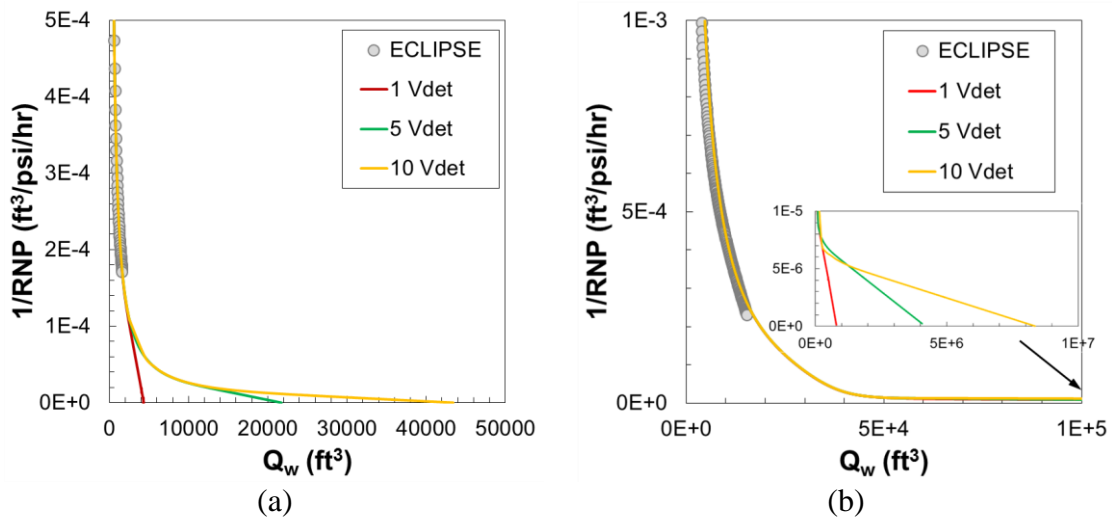


Figure 4.20 Reservoir volume sensitivity for EUR prediction on $1/RNP$ vs. Q_w plot of (a) bounded linear flow; (b) 10-HF MTFW case (reprinted with permission from Wang et al, 2018)

4.3 Field Application: Montney Field

In this section, I will take a well with multiple hydraulic fractures from Montney field as an example to evaluate the matrix permeability as well as predict EUR at different production cutoffs. For the matrix permeability, I will also conduct traditional PTA as well as buildup analysis to validate the one yielded by the asymptotic approximation.

4.3.1 Field Introduction and Production Data Illustration

The Montney field is located in British Columbia, Canada. The well of interest has a production history of nearly two years. The production history is illustrated in Figure 4.21. The RNP vs. material balance time of the well is plotted in Figure 4.22. For Montney Well, material balance time doesn't work well during the latter part of the production history, and generates outliers as indicated by the trend of jumping back and forth in time.

This is mainly caused by the large variations in production rate during the latter period shown in Figure 4.21. Thus, those data are not suitable for PTA analysis.

Early time data was used for production analysis (green shadow) and six buildup (BU) periods can be found in the entire history. The production data will be interpreted using our new methodology. The first buildup will also be interpreted for comparison.

As this is an example of gas production, adjusted (pseudo) pressures are used in both the Diagnostic and Specialized plots (Lee *et al.*, 2003). This allows the analysis to proceed as if it were a slightly compressible (liquid) system.

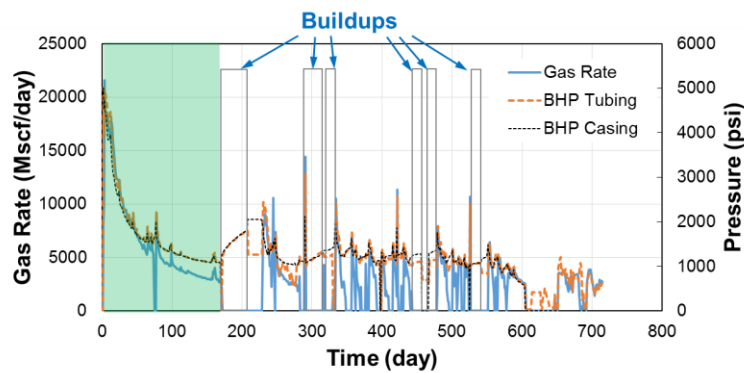


Figure 4.21 Overview of production history (reprinted with permission from Wang et al, 2018)

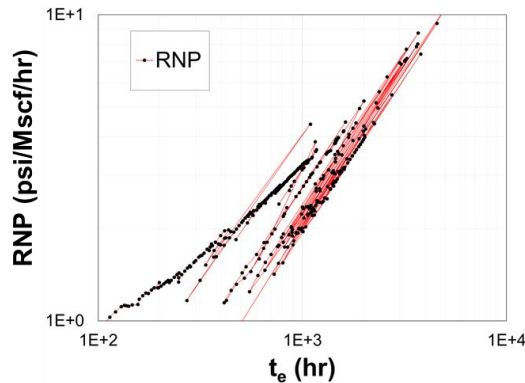


Figure 4.22 Illustration of RNP vs. material balance time of Montney Well

Property	Value	Unit
h	200	<i>ft</i>
n_f	28	
x_f	250	<i>ft</i>
x_s	182	<i>ft</i>
p_i	4620	<i>psi</i>
T_{res}	190	$^{\circ}F$
ϕ	0.045	-
S_w	0.25	-
L_w	5000	<i>ft</i>
<i>Buildup Information</i>		
q_{last}	2867	<i>Mscf/day</i>
\bar{p}	1080	<i>psi</i>
$\bar{\mu}_g$	0.0183	<i>cp</i>
\bar{c}_t	1.21×10^{-4}	<i>psi⁻¹</i>
\bar{B}_g	0.0161	<i>Mcf/Mscf</i>
<i>PTA Information</i>		
\bar{p}	3350	<i>psi</i>
$\bar{\mu}_g$	0.0172	<i>cp</i>
\bar{c}_t	2.06×10^{-4}	<i>psi⁻¹</i>

Table 4.2 Reservoir, fluid and wellbore properties of Montney field (reprinted with permission from Wang et al, 2018)

4.3.2 Traditional Pressure Transient Analysis

4.3.2.1 Permeability Estimation from t_{elf}

As described earlier, in PTA for a MTFW, the estimate of matrix permeability is based upon the time for the end of linear flow, obtained from the beginning of a transition away from the ½ slope line in the welltest derivative curve of the Diagnostic plot, Figure

4.23 (a). Obtaining the break is a challenging task in most cases because of the scatter of the data. It is really hard to find the end of linear flow in the red cloud of RNP' as shown in Figure 4.23 (a). An alternative approach is to work directly with the RNP curve on the specialized plot, Figure 4.23 (b), but as discussed earlier, the signature for the end of linear flow is less obvious in comparison to the signature on the derivative plot. We have chosen to fit the data on the specialized plot (vs. $\sqrt{t_e}$) to estimate the time coming off linear flow as $\sqrt{t_{elf}} = 18 \pm 2 \text{ hr}^{1/2} \Rightarrow t_{elf} = 256 \sim 400 \text{ hr}$, as illustrated in Figure 4.23. This information can be further used for matrix permeability estimation following Song and Ehlig-Economides (2011) as:

$$k_m = \frac{\pi \phi \bar{\mu}_g \bar{c}_t x_s^2}{64 t_{elf}} = 3.0 \pm 0.6 \mu d \quad (4.26)$$

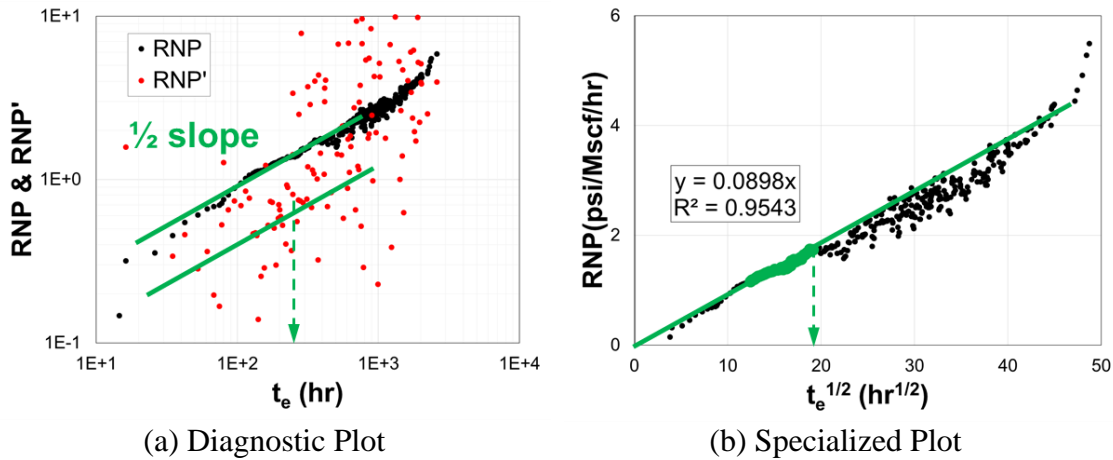


Figure 4.23 Pressure transient analysis for t_{elf} with (a) Diagnostic plot (b) Specialized plot (reprinted with permission from Wang et al, 2018)

Since we previously showed the approach for a better estimate of RNP' , we can conduct PTA analysis with processed RNP' instead and both the Diagnostic and Specialized plots are shown in Figure 4.24. We now have a clearer trend of end of linear flow as well as a more obvious t_{elf} identification $\sqrt{t_{elf}} = 17 \pm 1 \text{ hr}^{1/2} \Rightarrow t_{elf} = 256 \sim 324 \text{ hr}$. As shown in the Specialized plot, Figure 4.24 (b), it is better seen in the processed RNP' trend than the RNP trend. The matrix permeability estimation now becomes:

$$k_m = \frac{\pi\phi\bar{\mu}_g\bar{c}_t x_s^2}{64t_{elf}} = 3.4 \pm 0.4 \mu d \quad (4.27)$$

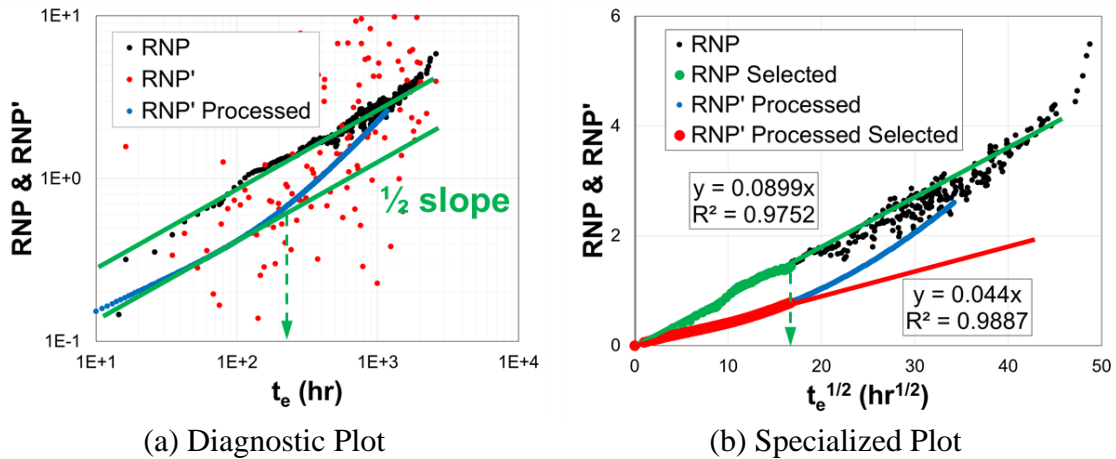


Figure 4.24 Pressure transient analysis for t_{elf} with (a) Diagnostic plot (b) Specialized plot using processed RNP'

4.3.2.2 Permeability Calculation via Buildup Analysis

Here we use the first buildup for pressure transient analysis. For the remaining 5 buildups, the signature is not consistent with a linear response for the other shut-in periods and thus they are excluded from analysis. As demonstrated in Figure 4.25, buildup 1 is the only one which shows a clear $\frac{1}{2}$ slope among all the six buildups. Following the usual

PTA analysis, data that shows the $\frac{1}{2}$ slope line signature is identified in the Diagnostic plot and the slope vs. $\sqrt{t_e}$ is used to calibrate properties, as shown in Figure 4.26. All the other quantities are known as shown in Table 4.2 and the slope in Figure 4.26 (b) can be determined as $m = 30 \text{ psi} \cdot \text{hr}^{-1/2}$. This estimate of matrix permeability utilizes the fracture half length provided by the operator.

$$k_m = \left(4.06 \cdot \frac{q_{last} \bar{B}_g}{x_f h n_f m} \right)^2 \frac{\bar{\mu}_g}{\phi \bar{c}_i} = 2.1 \mu d \quad (4.28)$$

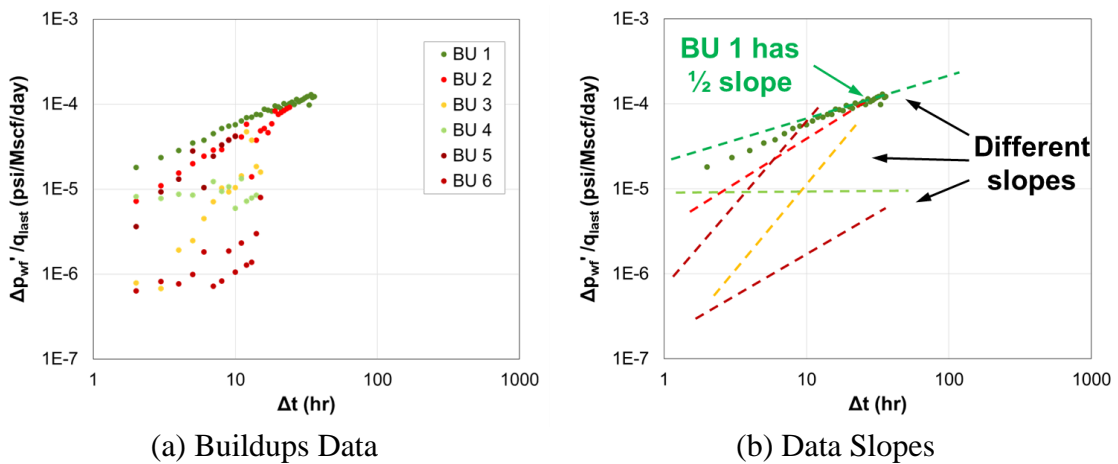


Figure 4.25 Illustration of six buildup periods with (a) buildup data (b) data slopes

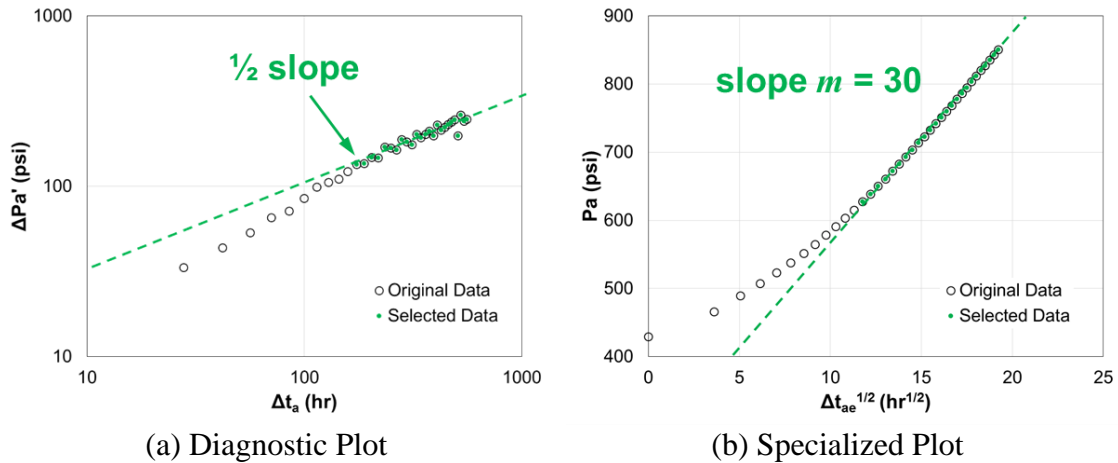
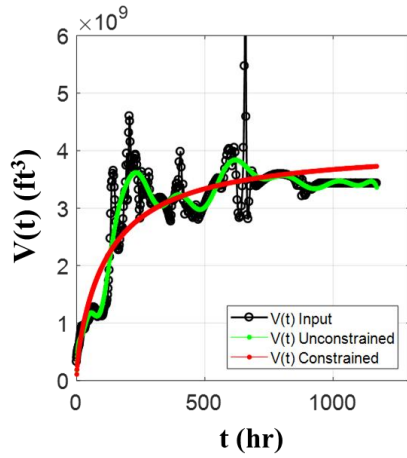


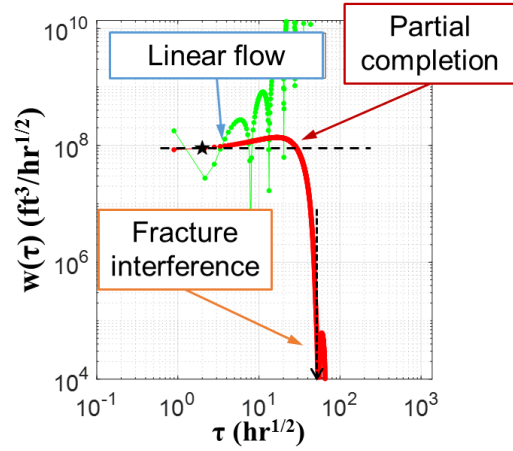
Figure 4.26 Buildup analysis with (a) Diagnostic plot (b) Specialized plot (reprinted with permission from Wang et al, 2018)

4.3.3 Diagnostic Analysis based on the Drainage Volume

The drainage volume was calculated from production data and was used as input for the $w(\tau)$ inversion, as shown in Figure 4.27, where we observe that the signature for fracture interference occurs at $\tau_{fs} = 50 \text{ hr}^{1/2}$, as shown in the figure. Fracture interference in the drainage volume occurs when the drainage volumes from each fracture begin to overlap, i.e., at the stagnation line between fractures. We will use this value of τ to estimate the matrix permeability. Another observation that $w(\tau)$ drops below its value near the wellbore at $\tau = 30 \text{ hr}^{1/2}$, implying the end of linear flow, which can be used to estimate t_{elf} for comparison with the Diagnostic plot and Specialized plot for PTA analysis. Other observations from $w(\tau)$ drainage volume Diagnostic plot include linear flow near the wellbore and partial competition effects. Note that the partial completion effects are not resolved on the usual diagnostic plots and this is the interpretation by Xue *et al.* (2016) seen in other synthetic examples and field cases, and now observed here too.



(a) Drainage Volume



(b) Diagnostic Plot

Figure 4.27 (a) $V(t)$ comparison among optimization input from field production data (black curve), unconstrained (green curve), and constrained (red curve) optimizations; (b) $w(\tau)$ comparison among unconstrained (green curve) and constrained (red curve) optimizations (reprinted with permission from Wang et al, 2018)

We can also see the performance of the different inversion algorithms in this field example. Although the input $V(t)$ was calculated using the data smoothing and outlier described earlier, it is still not a smooth curve. However, the model $V(t)$ obtained by the constrained optimization is monotonic, and $w(\tau)$ is positive, as expected physically. The unconstrained inversion is also shown as reference, and is not suitable for analysis.

4.3.3.1 t_{elf} Estimation

In the discussion above, the end of linear flow occurs at $\tau = 30 \text{ hr}^{1/2}$. The limit of detectability allows us to calculate the time coming off linear flow t_{elf} .

$$\frac{(2\tau)^2}{4t_{elf}} = 4 \Rightarrow t_{elf} = \frac{\tau^2}{4} = 225 \text{ hr} \quad \text{and} \quad \sqrt{t_{elf}} = 15 \sqrt{hr} \quad (4.29)$$

This is close to the value obtained previously, although clearly this value for τ is easier to select than t_{elf} on the Diagnostic plot or Specialized plot, while the latter one requires a careful linear regression analysis to find the right time on the Specialized plot.

4.3.3.2 Permeability Calculation

As shown in the discussion before, the signature for fracture interference occurs at $\tau_{fs} = 50 \text{ hr}^{1/2}$. Based on Eikonal equation, we can estimate the matrix permeability as:

$$\tau_{fs} = \frac{x_s}{2\sqrt{\alpha}} \Rightarrow k_m = \left(\frac{x_s}{2\tau_{fs}} \right)^2 \phi \mu c_t = 3.7 \text{ } \mu d \quad (4.30)$$

The result is close to those estimated from both buildup and PTA with end of linear flow during production.

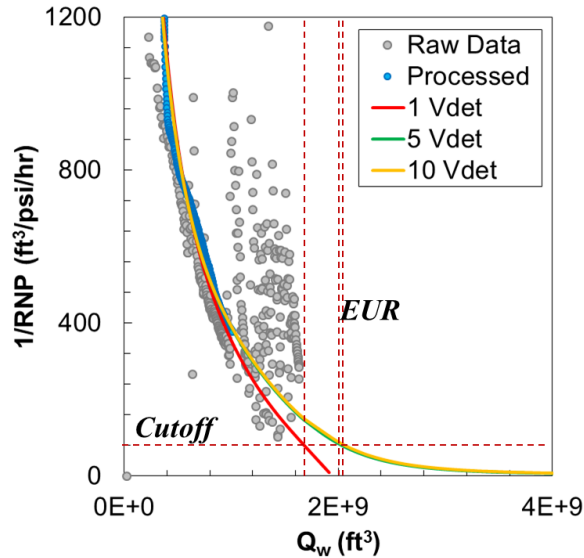
4.3.4 EUR Prediction

After interpreting $w(\tau)$ from Montney well production data, we can further use it as forward model and estimate EUR for the well. We do not observe BDF in the field data, so only the near well $w(\tau)$ is calibrated by field history. As described previously, we choose the fundamental uncertainty in unconventional, the reservoir size V_{res} , to be 1, 5, & 10 times of V_{det} interpreted from production history and assume $w(\tau) = w(\tau_{det})$ for region $\tau > \tau_{det}$ in order to determine the corresponding reservoir boundary τ_{res} . After performing production prediction with 3-exponential term asymptotic approximation, we plot the results in Figure 4.28. It shows an example of EUR prediction at a constant BHP

drawdown of $\Delta p_{wf} = 3500 \text{ psi}$ with two cutoff production rates, where the gray dots represent the raw production data and blue ones stand for the processed production data with the approach proposed for drainage volume calculation. The reservoir volume uncertainty won't affect EUR estimate if the cutoff production rate $q_{w,cutoff} > 3.36 \times 10^4 \text{ Mscf/day}$ ($1/RNP > 400 \text{ ft}^3/\text{psi/hr}$). Figure 4.28 is convenient for EUR predictions. For example, given a certain cutoff production rate $q_{w,cutoff} = 6.72 \times 10^3 \text{ Mscf/day}$ ($1/RNP = 80 \text{ ft}^3/\text{psi/hr}$), the corresponding EUR uncertainty range can be estimated as $1.68 \times 10^9 \text{ ft}^3 < EUR < 2.06 \times 10^9 \text{ ft}^3$, as listed in Figure 4.28 (a). If the cutoff production rate is lowered down to $q_{w,cutoff} = 3.36 \times 10^3 \text{ Mscf/day}$ ($1/RNP = 40 \text{ ft}^3/\text{psi/hr}$), the corresponding EUR uncertainty range become as wide as $1.80 \times 10^9 \text{ ft}^3 < EUR < 2.50 \times 10^9 \text{ ft}^3$, as listed in Figure 4.28 (b). This is an example to show how we can easily estimate EUR with various economic production rates via our proposed approach. If we take a further look at the uncertainty range of EUR vs. uncertainty range of V_{res} for both the Montney Well and previous synthetic cases in Figure 4.20, we can see that even though the unknown V_{res} is an order of magnitude uncertain, it would only result in an uncertainty of EUR prediction by a factor of 1.3. It is because the EUR is pinned down by the production history.

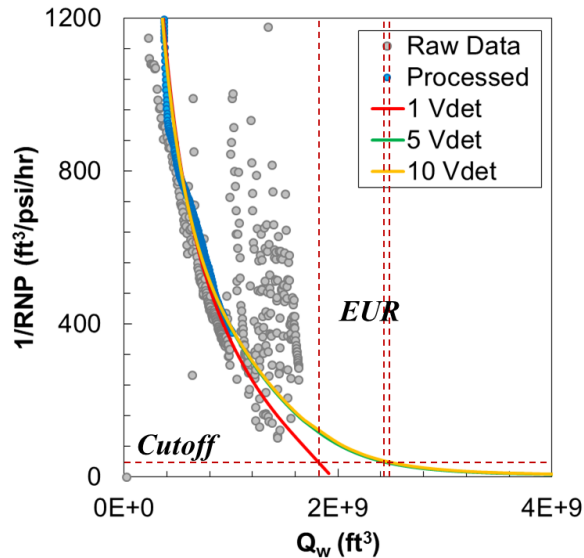
Throughout the field application, we know in order to achieve a reliable EUR prediction, the proposed drainage volume calculation technique helps to remove outliers and provides a smooth RNP time derivative for drainage volume calculation; and the proposed $w(\tau)$ inversion algorithm guarantees a both smooth and positive $w(\tau)$ curve which

is both well-calibrated by production data and to be used as a forward model for EUR prediction.



$V_{res} (ft^3)$	EUR (ft^3)
4.59×10^9	1.68×10^9
2.30×10^{10}	2.00×10^9
4.59×10^{10}	2.06×10^9

(a) EUR Prediction with $q_{w,cutoff} = 6.72 \times 10^3$ Mscf/day



$V_{res} (ft^3)$	EUR (ft^3)
4.59×10^9	1.80×10^9
2.30×10^{10}	2.42×10^9
4.59×10^{10}	2.50×10^9

(b) EUR Prediction with $q_{w,cutoff} = 3.36 \times 10^3$ Mscf/day

Figure 4.28 Montney well EUR predictions with (a) $q_{w,cutoff} = 6.72 \times 10^3$ Mscf/day and (b) $q_{w,cutoff} = 3.36 \times 10^3$ Mscf/day as well as reservoir volume uncertainty on 1/RNP vs. Q_w plot

4.4 Discussion

Let's first talk about the advantage of using $w(\tau)$ diagnostic analysis based upon drainage volume inversion over the traditional PTA. We know that the diffusivity equation has a solution that is infinite acting even at $t=0$. Thus, diffusion (pressure) goes everywhere once production occurs. It is important to know when the pressure drop is seen in the entire reservoir. The answer is actually right at the beginning. In traditional PTA, one may ask when we will see the additional contribution to the change of the welltest derivative curve. The answer is right at the limit of detectability. As mentioned in the previous chapters, working in τ (space) is more accurate than working in time. The main reason is that the $w(\tau)$ inversion process is actually more sensitive than the limit of detectability (t_{LOD}), since t_{LOD} is very specifically looking at when the welltest derivative of the reflection becomes about 1% compared to the value of unity, while for the inversion process it is not unnecessary to wait as long as t_{LOD} . Accordingly to the sensitivity tests on the length of production history used in the $w(\tau)$ inversion process, we don't need to include production history until t_{LOD} during inversion to detect the reservoir boundary from the novel $w(\tau)$ diagnostic plot.

For Montney Well, $x_s = 182\text{ ft}$ and $x_f = 250\text{ ft}$, we will see the fracture interference before the transition from pillbox to eclipse, so the pillbox is good enough. Montney Well data were collected six years ago, and the cluster spacing is become smaller and smaller during the past several years. This means that the pillbox is even better suited for the tighter spacing nowadays.

If we knew the size of the reservoir, we can get a really good $w(\tau)$ inversion even in boundary dominated flow when we use 3-term exponential kernel. If we have no idea about the reservoir size, we will just assume the reservoir is infinite acting, and thus we have a model where the assumptions that go into the inversion are incorrect. Even though, we can still interpret the reservoir size information from the $w(\tau)$ Diagnostic plot. This is what we do when we do our field analysis.

The proposed data-driven model-free approach is powerful in production data analysis for unconventional reservoirs. Compared to other popular and widely used PTA and RTA methods, it provides a simple and intuitive understanding of the transient drainage volume irrespective of the complexity of the reservoir depletion geometry. Unlike simple curve-fitting DCA or our previous studies, it has physical interpretation and yields better resolution, which can identify more detailed characteristics of the underlying flow geometry. Through Montney well application, we showed an improved quantitative interpretation for formation permeability from production data based on fracture cluster interference seen in the improved $w(\tau)$ plot, which is validated by buildup analysis and traditional PTA. Due to the improvements on numerical inversion for $w(\tau)$, we can easily make predictions on EUR at specified cutoffs using the interpreted $w(\tau)$ as a forward reservoir model.

With the unknown reservoir volume being orders of magnitude uncertain, the unknown EUR is much tighter, because the EUR is pinned down by the history.

4.5 Chapter Summary

In this chapter, I have shown how we proposed the approach for data-driven model-free analysis of production data without the presumption of specific flow regimes. The application to Montney well provides a simple and intuitive understanding of the transient drainage volume irrespective of the complexity of the reservoir depletion geometry. Beyond that, I explained how we developed an improved approach for the $w(\tau)$ inversion which yields better physical resolution and which can identify more detailed characteristics of the underlying flow geometry than previous studies, e.g., complex near fracture flow, linear flow, fracture interference, etc. The power and utility of the proposed methodology was first validated with synthetic examples and then demonstrated using a field example of a well from the Montney shale.

The improved methods for both drainage volume calculation as well as $w(\tau)$ inversion which shows more detailed features:

- The drainage volume calculation is no longer based on global curve fitting.
- The proposed approach improves upon the numerical inversion for $w(\tau)$.
- Inversion with 1-term exponential gives consistent $w(\tau)$ result until the well sees the boundary effects; inversion with 3-term gives consistent inversion results irregardless of boundary effects.
- $w(\tau)$ inversion process shows sensitivity in detecting boundary size effects.

I showed how we improved quantitative interpretation for formation permeability as well as successfully predicted EUR from production data for Montney well:

- The formation permeability interpretation is based on fracture cluster interference seen in $w(\tau)$ Diagnostic plot. The value is validated by both traditional PTA and buildup analysis.
- Various flow regimes can also be observed from our novel diagnostic plot, e.g., linear flow, partial completion, as well as fracture interference, following the conclusions by some other researchers.
- New methodology to predict EUR with reservoir volume uncertainty based on $w(\tau)$.

CHAPTER V

CONCLUSIONS AND FUTURE RESEARCH DIRECTIONS

5.1 Summary and Conclusions

In this dissertation, we have tried to combine the novel τ coordinate system with a series of semi-analytic approximations, in order to shed new light on the direct relationship between production data and the reservoir drainage volume, and further predict EUR.

We have learned how a pressure front propagates in infinite reservoir formations under a fixed rate drawdown, which is very important to welltest analysis and transient reservoir drainage volume calculation. We successfully avoided expensive numerical simulations and developed an alternative approach by directly solving the Eikonal equation which captures the pressure front propagation. The analogy between the propagating pressure front and a propagating wave front, making it applicable to pressure transient analysis in the petroleum industry. The validity of this assumption was also explored using some cases either with extremely heterogeneous permeability or a multi-point source. This chapter served as the foundation and starting point of the following study.

Next, we have developed and validated new asymptotic analytic approximations to handle both variable rate drawdown and boundary effects, based on the fixed rate solutions. We conducted a systemic validation of the proposed semi-analytic solution technique and extended its utility to more realistic cases, including large changes in reservoir properties, pressure transient analysis with wellbore storage, and rate transient

analysis in bounded reservoirs with fixed rate or fixed BHP production. We used this technique to describe pressure propagation from fractured wells into the surrounding formations and a better drainage volume characterization, which have been applied for both well spacing calculation and multi-stage fracture spacing optimization in unconventional reservoirs. Not only is it useful for the direct calculation of various welltest, rate transient and well performance concepts such as depth of investigation, welltest derivative, flow regimes and well productivity, but it is also helpful to predict pressure and flux spatial distributions at any time of interest.

Finally, we demonstrated the capability of the proposed data-driven model-free approach for production data analysis which does not require the presumption of specific flow regimes. The applications to synthetic models and field case showed that it provides a simple and intuitive understanding of the transient drainage volume and instantaneous recovery efficiency, irrespective of the complexity of the reservoir depletion geometry. In the current study we develop an improved approach for the $w(\tau)$ inversion which yields a better physical resolution and which can identify more detailed characteristics of the underlying flow geometry than previous studies, e.g., complex near fracture flow, linear flow, fracture interference, etc. The results of the analysis have been used for the characterization of hydraulic fracture and reservoir properties, including the prediction of fracture surface area, matrix permeability, and extended to the calculation of EUR. The power and utility of the proposed methodology was first validated with synthetic examples and then demonstrated with the Montney well.

The important findings and conclusions are listed below:

τ will serve as a good spatial coordinate such that $p(\bar{x}, t) \approx p(\tau(\bar{x}), t)$ and $q(\tau, t) \approx c_i w(\tau) \frac{\partial p}{\partial \tau}$, until we reach the following scenarios.

- First, since τ represents the propagation geometry for the first pressure front, it only gives satisfactory performance during early time ($t_d < 1$) for cases with a multi-point source like infinite conductivity hydraulic fractures.
- Second, when boundary dominated flow established, again, a single series of τ contours are no longer a good representative of the pressure contours, since it does not represent pressure front reflections at the boundary.
- Third, the bi-linear flow for finite conductivity fractures have the $t^{1/4}$ pressure drop response. However, all of the drainage volume approaches based on a single $\tau(\bar{x})$ have the $t^{1/2}$ pressure drop response, also at early time. The same value of τ exists in the fracture and in the matrix, but the solutions at these two locations follow different pressure transients and have different pressure drops.

However, modifications and improvements can be made with a combination of asymptotic solutions with superposition theory or introduction of multiple τ contours with superposition to improve or even overcome these imperfect sides.

The asymptotic approximation allows us to develop a number of interpretations of our production data. At a fundamental level, the formulation allows us to relate the pressure drop seen at a producing well to depletion within the reservoir. As a consequence,

the production data can be used to infer the instantaneous drainage volume of a well. It also provides a simple interpretation of the welltest derivative in terms of this drainage volume. The asymptotic pressure approximation works well until $w(\tau)$ is no longer sufficiently smooth and that $\frac{d\ln w(\tau)}{d\ln \tau}$ becomes negative. Our study shows that when reservoir heterogeneity has a large variance of heterogeneity or uncorrelated distribution ($L_{DCL} \rightarrow 0$), the value range of $\frac{d\ln w(\tau)}{d\ln \tau}$ becomes unbounded or even negative: the numerator scales as variance while denominator scales at correlation length. The successful generalization to variable rate and bounded reservoirs demonstrates the feasibility and capability of the generalized asymptotic approximation as well as its promising application to the analysis of field production data.

The proposed data-driven model-free approach is powerful in production data analysis for unconventional reservoirs. Compared to other popular and widely used PTA and RTA methods, it provides a simple and intuitive understanding of the transient drainage volume irrespective of the complexity of the reservoir depletion geometry. Unlike simple curve-fitting DCA or our previous studies, it has physical interpretation and yields better resolution, which can identify more detailed characteristics of the underlying flow geometry. Through Montney well application, we showed an improved quantitative interpretation for formation permeability from production data based on fracture cluster interference seen in the improved $w(\tau)$ plot, which is validated by buildup analysis and traditional PTA. Due to the improvements on numerical inversion for $w(\tau)$, we can easily

make predictions on EUR at specified cutoffs using the interpreted $w(\tau)$ as a forward reservoir model.

5.2 Future Research Directions

Based on the experiences obtained and lessons learned throughout various tests and comparisons, we would like to share several directions that are worth to be investigated in the future study, as summarized below:

- Application of superposition theory for cases with a multi-point source or interference, including but not limited to cases with wells connected to finite or infinite hydraulic fractures (or even with natural fractures), early interference between fractures caused by close well/fracture spacing due to infill drilling or refracturing, etc.
- Application of superposition in time for $w(\tau)$ interpretation with buildup data, which has high resolution BHP data and zero production rate
- Further enhanced discretization approach, which considers multiple transmission/reflection between each location and its adjacent neighbors with superposition algorithm and asymptotic solutions to reduce the mismatch between pressure front and τ contours caused by large heterogeneity

NOMENCLATURE

Roman symbols

A	cross-sectional area (ft^2)
$A_n(t)$	pressure amplitude of the n^{th} order in the time domain ($1/hr^{(n+2)/2}$)
$\tilde{A}_n(\bar{x})$	pressure amplitude of the n^{th} order in the frequency domain ($1/hr^{(n+2)/2}$)
b	decline curve exponent (dimensionless)
B	fluid formation volume factor (rb/stb)
\bar{B}_g	average gas formation volume factor ($Mcf/Mscf$)
c_t	total compressibility ($1/psi$)
\bar{c}_t	average total compressibility ($1/psi$)
D	decline rate ($1/hr$)
h	payzone thickness (ft)
HI	Heterogeneity Index (dimensionless)
i	imaginary unit
J	well productivity ($stb/psi/day$)
J_{BDF}	well productivity under boundary dominated flow ($stb/psi/day$)
J_{PSS}	well productivity under pseudo steady state ($stb/psi/day$)
k	permeability (md)
k_f	fracture permeability (md)

k_m	matrix permeability (<i>nd</i>)
$K(\tau, t)$	generalized diffusion kernel
$K_n(\tau, t)$	diffusion kernel of the n^{th} order
L_{DCL}	dimensionless correlation length (dimensionless)
L_{res}	reservoir length (<i>ft</i>)
L_w	well lateral length (<i>ft</i>)
m	exponent depending on flow geometry (dimensionless)
M	mobility ratio between inner and outer domain (dimensionless)
n_{basis}	number of basis functions
n_f	number of hydraulic fractures
n_t	number of data points in the production history
N_i	number of data points in the interval i
p	pressure (<i>psi</i>)
\bar{p}	average pressure (<i>psi</i>)
\tilde{p}	pressure in frequency domain (<i>psi</i>)
p_a	adjusted pressure for gas (<i>psi</i>)
p_D	dimensionless pressure drop (dimensionless)
p_i	initial reservoir pressure (<i>psi</i>)
p_{wf}	bottomhole flowing pressure (<i>psi</i>)

p_{wfD}	dimensionless bottomhole flowing pressure drop (dimensionless)
p'_{wfD}	dimensionless welltest derivative (dimensionless)
PV	reservoir pore volume (ft^3)
q	flux (stb/day)
q_{Dd}	dimensionless decline-curve flux (dimensionless)
q_{last}	last production rate before buildup period ($Mscf/day$)
q_{sf}	flux at sandface (stb/day)
q_{sFD}	dimensionless flux at sandface (dimensionless)
q'_{sFD}	dimensionless welltest derivative of flux at sandface (dimensionless)
q_w	flux at surface (stb/day)
$q_{w,cutoff}$	cutoff production rate at surface ($Mscf/day$)
Q_w	cumulative production (ft^3)
r	distance (ft)
r_{DOI}	depth of investigation (ft)
r_{eD}	dimensionless reservoir radius (dimensionless)
r_{res}	reservoir radius (ft)
r_{weff}	effective wellbore radius (ft)
r_w	wellbore radius (ft)
R	reflection coefficient (dimensionless)

R^2	coefficient of determination (dimensionless)
S	skin (dimensionless)
S_w	water saturation (fraction)
t	time (hr)
t_a	adjusted time for gas (hr)
t_D	dimensionless time (dimensionless)
t_{Dd}	dimensionless decline-curve time (dimensionless)
t_e	material balance time (hr)
t_{elf}	time of end of linear flow (hr)
t_h	production history used for $w(\tau)$ inversion (day)
t_{LOD}	time to detect roundtrip pressure front propagation under LOD (day)
t_p	total production time before shut-in or other rate change (hr)
t_{prod}	production period (day)
t_s	superposition time (hr)
$t(a/2, dof)$	Student's t-distribution with confidence level a and degree of freedom
T	transmission coefficient (dimensionless)
T_{res}	reservoir temperature ($^{\circ}F$)
$V(t)$	generalized time-dependent volume integral (ft^3)
$V(\tau, t)$	generalized incomplete volume integral (ft^3)

$V_d(t)$	generalized drainage volume (ft^3)
V_{det}	reservoir pore volume detected during inversion (ft^3)
V_{DP}	Dykstra-Parsons coefficient (dimensionless)
$V_n(t)$	volume moment integral ($ft^3 \cdot hr^{n/2}$)
$V_n(\tau, t)$	incomplete volume moment integral ($ft^3 \cdot hr^{n/2}$)
$V_p(\tau)$	pore volume (ft^3)
V_{res}	reservoir volume (ft^3)
V_w	wellbore volume (ft^3)
$w(\tau)$	derivative of pore volume with respect to τ ($ft^3/hr^{1/2}$)
w_f	fracture width (in)
w_{Left}	$w(\tau)$ at the outer edge of the inner domain ($ft^3/hr^{1/2}$)
w_{res}	reservoir width (ft)
w_{Right}	$w(\tau)$ at the inner edge of the outer domain ($ft^3/hr^{1/2}$)
$W(t)$	generalized pressure drop integral (hr)
$W(\tau, t)$	generalized incomplete pressure drop integral (hr)
$W_n(t)$	pressure drop moment integral ($hr^{(n+2)/2}$)
$W_n(\tau, t)$	incomplete pressure drop moment integral ($hr^{(n+2)/2}$)
\vec{x}	Cartesian spatial coordinate vector

x_f	fracture half length (<i>ft</i>)
x_s	fracture spacing (<i>ft</i>)
$X(t)$	generalized average pressure drop integral ($ft^3 \cdot hr$)
$X(\tau, t)$	generalized incomplete average pressure drop integral ($ft^3 \cdot hr$)
$X_n(t)$	average pressure drop moment integral ($ft^3 \cdot hr^{(n+2)/2}$)
$X_n(\tau, t)$	incomplete average pressure drop moment integral ($ft^3 \cdot hr^{(n+2)/2}$)
\hat{y}	data estimate from linear regression analysis

Greek letters

α	hydraulic diffusivity (ft^2/hr)
α_i	hydraulic diffusivity of the inner domain (ft^2/hr)
α_k	coefficient of the k^{th} basis function
δ	Dirac delta function
Δp	pressure drop (in time) (<i>psi</i>)
Δp_{PSS}	PSS pressure difference (in space) (<i>psi</i>)
Δp_u	pressure drop of the fixed unit rate drawdown ($psi/stb/day$)
Δp_{ws}	BHP change during shut-in period (<i>psi</i>)
$\Delta p'$	welltest derivative (<i>psi</i>)
Δt	shut-in time (<i>hr</i>)

Δt_s	effective shut-in time (hr)
Θ	Heaviside step function
λ	weight of the roughness penalty term (dimensionless)
μ	fluid viscosity (cp)
$\mu_{\ln k}$	average of the natural log permeability (dimensionless)
$\bar{\mu}_g$	average gas viscosity (cp)
ξ	Boltzmann variable (dimensionless)
ξ_{DOI}	depth of investigation in terms of the Boltzmann variable (dimensionless)
$\sigma_{\ln k}$	standard deviation of the natural log permeability (dimensionless)
τ	diffusive time of flight ($hr^{1/2}$)
τ_{DOI}	depth of investigation in terms of the diffusive time of flight ($hr^{1/2}$)
τ_{fs}	fracture spacing in terms of the diffusive time of flight ($hr^{1/2}$)
τ_{LOD}	limit of detectability in terms of the diffusive time of flight ($hr^{1/2}$)
τ_d	diffusive time of flight at the discontinuity in $w(\tau)$ ($hr^{1/2}$)
τ_{det}	diffusive time of flight detected during inversion ($hr^{1/2}$)
τ_{max}	upper limit of diffusive time of flight during inversion ($hr^{1/2}$)
τ_w	diffusive time of flight at wellbore radius ($hr^{1/2}$)
τ_{wf}	diffusive time of flight at effective radius ($hr^{1/2}$)
τ_{res}	diffusive time of flight at reservoir boundary ($hr^{1/2}$)

ϕ	porosity (fraction)
$\phi_k(\tau)$	the k^{th} basis function
ψ	bi-streamfunction (dimensionless)
χ	bi-streamfunction (dimensionless)
ω	frequency of the asymptotic expansion (s^{-1})

Abbreviations

1-D	one dimensional
2-D	two dimensional
3-D	three dimensional
BDF	boundary dominated flow
BLF	bounded linear flow
BRF	bounded radial flow
BU	buildup
DCA	decline curve analysis
DCL	dimensionless correlation length
DOI	depth of investigation
DTOF	diffusive time of flight
EUR	estimated ultimate recovery
FMB	flowing material balance
FMM	Fast Marching Methods
HF	hydraulic fracture

HI	Heterogeneity Index
IALF	infinite acting linear flow
IARF	infinite acting radial flow
IASF	infinite acting spherical flow
ICF	infinite conductivity fracture flow
LOD	limit of detectability
MFSS	modified Friedman's Super Smoother
MLRA	Moving Linear Regression Analysis
MTFW	multiple transverse fracture wells
ODE	ordinary differential equation
PSS	pseudo steady state
PPSS	pseudo pseudo steady state
PTA	pressure transient analysis
PV	pore volume
RNP	rate normalized pressure drop
RTA	rate transient analysis
SRV	stimulated reservoir volume
UR	ultimate recovery

REFERENCES

- Agarwal, R.G., Al-Hussainy, R., and Ramey, H.J., Jr. 1970. An Investigation of Wellbore Storage and Skin Effect in Unsteady Liquid Flow: I. Analytical Treatment. *SPE Journal* **10** (03): 279-290. DOI: 10.2118/2466-PA
- Agarwal, R.G., Gardner, D.C., Kleinstieber, S.W. et al. 1999. Analyzing Well Production Data Using Combined-Type-Curve and Decline-Curve Analysis Concepts. *SPE Reservoir Evaluation & Engineering* **2** (05): 478-486. DOI: 10.2118/57916-PA
- An, C., Fang, Y., Liu, S. et al. 2017. Impacts of Matrix Shrinkage and Stress Changes on Permeability and Gas Production of Organic-Rich Shale Reservoirs. Paper presented at the SPE Reservoir Characterisation and Simulation Conference and Exhibition, Abu Dhabi, UAE, 8–10 May 2017. Society of Petroleum Engineers. DOI: 10.2118/186029-MS.
- Arps, J.J. 1945. Analysis of Decline Curves. *Transactions of the AIME* **160** (1). DOI: 10.2118/945228-G
- Barker, J.A. 1988. A Generalized Radial Flow Model for Hydraulic Tests in Fractured Rock. *Water Resources Research* **24** (10): 1796-1804. DOI: 10.1029/WR024i010p01796
- Bear, J. 1972. *Dynamics of Fluids in Porous Media*. Mineola, NY: Dover. Original edition. ISBN 978-0486656755.
- Bello, R.O. and Wattenbarger, R.A. 2010. Modelling and Analysis of Shale Gas Production with a Skin Effect. *Journal of Canadian Petroleum Technology* **49** (12): 37-48. DOI: 10.2118/143229-PA
- Bourdet, D. 2002. *Well Test Analysis: The Use of Advanced Interpretation Models*. Amsterdam, The Netherlands: Elsevier. Original edition. ISBN 978-0444509680.
- Bourdet, D., Whittle, T., Douglas, A. et al. 1983. A New Set of Type Curves Simplifies Well Test Analysis. *World Oil*: 95-106.
- Cipolla, C. and Wallace, J. 2014. Stimulated Reservoir Volume: A Misapplied Concept? Paper presented at the SPE Hydraulic Fracturing Technology Conference, The Woodlands, Texas, 4-6 February 2014. Society of Petroleum Engineers. DOI: 10.2118/168596-MS.

- Datta-Gupta, A. and King, M.J. 2007. *Streamline Simulation: Theory and Practice*. Richardson, Texas: Society of Petroleum Engineers. Original edition. ISBN 978-1555631116.
- Datta-Gupta, A., Xie, J., Gupta, N. et al. 2011. Radius of Investigation and Its Generalization to Unconventional Reservoirs. *Journal of Petroleum Technology* **63** (07): 52-55. DOI: 10.2118/0711-0052-JPT
- Deng, L. and King, M.J. 2018. Theoretical Investigation of the Transition from Spontaneous to Forced Imbibition. Paper presented at the SPE Improved Oil Recovery Conference, Tulsa, Oklahoma, 14-18 April 2018. Society of Petroleum Engineers. DOI: 10.2118/190309-MS.
- Duong, A.N. 2011. Rate-Decline Analysis for Fracture-Dominated Shale Reservoirs. *SPE Reservoir Evaluation & Engineering* **14** (03): 377-387. DOI: 10.2118/137748-PA
- Dykstra, H. and Parsons, R. 1950. The Prediction of Oil Recovery by Water Flood. *Secondary Recovery of Oil in the United States (2nd Edition)*: 160-174.
- Fetkovich, M.J. 1980. Decline Curve Analysis Using Type Curves. *Journal of Petroleum Technology* **32** (06): 1065-1077. DOI: 10.2118/4629-PA
- Friedman, J.H. 1984. A Variable Span Smoother. *Laboratory for Computational Statistics*.
- Fujita, Y., Datta-Gupta, A., and King, M.J. 2016. A Comprehensive Reservoir Simulator for Unconventional Reservoirs That Is Based on the Fast Marching Method and Diffusive Time of Flight. *SPE Journal* **21** (06): 2276-2288. DOI: 10.2118/173269-PA
- Gelhar, L.W. and Axness, C.L. 1983. Three - Dimensional Stochastic Analysis of Macrodispersion in Aquifers. *Water Resour. Res.* **19** (1): 161-180. DOI: 10.1029/WR019i001p00161
- Green, P.J. and Silverman, B.W. 1994. *Nonparametric Regression and Generalized Linear Models a Roughness Penalty Approach*. Boca Raton, Florida: Chapman and Hall/CRC. Original edition. ISBN 978-0-412-30040-0.
- Gringarten, A.C., Al-Lamki, A., Daungkaew, S. et al. 2000. Well Test Analysis in Gas-Condensate Reservoirs. Paper presented at the SPE Annual Technical Conference and Exhibition, Dallas, Texas, 1-4 October 2000. Society of Petroleum Engineers. DOI: 10.2118/62920-MS.

- Gringarten, A.C., Ramey, H.J., Jr., and Raghavan, R. 1975. Applied Pressure Analysis for Fractured Wells. *Journal of Petroleum Technology* **27** (07): 887-892. DOI: 10.2118/5496-PA
- Guo, X., Kim, J., and Killough, J.E. 2017. Hybrid Mpi-Openmp Scalable Parallelization for Coupled Non-Isothermal Fluid-Heat Flow and Elastoplastic Geomechanics. Paper presented at the SPE Reservoir Simulation Conference, Montgomery, Texas, 20-22 February 2017. Society of Petroleum Engineers. DOI: 10.2118/182665-MS.
- Guo, X., Song, H., Wu, K. et al. 2018. Pressure Characteristics and Performance of Multi-Stage Fractured Horizontal Well in Shale Gas Reservoirs with Coupled Flow and Geomechanics. *Journal of Petroleum Science and Engineering* **163**: 1-15. DOI: <https://doi.org/10.1016/j.petrol.2017.12.038>
- Gupta, N. 2012. A Novel Approach for the Rapid Estimation of Drainage Volume, Pressure and Well Rates, Texas A&M University.
- Havlena, D. and Odeh, A.S. 1963. The Material Balance as an Equation of a Straight Line. *Journal of Petroleum Technology* **15** (08): 896-900. DOI: 10.2118/559-PA
- Havlena, D. and Odeh, A.S. 1964. The Material Balance as an Equation of a Straight Line—Part II, Field Cases. *Journal of Petroleum Technology* **16** (07): 815-822. DOI: 10.2118/869-PA
- Hawkins, M.F., Jr. 1956. A Note on the Skin Effect. *Journal of Petroleum Technology* **8** (12): 65-66. DOI: 10.2118/732-G
- He, Y., Cheng, S., Qin, J. et al. 2018a. Pressure-Transient Behavior of Multisegment Horizontal Wells with Nonuniform Production: Theory and Case Study. *Journal of Energy Resources Technology* **140** (9): 093101-093101-093109. DOI: 10.1115/1.4039875
- He, Y., Cheng, S., Rui, Z. et al. 2018b. An Improved Rate-Transient Analysis Model of Multi-Fractured Horizontal Wells with Non-Uniform Hydraulic Fracture Properties. *Energies* **11** (2). DOI: 10.3390/en11020393
- Holditch, S.A. 2013. Unconventional Oil and Gas Resource Development—Let's Do It Right. *Journal of Unconventional Oil and Gas Resources* **1-2**: 2-8. DOI: doi.org/10.1016/j.juogr.2013.05.001
- Horne, R.N. 1995. *Modern Well Test Analysis: A Computer-Aided Approach*. Palo Alto, CA: Petroway, Inc. Original edition. ISBN 978-0962699214.
- Houze, O., Viturat, D., and Fjare, O.S. 2015. *Dynamic Data Analysis*.

- Huang, J., Olalotiti-Lawal, F., King, M.J. et al. 2017. Modeling Well Interference and Optimal Well Spacing in Unconventional Reservoirs Using the Fast Marching Method. Paper presented at the SPE/AAPG/SEG Unconventional Resources Technology Conference, Austin, Texas, 24-26 July 2017. DOI: 10.15530/URTEC-2017-2688841.
- Hurst, W. 1953. Establishment of the Skin Effect and Its Impediment to Fluid-Flow into a Well Bore. *The Petroleum Engineer* **25**: B6-B16.
- Iino, A., Vyas, A., Huang, J. et al. 2017. Rapid Compositional Simulation and History Matching of Shale Oil Reservoirs Using the Fast Marching Method. In *Unconventional Resources Technology Conference*. Austin, Texas, 24-26 July 2017.
- Ilk, D., Okouma Mangha, V., and Blasingame, T.A. 2011. Characterization of Well Performance in Unconventional Reservoirs Using Production Data Diagnostics. Paper presented at the SPE Annual Technical Conference and Exhibition, Denver, Colorado, 30 October-2 November 2011. Society of Petroleum Engineers. DOI: 10.2118/147604-MS.
- Jackson, J.D. 1998. *Classical Electrodynamics*. New York: John Wiley & Sons. Original edition. ISBN 978-0-471-30932-1.
- Jauch, J.M. and Rohrlich, F. 1976. *The Theory of Photons and Electrons*. New York: Springer-Verlag. Original edition. ISBN 978-0387072951.
- Jennings Jr., J.W., Ruppel, S.C., and Ward, W.B. 2000. Geostatistical Analysis of Permeability Data and Modeling of Fluid-Flow Effects in Carbonate Outcrops. *SPE Reservoir Evaluation & Engineering* **3** (04): 292-303. DOI: 10.2118/65370-PA
- Jensen, J.L., Lake, L.W., Corbett, P.W.M. et al. 1997. *Statistics for Petroleum Engineers and Geoscientists*. Upper Saddle River, New Jersey: Prentice Hall PTR. Original edition. ISBN 978-0131318557.
- King, M.J., Wang, Z., and Datta-Gupta, A. 2016. Asymptotic Solutions of the Diffusivity Equation and Their Applications. Paper presented at the SPE Europec featured at 78th EAGE Conference and Exhibition, Vienna, Austria, 30 May-2 June 2016. Society of Petroleum Engineers. DOI: 10.2118/180149-MS.
- Kou, R., Alafnan, S.F.K., and Akkutlu, I.Y. 2017. Multi-Scale Analysis of Gas Transport Mechanisms in Kerogen. *Transport in Porous Media* **116** (2): 493-519. DOI: 10.1007/s11242-016-0787-7

- Kou, R., Moridis, G.J., and Blasingame, T.A. 2018. Analysis and Modeling of Proppant Transport in Inclined Hydraulic Fractures. Paper presented at the SPE Hydraulic Fracturing Technology Conference and Exhibition, The Woodlands, Texas, 23-25 January 2018. Society of Petroleum Engineers. DOI: 10.2118/189856-MS.
- Kuchuk, F., Biryukov, D., and Fitzpatrick, T. 2015. Fractured-Reservoir Modeling and Interpretation. *SPE Journal* **20** (05): 983-1004. DOI: 10.2118/176030-PA
- Kuchuk, F.J. 2009. Radius of Investigation for Reserve Estimation from Pressure Transient Well Tests. Paper presented at the SPE Middle East Oil and Gas Show and Conference, Manama, Bahrain, 15-18 March 2009. Society of Petroleum Engineers. DOI: 10.2118/120515-MS.
- Kucuk, F. and Brigham, W.E. 1979. Transient Flow in Elliptical Systems. *SPE Journal* **19** (06): 401-410. DOI: 10.2118/7488-PA
- Kulkarni, K.N., Datta-Gupta, A., and Vasco, D.W. 2001. A Streamline Approach for Integrating Transient Pressure Data into High-Resolution Reservoir Models. *SPE Journal* **6** (03): 273-282. DOI: 10.2118/74135-PA
- Lee, J. 1982. *Well Testing*. Richardson, TX: Society of Petroleum Engineers. Original edition. ISBN 978-0895203175.
- Lee, J., Rollins, J.N., and Spivey, J.P. 2003. *Pressure Transient Testing*. Richardson, TX: Society of Petroleum Engineers. Original edition. ISBN 978-1555630997.
- Lee, W.J. and Sidle, R.E. 2010. Gas Reserves Estimation in Resource Plays. Paper presented at the SPE Unconventional Gas Conference, Pittsburgh, Pennsylvania, 23-25 February 2010. Society of Petroleum Engineers. DOI: 10.2118/130102-MS.
- Li, C. and King, M.J. 2016. Integration of Pressure Transient Data into Reservoir Models Using the Fast Marching Method. Paper presented at the SPE Europec featured at 78th EAGE Conference and Exhibition, Vienna, Austria, 30 May-2 June 2016. Society of Petroleum Engineers. DOI: 10.2118/180148-MS.
- Li, H. 2016. Wave Propagation Models Capture Pressure Behavior in Heterogeneous Unconventional Reservoirs. Paper presented at the SPE Annual Technical Conference and Exhibition, Dubai, UAE, 26-28 September 2016. Society of Petroleum Engineers. DOI: 10.2118/184504-STU.
- Li, J., Yu, W., Guerra, D. et al. 2018. Modeling Wettability Alteration Effect on Well Performance in Permian Basin with Complex Fracture Networks. *Fuel* **224**: 740-751. DOI: <https://doi.org/10.1016/j.fuel.2018.03.059>

- Liu, S. and Valkó, P.P. 2017. Optimization of Spacing and Penetration Ratio for Infinite-Conductivity Fractures in Unconventional Reservoirs: A Section-Based Approach. *SPE Journal* **22** (06): 1877-1892. DOI: 10.2118/186107-PA
- Mahmoud, O., Ibrahim, M., Pieprzica, C. et al. 2018. Eur Prediction for Unconventional Reservoirs: State of the Art and Field Case. Paper presented at the SPE Trinidad and Tobago Section Energy Resources Conference, Port of Spain, Trinidad and Tobago, 25-26 June 2018. Society of Petroleum Engineers. DOI: 10.2118/191160-MS.
- Matthews, C.S., Brons, F., and Hazebroek, P. 1954. A Method for Determination of Average Pressure in a Bounded Reservoir. *Petroleum Transactions* **201**: 182-191.
- Muskat, M. 1949. *Physical Principles of Oil Field Production*. New York: McGraw-Hill Book Co. Original edition. ISBN 978-0934634076.
- Nunna, K., Zhou, P., and King, M.J. 2015. Novel Diffuse Source Pressure Transient Upscaling. Paper presented at the SPE Reservoir Simulation Symposium, Houston, Texas, 23-25 February 2015. Society of Petroleum Engineers. DOI: 10.2118/173293-MS.
- Palacio, J.C. and Blasingame, T.A. 1993. Decline-Curve Analysis with Type Curves - Analysis of Gas Well Production Data. Paper presented at the Low Permeability Reservoirs Symposium, Denver, Colorado, 26-28 April 1993. Society of Petroleum Engineers. DOI: 10.2118/25909-MS.
- Pasumarti, A., Sengupta, S., and Michael, J.K. 2015. A Novel Transient Simulation Based Methodology for the Calculation of Permeability in Pore Network Models. Paper presented at the Abu Dhabi International Petroleum Exhibition and Conference, Abu Dhabi, UAE, 9-12 November 2015. Society of Petroleum Engineers. DOI: 10.2118/177884-MS.
- Prats, M. 1961. Effect of Vertical Fractures on Reservoir Behavior-Incompressible Fluid Case. *SPE Journal* **1** (02): 105-118. DOI: 10.2118/1575-G
- Ramsay, J.O., Hooker, G., and Graves, S. 2009. *Functional Data Analysis with R and Matlab*. New York: Springer Science+Business Media, LLC. Original edition. ISBN 978-0-387-98184-0.
- Satman, A., Eggenschwiler, M., and Ramey, H.J., Jr. 1980. Interpretation of Injection Well Pressure Transient Data in Thermal Oil Recovery. Paper presented at the SPE California Regional Meeting, Los Angeles, California, 9-11 April 1980. Society of Petroleum Engineers. DOI: 10.2118/8908-MS.
- Sethian, J. 1999. Fast Marching Methods. *SIAM Review* **41** (2): 199-235.

- Shanley, K.W., Cluff, R.M., and Robinson, J.W. 2004. Factors Controlling Prolific Gas Production from Low-Permeability Sandstone Reservoirs: Implications for Resource Assessment, Prospect Development, and Risk Analysis. *AAPG Bulletin* **88** (8): 1083-1121. DOI: 10.1306/03250403051
- Sharma, V.K. 2016. New Approach for Production Analysis of Shale Gas/Oil Reservoirs, Texas A&M University.
- Song, B. and Ehlig-Economides, C.A. 2011. Rate-Normalized Pressure Analysis for Determination of Shale Gas Well Performance. Paper presented at the North American Unconventional Gas Conference and Exhibition, The Woodlands, Texas, 14-16 June 2011. Society of Petroleum Engineers. DOI: 10.2118/144031-MS.
- Thambynayagam, M. 2011. *The Diffusion Handbook: Applied Solutions for Engineers*. New York: McGraw-Hill. Original edition. ISBN 978-0-07-175184-1.
- Valkó, P.P. 2009. Assigning Value to Stimulation in the Barnett Shale: A Simultaneous Analysis of 7000 Plus Production Histories and Well Completion Records. Paper presented at the SPE Hydraulic Fracturing Technology Conference, The Woodlands, Texas, 19-21 January 2009. Society of Petroleum Engineers. DOI: 10.2118/119369-MS.
- Valkó, P.P. and Lee, W.J. 2010. A Better Way to Forecast Production from Unconventional Gas Wells. Paper presented at the SPE Annual Technical Conference and Exhibition, Florence, Italy, 19-22 September 2010. Society of Petroleum Engineers. DOI: 10.2118/134231-MS.
- Van Everdingen, A.F. 1953. The Skin Effect and Its Influence on the Productive Capacity of a Well. *Journal of Petroleum Technology* **5** (06): 171-176. DOI: 10.2118/203-G
- Van Everdingen, A.F. and Hurst, W. 1949. The Application of the Laplace Transformation to Flow Problems in Reservoirs. *Journal of Petroleum Technology* **1** (12): 305-324. DOI: 10.2118/949305-G
- Vasco, D.W., Keers, H., and Karasaki, K. 2000. Estimation of Reservoir Properties Using Transient Pressure Data an Asymptotic Approach. *Water Resources Research* **36** (12): 3447-3465. DOI: 10.1029/2000WR900179
- Virieux, J., Flores-Luna, C., and Gibert, D. 1994. Asymptotic Theory for Diffusive Electromagnetic Imaging. *Geophysics J. Int.* **119** (3): 857-868.
- Wang, Z. 2013. A Parametric Study on Reservoir Cooling for Enhanced Oil Recovery from Co₂ Injection, The Pennsylvania State University.

- Wang, Z., Khanzode, A., and Johns, R.T. 2016. A Parametric Study of Reservoir Cooling for Enhanced Recovery by Carbon Dioxide Flooding. *SPE Journal* **21** (03): 839-852. DOI: 10.2118/170626-PA
- Wang, Z., Khanzode, A.M., and Johns, R.T. 2014. A Parametric Study of Reservoir Cooling for Enhanced Recovery by Co2 Flooding. Paper presented at the SPE Annual Technical Conference and Exhibition, Amsterdam, The Netherlands, 27-29 October 2014. Society of Petroleum Engineers. DOI: 10.2118/170626-MS.
- Wang, Z., Li, C., and King, M.J. 2017. Validation and Extension of Asymptotic Solutions of Diffusivity Equation and Their Applications to Synthetic Cases. Paper presented at the SPE Reservoir Simulation Conference, Montgomery, Texas, USA, 20-22 February 2017. Society of Petroleum Engineers. DOI: 10.2118/182716-MS.
- Wang, Z., Malone, A., and King, M.J. 2018. Quantitative Production Analysis and EUR Prediction from Unconventional Reservoirs Using a Data-Driven Drainage Volume Formulation. Paper presented at the 16th European Conference on the Mathematics of Oil Recovery, Barcelona, Spain. EAGE.
- Wattenbarger, R.A., El-Banbi, A.H., Villegas, M.E. et al. 1998. Production Analysis of Linear Flow into Fractured Tight Gas Wells. Paper presented at the SPE Rocky Mountain Regional/Low-Permeability Reservoirs Symposium, Denver, Colorado, 5-8 April 1998. Society of Petroleum Engineers. DOI: 10.2118/39931-MS.
- Wattenbarger, R.A. and Ramey, H.J., Jr. 1970. An Investigation of Wellbore Storage and Skin Effect in Unsteady Liquid Flow: Ii. Finite Difference Treatment. *SPE Journal* **10** (03): 291-297. DOI: 10.2118/2467-PA
- Willhite, G.P. 1986. *Waterflooding*. Spe Textbook Series. Richardson, TX: Society of Petroleum Engineers. Original edition. ISBN 978-1555630058.
- Winestock, A.G. and Colpitts, G.P. 1965. Advances in Estimating Gas Well Deliverability. *Journal of Canadian Petroleum Technology* **4** (03): 111-119. DOI: 10.2118/65-03-01
- Xie, J., Gupta, N., King, M.J. et al. 2012a. Depth of Investigation and Depletion Behavior in Unconventional Reservoirs Using Fast Marching Methods. Paper presented at the SPE Europec/EAGE Annual Conference, Copenhagen, Denmark, 4-7 June 2012. Society of Petroleum Engineers. DOI: 10.2118/154532-MS.
- Xie, J., Yang, C., Gupta, N. et al. 2012b. Integration of Shale Gas Production Data and Microseismic for Fracture and Reservoir Properties Using Fast Marching Method. Paper presented at the SPE Eastern Regional Meeting, Lexington, Kentucky, 3-5 October 2012. Society of Petroleum Engineers. DOI: 10.2118/161357-MS.

- Xie, J., Yang, C., Gupta, N. et al. 2015a. Depth of Investigation and Depletion in Unconventional Reservoirs with Fast-Marching Methods. *SPE Journal* **20** (04): 831-841. DOI: 10.2118/154532-PA
- Xie, J., Yang, C., Gupta, N. et al. 2015b. Integration of Shale-Gas-Production Data and Microseismic for Fracture and Reservoir Properties with the Fast Marching Method. *SPE Journal* **20** (02): 347-359. DOI: 10.2118/161357-PA
- Xue, X., Yang, C., Sharma, V.K. et al. 2016. Reservoir and Fracture Flow Characterization Using a Novel W(T) Formulation. Paper presented at the SPE/AAPG/SEG Unconventional Resources Technology Conference, San Antonio, Texas, 1-3 August 2016. Unconventional Resources Technology Conference. DOI: 10.15530/URTEC-2016-2440083.
- Yang, C. 2017. Simulation and Analysis of Unconventional Reservoirs Using Fast Marching Method and Transient Drainage Volume, Texas A&M University.
- Yang, C., Sharma, V.K., Datta-Gupta, A. et al. 2015. A Novel Approach for Production Transient Analysis of Shale Gas/Oil Reservoirs. Paper presented at the Unconventional Resources Technology Conference, San Antonio, Texas, 20-22 July 2015. Unconventional Resources Technology Conference. DOI: 10.15530/URTEC-2015-2176280.
- Yang, C., Xue, X., Huang, J. et al. 2016. Rapid Refracturing Candidate Selection in Shale Reservoirs Using Drainage Volume and Instantaneous Recovery Ratio. Paper presented at the Unconventional Resources Technology Conference, San Antonio, Texas, USA, 1-3 August 2016.
- Zhang, Y., Bansal, N., Fujita, Y. et al. 2014. From Streamlines to Fast Marching: Rapid Simulation and Performance Assessment of Shale Gas Reservoirs Using Diffusive Time of Flight as a Spatial Coordinate. Paper presented at the SPE Unconventional Resources Conference, The Woodlands, Texas, 1-3 April 2014. Society of Petroleum Engineers. DOI: 10.2118/168997-MS.
- Zhang, Y., Yang, C., King, M.J. et al. 2013. Fast-Marching Methods for Complex Grids and Anisotropic Permeabilities: Application to Unconventional Reservoirs. Paper presented at the SPE Reservoir Simulation Symposium, The Woodlands, Texas, 18-20 February 2013. Society of Petroleum Engineers. DOI: 10.2118/163637-MS.